



UNIVERSITÀ  
DEGLI STUDI  
DI PADOVA

UNIVERSITA' DEGLI STUDI DI PADOVA  
**Department of Industrial Engineering**  
Master's Degree Course in Materials Engineering

***Additive manufacturing of SiOC glass with the UV Assisted-  
Direct Ink Writing technique***

Supervisor: Prof. Paolo Colombo

Student: Alessia Barbisan,  
2018729

Academic year 2021/2022

## Abstract

The use of additive manufacturing techniques allows to build complex 3D structures from a virtual model and to overcome many problems of traditional ceramic materials production techniques. Among the various AM techniques, a relatively new hybrid technique is DIW UV Assisted, which allows you to print complex structures through the extrusion of photocurable ink which cures through UV illumination. The use of photocurable preceramic polymer resins allows to exploit the advantage offered by the polymeric state for forming by extrusion and at the same time allows the obtaining of ceramic products through the exposure of the printed pieces to the pyrolysis heat treatment, maintaining the desired shape.

This thesis work is focused on the development of an ink based on preceramic polymers that possessed the suitable characteristics to be used in the DIW UV Assisted technique to produce suspended structures of various shapes capable of resisting the pyrolysis treatment to obtain formed ceramic structures. The inks produced were then characterized from the rheological and photoreactive point of view and the various printed structures were characterized from the morphological, microstructural and mechanical point of view. The work is divided into 5 chapters. In the first chapter an introduction is made on what are the main AM techniques, the DIW UV Assisted technique is described with particular focus on the characteristics that the inks must possess to be usable and an overview of what preceramic polymers are and what is their microstructure after pyrolysis heat treatment is provided. The second chapter describes the main characterization techniques used from a theoretical point of view. The third chapter, *Materials and methods*, describes the materials used and the analysis procedures carried out during the experimental work; the fourth chapter illustrates in the first part the ink optimization and then reports the results for each characterization technique. A final section of this chapter reports new approaches to the use of inks, through the use of a robotic arm or for the construction of more complex structures. In the final chapter the conclusions are drawn.

## **Acknowledgements**

I would like to thank Prof. Paolo Colombo for the opportunity offered to me to carry out this thesis work and Kai Huang for supporting me during the months of activity in the laboratory and offering me valuable teachings. I also want to thank my family and everyone who supported me along the way.

## List of Tables

**Table 1.1.** *Main Characteristics of Additive Manufacturing Technologies used for Ceramics.*

**Table 2.1.** *Definitions of various types of densities.*

**Table 2.2.** *A comparison between OM and SEM microscopies is reported.*

**Table 2.3.** *Comparison of the characteristic values of the tensile test and the compression test.*

**Table 3.1.** *Chemicals.*

**Tables 3.2.** *Inks compositions.*

**Table 3.3.** *Absorption characteristics of photoinitiators.*

**Table 3.4.** *Molecular and thermal properties of silicone resins.*

**Table 3.5.** *Absolute values of the intensity of the lamp [Omniculture, series 2000].*

**Table 3.6.** *Ceramization/Consolidation Techniques Applied to Preceramic Polymers.*

**Table 4.1.** *Linear variation of the diameter along the cantilever beams.*

**Table 4.2.** *Deflection angle.*

**Table 4.3.** *Average filament cross-section.*

**Table 4.4.** *Minimum height reached by the filament and percentage variation compared to the initial extreme.*

**Table 4.5.** *Values of  $n$  and  $K$  obtained from the viscosity curves.*

**Table 4.6.** *Numerical values of variation of gel point as a function of UV intensity.*

**Table 4.7.** *Shrinkage.*

**Table 4.8.** *Skeletal and true density for the three inks.*

**Table 4.9.** *Mean stress and strain values and standard deviations.*

## List of Figures

**Figure 1.1.** Phases of an additive manufacturing process.

**Figure 1.2.** The use of additive manufacturing in the different sectors.

**Figure 1.3.** Schematic of AM technologies.

**Figure 1.4.** Photoinduced radical generation, initiation and propagation.

**Figure 1.5.** Thiol-ene reaction.

**Figure 1.6.** Network formation via step-growth polymerization of epoxy thermosets (above) and radical chain growth of acrylates (below).

**Figure 1.7.** Epoxy structural monomers and reactive diluents for thermoset resins.

**Figure 1.8.** Main classes of Si-polymer as precursors for ceramics (left); general oversimplified representation of the molecular structure of preceramic organosilicon compounds (right).

**Figure 1.9.** Thermal decomposition of silicon-based polymers.

**Figure 1.10.** General types of poly(organo)silsesquioxanes.

**Figure 1.11.** Schematic representation of an amorphous 800-1000°C silicon oxycarbide glass structure.

**Figure 1.12.** Illustration of the structural evolution of free carbon during pyrolysis of preceramic polymers.

**Figure 2.1.** Methods of Thermal Analysis.

**Figure 2.2.** Examples of thermobalances (left); thermocouple positioning (right).

**Figure 2.3.** Geometry of Bragg-Brentano.

**Figure 2.4.** Peak width (left); influence of crystalline deformation (right).

**Figure 2.5.** Michelson interferometer.

**Figure 2.6.** Example of a helium pycnometer with the sample chamber before the reference chamber.

**Figure 2.7.** Rotational rheometer. Schemes of the commercial geometrical configurations.

**Figure 2.8.** The first two images from the left represent a cone-plate configuration while the rightmost image represents a parallel plate geometry.

**Figure 2.9.** SEM structure.

**Figure 2.10.** Stress-compression curve.

**Figure 3.1.** Conditioning mixer (ARE-250, THINKY).

**Figure 3.2.** Photoinduced cleavage of Irgacure 819.

**Figure 3.3.** (a) Section of the molecular structure of the commercial poly(methyl-silsesquioxane) MK linear and crosslinked polymer network units; (b) structural units containing OH- and OEt- functional groups; (c) H44 structure.

**Figure 3.4.** Chemical structure of TEGO RC 711 (left); TEGDA (center); PETTA (right).

**Figure 3.5.** LEDs orientation.

**Figure 3.6.** Examples of Gcode files: spiral (left); "A" test (center); scaffold (right).

**Figure 3.7.** Decrease over time in the intensity of the UV setup, measured on the power meter (Thorlabs, PM400 Optical Power Meter).

**Figure 4.1.** Two-layer structure used in the first prints.

**Figure 4.2.** Diameter-speed correlation for ink C at a pressure of 0.5 bar.

**Figure 4.3.** Comparison between two sections of filaments printed with C ink at 0.5 bar. Left speed 20%, right speed 100%.

**Figure 4.4.** Composition spirals in the figure with 2% of the total FS. The shape is not maintained.

**Figure 4.5.** Formation of the continuous filament of the ink composition 6H44-2PETTA-2%PI.

**Figure 4.6.** Vertical and inclined structures.

**Figure 4.7.** Increase in diameter and pitch as print speed increases for 6H44-2PETTA-2%PI ink.

**Figure 4.8.** The two graphs at the top represent the increase in the diameter and pitch of the spirals as the printing speed for the 6H44-2PETTA-2%PI ink increases. The graph below represents filament diameter vs. extrusion pressure according to different printing speeds for the ink 6H44-2PETTA-4%PI.

**Figure 4.9.** Comparison of spirals printed with 6H44-2PETTA-2%PI (left) and 6H44-2PETTA-4%PI (right) inks.

**Figure 4.10.** Graphics relating to 6H44-3PETTA-4%PI ink and image of the spiral.

**Figure 4.11.** Free form structure.

**Figure 4.12.** Results relating to 6H44-6TEGO-4%PI ink.

**Figure 4.13.** Cantilever beam structures.

**Figure 4.14.** "A" test.

**Figure 4.15.** Height variation at various measurement points for the longer filament for the ink 6H44-2PETTA.4% (top left) and 6H44-3PETTA-4% (top and right and bottom) at different printing speeds.

**Figure 4.16.** Images of the "A" test samples. Figures A and B represent the 6H44-2PETTA ink at 80% printing speed. The deflection of the filament can be seen. Figure C represents the 6H44-3PETTA ink at 0.5 bar 100%. It can be seen that the filaments, even the longest, appear straight.

**Figure 4.17.** Viscoelastic behaviour.

**Figure 4.18.** Viscosity profiles.

**Figure 4.19.** Shear stress versus shear rate where the red lines are the Herschel-Buckley fits.

**Figure 4.20.a,b.** Amplitude sweep test at a frequency of 1 Hz of 6H44-2PETTA-4%PI and 6H44-3PETTA-4%PI and 6H44-6TEGO-4%PI.

**Figure 4.21.** 3ITT chart for the two PETTA-containing inks.

**Figure 4.22.a,b,c.** Reaching the gelation point for the three inks at 4-5% and 20% UV intensity.

**Figure 4.23.** Variation of the gel point according to the intensity of the UV light.

**Figure 4.24.** Variation of viscosity as a function of time.

**Figure 4.25.** Curing depth of the three inks as a function of exposure time.

**Figure 4.26.** TGA pure components of the inks.

**Figure 4.27.** Comparison of TGA inks with each other and with respect to pure components.

**Figure 4.28.** The scaffolds were printed 0.75 bar for 3 PETTA, 1 bar for 2 PETTA and 0.25 bar for TEGO with a speed up to 150-200% of the 450 mm/min of the Gcode.

**Figure 4.29.** Internal section of 6H44-2PETTA scaffold.

**Figure 4.30.** Pyrolyzed scaffolds.

**Figure 4.31.** Comparison between scaffolds before and after pyrolysis.

**Figure 4.32.** SEM images for the three inks.

**Figure 4.33.** Helium pycnometer (Ultrapyc 3000, Anton Paar).

**Figure 4.34.** Strain-strain graphs for scaffolds produced with inks: 6H44-2PETTA-4%PI (left), 6H44-6TEGO-4%PI (center), 6H44-3PETTA-4% PI (right).

**Figure 4.35.** Image of the compressive strength as a function of density generated with the "CES edupack" program.

**Figure 4.36.** X-ray diffraction pattern of SiOC ceramic obtained at increasing pyrolysis temperature.

**Figure 4.37.** XRD patterns of SiOC samples annealed in air environment at various temperatures.

**Figure 4.38.** X-ray patterns of the pyrolyzed samples of each ink.

**Figure 4.39.** Green body of 6H44-3PETTA-4% ink in Match! software and revelation of impurities.

**Figure 4.40.** Infrared absorption spectra of the ink during the light-curing process.

**Figure 4.41.** FTIR spectrum in the region  $1602-1647\text{ cm}^{-1}$  and  $1761-1805\text{ cm}^{-1}$  for the three inks.

**Figure 4.42.** Conversion rate of C=C as function of ultraviolet irradiation times.

**Figure 4.43.** Robotic Arm.

**Figure 4.44.** Vertical filament (10 cm, 0.4 mm/min),

**Figure 4.45.** The intensity of the UV radiation decreases as a function of the time measured with the power meter (Thorlabs, PM400 Optical Power Meter).

**Figure 4.46.** Tetrahedra printed with the robotic arm.

**Figure 4.47.** Non-pyrolyzed knots.

**Figure 4.48.** Arched and cylindrical structures.

**Figure 4.49.** Pyrolyzed samples.

## List of Contents

<b>Abstract</b> .....	<b>2</b>
<b>Acknowledgements</b> .....	<b>3</b>
<b>List of Tables</b> .....	<b>4</b>
<b>List of Figures</b> .....	<b>5</b>
<b>Introduction</b> .....	<b>11</b>
<b>Chapter 1 – Additive manufacturing of ceramics</b> .....	<b>13</b>
1.1 – Additive manufacturing .....	13
1.2 – Advanced ceramics and AM Processing of Ceramics .....	15
1.2.1 – Indirect technologies .....	16
1.2.1.1 – Powder-Based 3D Printing (P-3DP).....	16
1.2.1.2 – Powder-Based Selective Laser sintering (P-SLS).....	16
1.2.1.3 – Stereolithography (SL) .....	16
1.2.1.4 – Slurry-Based 3DP (S-3DP) and Slurry-Based SLS (S-SLS) <sup>7</sup> .....	17
1.2.1.5 – Laminated Object Manufacturing (LOM) .....	17
1.2.2 – Direct technologies.....	18
1.2.2.1 – Direct Inkjet Printing (DIP) <sup>17</sup> .....	18
1.2.2.2 – Filament Extrusion 3D Printing: Robocasting (RC)/Direct Ink Writing (DIW), Fused Deposition Modeling (FDM).....	19
1.3 – Direct Ink Writing technique and inks.....	22
1.4 – Direct Ink Writing UV Assisted .....	24
1.4.1 – Photoresins for AM Processes.....	24
1.4.1.1 – Radical systems.....	24
1.4.1.2 – Cationic systems .....	26
1.4.1.3 – Two-Photon Initiators (2PP).....	26
1.4.2 – Fundamentals of photopolymerization .....	27
1.4.3 – Preceramic polymers inks for DIW + UV .....	29
1.5 – Preceramic Polymers .....	30
1.5.1 – Poly(organosiloxanes) <sup>58</sup> .....	33
1.5.2 – Silicon Oxycarbide Glasses <sup>77</sup> .....	34
1.5.2.1 – Free carbon .....	36
<b>Chapter 2 – Characterization techniques</b> .....	<b>39</b>
2.1 – TGA, ThermoGravimetric Analysis (“Thermal Analysis of Polymers: Fundamentals and Applications, Joseph D. Menczel, R. Bruce Prime, Wiley).....	39
2.2 – XRD, X-ray diffraction .....	42
2.3 – FTIR, Fourier-transform infrared spectroscopy .....	46
2.4 – Density measurement, Helium Pycnometer <sup>31,92,93</sup> .....	50



2.5 – Rheometer.....	53
2.6 – Microscopy (from the lectures of the "Characterization of materials" course) .....	54
2.7 – Mechanical characterization: compression test (tec-science.com).....	57
<b>Chapter 3 – Materials and methods .....</b>	<b>60</b>
3.1 – Preparation of the ink.....	60
3.1.1 – Chemicals .....	62
3.1.1.1 – Photoinitiator.....	62
3.1.1.2 – Preceramic polymer with high ceramic yield.....	63
3.1.1.3 – Photopolymer.....	65
3.2 – Printing process.....	67
3.2.1 – Printing parameters.....	70
3.2.1.1 – Effect of standoff distance.....	70
3.2.1.2 – Effect of printing speed and pressure .....	70
3.2.1.3 – Substrate <sup>101</sup> .....	72
3.2.2 – Computer-Aided Design Technology <sup>5</sup> and Gcode .....	73
3.2.3 – UV setup .....	74
3.3 – Polymer to ceramic conversion: Pyrolysis .....	76
3.4 – Characterization of the inks .....	78
3.5 – Characterization of printed and pyrolyzed samples .....	79
<b>Chapter 4 – Characterization .....</b>	<b>83</b>
4.1 – Inks .....	83
4.1.1 – Optimization .....	83
4.1.2 – Printability and Shape fidelity.....	90
4.1.2.1 – Spirals.....	91
4.1.2.2 – Deflection .....	97
4.1.3 – Rheology <sup>23</sup> .....	103
4.1.3.1 – Flow curve.....	106
4.1.3.2 – Amplitude sweep test .....	108
4.1.3.3 – Three interval thixotropy test.....	110
4.1.4 – Photorheology and UV response.....	111
4.1.4.1 – Photorheology .....	111
4.1.4.2 – Determination of cure depth.....	113
4.2 – Printed and pyrolyzed samples.....	115
4.2.1 – TGA.....	115
4.2.2 – Scaffolds .....	117
4.2.3 – Shrinkage.....	122
4.2.4 – SEM .....	123
4.2.5 – Density.....	128

4.2.6 – <i>Mechanical properties</i> .....	129
4.2.7 – <i>XRD</i> .....	132
4.2.8 – <i>FTIR</i> .....	135
4.3 – <i>Robotic arm and complex structures</i> .....	138
4.3.1 – <i>Robotic arm</i> .....	138
4.3.2 – <i>Complex structures</i> .....	140
<b>Chapter 5 – Conclusions</b> .....	<b>143</b>
<b>Appendix</b> .....	<b>145</b>
<b>Bibliography</b> .....	<b>150</b>

## Introduction

Additive Manufacturing (AM) enables the production of parts with complex 3D architectures not easily achievable with traditional manufacturing processes. The demands for products with increasing higher structural complexity and resolution, have led to the development of a number of AM technologies, such as Direct Ink Writing (DIW), Stereolithography, Powder-Based Selective Laser sintering and so on. In particular, DIW is the most common-used AM approach which was first developed in 1996 as a method for producing geometrically complex ceramic green bodies<sup>1</sup>. During the printing process, the ink comes out of a nozzle and moves in a plane following a .stl file to fabricate 3D structures layer by layer. This technique can be employed with a wide range of different raw materials for different applications and can be associated with different solidification techniques of the ink, which must be able to maintain its shape as soon as it comes out of the nozzle. In particular, the Ultraviolet-assisted direct ink write (UV-DIW) technique is a subcategory of DIW, which utilizes UV-irradiation to cross-link the extruded photopolymer resins during printing to induce gelation and shape retention after ink placement<sup>2</sup>. This and other AM techniques provides a suitable approach for fulfilling the need for near net-shape three dimensional ceramic parts with a complicated morphology. Standard techniques for ceramic processing, in fact, do not easily allow the production of complicated structures with undercuts or porosity and have numerous disadvantages including the need for hard machining post treatments that increase costs and risk damaging fragile components and the need to produce molds for each new design, making the production of a few pieces excessively expensive. Furthermore, in the last two decades, ceramic materials which can be produced from the conversion of polymeric precursors (preceramic polymers) have become particularly attractive. The preceramic polymers represent a special class of inorganic/organometallic polymer that provide ceramics with a tailored chemical composition and a closely defined nanostructural organization by proper thermal treatment, pyrolysis, under a controlled atmosphere. The possibility to manipulate the precursors of these ceramics in the polymeric phase offers the capability to model fine shapes using techniques proper of polymers. The production of Polymer-Derived-Ceramics (PDC), from silicone resins, has undergone considerable development in many areas in which advanced ceramics are required, such as automotive, aerospace, defense, energy, environmental and biomedical. They provide a good combination of high strength, superior hardness, outstanding oxidation resistance as well as excellent thermal and chemical stability. SiOC is a ceramic material that can be synthesized from silicone-based polymers precursors at much lower temperatures than SiO<sub>2</sub>, its properties are tunable depending on its carbon content and the pyrolysis temperature; for example, if the carbon content is high and the pyrolysis temperature is around 1400°C, SiOC can exhibit electrical conductivity. Recently, therefore, the advantage offered by AM techniques has been recognized on the one hand and the opportunities presented by the use of preceramic polymers on the other, so ceramic components have been produced from preceramic polymers using additive manufacturing (AM) techniques<sup>3</sup>. As regards the use of ceramic precursors in the Ultraviolet-assisted direct ink write technique, the formulations of the inks must contain precursors able of supplying the functional groups capable of reacting and giving rise to the polymerization and solidification process of the ink and other

precursors with a high ceramic content, so that after the heat treatment the printed piece maintains its shape without excessive shrinkage, deformation or breakage.

This thesis concerns the formulation of an ink composition suitable to be applied in the Ultraviolet-assisted direct ink write AM technique for the production of self-supporting suspended structures, able to maintain the shape during printing and after heat treatment, give rise to ceramic materials of SiOC composition. The work foresees a first part of optimization of the composition of the mixture of polymeric precursors and subsequently the characterization of the inks optimized from the rheological point of view and the UV response. Furthermore, the printed samples were analysed from a thermal, microstructural, morphological point of view and their mechanical properties were evaluated.

# Chapter 1

## Additive Manufacturing of ceramics

### 1.1 – Additive manufacturing

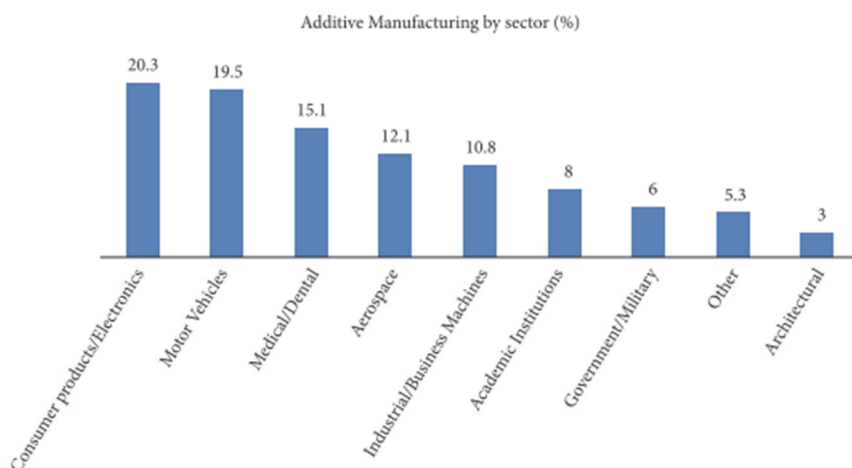
Additive manufacturing (AM) is defined as a process of joining materials to make parts from 3D model data, usually layer upon layer, as opposed to subtractive and formative manufacturing methodologies [ISO/ASTM 52900,2015, <https://www.iso.org/>]. The beginning of the use of Additive Manufacturing can be traced back to 9<sup>th</sup> March 1983, when Charles W. Hull successfully printed a teacup on the first additive manufacturing system, the stereolithography apparatus SLA-1, which he built himself [2017, <https://es.3dsystems.com/our-story>]. The terms used to indicate AM have undergone an evolution parallel to technological developments, starting from a prevalent use in the production of prototypes, passing through the creation of simple functional parts, tools and molds, up to obtain complex functional parts. To date, there are many AM techniques and their classification is a controversial issue: numerous classifications have been proposed, based on the starting material, on the equipment used, on the process itself or on the transformation of materials<sup>4</sup>. The ISO and ASTM classifications have some inconsistencies and disadvantages; in any case some techniques remain excluded and cannot be placed in any group, for example mask sintering or digital light processing remain excluded from the categories of ASTM F2792 [2018, <https://www.astm.org/>]. For a systematic classification, the four fundamental elements of every manufacturing system must be considered: the solid, liquid or powder material, the form of energy required, whether it is heat, UV or chemical, machine and tool and technology<sup>4</sup>. Despite the divergences, all these techniques have in common the fact that they are able to create a 3D object starting from a CAD model, through the addition of successive layers, each of which represents a thin cross-section of the part derived from the original CAD data<sup>5</sup>. They also share a series of steps that lead from conceptual development to the finished product and are represented in **Fig. 1.1**.

Detailed process of a model	Conceptual process
1. Conceptual development of the idea.	• Conceptual development 1
2. Design of the model in a 3D CAD application.	• 3D CAD application 2
3. Generation of an .stl or .amf file to enable the additive manufacturing equipment to interpret the geometrical information (triangulation) modelled in CAD.	• Generation the .stl file 3
4. Orientation within the machine and generation of the NC code (G code) by the additive manufacturing equipment.	• Generation the G code 4
5. Manufacturing of the component.	• Manufacturing 5
6. Cleaning. Removal of the support material (if the technology uses support material and the component so requires).	• Cleaning 6
7. Post-process phase: (improving the finish and hardening. Some technologies do not require this).	• Post-processing 7

**Figure 1.1.** Phases of an additive manufacturing process<sup>4</sup>.

An infinite series of variables must be taken into consideration when choosing which AM technology to use, but among all, the most important to consider are resolution, precision, the mechanical and thermal properties of the material, surface finish, production time and the cost. AM has revolutionized product development and manufacturing and its benefits<sup>4,5</sup> compared to traditional production techniques are: (i) the rapid character of this technology, not only in the creation of objects, but also in leading to a reduction of the time for new designs to reach the market: numerous design and validation phases can be avoided and moreover it allows great flexibility in production since variations in the model do not involve time dilation or the need to change machines as in conventional methods; (ii) the reduction of the steps necessary for production, since even complex geometries can be produced in a single step, with the consequent advantages of reducing tool investment costs, reducing assembly errors and their associated costs and the general simplification of multistage processes; (iii) the possibility of creating hybrid processes by combining AM techniques with conventional techniques to achieve, for example, excellent surface qualities; (iv) the possibility of having very low production numbers thanks to the absence of customized molds or tools that change every time; (v) optimum usage of materials, in fact wastage is reduced to a minimum and there is greater sustainability. However additive manufacturing technologies have a number of drawbacks<sup>4</sup> which must be taken into consideration in the choice of technique and on which the development and optimization of processes must work: not always the surface properties of the product are good; slowness of some processes especially for large pieces; the materials used in some technologies might not be suitable; the mechanical inadequacy of some pieces due to the anisotropy resulting from the deposition of the material in layers and the tolerances are worse than those of techniques based on the removal of material.

AM has significantly evolved since it appeared, leading to improvements in accuracy, better mechanical properties, broader range of applications and reductions in costs of machines and the parts made by them. AM has found applications in design and development within almost every consumer product sector and even though AM is applicable to every major industry in one way or another (**Fig. 1.2, Wohlers Report 2013**), many of the improvements to AM today have been driven by the needs of specific industries, automotive industry, medicine and medical engineering, aviation industry, architecture, construction and food.



**Figure 1.2.** The use of additive manufacturing in the different sectors (Wohlers Report 2013).

## *1.2 – Advanced ceramics and AM Processing of Ceramics*

Advanced ceramics, which provide a good combination of high strength, superior hardness, outstanding oxidation resistance as well as excellent thermal and chemical stability, are one of the most important classes of advanced materials, so their design and development for high-performance applications ranging from automotive to aerospace, defense-oriented, energy, environmental, and biomedical applications is one of the most challenging tasks of modern engineering.

The demand for advanced ceramics is related to the growth of the side market of use, which in turn, is related to the technological innovation that allows to improve their performance and the production process. The wide use of advanced ceramics depends on being able to obtain a near-net-shape and a geometrically accurate three-dimensional product. Traditional techniques for the production of ceramics, such as dry forming by means of pressing powders, plastic forming like extrusion and tape and slurry casting in molds, are not able to produce very complex shapes and often employ a process that includes several steps and pre- and post- processing. In particular, the post-hard machining of ceramics is time-consuming, risky as regards the damage of fragile products and an expensive process that generally requires diamond tools. Thus, in many cases, it incurs up to 80% of the overall manufacturing costs of a ceramic product<sup>6</sup>. Furthermore, the high cost of molds and model production and the limited molding shaping technologies slow down the possibility of implementing new designs quickly, making processes inflexible and very expensive for small lot productions.

The need to overcome the limitations of current production techniques has led to the use of new techniques such as additive manufacturing.

As regards AM techniques for ceramic materials, they can be divided into three categories: direct, indirect and negative<sup>7</sup>. Direct means that the material is directly deposited only in the position giving the desired shape of the final object, indirect instead, means that first a layer of the material is deposited, then the cross section of the final piece is registered in a layer and after completing all layers, the excess material surrounding the product is removed. Negative means that AM technology is used to produce a mold, which is successively used to produce the final part<sup>7</sup>. Furthermore, it is appropriate to distinguish the techniques based on the macroscopic physical properties and the architecture of the ceramic parts generated. The first category contains technologies not capable of producing dense structures, which means, a microstructure without residual porosity; the second includes technologies capable of producing fully dense monolithic ceramic bodies of reduced dimensions, i.e., parts without residual microporosity; the third class represents technologies capable of producing fully dense monolithic ceramic bodies without restriction in dimension<sup>7</sup>.

Many AM technologies are able to successfully produce numerous porous structures and research has focused on this type of product since first of all, the possibility of producing complex-shaped porous architectures with AM processes with a precise control of the dimension, shape and amount of pores is not reachable by any current technique and has opened up new fields of research and applications, and subsequently because many of the AM technologies existing nowadays are intrinsically particularly suited for the generation of fine filigree structures. AM of fully dense monolithic ceramics is still a challenge and remains the most important task that needs to be solved to promote AM of ceramics to more than a niche technology. **Table 1.1** shows the main characteristics of additive

manufacturing technologies used for ceramics and a brief description of them will be presented in the following sections.

Technology <sup>†</sup>	Feedstock (liquid or solid)	Dense struts (dense ceramic, but limited volume)	Monolithic	Part dimension <sup>‡</sup> (size that can be produced economically)	Surface (quality of parts, not of single struts)	Precision	Cost of feedstock preparation	Cost of process	Direct versus indirect
P-3DP	Solid	No	No	M-XL	Medium	100 μm	Low	Medium	Indirect
P-SLS	Solid	No	No	M-L	Medium	100 μm	Low	High	Indirect
P-SLM	Solid	No	No	M-L	Medium	100 μm	Low	High	Indirect
S-3DP	Liquid	Yes	Yes	M-XL	High	100 μm	Low	Medium	Indirect
S-SLS	Liquid	Yes	Yes	M-L	High	100 μm	Low	High	Indirect
SL	Liquid	Yes	No	XS-M	High	<1 μm	Medium-High	Medium	Indirect
LOM	Solid	Yes	Yes	M-L	Medium	100 μm	Medium	Medium	Indirect
DIW/ Robocasting	Liquid	Yes	No	S-XL	Low	10 μm	Low-Medium	Low	Direct
FDM	Liquid	Yes	No	S-M	Low	100 μm	Medium	Low	Direct
DIP	Liquid	Yes	Yes	S-M	Medium	10 μm	High	Medium	Direct
Direct Dep	Liquid				Low				Direct

<sup>†</sup>The definition of the acronyms for each technology is given later in the text.

<sup>‡</sup>XS = 100 μm; S = 1 mm; M = 10 mm; L = 0.1 m; XL = 1 m.

**Table 1.1.** Main Characteristics of Additive Manufacturing Technologies used for Ceramics<sup>7</sup>.

## 1.2.1 – Indirect technologies

### 1.2.1.1 – Powder-Based 3D Printing (P-3DP)

A layer of powdered material is first spread and then an inkjet printing head spits a binding liquid onto the powder bed, thus defining the cross section of the object in that layer. The 3DP method can create parts with geometries of any complexity, including undercuts, overhangs and internal volumes, from any powder material without any additional support structures, thanks to the powder bed<sup>6</sup>. Pure preceramic polymer powders were used, which allow to achieve a high polymeric density (~ 80%) because the sprayed solvent locally dissolves the preceramic polymer binding the particles together. The resulting ceramic part after heat treatment still had a similar level of residual porosity, as the material does not sinter during the process<sup>8</sup>.

### 1.2.1.2 – Powder-Based Selective Laser sintering (P-SLS)

The P-SLS process works similarly to the P-3DP one, with the difference that the cross sections of the part to be built are inscribed by means of a laser beam that can either directly sintering the ceramic powder or can melt a possible binder phase mixed<sup>7</sup>. Preceramic polymers can offer some interesting opportunities: Friedel *et al.*<sup>9</sup> produced polymer derived ceramic parts of complex shape by sequentially irradiating layers consisting of SiC loaded polysiloxane powder with a CO<sub>2</sub>-laser beam ( $\lambda = 10.6 \mu\text{m}$ ), which locally induces curing reaction of the polymer phase at moderate temperatures around 400°C.

### 1.2.1.3 – Stereolithography (SL)

Starting from a complex CAD model, a solid structure is built up layer by layer from a photosensitized liquid resin or solution filled with ceramic particles and containing a photosensitized monomer. In the process, certain areas on the surface of the photocuring liquid are converted into solid parts through exposure to light of certain wavelengths. Single layers are created and stacked onto each



other. Contrary to powder-based AM, in stereolithography the material surrounding the part is liquid and therefore it is unable to provide any support; for this reason support structures are built together with the part, requiring subsequent removal<sup>7</sup>. There are three main configurations: vector scan, or point-wise, approach; mask projection, or layer-wise approach that irradiate entire layers at one time, and two-photon approach that is essentially high-resolution point-by-point approach<sup>5</sup>. By increasing the crosslinking density of the photocured polymer of the green body, the density of the sintered ceramic can be increased while reducing the shrinkage due to heat treatment<sup>6</sup>. It is possible to obtain objects with complex geometries, which present good quality and surface finishing. As regards the use of preceramic polymers, Pham *et al.* modified a polyvinylsilazane preceramic polymer and used it to shape complex micrometer-sized structures<sup>10</sup> and more recently Schmidt and Colombo fabricated SiOC ceramic structures by utilizing a simple physical blend between two different preceramic polysiloxanes with SL technique<sup>11</sup>.

#### 1.2.1.4 – Slurry-Based 3DP (S-3DP) and Slurry-Based SLS (S-SLS)<sup>7</sup>

The operating concept is similar to that of the P-3DP and P-SLS techniques, but in this case, instead of using a dry powder, ceramic slurry is used to increase the degree of packing of the powder bed. A liquid suspension of ceramic particles is spread as a thin layer (tape casting), whereas within this layer a cast is formed (slip casting), thanks to the capillary forces, which drag the liquid phase of the suspension into the porous mold and allow particles start to form a powder compact at the interface with the already deposited and dried layers. An important parameter is the speed of the doctor blade relative to the dry layers, which must be optimized in order to prevent collisions and guarantee a deposition as uniform as possible. Another aspect to be taken into consideration is the fact that after building up the desired geometry, the body is embedded in the powder bed which is a block of densely packed particles and must be dissolved by a solvent. The speed of the doctor blade relative to the dry layers must be high enough to prevent collision of the cast with the doctor blade. On the other hand, when the speed of the doctor blade is too high, layer deposition is not uniform, because shear stresses within the suspension will result in an inhomogeneous deposition. For the manufacturing of powder compacts with properties comparable to those produced by classical powder processing, S-3DP has the highest potential, by the use of small amounts of organic or inorganic binders which make sure that the particles in the densely packed powder bed are locally glued together. The laser treatment in S-SLS, however, will affect the microstructure of the powder compact typically in a direction which is not favourable for the manufacture of advanced ceramic.

#### 1.2.1.5 – Laminated Object Manufacturing (LOM)

The history of laminated object manufacturing (LOM) is related to the development of two crafts techniques: *photo-sculpturing*, as invented by the French sculptor Willème in the 1860s, in which a person (or an object) was simultaneously photographed within a circular room, by means of 24 cameras at equal radial positions with respect to the person (or the object) and then the sculptor used the silhouettes on each of the photographs to gradually carve out a 1/24<sup>th</sup> cylindrical portion from a sculpture in each iterative processing step; and the patents of DiMatteo (1974), in which a computer-driven tool for cutting-out 2D shapes from layers of a sheet material was presented. The commercialization of LOM machines has been driven by the former Helisys Corporation starting from 1986.<sup>12</sup>

This process allows the creation of three-dimensional objects through lamination of paper, tapes, or similar shapes at low-medium temperature and pressure<sup>7</sup>. LOM involved layer-by-layer lamination

of paper material sheets that can be tied together through gluing or adhesive bonding, thermal bonding, clamping, and ultrasonic welding<sup>5</sup> and cut using a CO<sub>2</sub> laser. Each sheet representing one cross sectional layer of the CAD model of the part. The unused material is left in place, diced with cross-hatches for easy removal<sup>13</sup>. The main advantages<sup>7</sup> of this technique are the possibility of producing laminates directly from green tapes, it does not require the addition of solvents, the pressures and temperatures required are low so the risk of delamination is reduced. The main disadvantages are related to the quality of the interfaces, the presence of defects, porosity and differential shrinkage<sup>14</sup>.

Generally, the LOM technique was developed for processing paper. In transferring it to ceramic processing, research has focused on using ceramic tapes as building materials. LOM of ceramics started with Al<sub>2</sub>O<sub>3</sub> tapes, which exhibited mechanical properties comparable to pressed samples<sup>6</sup>. Internal structures for electronic devices have also been prepared with low-temperature co-fired ceramics (LTCC) containing a SiO<sub>2</sub>–Al<sub>2</sub>O<sub>3</sub>–RO glass and Al<sub>2</sub>O<sub>3</sub> particles. These tapes were cut using a milling plotter and cold laminated with a double-sided adhesive tape with a thickness of 12 mm. Binder decomposition was finished at 425°C and sintering at 870°C and leads to a density of 99%<sup>15</sup>. Other material systems like glass-fiber reinforced polymers, SiC, SiC-fiber-SiC, AlN, Si<sub>3</sub>N<sub>4</sub>, HA, and TiC/Ni were used. For example, for SiC samples, a tape casting slurry containing a bimodal SiC mixture, carbon black and graphitic powder, was mixed with a polymeric binder. The LOMed parts of these tapes were pressed in a powder bed to affect densification in the z-direction. After pyrolysis of the binder, the SiC/C composite was infiltrated with Si to build secondary SiC. Mechanical properties were decreased in comparison to commercial SiC due to residual Si layers at the interfaces. Curved body armor parts were produced from the SiC tapes, but large overlap areas led to complications while removing waste material<sup>16</sup>.

## *1.2.2 – Direct technologies*

### *1.2.2.1 – Direct Inkjet Printing (DIP)<sup>17</sup>*

In this technology, a ceramic suspension, consisting of ceramic particles (typically < 30 vol.%) dispersed in a liquid carrier (water or organic solvent) and different additives that act as stabilizers and control viscosity, the spreading and drying of the ink, or a wax-based ink containing submicron ceramic particles, is loaded into a printing head and deposited on a substrate, leading to the formation of structures. DIP can be performed either by jetting a constant flow of ceramic ink or by adopting a drop-on-demand (DoD) approach. In the continuous approach an uninterrupted flow of droplets electrically charged is generated and thanks to the use of deflecting electrodes, the droplets that must not reach the substrate are caught and redistributed to the ink reservoir to be reused. In the DoD approach instead, individual droplets are generated by a piezoelectric or thermal actuator at controlled frequencies and they are deposited only where are required. The physical characteristics of the ink, its viscosity and surface tension, are extremely important for the jettability of a printing ink which is often determined using the dimensionless Z parameter, inverse of the Ohnesorge number Oh (the ratio of the square root of the Weber number and the Reynolds number), which is a function of the density, viscosity and surface tension of the fluid as well as the diameter of the printing nozzle and should be in the range  $4 < Z < 15$ . Beside ink properties, printing parameters such as jetting frequency,

travel speed, acoustic wave speed, and nozzle-substrate distance also have a strong influence on the jettability. It is important to optimize the size and quantity of particles in order to avoid nozzle clogging and improve suspension stability and to obtain a high green density and to avoid issues with excessive shrinkage and cracking, keeping the viscosity low enough for the ink to be printable. This technique allows to obtain high resolution and fully dense components with an excellent surface finish. The printing of complex-shaped structures with overhangs and undercuts can be realized by printing support structures with an ink providing a sacrificial material, which is conveniently removed during firing in oxidizing condition<sup>7</sup>. The main advantage of DIP is the ability to deposit droplets of multiple materials simultaneously, leading to the formation of FGMs (functionally gradient porous materials) and voxel-wise microstructure tailoring. The main problems appear to be the nozzle clogging that leads to deposition inaccuracies, the formation of defects and the relatively slow building rate. An alternative approach is the direct printing of a preceramic polymer solution, which takes advantage of their solubility in several solvents. Mott *et al.* for example used polycarbosilane to produce silicon carbide parts using DIP, with or without the use of SiC particles in the ink<sup>18</sup>.

#### 1.2.2.2 – Filament Extrusion 3D Printing: Robocasting (RC)/Direct Ink Writing (DIW), Fused Deposition Modeling (FDM)

The many different names used to refer to ceramic material extrusion technologies can be rather confusing, despite this, the entire class of AM techniques based on ceramic material extrusion are united by the fact that a ceramic-loaded filament is extruded through a nozzle and deposited onto a platform layer-by-layer to form a 3D structure. The deposition of ceramic materials with robotic devices was first applied in the 1990s<sup>6</sup>. A first publication reporting of RC, developed at Sandia National Labs in 1996 (*U.S. Patent 6,027,326*), was published by Cesarano *et al.*<sup>19</sup>, while FDC was first mentioned in 1995<sup>6</sup>.

The main parameter to check to obtain a filament of the correct and stable size is the rheology of the feedstock, which influences the printability and retention of the shape. The feedstock must exhibit a shear-thinning behaviour to allow the viscosity to descend during the application of the shear stresses in the nozzle, but to immediately recover a high value, in order to prevent deformation of the filament once extruded. These viscoelastic materials are also designed to have a significant yield stress and can be fitted to the Herschel-Bulkley model for yield-pseudoplastic fluids<sup>17</sup>. Yield stress increases with ceramic solids loading, which has to be high to minimise shrinkage and prevent the formation of porosity and cracks during debinding and sintering heat treatments<sup>17</sup>. There are two main types of ceramic material extrusion processes: wax-based extrusion processes, in which ceramic powders are suspended in a polymeric dispersion medium and water-based extrusion processes, in which a small amount of organic is used to avoid problems during debinding and a high ceramic powder loading. Other features that the feedstock must respect are the fact of having a homogeneous particle distribution to avoid flaws and agglomerates, having minimized the trapped air (degassing) and having a binder phase that is easy to drain, dry or burn out<sup>6</sup>.

In the Robocasting (RC)/direct ink writing (DIW) technique, a highly loaded viscous ceramic paste is extruded through a nozzle at ambient temperature and solidifies onto the substrate upon drying in air. For the formation of a homogeneous and well-dispersed paste the use of dispersant, thickener, plasticiser and viscosifier to enhance suspension stability and impart specific rheological properties is important. Further developments led to the formulation of reversible colloidal gels that can coagulate by controlled flocculation with additions of salts or polyelectrolytes, and set immediately

after deposition without drying; in this way it's possible to fabricate free spanning geometries such as lattices without support structures<sup>17</sup>. The DIW technique will be further explored in the next sections. FDM of ceramics is based on the extrusion of a mixture of a ceramic powder mixed with a significant amount of a polymer, which is melted during the extrusion because the printing head is heated and solidifies by cooling immediately after, to prevent deformation of the filament<sup>7</sup>. The mixture of feedstock includes the base polymer, an elastomer, a tackifier, a plasticiser, which respectively provide strength, elasticity, flexibility and plasticity to the filament and a wax is also added to lower the viscosity<sup>17</sup>. After printing, the polymeric binder is burnt out and the ceramic phase is sintered. Kalita *et al.* produced polypropylene-TCP composites by FDM and obtained scaffolds with a compressive strength of 12.7 MPa for 36% total porosity and a pore size of 160  $\mu\text{m}$ <sup>20</sup>. Bandyopadhyay *et al.* investigated the processing of piezocomposites by FDM, extruding a polymeric filament loaded with 50-55 vol% PZT powder. A spool of filament was first produced and extruded through the nozzle of a commercial FDM 3D-printer, at a temperature of 140°C-200°C, to produce a piezocomposite ladder structure after sintering and impregnation with epoxy resin<sup>21</sup>.

Benefits<sup>17</sup> and applications of AM in the ceramic industry are those already presented in §1.1.1: the reduction of the need for machining, especially in the case of ultra-hard ceramics such as SiC and B<sub>4</sub>C; cost reduction and much shorter production times; possibility of having low volume production series, which enhanced design freedom at no extra-cost in varying geometries and producing complex ones. The principal applications<sup>17</sup> in the ceramics industry are for dentistry, dental crowns scaffolds for tissue engineering, ballistic armour, vehicle panels and personal protection cutting tool, electrical components, substrates, connectors, spark plug insulators, filters and in future, this range of applications could be further expended and strengthened. The limitations<sup>17</sup> concern the possibility of producing ceramic through single-step AM processes; the possibility of producing multi-material, such as ceramic-metal, ceramic-polymer, and even ceramic-metal-polymer composites, whose main problem is to make other metal or polymeric materials survive at the temperatures necessary for pyrolysis and can be solved by first printing the ceramic structure and then, infiltrating with ceramic, polymer, metal materials<sup>22</sup>, or AM deposition of additional materials onto ceramic components using either extrusion-based processes (DIW) or inkjet printing (DIP); the presence of bulk and surface defects, such as low surface quality, lumps, internal porosity, and surface micro- and macro-cracks caused by deformations, air bubbles and more; difficulty in manufacturing monolithic and mechanically-strong ceramic components; the limitation in the choice of materials. Polymer-derived ceramics have been shaped using LS, DIW, binder jetting, vat photopolymerization, LOM, and SPPW, and this class of ceramic materials provides a significant opportunity to expand the range of ceramics that can be shaped using AM.

Furthermore, for the widespread use of AM to become a reality in the ceramic industry, the performance of additively manufactured components must be comparable to at least those of parts fabricated using conventional manufacturing technologies, such as high sintered density and absence of cracks; reliability must be increased and costs reduced.

indirect AM technologies

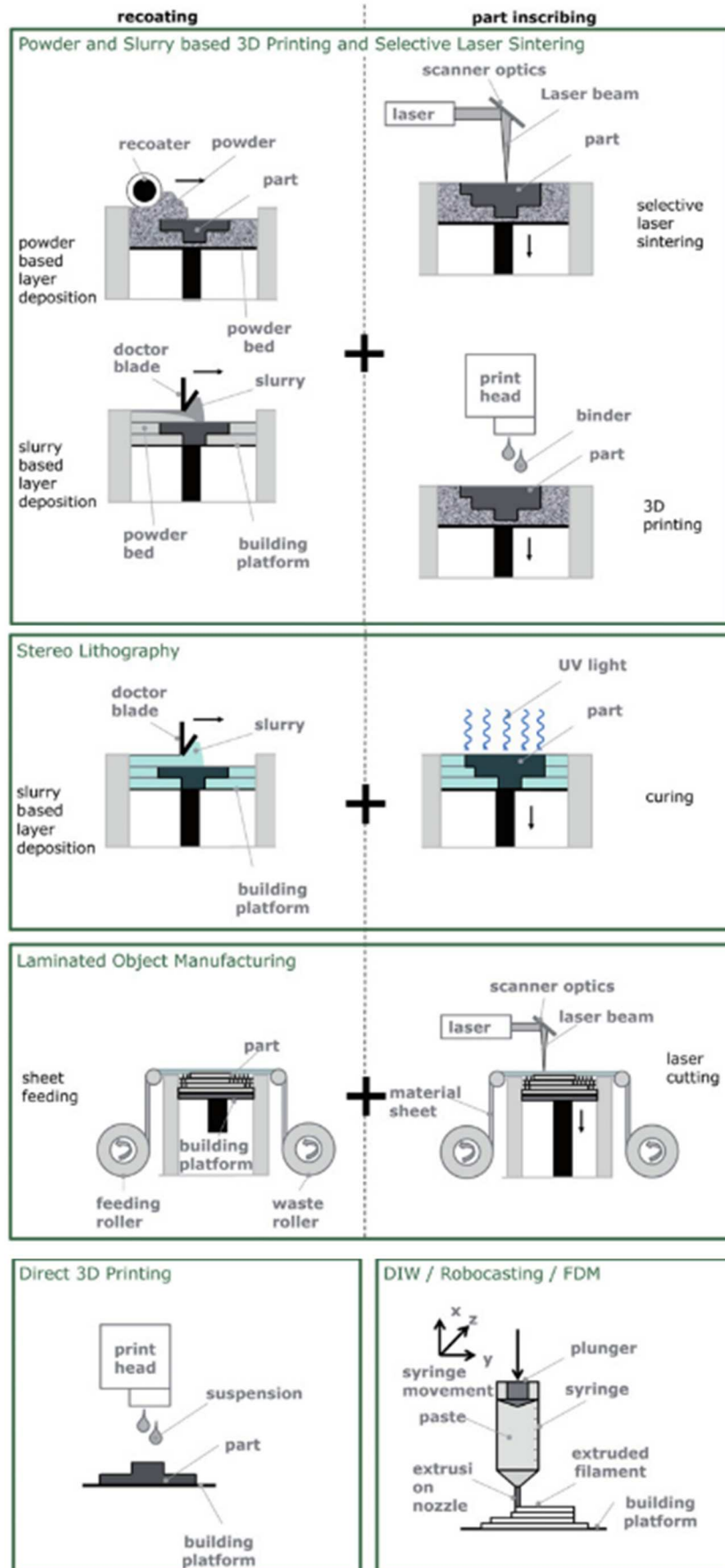


Figure 1.3. Schematic of AM technologies<sup>7</sup>.

### *1.3 – Direct Ink Writing technique and inks*

It is one of the most used AM techniques because it allows the fabrication of complex structures at relatively moderate costs; different inks have been developed for different applications including bone tissue engineering, structural, electronic and optical applications<sup>23</sup>. This technique is based on the extrusion through a nozzle, which can vary a lot in size, as small as 0.1  $\mu\text{m}$  used in microfabrication to nozzles as big as several dm for concrete printing in building applications<sup>23</sup>, of a ceramic paste or ink and on the creation of three-dimensional objects by stacking filaments. After printing, the green bodies need to be hardened through post-printing treatments, such as pyrolysis, in which a dimensional shrinkage of the object occurs, depending on the composition of the ink and in particular on its organic content which undergoes thermal debinding. The ink design is the most critical aspect. The ink must be homogeneous, have stability for the entire duration of the print, have a sufficient ceramic content to avoid shrinkage during pyrolysis and ensure optimal rheological properties for extrusion and for maintaining the shape once deposited. The ink must therefore be smooth enough on one hand to be extruded into a filament without creating clogging and, on the other hand, it must be able to maintain the shape of the orifice and support a stacking of layers without collapsing. The ink must therefore behave like a liquid during extrusion through the nozzle and exhibit an elastic behaviour once it is at rest and the applied stresses cease<sup>23</sup>. Two main approaches have been used to obtain inks with suitable rheological properties<sup>23</sup>, colloidal suspension and gel-embedded suspensions, either hydrogel or organogel based<sup>24</sup>. Colloidal suspensions are highly concentrated slurries of ceramic particles (typically 40-50 vol.% or 60-80 wt.%) in a low-viscosity liquid, typically water and few organic additives<sup>25</sup> (< 2 vol.% or  $\leq 1$  wt.%) for tuning the interactions between particles<sup>26</sup>, which sets when extruded in air upon minimal drying; their extrudability can be increased through the addition of plasticizers, however these inks are very sensitive to the pH of the environment so they can be unstable and difficult to control and this approach is viable only for printing nozzles with a diameter larger than  $\sim 500 \mu\text{m}$ , otherwise clogging issues become frequent<sup>27</sup>. An alternative is the use of inks that have a gel transformation, behaviour that can be achieved by controlled flocculation of a ceramic suspension to form a gel, or by using gelling additives<sup>27</sup>. The second category are gel-embedded suspension or organic based suspension, in which the ink formulation provides a high content of polymeric binders and plasticizers. The rheological properties do not depend on the interactions between the particles, but on the gel phase in which they are embedded, so they are more stable at the expense of solid content.

A different approach appears to be the use of preceramic polymer in the ink composition<sup>27</sup>. Preceramic polymers are a class of inorganic polymers which can be converted to a ceramic with high yield. Different from traditional ceramic raw materials, preceramic polymers can be manipulated in the polymeric phase and can be dissolved in a variety of solvents, thus the inhomogeneous dispersion of ceramic powder in printing inks can be avoided. Moreover, molecule chains of preceramic polymers are editable, they can be modified to meet the demands of specific 3D printing methods<sup>28,29</sup>. In this category of inks the preceramic polymers, used both as binders and additives and as a ceramic source, are filled with ceramic powders or particles of preceramic polymer<sup>30</sup> and their use has two objectives: the first is to have a polymeric additive to control the rheological properties of the ink, the second is to react with the fillers upon heat treatment in order to form the desired ceramic phase<sup>27</sup>. Moreover they have a low decomposition mass loss therefore, as additives, they are less negative with

regard to shrinkage during the heat treatment. Several papers report the use of inks based on preceramic polymers and fillers: Zocca *et al.*<sup>27</sup> report the use of silicon-based polymers which give a SiO<sub>2</sub> residue upon materials firing in air, which can react with other oxides introduced as fillers in order to form silicate ceramic Hardystonite (Ca<sub>2</sub>ZnSi<sub>2</sub>O<sub>7</sub>) for bioceramic scaffolds. Fiocco *et al.*<sup>31</sup> have successfully 3D-printed, by direct ink writing, silica-bonded calcite scaffolds starting from a paste comprising a silicone preceramic polymer and calcite powders; Pierin *et al.*<sup>3</sup> realized porous ceramic scaffolds with the lateral dimension of a few millimetres and composed of a continuous ceramic filament ~120 µm thick by DIW of a mixture of cross-linked preceramic particles with a siloxane resin dissolved in a solvent, with the addition also of graphene oxide to the ink formulation to improve the structural stability during pyrolysis. In these works, the use of fillers, both ceramic powders and polymer particles, serves to control the rheological properties of the ink such as viscosity and elastic modulus, to avoid excessive deformation of the structures after heat treatments and to obtain the desired phase. The use of fillers also allows to increase the quality since some types of fillers can form the liquid phase upon firing, which can relax stresses and infiltrate porosity, enhancing mechanical properties<sup>32</sup>. However, the use of fillers has disadvantages since it is difficult to disperse it uniformly and if this doesn't happen, the nozzle can be occluded, which causes the loss of continuity and quality of the print<sup>30</sup>. The use of viscoelastic preceramic polymers with good fluidity, easy shaping ability and controllable conversion to ceramics can also get required rheological properties without using fillers. Chen *et al.*<sup>30</sup> proposed a new pathway to replace the suspensions, with polymer solutions without fillers as a type of feedstock in DIW of ceramics. They used a commercially available polycarbosilane as the precursor for SiC ceramic 3D structures with the different feature sizes range from 400 µm to 100 µm. After printing the structures were dried under ambient conditions, then heated to 200°C in air for oxidative crosslinking and finally pyrolyzed at 1400°C under argon flows. They show homogeneous shrinkage and good shape retention, demonstrating that the fabrication of 3D SiC ceramics is easily achieved by preceramic polymer solutions via direct ink writing.

As regards the solidification mechanism of the ink once it has come out of the nozzle, there are different mechanisms depending on the type of ink itself, including: change in pH of the suspension<sup>33</sup>, inks that have a yield stress that allows it to maintain its shape once the shear stress terminates<sup>34</sup>; solidification by evaporation of solvent<sup>35</sup> in which the composition of the ink provides a rapidly evaporating solvent that evaporates as soon as the filament comes out of the nozzle and increases its rigidity over time allowing to maintain the shape of the extruded component; solidification in a coagulation reservoir<sup>36</sup>; gelation, a mechanism in which in a polymeric system, through either physical linking or chemical crosslinking, the chains progressively bind to each other until a single molecule is obtained, the gel point, that is accompanied by a sudden increase in viscosity; UV polymerization<sup>2,37</sup>.

The last solidification method, UV polymerization, is used in the Ultraviolet-assisted direct ink write (UV-DIW), a subcategory of DIW, which precisely utilizes UV-irradiation to cross-link the extruded photopolymer resins during printing to induce gelation and shape retention after ink placement<sup>2</sup>.

## 1.4 – Direct Ink Writing UV Assisted

This hybrid AM technique enable the in-situ photocuring of a deposited filament. Upon the extrusion of the viscous photocurable ink at room temperature, UV curing enables instant cross-linking to fix the final polymerized shape<sup>38</sup>. UV-DIW technique requires an ink with a short gel time and a high gel state modulus which guarantee shape retention of the deposited lines and allowed for printing of self-supporting structures<sup>2</sup>; slow photocuring caused poor layer fidelity after ink deposition and precluded precise printing. The request for an ink that has a short gelation time unites it to VP, but contrary to VP, it demanded high solution viscosities and shear-thinning flow behaviour<sup>2</sup>. An advantage of this technique over VP and inkjet material jetting AM processes is the ability to deposit a wide range of viscoelastic materials with viscosities in excess of 10 000 Pa·s.<sup>2</sup> This technique however still presents several challenges<sup>38</sup>: the extrusion nozzle can easily be clogged as photopolymerization can propagate inside it and the mechanical properties of the printed piece are strongly influenced by the printing parameters.

### 1.4.1 – Photoresins for AM Processes

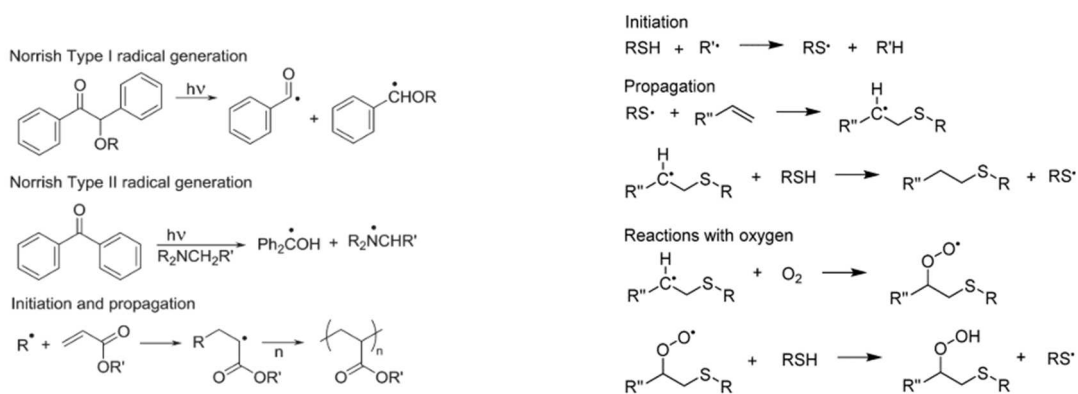
The first photocurable materials to be utilized for AM was initially presented as UV curable adhesive, consisted of a urethane dimethacrylate with a small fraction of acrylic acid, benzophenone as photoinitiator, and methyl ethyl hydroquinone (MEHQ)/triallyl phosphate to inhibit premature polymerization<sup>39</sup>.

#### 1.4.1.1 – Radical systems

Radical polymerization is a chain polymerization reaction through which, a polymer is formed by the subsequent addition of a radical, which occurs in three phases: initiation, propagation and termination. Radical generation, initiation, and propagation are all relatively rapid processes and are thus commonly used for rapid prototyping. During the initiation or activation phase, a free radical is generated starting from an initiator. The initiator is a molecule capable of decomposing through the homolytic breaking of a bond with the relative formation of the radical; a photoinitiator is capable of converts photolytic energy into these reactive species to induce polymerization. Generally speaking, radical photoinitiators may be classified as either Norrish Type I or Type II<sup>39</sup>, represented in **Fig. 1.4**. Type I initiators are single molecules that cleave into radical fragments when exposed to light of an appropriate wavelength. Common Type I initiators are benzil ketals with low energy  $n \rightarrow \pi^*$  transitions (350-360 nm) and acyl phosphine oxides such as TPO and BAPO (higher wavelength, 400 nm). Type II photoinitiation systems are two-component systems consisting of a light absorbing molecule (or sensitizer) along with a co-initiator (or synergist). When irradiated, the latter donates a hydrogen atom to the excited sensitizer and in the process provides the initiating radical. The choice of the type of photoinitiator and its performance depend on the light source and often multiple radical photoinitiators are used. As for the monomers, the most used to produce photocurable resins are acrylates<sup>40-42</sup>, already used at the beginning of the development of resins for SLA. Murphy *et al.* filed a patent in 1988 describing a resin consisting of a combination of a high viscosity oligomeric diacrylate or dimethacrylate dissolved in a liquid acrylate or methacrylate and an N-vinyl monomer. They state that a system consisting of both an acrylate and a methacrylate is preferable because



methacrylates cure too slowly on their own and because the pure acrylate system leads to distortions in the printed object<sup>39</sup>. Resins based on urethane acrylates<sup>42</sup> and bisphenol A diglycidyl ether, produced by reacting hydroxy acrylates, such as HEMA, with isocyanates are also common. Despite the numerous advantages, acrylates, as all other vinyl monomers, undergo shrinkage during polymerization<sup>39</sup> whose amount depends on the structure of the monomer and which causes non-homogeneous stress and deformation of the printed piece. A common method to reduce the shrinkage is the use of higher molecular weight oligomeric acrylates<sup>43</sup>. Another problem of acrylate monomers is related to the inhibition of radical propagation due to molecular oxygen<sup>44</sup>. A first alternative to acrylate monomers is the “thiol–ene” chemistry<sup>45</sup>. The ideal thiol–ene radical reaction revolves around the alternation between thiyl radical propagation across the ene functional group and the chain-transfer reaction, which involves abstraction of a hydrogen radical from the thiol by the carbon-centered radical. The net reaction, therefore, is simply the combination of the thiol and ene functional groups, which causes the molecular weight and network structure to evolve in a manner that is identical to other step-growth polymerization reactions, whilst simultaneously enabling all of the benefits of a rapid, photoinitiated radical-mediated process<sup>45</sup>. Thiols can alleviate oxygen inhibition by donating an hydrogen atom to a formed peroxy radical and in the process providing a reactive thiyl radical, in **Fig. 1.5**. The thiol-ene-based resins demonstrate less shrinkage and less stress related to it than those based on acrylates<sup>39</sup> due to the displacement of the gel point toward higher conversion of double bonds and also tend to be less brittle than acrylate networks due to a more homogeneous polymer architecture. Typical photo-curable acrylate resins consist mainly of multifunctional monomers where termination reactions are mobility restricted and thus auto-acceleration is observed in the early stages of polymerization. Usually the kinetic chain length in early stages of polymerization is rather high, which contributes greatly to the formation of inhomogeneous polymer networks<sup>46</sup> conversely of thiol–ene networks, which form by step growth kinetics and so are comparatively more regular in structure (**Fig. 1.6**), even if sometimes are too soft. An approach to improving thiol–ene mechanical properties has been to use ternary monomer systems such as thiols with allyl ethers and methacrylates<sup>39</sup>. Another approach used to improve the defects of acrylate resins is to introduce chain transfer agents, which can change the uncontrolled radical chain growth mechanism to a step-growth type polymerization process, enabling good regulation over the final polymer architecture by tuning crosslinking density, average kinetic chain length and distribution of crosslinks alongside the polymer backbone<sup>46</sup>. Recently, Gorsche *et al.* have tested  $\beta$ -allyl sulfones with dimethacrylate monomers and found them to be very efficient in regulating network formation<sup>47</sup>.



**Figure 1.4.** Photoinduced radical generation, initiation and propagation (left). **Figure 1.5.** Thiol-ene reaction (right).

#### 1.4.1.2 – Cationic systems

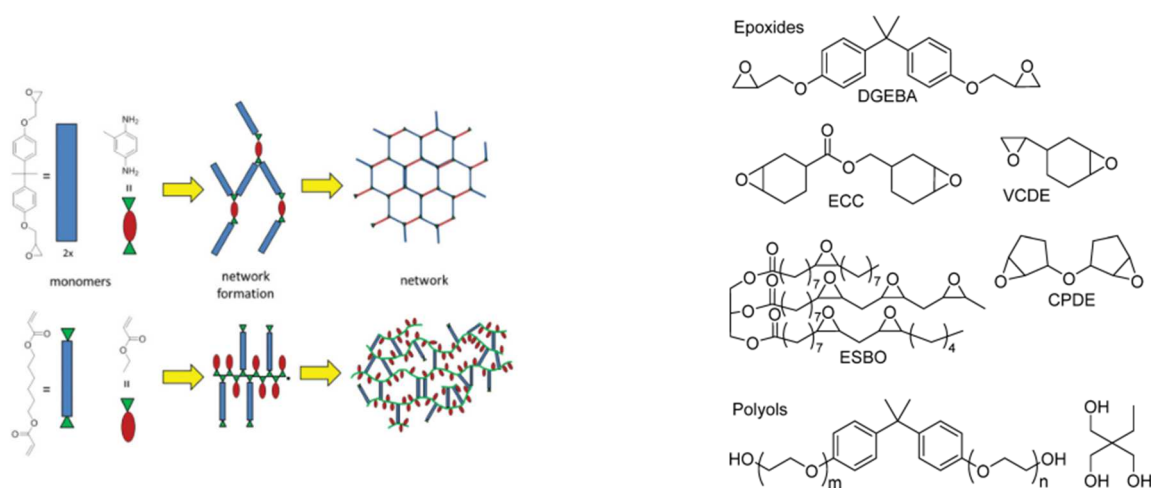
The first successful cationic photoinitiators were aryl iodonium salts ( $\text{Ar}_2\text{I}^+ \text{X}^-$ ) with non-nucleophilic counterions<sup>39</sup>: these compounds, upon exposure to UV light, decompose forming cations, radical cations and radical intermediates which react with solvent or monomer lead to the formation of super acid  $\text{HMX}_n$ , which acts as the principal initiator for cationic polymerization. Other cationic initiators based on Aryl iodoniums with alkyl substituents on both rings, triaryl sulfonium salts have been developed and also Type I radical initiators can also be used in combination with cationic initiators. Cationic polymerization can also be induced with visible light by use of a metallocene initiator such as Irgacure 261<sup>39</sup>. Among the cationic systems, the most used class of monomers is that of epoxides, some examples in **Fig. 1.7**. They show less shrinkage than acrylates during photocuring due to the ring opening reaction of the epoxy group and furthermore the resulting polymer has good mechanical properties; their reactivity depends on the structure: cycloaliphatic epoxides with high double ring strain cross-link most rapidly compared to epoxy monomers with nucleophilic groups including ester moieties, which may be protonated and have reduced reactivity<sup>39</sup>. Cationically cured epoxides are polymers that are fundamentally different from the more common amine cured epoxy resins. While cationic curing proceeds in a chain growth manner, the amine curing is based on a step growth polymerization. This leads to a significantly different polymer architecture. The cationic cured network has a quite high number of cross-linking points along the polymer backbone (in theory every third atom), leading to increased brittleness. To counteract this high cross-link density, alcohols are often used as chain transfer agents. Polyester and polyether diols are cited in patents and used at concentrations from 5 to 20 wt.%, where modulus becomes undesirably low at higher concentrations<sup>39,48</sup>. In combination with epoxides, vinyl ethers can be used, which speed cure and minimize shrinkage, or oxetane monomers (i.e., DSO) can be used, which are more reactive than epoxides and offer similar low shrinkage advantages and provide an additional advantage by imparting improved water resistance to cross-linked materials<sup>46</sup>. It is also possible to use a photo curing resin composed of two different types of monomer<sup>39</sup>. Resins based only on fast-reacting monomers (acrylate or vinyl ether) exhibited catastrophic curl distortions due to rapid and inhomogeneous shrinkage, while mixtures with less reactive monomers (acrylate/methacrylate or vinyl ether/epoxide) had significantly lower curl factors and could be further cured after building. Acrylates and epoxides undergo two different polymerization modes and substantially do not react with each other: what is formed is therefore not a copolymer but rather an interpenetrating network (IPN), as long as there is the compatibility of the monomers.

#### 1.4.1.3 – Two-Photon Initiators (2PP)

Regarding the 2PP technique, a resin commonly used was SCR500 from Japan Synthetic Rubber, which consists of a blend of urethane acrylates and a free radical initiator (either Irgacure 369 or Irgacure 184)<sup>39</sup>. However, traditional photo initiators show a low two-photon absorption (TPA). Fluorescent dyes have been studied such as coumarin and rhodamine B<sup>49</sup> which have slightly higher  $\sigma_{\text{TPA}}$  values than traditional photoinitiators; the breakthrough can be obtained with the recognition that molecules with extended planar  $\pi$ -conjugated cores connecting electron donating (D) and accepting (A) moieties have lower energy excited states with large dipolar transitions, which increases the likelihood for multiphoton events. TPA of dipolar, quadrupolar, and octopolar chromophores are found to be orders of magnitude better than traditional photoinitiators. Substituted

derivatives of stilbene are some of the simplest organic dipolar and quadrupolar chromophores<sup>39</sup>. TPA initiators are often used at low concentrations (< 0.5 wt.%) in acrylate resins, which consist of essentially the same monomers as those used for traditional SLA.

In photoresins for AM there are usually also stabilizers, light absorbers, and other additives. They are present in small concentration radical inhibitors such as BHT and MEHQ (butylated hydroxy toluene and methoxy hydroquinone) which require the presence of oxygen in the resin to be effective; benzyl N,N' dimethyl amine (BDMA) is a mild base and effectively neutralizes radical cations and pyrene and substituted anthracenes are described in several patents to serve as both sensitizers and light absorbers for SLA<sup>39</sup>.



**Figure 1.6.** Network formation via step-growth polymerization of epoxy thermosets (above) and radical chain growth of acrylates (below), (left). **Figure 1.7.** Epoxy structural monomers and reactive diluents for thermoset resins (right).

### 1.4.2 – Fundamentals of photopolymerization

When illuminated, the photoinitiator is excited by the source of light and possessing a low dissociation energy, a chemical bond in it is cleaved and free radicals are created. They attack the unstable double bonds of the monomers or oligomers forming a covalent bond and leaving free one of the electrons of the double bond, which becomes a radical from which polymerization can then continue. The polymerization continues through the succession of double bond breaks and the formation of free radicals. If several double bonds are present in a monomer, an interconnected branched solid 3D network of a highly cross-linked polymer forms. The extent of polymerization ( $\alpha$ ) increases with illumination until the resin reaches the gel point, at which it is a soft solid ( $\alpha = \alpha_{gel}$ ). The intensity of the light attenuates as it propagates into the depth beneath the surface (depth  $z$ ), so the energy dose received is a function of  $z$ . The cure depth ( $C_d$ ) is the depth at which the gel point occurs, i.e., is the depth  $z$  at which the energy dose suffices to bring the degree of polymerization to the gel point ( $\alpha_{gel}$ ) and the energy dose at that depth is the critical energy dose  $E_c$ <sup>50</sup>.

The relation between the depth of cure,  $C_d$ , and the energy dose,  $E$ , is described by the Jacobs Equation<sup>51</sup>:

$$C_d = D_p \ln \left( \frac{E}{E_c} \right) \quad \text{Eq. (1.I)}$$

in which  $D_p$  is attenuation length. The two quantities that define the behaviour of a photocurable resin are  $E_c$  and  $D_p$ . Predictive models have been proposed to describe  $D_p$  and  $E_c$  in terms of the composition and properties of the photoactive components, the ceramic particle loading, and the scattering power of the particles<sup>50,51</sup>, which can be combined in the Eq. (1.II).  $D_p$  is described through an attenuation model that is expressed in terms of the attenuation by absorption of UV photons and by scattering of photons, which redirects photons from the forward beam (with the scattered photons broadening the beam). Absorption derives from inert dyes (which simply absorb photons without creating radicals) and photoinitiators and it depends on the concentrations and extinction coefficients of the absorbing species. The light beam is also attenuated by scattering from the particles, which depends on the ceramic volume fraction, particle size and the refractive index difference between the ceramic and the liquid<sup>50</sup>. The presence of particles therefore attenuates the UV light by diluting the photoactive medium through the  $(1 - \Phi)$  term and by scattering through the  $l_{sc}$  term in the Eq. (1.II), which in turn depends on the ceramic volume fraction and on the refractive index difference between the ceramic and the liquid<sup>50</sup>.  $C_d$  varies in fact as  $1/(\Delta n)^2$ , where  $\Delta n$  is the refractive index contrast, the difference in refractive index between the powder and the liquid<sup>50</sup>: the smaller the difference in refractive index, the more the scattering and absorption are reduced. The intensity of the beam decreases instead by increasing ceramic volume fraction, decreasing particle size and increasing refractive index difference.

$$C_d(E) = \frac{1}{\frac{1}{l_{sc}} + (1-\Phi)(c_p \varepsilon_p + c_D \varepsilon_D)} (\ln E - \ln [(1 - \Phi) \frac{h\nu}{\Omega} (\gamma_Q Q + \gamma_D c_D) \frac{1}{\varepsilon_p c_p}]) \quad \text{Eq. (1.II)}$$

Where the volume fraction of ceramic is  $\Phi$ ,  $l_{sc}$  is the scattering length,  $c_p$  e  $\varepsilon_p$  are respectively the concentration and extinction coefficient for the photoinitiator, while the same terms with subscript D are related to inert dyes,  $Q$  is the concentration of inhibitors and  $\Omega$  is the quantum yield for photogeneration.

The term  $E_c$  can be calculated through a model whose hypothesis shows the fact that  $E_c$  is given by the dose of UV photons that are not absorbed by inert dyes and that produce a population of free radicals large enough to exhaust the population of inhibitors in the monomer solution to provide surplus free radicals to begin the polymerization reaction. The critical energy then depends upon the number and effectiveness of inhibitors, on the concentration and absorption coefficients of inert dyes that absorb photons, and on the concentration and absorption coefficients of photoinitiators that create free radicals; the ceramic powder plays a passive role by diluting the active monomer and an active role by limiting photon penetration depth by scattering<sup>50</sup>.

Another model<sup>6</sup>, the Kubelka–Munk model, takes into account the changes in reflectance, transmittance and absorbance that arise when ceramic particles are added to the photocuring resins. The value of the radiation energy released at a certain depth  $z$ , inside the photocurable suspension with ceramic particles is given by the following relation:

$$E = E_{max} \cdot \exp [-(\sqrt{K(K + 2 \cdot S)} \cdot z)] \quad \text{Eq. (1.III)}$$

in which  $S$  is the specific scattering coefficient and  $K$  the specific absorption coefficient. The term  $D_p$  becomes proportional to  $1/S$  and to the terms of Eq. (1.IV):

$$D_p \propto \frac{2}{3} \cdot \frac{d_{50} \cdot \lambda \cdot n_0}{\phi \cdot \Delta n^2} \quad \text{Eq. (1.IV)}$$

where  $d_{50}$  is the average size of the ceramic particles,  $\lambda$  the wavelength of incoming light,  $\phi$  the interparticle spacing,  $n_0$  the reflective indices of the photocuring liquid.

#### 1.4.3 – Preceramic polymers inks for DIW + UV

Traditional inks for SL and digital light processing (DLP) are made up of ceramic powders in photocurable resins<sup>32</sup> previously seen. The main problem appears to be sedimentation both during printing and in ink storage, which causes differential shrinkage after pyrolysis. For the UV Assisted DIW technique, acrylates are typically used for the UV-assisted crosslinking reaction and many are commercial available<sup>52</sup>. Several non-ceramic polymer systems have been modified for use in UV-DIW<sup>52,53,54</sup>.

The use of preceramic polymers can solve the problem of sedimentation or limitations in the composition of the inks due to the need to have a high solid loading to obtain the right rheological properties for the DIW and a high ceramic content; they can be homogeneously dispersed in printing inks, provide good dimensional stability and overcome other shortcomings, such as the need for dispersants, inhomogeneity, light absorbance, and scattering from ceramic particles<sup>11</sup>.

Obviously, in order to use preceramic polymers in the DIW + UV technique, they must be sensitive to UV light. To make preceramic polymers sensitive to UV light, they must possess photocurable moieties. In commerce there is a small number of UV curable preceramic polymers, such as polysilicone acrylates from Evonic/Tego but the ceramic yield of such materials upon pyrolysis is rather low<sup>55</sup>. Some instead contain an acceptable ceramic content (<https://www.starfiresystems.com/data-sheets/>), between 60-80%.

There are three approaches to using preceramic polymers with UV light<sup>11</sup>:

- Chemical modification of a commercially available high ceramic yield preceramic polymer by grafting of photocurable moieties;
- building up of a preceramic polymeric structure starting from the photoinduced reaction of two distinct (often oligomeric) precursors;
- blending of a photocurable preceramic polymer with a non-photocurable, high ceramic yield preceramic polymer (which does not require specific functional groups).

In the first case only one material is used but a long chemical synthesis is required to give the ceramic precursor the suitable functional groups<sup>56</sup>. In the second case two components are required possessing different functional groups which crosslink together upon light illumination. Both components are participating during the photoinduced crosslinking reaction via a thiol-vinyl<sup>57</sup> or an acrylate-vinyl<sup>55</sup> copolymerization, therefore requiring specific functional groups (e.g. vinyl, acrylate, thiol) which limits the selection of the components. The third approach was presented for the first time in the work of J. Schmidt and P. Colombo<sup>11</sup> and consists in the blending of two preceramic polymers, one photocurable and one non-photocurable. The primary polymer contains functional reactive groups necessary to form a polymerized network upon light illumination, while the secondary preceramic polymer, although non-photosensitive, possesses a high ceramic yield, but otherwise leaves a high

degree of freedom in selection. This method has the advantage to benefit from commercially available preceramic polymers and furthermore, the ceramic yield, and therefore the shrinkage upon pyrolysis, can be varied by simply changing the ratio between the two polymers in the blend allowing the control of the dimensions of the printed bodies after pyrolysis.

In this thesis work, the line introduced by the previously mentioned work was followed, for which the ink composition was sought consisting of two types of preceramic polymers, one photocurable and one non-photocurable, which would allow, through the DIW + UV technique, to obtain suspended structures able to keep shape after pyrolysis heat treatment.

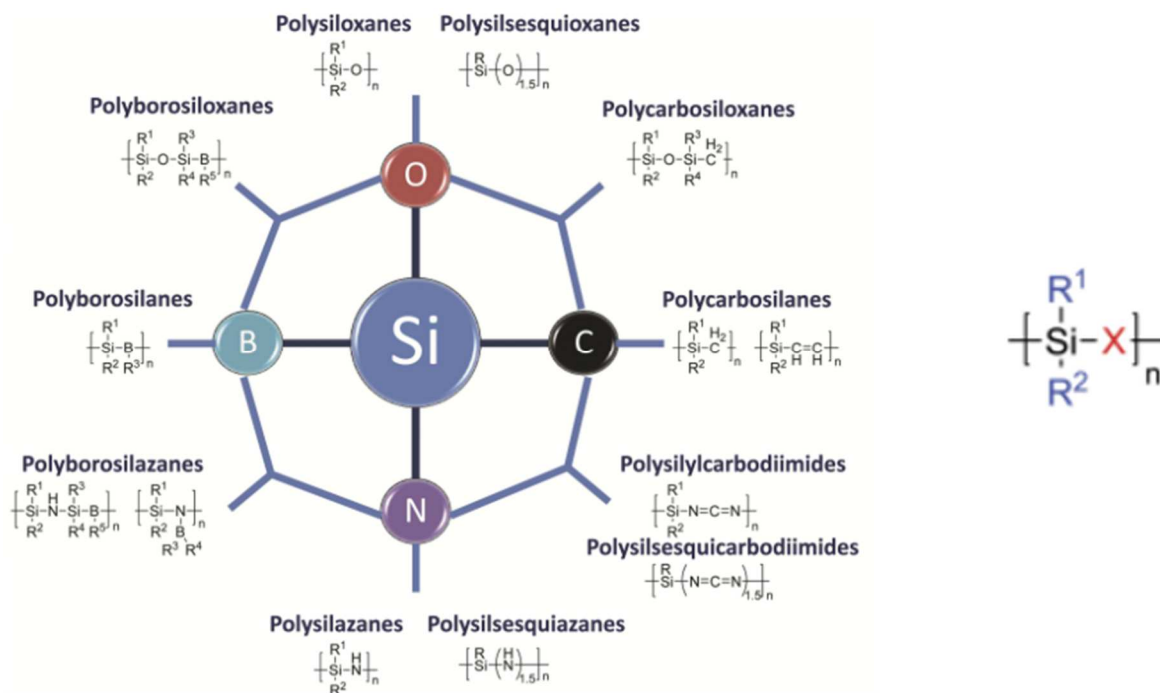
### *1.5 – Preceramic Polymers*

The preceramic polymer represent a special class of inorganic/organometallic polymer that provide ceramics with a tailored chemical composition and a closely defined nanostructural organization by proper thermal treatment under a controlled atmosphere<sup>58</sup>. The main attraction of using these precursor to fabricate ceramics is that they have a polymeric nature during forming and shaping into components, so they can be subjected to a large variety of forming methods typically used for polymeric materials, to then give rise to ceramic objects through low temperature heat treatment (1000-1300°C), which removes the organic content and requires less energy and is economically advantageous compared to that of classical powder technology; furthermore, the ceramic products obtained are additives free, have good thermo-mechanical characteristics and complexity that are difficult to obtain through traditional powder technology<sup>58</sup>. In the early 1960s, organosilicon polymers have been proposed for the preparation of Si-based ceramics via a polymer-to-ceramic transformation process, and the resulting ceramics are denoted as polymer-derived ceramics (PDCs)<sup>59</sup>. The potential of such preceramic polymers for materials science was not recognized until the first practical application reported by Veerbeek<sup>60</sup>, which was the production of shaped articles, in particular fibers with small-diameters of tens of  $\mu\text{m}$ , comprising homogeneous mixtures of SiC/Si<sub>3</sub>N<sub>4</sub> from the polymer to ceramic transformation of polysilazanes, polysiloxanes, and polycarbosilanes. Since then numerous preceramic polymers have been developed for the synthesis of Si-based ceramics and thanks to the promising structural and functional properties and to their formability, the PDCs have found fundamental and technological interest for a variety of applications in several key fields, such as high temperature resistant materials<sup>61</sup>, ceramic heaters<sup>62</sup>, microelectromechanical systems (MEMS)<sup>63</sup>, energy and environmental applications<sup>42</sup>, biomedical components<sup>64</sup> and others<sup>59</sup>.

The synthesis of PDCs generally comprises three phases: the synthesis of the ceramic precursor, shaping and crosslinking at low temperatures and the polymer-to-ceramic transformation (ceramization) through pyrolysis. As already reported, the use of polymeric precursors allows to use a large number of different methods of shaping before ceramization, which avoids the problem of tool wear and brittle fractures. Moreover allows to synthesize non-oxide advanced ceramics, does not require long times for gelation and drying, does not require solvents, the solutions are stable over time and available for large-scale production in industrial application<sup>58</sup>. The cross-linking step is extremely important, the preceramic precursors should be converted into infusible organic/inorganic materials in order to not only increase the ceramic yield but also to retain the shape of the precursors

during the polymer-to-ceramic transformation; the cross-linking process can be initiated by different mechanisms and through the introduction of a catalyst it can also occur in the shaping process itself instead of during heat treatment<sup>58</sup>. Polymer-to-ceramic conversion involves the elimination of organic moieties and the most used treatment is pyrolysis but other techniques of ceramization and consolidation<sup>58</sup>, such as chemical vapor deposition, plasma spraying and laser pyrolysis, have also been used.

The best known classes of PDCs are the Si<sub>3</sub>N<sub>4</sub>, SiC, BN binary systems, the SiCN, SiCO and BCN ternary systems and the SiCNO, SiBCN, SiBCO, SiAlCN and SiAlCO quaternary systems<sup>58</sup>. The type of the preceramic polymer influences the composition and the microstructure of the final ceramic produced, so is possible to control the structural and functional properties of the PDC by molecular design of the preceramic precursors.<sup>59</sup> A simplified formula<sup>58</sup> of an organosilicon polymer suitable for be used as precursor for the synthesis of PDCs is represented in **Fig. 1.8**. The variation of the group X in the polymer backbone results in different classes of Si-based polymeric precursors (poly(organosiloxanes) with X = O, poly(organosilanes) with X = Si, poly(organosilazanes) with X = NH and others presented in **Fig 1.8**) and many properties including the chemical and thermal stability, the solubility, the optical, electronic and rheological characteristics can be modified by changing the functional groups R<sup>1</sup> and R<sup>2</sup>.



**Figure 1.8.** Main classes of Si-polymer as precursors for ceramics (left); general oversimplified representation of the molecular structure of preceramic organosilicon compounds (right)<sup>58</sup>.

Starting from the different classes of silicon-based polymers, SiC, Si<sub>x</sub>C<sub>y</sub>O<sub>z</sub> e Si<sub>x</sub>C<sub>y</sub>N<sub>z</sub><sup>58</sup> can be obtained after heat treatment, as shown in **Fig. 1.9**.

The microstructure of PDCs is complex and undergoes microstructural changes at temperatures greater than 1000°C. One of the peculiarities of PDCs is the presence of nanodomains<sup>65</sup> in the microstructure that persist at high temperatures and confer high resistance to crystallization. PDCs can be amorphous in the temperature range 1000-1800°C depending on the molecular structure and composition of the polymeric precursor and at high temperatures the devitrification process of the initial amorphous network starts and leads to local crystallization of different phases<sup>58</sup>, process during which, the entire bulk of the material undergoes a phase separation process; with increasing temperature the local formation of nanocrystals occurs and the separation of a “free” carbon phase is subjected to a graphitization process<sup>58</sup>. Free carbon derives from the hydrocarbon groups attached to the backbone ( $R^1$  and  $R^2$ ) after the removal of the hydrogen atoms during pyrolysis and its distribution is closely related to the structure of the preceramic polymer<sup>59</sup>. The results show that for the saturated R groups the free carbon content is low while the unsaturated R groups lead to a greater content of free carbon and in general, the free carbon content in the ceramics increases as the number of carbon atoms in the R group increases<sup>59,66</sup> and also the heat treatment influences its fate, in the sense that at low temperature the carbon is homogeneously distributed in the amorphous material, while it forms structural units or locally enriched regions of turbostratic graphite at higher temperatures<sup>58</sup>. Formerly free carbon was thought to be negative for the mechanical properties of the final PDCs<sup>67,68</sup>. However, recently the evaluation of free carbon has been reversed as it has been shown that several carbon-rich PDCs exhibit better resistance toward crystallization, decomposition and oxidation than those with lower free carbon content<sup>66,69</sup> and it also has been proven to be beneficial for a number of other structural and functional properties of the PDCs, such as electrical conductivity<sup>70</sup>, electromagnetic properties<sup>71</sup>, creep<sup>72</sup> resistance and many others<sup>59</sup>.

Polymer-derived silicon oxycarbide (SiOC) and silicon carbonitride (SiCN) based ceramics are two typical PDCs possessing unique microstructures and resultant interesting properties. In particular, the SiOC-based ceramics can be characterized as amorphous materials with silicon atoms tetrahedrally coordinated by oxygen and carbon atoms, which have two hybridization methods:  $sp^3$  for the C–Si bond in the Si-based ceramic matrix and  $sp^2$  for the C–C bond in the segregated or free carbon phase<sup>59</sup>. Two models have been proposed for the microstructure of SiOC-based materials<sup>73</sup>: in the first model there are three constituents, clusters of silica tetrahedra that form the heart of the nanodomains, the graphene cage-like network that encases the nanodomains and the monolayer of  $SiC_xO_{4-x}$  mixed bonds ( $0 \leq x \leq 4$ ) that interconnect the silica clusters with the graphene network; the second model consists of two continuous interpenetrating phases (i.e., silica-rich phase and free carbon) and a carbon-rich  $SiC_xO_{4-x}$  interface.

The microstructure of PDCs can be investigated by various techniques which can provide average or integral information of the microstructures, such as X-ray diffraction (XRD), small-angle X-ray scattering (SAXS), small-angle neutron scattering (SANS) as well as MAS-NMR, FTIR and Raman spectroscopy and are able to provide the information regarding the local properties at the nanometer scale, such as SEM, TEM and electron energy loss spectroscopy (EELS).



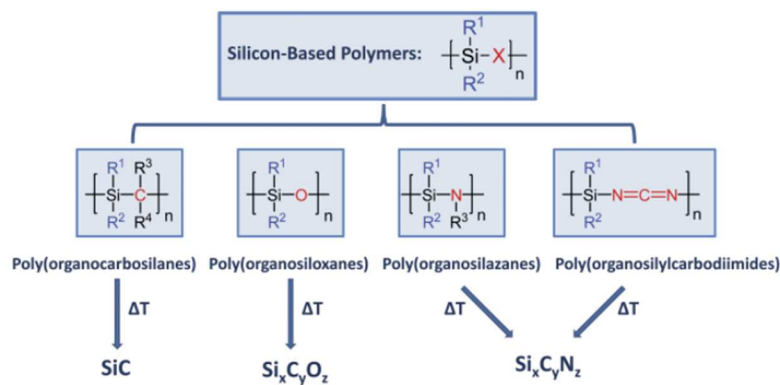


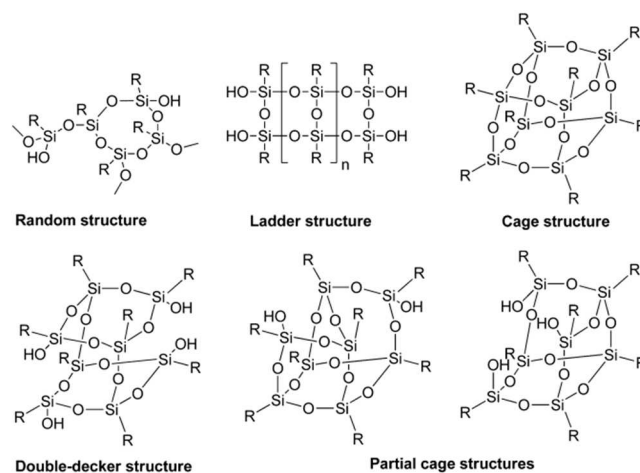
Figure 1.9. Thermal decomposition of silicon-based polymers<sup>58</sup>.

There are some requirements for preceramic polymers in order to be used<sup>58</sup>: they should possess sufficiently high molecular weight in order to avoid volatilization of low-molecular components during heat treatment which can lead to excessive shrinkage, deformation and fractures; they should have appropriate rheological properties and solubility for the shaping process; they should have latent reactivity (presence of functional groups) in order to have thermosetting and curing properties and they should have polymeric structures with cages or rings to reduce the volatilization of the fragments due to the backbone cleavage. Linear polymers without latent reactivity are unfavourable preceramic, while branched, cross-linked, or ring-type polymers exhibit higher ceramic yields and avoid the splitting out of volatile cyclomers and linear oligomers from the polymer skeleton, resulting in efficient precursors<sup>74</sup>.

### 1.5.1 – Poly(organosiloxanes)<sup>58</sup>

Poly(organosiloxanes), generally denoted as silicones, are important construction materials, usually inexpensive and a great variety of derivatives is commercially available. The general synthesis method for the preparation of polysiloxanes comprises the reaction of chloro(organo)silanes [R<sub>x</sub>SiCl<sub>4-x</sub>, x = 0-3; R = organic side group] with water. Interesting “nanoblock” preceramic polymers are the branched poly(organo)silsesquioxanes  $-\text{[RSi-O}_{1.5}]_n-$ <sup>75,76</sup>, which can have different configurations, represented in **Fig. 1.10** and are obtained through polycondensation of functionalized linear silanes and by the ROP of cyclic silaethers.

Cross-linked Poly(organosiloxanes) can also be prepared by the sol-gel process through hydrolysis and condensation reactions of hybrid silicon alkoxides<sup>77,78</sup>. Precursors are organically modified silicon alkoxides of the general formula: R<sub>x</sub>Si(OR')<sub>4-x</sub>, which after gelation lead to the corresponding silicon resin R<sub>x</sub>SiO<sub>(4-x)/2</sub> in which R is an alkyl, allyl, or aryl group and R' is usually a CH<sub>3</sub> or C<sub>2</sub>H<sub>5</sub>. The sol-gel process allows a precise control of the composition of the starting silicon resin by cohydrolysing different hybrid silicon alkoxides; the disadvantage is the little control over viscosity. After the pyrolysis heat treatment, as shown in **Fig. 1.9**, Poly (organosiloxanes) give rise to amorphous Si<sub>x</sub>C<sub>y</sub>O<sub>z</sub> PDCs with various Si/O and Si/C ratios.



**Figure 1.10.** General types of poly(organo)silsesquioxanes.

### 1.5.2 – Silicon Oxycarbide Glasses<sup>77</sup>

Silicon oxycarbide is a term used to denote the chemical structure in which silicon is simultaneously bonded with carbon and oxygen, generally described as  $[C_xSiO_{4-x}]$ . The replacement of some oxygen atoms in the network of a silicate glass with carbon atoms, which can be four-coordinated, increases the bonding per anion, leading to an increase of the strength of the molecular structure of the glass network, improving thermal and mechanical properties. One of the first attempt of incorporate carbon in glass was made by Ellis<sup>79</sup>: he impregnated tubes of porous silicate glass with different solutions containing carbohydrates in water and subsequently they have been heated to 1250°C in a nitrogen atmosphere; the carbohydrates are decomposed to carbon and with an aqueous solution containing about 90% by weight of sucrose produces a glass containing over 6% of carbon and its electrical resistivity is less than one ohm-cm. Other studies<sup>77</sup> then attempted to produce carbon-containing glasses starting from sources separate for silica and carbon, mixing and pyrolyzing them at high temperature to allow them to react to yield intimate mixtures of the two phases, such as Homeny *et al.*, which used SiC as the carbon source and synthesized glasses containing up to 2.5% carbon in the Mg-Al-Si-O-C system by melting at 1750-1800°C under nitrogen. The control of the final composition is difficult, but X-ray analysis has shown the obtainment of homogeneous glasses and free of crystallites.

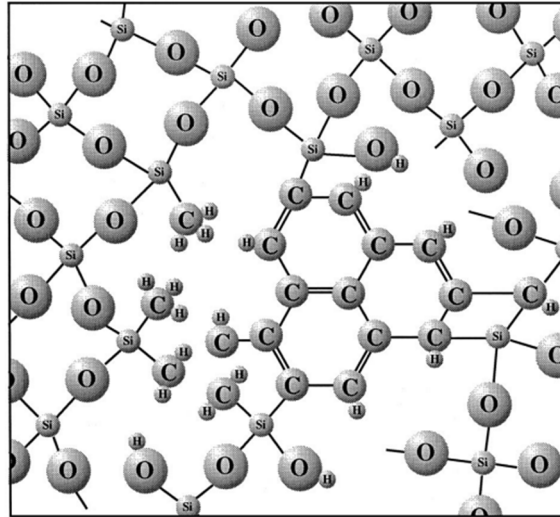
The introduction of carbon was successful through the sol-gel method, which enables the low-temperature synthesis of silicon oxycarbide glasses without the problems of decomposition and oxidation during melting, and uses alkyl-substituted silicon alkoxides (contain Si-C bonds) as precursors, which form gels containing Si atoms bonded simultaneously to carbon and oxygen, thus creating a silicon oxycarbide structure from which to synthesize silicon oxycarbide glasses; pyrolysis at higher temperatures is required in order to dehydrogenate and cross-link the terminal organic groups and to achieve the original goal of coordinating the carbon atoms to two, three or four Si atoms. The carbon chain-length, and the number and nature of the ‘R’ group modifications, allow a control of the amount of carbon introduced. An additional degree of compositional control is afforded by mixing the organically modified alkoxysilanes, in desired molar ratios, with other alkoxysilanes. A systematic series of silane precursors were used to prepare oxycarbide glasses<sup>77</sup>: <sup>1</sup>H NMR indicated

that the majority of Si–OR groups had been hydrolyzed to Si–OH, while the methyl, ethyl, propyl and phenyl groups bonded directly to Si, were retained.  $^{13}\text{C}$  and  $^{29}\text{Si}$  MAS NMR of these gels showed that the alkyl groups were still present in the gels, while the Si–OH terminal bonds had been largely replaced by Si–O–Si through condensation. From the analysis  $^{29}\text{Si}$  MAS-NMR it can be seen that the final black glass has a wider distribution of Si-species, and clearly, two of these have been created during the pyrolysis/densification step: one new phase is a silicon-oxygen tetrahedra  $-\text{[SiO}_4\text{]}$  and its presence indicates that some decomposition of the oxycarbide species occurred in the gel during pyrolysis, the other new phase is a Si tetrahedra with two bridging oxygens and two carbon bonds  $[\text{C}_2\text{SiO}_2]$ . It has also been shown that precursors having saturated hydrocarbon group modifications, e.g., methyl, ethyl, propyl groups attached directly to the Si atom were subjected to hydrolysis and condensation and that the carbon content of the gels was found to increase proportionately with increasing carbon chain length of the alkyl group. The glass produced from precursors having unsaturated hydrocarbon modifications (e.g., vinyl, allyl and phenyl groups) showed much higher carbon-contents.

The analysis of the structure of silicon oxycarbide glasses<sup>77</sup> through the  $^{29}\text{Si}$  NMR analysis of oxycarbide glasses prepared by pyrolysis of gels in the range 800-1000°C, has therefore shown that it consist primarily of  $[\text{SiO}_4]$ ,  $[\text{CSiO}_3]$ ,  $[\text{C}_2\text{SiO}_2]$  and  $[\text{CSiO}_2(\text{OH})]$  species; in some cases,  $[\text{C}_3\text{SiO}]$  and  $[\text{SiC}_4]$  may also be present.<sup>77</sup> There is a high presence of hydrogen in these glasses, associated with carbon atoms: the  $^{13}\text{C}$  NMR spectra shows the presence of  $[\equiv\text{SiCH}_3]$  species which probably represent terminations in the network which are analogous to non-bridging oxygens and the presence of free carbon in the form of polyaromatics  $[\text{nC}_6\text{H}_x]$ , evidenced by the black colour of the glass itself. The presence of  $\text{SiO}_4$  groups reveals some dissociation of SiC bonds and formation of free carbon during pyrolysis. For the characterization of this free carbon, various techniques can be used including high-resolution transmission electron microscopy (HRTEM) and Raman spectroscopy. While for pyrolyzed glasses at temperatures in excess of 1400°C both techniques show the presence of amorphous and graphitic carbon phases, for glasses synthesized at lower temperatures, 800-1000 °C, no traces of the same can be observed. However, since the NMR technique demonstrates the presence of elemental carbon, this means that the size of the elemental carbon species is below the critical size to create the Raman signal, < 2.5 nm. A schematic representation of an amorphous 800-1000°C silicon oxycarbide glass structure is given in **Fig. 1.11**.

The heat treatment temperature greatly influences the structure of the Silicon Oxycarbide Glasses. In the range 1000-1400°C the carbon, oxygen and silicon concentrations are reasonably constant but there is a significant loss of hydrogen and there is a drastic change of the distribution of oxycarbide species verifiable with NMR analysis: the concentration of  $[\text{CSiO}_3]$  decreases relative to  $[\text{SiO}_4]$ , accompanied by an increase in higher order oxycarbide and carbide species  $[\text{C}_x\text{SiO}_{4-x}]$  ( $x = 2 \text{ e } 4$ ). In fact it appears to be an equilibrium distribution of the various oxycarbide species at each temperature due to exchange reactions, or redistribution reactions of two or more atomic or molecular species exchange sites with each other, acid or base catalysed, or thermally activated. The formation of  $[\text{SiC}_4]$  are created through exchange reactions and decomposition of the  $[\text{SiO}_x\text{C}_y]$  species and occurs at different temperatures depending on the precursor used. At 1400°C, the oxycarbide structure has completely decomposed into an amorphous mixture of  $[\text{SiO}_4]$  and  $[\text{SiC}_4]$  species. At higher temperature,  $\geq 1500^\circ\text{C}$ , the carbothermal reduction of  $\text{SiO}_2$  (by C) occurs and SiC is formed. For heat treatment temperatures of 1600-1700°C, the  $^{29}\text{Si}$  MAS-NMR analysis show that SiC was the major

phase, although there was still some amorphous SiO<sub>2</sub> present. Upon heat treatment at 1750°C, the amorphous SiO<sub>2</sub> disappeared, leaving only a (broad) SiC peak in the spectrum. The broad peak is due to a mixture of α-, β- and other SiC polymorphs.



**Figure 1.11.** Schematic representation of an amorphous 800-1000°C silicon oxycarbide glass structure. Most of the carbon in the oxycarbide network is in the form of  $\equiv\text{Si}-\text{CH}_3$  non-bridging sites. It is possible that bridging network carbon species ( $\equiv\text{Si}-\text{CH}_2-\text{Si}\equiv$ ) are also present. The polyaromatic carbon species are shown bonded to the oxycarbide network, but an equally valid interpretation would show them as distinct polyaromatic carbon species ( $n\text{C}_6\text{H}_x$ ) embedded in the glass structure. These polyaromatic carbon species-bonded to the network or simply embedded-could range in size from single carbon rings to polyaromatics with dimensions up to 2.5 nm<sup>77</sup>.

#### 1.5.2.1 – Free carbon

The formation of free carbon has been widely reported<sup>80,81</sup> during the polymer to ceramic conversion of preceramic polymers. As regards the microstructural characterization of the in situ formed carbon, a number of techniques have been used that allow us to obtain a lot of information. From TEM analysis, it follows that generally the PDCs prepared through pyrolysis at 800-1100°C are characterized by a random glassy network. The size of free carbon phase in the PDCs pyrolyzed at temperatures lower than 1200°C is rather small<sup>65,69</sup>. In the PDCs heat-treated at temperatures  $\geq 1400^\circ\text{C}$ , the lattice fringes of the free carbon with an interplanar distance of around 0.34 nm become clearer. The grain sizes of free carbon clusters enhance with increasing of carbon content and heating temperatures, and the entangled carbon ribbons forming a percolation network can usually be observed in the carbon-rich PDCs<sup>69,80</sup>. Raman spectroscopy is one of the most sensitive methods and an important non-destructive tool for characterization of the free carbon, particularly regarding its structural evolution at elevated temperatures. The Raman spectra of free carbon in the PDCs were firstly reported in the characterization of SiC fibers in 1980's<sup>82</sup>. The typical signals of free carbon in the first-order Raman spectra are the so-called D and G bands. The G band is due to stretching vibrations of sp<sup>2</sup>-carbon in the basal-plane of ideal graphitic lattice and generally it appears for highly oriented polycrystalline graphite (HOPG) or single graphitic crystals; the D band is a defect-induced band, which corresponds to a graphitic lattice vibration mode and it is well known to represent the disordering of the free carbon. The intensity ratio of the D band and G band [I(D)/I(G)] in the Raman

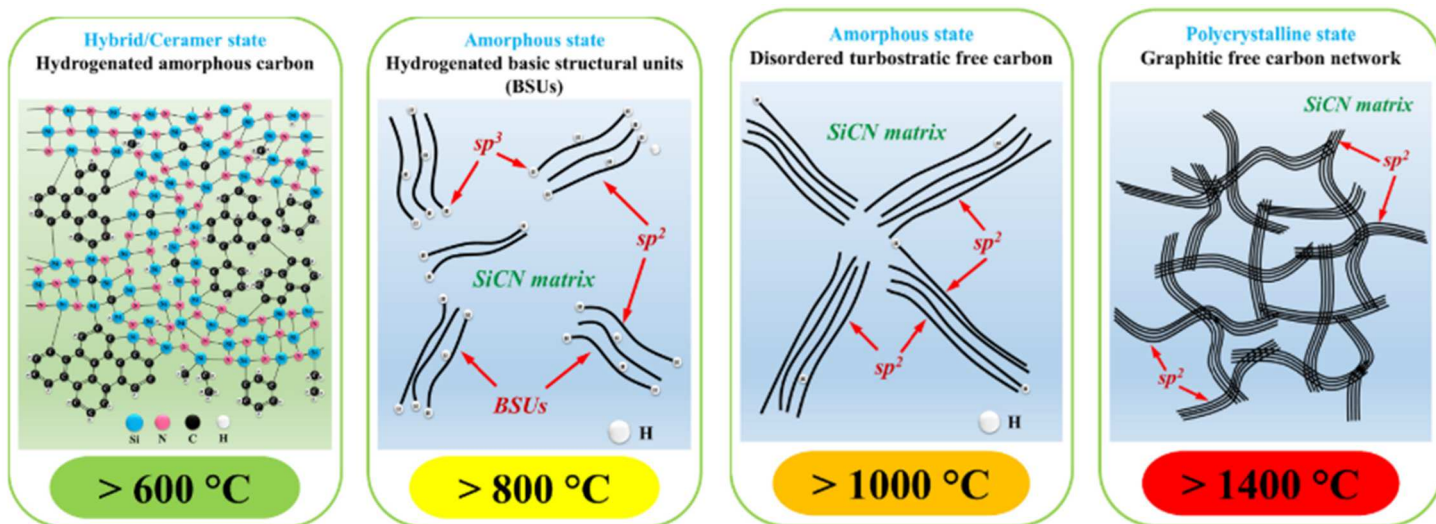
spectra is a measure of the structural disordering of free carbon. The higher the I(D)/I(G) value, the higher the disordering of free carbon. Three primary reasons can be attributed to the disordering of the free carbon phase in PDCs: (1) the presence of edges in the graphene layers; (2) the deviation from planarity of graphene layers; and (3) the presence of carbon atoms in  $sp^3$  hybridization state<sup>59</sup>. The I(D)/I(G) ratio can also be utilized to estimate the lateral crystallite size of the carbon clusters. The XRD technique allows to calculate the lateral crystallite size ( $L_a$ ) and the crystallite thickness ( $L_c$ ) of the crystallized free carbon using the Scherrer equations<sup>83</sup>.

The free-carbon phase can be analysed by means of  $^{13}\text{C}$  solid-state MAS-NMR. It is possible to distinguish  $sp^2$  hybridized carbon atoms from tetragonally coordinated  $sp^3$  carbon atoms with respect to the chemical shift values and spin-lattice relaxation time. From the analysis of the spectrum it can be understood that the free carbon formed at around  $600^\circ\text{C}$  in this system<sup>84</sup> and that it has an amorphous structure; at higher temperatures ( $1200\text{--}1500^\circ\text{C}$ ), the NMR signals show an increased ordering of the free carbon which is probably caused by the elimination of hydrogen atoms bonded to the periphery of the free carbon<sup>84</sup>. The evolution of free carbon in the PDCs can also be identified by characterization of the transition of chemical bonds using XPS. The C–Si, C=C, and C–C/H bonds should be the main chemical bonds related to the free carbon<sup>85</sup>. The C=C bonds ( $sp^2$  hybridization) are primary chemical bonds in the free carbon phase and the C–C bonds ( $sp^3$  hybridization) are in the aliphatic carbon chains of the precursors, which decrease with increasing of the pyrolysis temperature<sup>85</sup>; the C–H bonds ( $sp^3$  hybridization) are generally present in the periphery of the free carbon within the PDCs obtained at temperatures lower than  $1250^\circ\text{C}$ .

Using advanced characterization techniques as mentioned above, the structural evolution of the in situ formed free carbon with increasing of temperature has been intensively studied<sup>78</sup>. With increasing thermolysis temperatures, the general trends can be summarized as the following four steps: (1) precipitation of hydrogenated amorphous excess carbon by decomposition of aromatic hydrocarbons; (2) nucleation of basic structural units (BSU); (3) growth of the turbostratic free carbon clusters via edge-to-edge linkage of BSUs; (4) graphitization of free carbon network or nanodomains<sup>86</sup>. In **Fig. 1.12** is schematically presented the evolution free carbon in SiCN-based ceramics. The MAS-NMR spectroscopy reveals that the initial precipitation of free carbon during the polymer-to-ceramic transformation starts at  $600\text{--}800^\circ\text{C}$ , depending on the molecular structure of the polymers<sup>86</sup>. Generally, at lower temperatures ( $< 800^\circ\text{C}$ ), the hydrogenated excess carbon remains amorphous (mainly  $sp^3$ -hybridized) and homogeneously dispersed in the amorphous ceramic matrix; with increasing pyrolysis temperatures ( $800\text{--}1000^\circ\text{C}$ ), the carbon layers stack in turbostratic order, forming the basic structural units (BSUs) of free carbon (i.e., nucleation)<sup>87</sup>. The initially formed BSUs are isolated to each other, and the peripheral carbon atoms are saturated by hydrogen atoms. After pyrolysis at  $800\text{--}1000^\circ\text{C}$ , the PDCs mainly composes of a highly turbostratic free carbon phase and an amorphous Si-based ceramic matrix. When the heating temperature rises up to  $1000\text{--}1200^\circ\text{C}$ , the aromatic C–H groups in the periphery of the BSUs become not stable. Thus, the residual hydrogen atoms are removed as  $\text{H}_2$  in this temperature range, inducing an unsaturation of the peripheral carbon atoms. The unsaturations are subsequently eliminated by the edge-to-edge linkage of neighbouring BSUs, leading to the formation of elongated free carbon stacks with the length of around 3–4 nm and a significant transition of  $sp^3$  to  $sp^2$  hybridization. At temperatures higher than  $1250^\circ\text{C}$ , almost no hydrogen atoms appear in the PDCs<sup>86</sup>. After further heat treatment at elevated temperatures ( $>$

1400°C), the growth and rearrangement of free carbon regions continue and result in an entangled free carbon network or nanodomains with graphitic carbon nanocrystallites.

The presence of free carbon greatly influences the properties of PDCs. It was demonstrated that several carbon-rich PDCs exhibit better resistance toward crystallization, decomposition and oxidation than those with lower free carbon content<sup>66,69</sup> and it also has been proven to be beneficial for a number of other structural and functional properties of the PDCs, such as electrical conductivity<sup>70</sup>, electromagnetic properties<sup>71</sup>, creep<sup>72</sup> resistance and many others<sup>59</sup>.



*Figure 1.12. Illustration of the structural evolution of free carbon during pyrolysis of preceramic polymers<sup>59</sup>.*

## Chapter 2

### Characterization techniques

This chapter illustrates, from the theoretical point of view, some techniques and the instrumentation adopted for the analysis and characterization of inks and synthesized samples.

*2.1 – TGA, ThermoGravimetric Analysis* (“*Thermal Analysis of Polymers: Fundamentals and Applications*, Joseph D. Menczel, R. Bruce Prime, Wiley)

It is an experimental technique for the characterization of materials belonging to the broader family of thermal analyses, **Fig. 2.1**. The thermal analysis in general contribute to the study, both at the macroscopic and at the microscopic level, the properties of the material under examination. In particular, thermal analyses are useful in describing phase transformations from a kinetic and thermodynamic point of view, since during a phase transformation a change in the properties of the material occurs, induced by a variation of external variables, such as temperature and pressure. The TGA technique consists in the continuous measurement over time, through a thermo-balance, of the mass of the sample as a function of temperature through the application of a controlled program, under controlled, inert, reducing or oxidizing atmosphere conditions. This technique is mainly used for the study of the degradation of materials, and more generally in the reaction kinetics; it is also employed in the study of oxidation kinetics if carried out in an oxidative atmosphere and for the study of thermal-oxidative aging.

The heart of the analyser is the thermo-balance, which is capable of measuring the sample mass as a function of temperature and time; in **Fig. 2.2** three examples are shown. The temperature is measured through thermocouples that are positioned differently (**Fig 2.2**) depending on the type of support for the sample which must be a crucible of inert material; the most common materials are steel, platinum, alumina. The main factors affecting TGA results are the buoyancy and the thermal expansion of the sample, atmospheric turbulence, condensation and reactions with the electrostatic and magnetic forces. The buoyancy is the upward force on the sample produced by the surrounding atmosphere: as the density of the atmosphere in the balance decreases with increasing temperature, there appears to be an increase in mass of the sample. One approach to compensate for buoyancy and general baseline issues encountered with very small mass loss, is to perform a second experiment matching inert sample and subsequently subtracting this ‘blank’ experiment. The furnace is generally made of refractory material, such as (alumina,  $T_f > 2000^\circ\text{C}$ ; quartz,  $T_f > 1700^\circ\text{C}$ , and the ventilation and gas recirculation system is also important: it is useful for conditioning and keeping the atmosphere under control inside the furnace and eliminate any gases produced as a result of the degradation of the analysed material. The gases used during the analysis must be verified in terms of purity and in terms of flow to the furnace; purity can be checked by taking a sample of gas and analysing it with a gas chromatograph and flow through a flow meter. A commercial TGA can sense, in a reproducible fashion, mass changes as small as few tenths of microgram. With this level of sensitivity, it is seldom necessary to analyse large samples. Obviously smaller samples will equilibrate with the furnace temperature faster than will larger samples. In addition, during pyrolysis a heavy sample ( $> 10\text{ mg}$ )

as compared to a relatively light sample (< 5 mg) will result in more degradable products being trapped on the furnace itself or in the cooling walls and can cause turbulence inside TGA, leading to noise.

### **Methods of Thermal Analysis**

- **Calorimetric Effects**
  - DSC Differential Scanning Calorimeter
  - DTA Differential Thermal Analyser
- **Changes in Mass**
  - TGA Thermo Gravimetric Analyser
  - TG/DTA Thermo Gravimetric/ Differential Thermal Analyser
- **Dimension Change**
  - TMA Thermo Mechanical Analyser
  - TMA/SS Thermo Mechanical Analyser/Stress Strain
- **Viscoelastic Properties**
  - DMA Dynamic Mechanical Analyser
  - DMTA Dynamic Mechanical Thermal Analyser
  - DMS Dynamic Mechanical Spectrometer
- **Other Techniques and Combined Techniques**
  - EGA Evolved Gas Analyser
  - TG/MS Thermo Gravimetry/ Mass Spectroscopy
  - TG/GC/MS Thermo Gravimetry/Gas Chromatography/Mass Spectroscopy

*Figure 2.1. Methods of Thermal Analysis.*

The TGA technique provides a quantitative analysis of the mass change but does not provide information regarding the nature of the lost material. It is possible to associate it with an evolved gas analysis measurement, EGA. The most frequently used methods are the mass spectroscopy (MS) and Fourier transform infrared spectroscopy (FTIR). The energy information provided by DSC (differential scanning calorimetry) or DTA (differential thermal analysis) techniques complete the information of the TGA, since they provide not only information on the enthalpy of the process but also detect transitions and reactions that not result in a change in mass of the system, which is why simultaneous TGA/DSC (also called simultaneous thermal analysis STA) or TGA/DTA has several advantages over separate experimentations, in addition to saving costs, time and alleviating ambiguities due to different test conditions.

DTA (*Differential Thermal Analysis*) and DSC (*Differential Scanning Calorimetry*) are two thermal analysis that measure the temperature assumed by the sample during the analysis in progress and are used for the study of phase transformations. They measure a variation of the property, which makes it possible to considerably reduce the experimental errors. A quantity corresponding to the difference between the values of the property under examination taken from the sample and from an inert reference is measured. DTA reveals changes during the heating of a sample which involve evolution or absorption of energy. The sample and a chemically and thermally inert reference material (sintered alumina or precipitated silica) are mounted in a recessed heating block and slowly heated. The thermocouples in the two chambers are connected in opposition and the difference is amplified and plotted against temperature. Peak area on this trace is a function of the change in enthalpy  $H$  as well as the mass and thermal characteristics of the sample. DTA is generally regarded as a semi-quantitative or qualitative method. It has been used in studies of devitrification in oxide glasses and the glass transition in polymers. The DSC technique measures the amount of heat absorbed or released by the sample during heating or cooling and compares the sample flow to a reference. In this case,



therefore, the sample and the reference are subjected to a linear temperature ramp with a fixed heating rate and are kept at the same temperature. If at a certain temperature the sample undergoes exothermic or endothermic phenomena, the amount of heat necessary to keep it in isothermal with the reference will be less or greater (different power of the thermoresistances of the two furnaces). The graph obtained shows the enthalpy variations as a function of temperature: exothermic peaks indicate for example crystallization phenomena, endothermic ones, melting phenomena; variation of the slope of the curve indicate an increase in the heat capacity of the sample as in the case of a glass system, what is observed on the occasion of the glass transition.

In the TGA, a very important aspect is the calibration of the instrument. Most important in TGA is the linearity of mass measurement, in the sense that any percentage of mass lost must be measured with equal reproducibility and accuracy. For the calibration of the mass under changing temperature conditions, mixtures of liquids with markedly different vapor pressures or well characterized stable compounds are used, such as hydrates and carbonates that have reliable decomposition patterns and generally an inert gas (nitrogen or helium). Unwanted magnetic fields can be problematic if there are magnetic samples and electrostatic disturbances can alter the measurements: to stem these problems, configurations have been introduced that cancel the resulting magnetic field and also antistatic coatings have been introduced. The calibration of the temperature scale, measured and regulated by the control system of the machinery, can be carried out by exploiting a physical phenomenon characteristic of some metals or metal alloys called Curie temperature, or through an approach that utilizes the melting points of high-purity metals as defined in the International Temperature Scale (*Quinn 1990*).

The main choices in performing a TGA analysis are the quantity of the material studied, the thermal program used with the possible inclusion of isothermal steps, the type of crucible, the extent of the gas flows inside the furnace and the cleaning of the furnace.

As for kinetic information, the goal of kinetics is to provide mathematical relationship between time, temperature and conversion. At a constant pressure, the rate of many thermally activated processes can be described as a function of temperature (T), controlled by the TGA program, and the extent of conversion ( $\alpha$ ), determined from mass loss measurements:

$$\alpha = \frac{m_i - m_T}{m_i - m_f} \quad \text{Eq. (2.I)}$$

where  $m_T$  is the mass at temperature T,  $m_i$  and  $m_f$  are initial and final mass respectively for a given step of mass change. Regarding a measure of degradation, the  $\alpha - T$  curve represents the conversion of the sample to volatile degradation products. In the simplest case, the rate equation has the following form:

$$\frac{d\alpha}{dt} = k(T)f(\alpha) \quad \text{Eq. (2.II)}$$

where  $k(T)$  is the rate constant and  $f(\alpha)$  is the reaction model which may take various mathematical forms, depending on the physical mechanism assumed in the mathematical derivations (*Brown 2001*). The temperature dependence is almost universally described by Arrhenius equation:

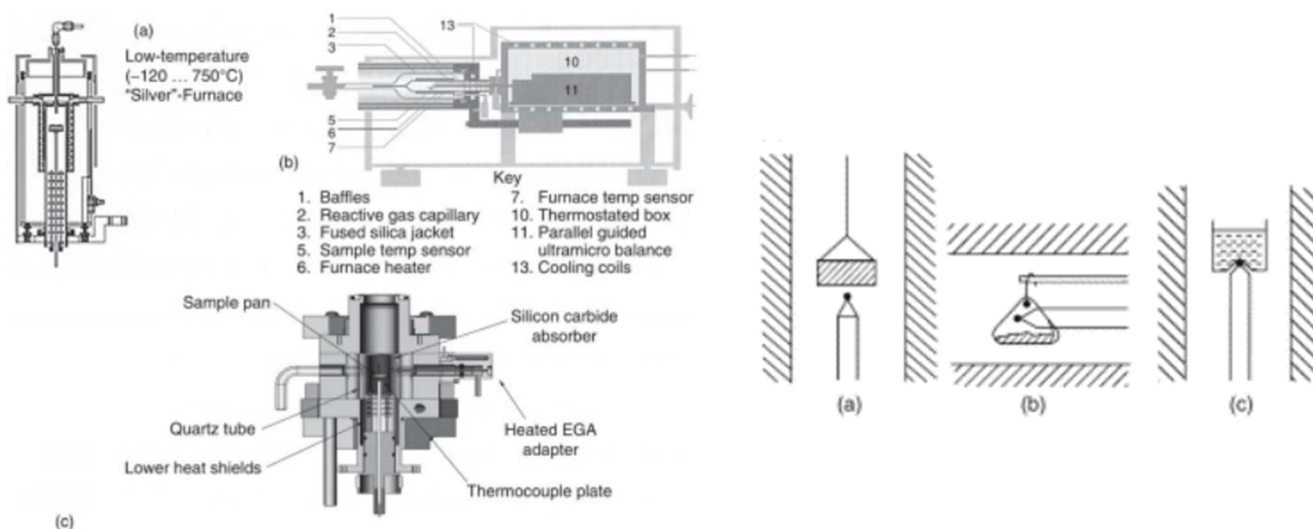
$$k(T) = A \exp\left(\frac{-E}{RT}\right) \quad \text{Eq. (2.III)}$$

where A and E are Arrhenius parameters and R the universal gas constant. The reaction rate depends on the conversion, which can follow one of three mathematical forms, accelerating, decelerating and autocatalytic for each of which there are power-law models.

For a first-order reaction model, the equation is obtained:

$$\alpha = 1 - \exp [-k(T)t] \quad \text{Eq. (2.IV)}$$

More in-depth considerations are beyond the scope of this paper.



**Figure 2.2.** Examples of thermobalances (left); thermocouple positioning (right).

## 2.2 – XRD, X-ray diffraction

Non-destructive technique that allows a quantitative and qualitative study of pure crystalline solids or multi-component mixtures. The X-ray diffraction by a crystal is the result of a diffusion process by the atoms within the crystal itself without variation in wavelength. Within a crystalline solid, the atoms are three-dimensionally arranged in a regular manner according to one of the 14 Bravais lattices and the distance between them is similar to the wavelength of the X radiation (0.1-10 Å).

When an X-ray beam hits matter, it can be partly absorbed, partly transmitted, partly scattered. In particular, diffraction is the interference that the electromagnetic radiation that diffuses from an object placed on its path undergoes. When the innermost electrons of the atoms that make up the material subject to diffractometric analysis interact with X-rays, they resonate with the latter, oscillating with the same frequency as the incident wave. At this point the electrons become sources of diffused X radiation, having the same wavelength as the incident beam. If the irradiated material is crystalline, the diffuse waves coherently interfere with each other, thus giving rise to the diffraction spectrum, characteristic of each crystalline sample, a fingerprint that identifies crystalline samples by matching the pattern with the Joint Committee on Powder Diffraction Standards library (JCPDS). Diffraction spectrum identifies crystal structure, degree of crystallinity, crystallite size and atomic spacing,

crystalline phase, transition and their quantitative proportion, microstructure, quantitative resolution of chemical species, isomorphous substitutions, unknown crystalline materials, and solids.

Depending on the nature of the sample under examination, it is divided into single crystal X-ray diffraction (SC-XRD, *single crystal X-ray diffraction*) and powder diffraction (XRPD, *X-ray powder diffraction*). The first technique is able to give three-dimensional information on the electronic density and on the thermal motions of each atom making up the crystal; however, the difficulty of obtaining single crystals and the complexity of data analysis make it a non-routine technique. Extremely more widespread is instead the X-ray diffraction of powders, which is much faster and cheaper and allows to quantify the various components of a solid sample, and to obtain information on the crystalline structure and on the size of the crystallites. In XRPD the sample is polycrystalline, with the particles randomly oriented with respect to the incident beam, with the result that each family of planes is able to reflect and considering a particular reflection  $hkl$  at a certain angle  $2\theta$ ; the typical diffraction cone is formed.

X-rays are produced by two types of interactions of charged particles, electrons, with the atoms that make up matter: when an incident electron ionizes an atom by displacing an electron of the innermost levels, its vacancy will be filled by an electron of the more external levels with the emission of an X-ray (characteristic radiation); when the incident electron is accelerated or decelerated by the electric field produced by the atomic nucleus it emits X electromagnetic radiation (called braking, *Bremsstrahlung*, continuous spectrum). When an X-ray beam hits a solid material with a crystalline structure, it causes therefore the vibration of the electrons surrounding a single atom which act as oscillating dipoles and emit electromagnetic radiation of wavelength  $\lambda$  in all directions. Diffuse waves can interfere both destructively and constructively. Coherent scattering of radiation occurs due to the dimensional regularity of unit cell and it happens only in specific directions: the directions of the scattered beam depend on the interatomic spacing ( $d_{hkl}$ ) of the plane and on the radiation wavelength, the intensity of the scattered beam depends on the orientation of the crystal relative to the direction of the incident x-ray and the position of each atom inside the unit cells. The angles at which there is constructive interference and the sample diffracts the radiation are those that comply with Bragg's law, which explains the relationship between the wavelength of the produced electromagnetic radiation, the lattice spacing of the crystalline sample and diffraction angle:

$$n\lambda = 2d_{hkl}\sin\theta \quad \text{Eq. (2.V)}$$

where  $n$  is an integer (1, 2, 3, 4...),  $d_{hkl}$  marks the inter-planar spacing generating the diffraction,  $\theta$  is the X-ray incident angle with respect to the planes considered and  $\lambda$  is the wavelength of the incident X-rays. A characteristic spectrum of diffraction spots is generated, which can be recorded by a detector and switched into a diffractogram or diffraction spectrum; this is a two-dimensional diagram, with a series of peaks relative to different intensities  $I$  and angular positions  $2\theta$  (shown on the abscissa) characteristic of each single phase. Knowing the wavelength ( $\lambda$ ) of the radiation used and the angular value ( $2\theta$ ) of the emitted rays, it is possible to trace the distances of the lattice planes " $d_{hkl}$ " that gave rise to the diffraction phenomenon and therefore to the nature of the phases present.

An X-ray diffractometer is the instrument used to determine the diffraction spectrum and consists of an X-ray source, monochromator filters, slides that limit the divergence of the primary beam, receiving slides of the diffracted beam that improve resolution and a detector able to rotate. X-rays

are generally produced inside an X-ray tube consisting of a vacuum glass bulb that contains a cathode, consisting of a heating filament, and an anode, generally consisting of a heavy metal sheet, both of them subjected to high voltages (20-100 kV). An electric current is passed into the filament from which electrons are emitted due to the thermionic effect, they are accelerated towards the anode by the potential difference with which they interact and produce X-rays that can leave the tube through a beryllium (Be) window. Richardson's law expresses the current density emitted by the thermionic effect:

$$J_c = AT^2 \exp(-E_w/KT) \quad \text{Eq. (2.VI)}$$

The X-ray tube is contained in a metal sheath (generally aluminium, with lead shields) filled with dielectric oil, cooled with air or water, capable of dissipating the heat generated by the tube and guaranteeing electrical insulation.

The intensity of the characteristic radiation increases with the voltage applied according to the relationship:

$$I_{\text{linea K}} \propto i(V - V_K)^n \quad [n \sim 1.5] \quad \text{Eq. (2.VII)}$$

where  $i$  is the tube current,  $V$  the voltage applied,  $V_K$  the critical excitation potential for the material used as anode, while the intensity of the continuous is proportional to the atomic number  $Z$  of the material and the applied voltage.

$$I_{\text{continuo}} \propto ZiV^m \quad [m \sim 2] \quad \text{Eq. (2.VIII)}$$

The most important feature of the diffractometer is the geometry which depends on the relative position between the source, the sample and the detector during the measurement. As regards the application of the powder method, there are two applicable geometries: the Debye-Scherrer or the Bragg-Brentano. In the Debye-Scherrer chamber an X-ray source emits an uncollimated polychromatic radiation that passes through a monochromator filter and a collimator before striking the sample positioned in the center of the chamber, whose internal walls are covered with photographic film that simultaneously records the intensity of the radiation diffracted by the sample for each angle  $2\theta$ . The most common geometry, on the other hand, is the Bragg-Brentano one, in **Fig. 2.3**: in this configuration the source and the detector rotate simultaneously around the sample that remains fixed (*Bragg – Brentano  $\theta - \theta$  geometry with a fixed sample*) or what remains fixed is the X-ray tube ( *$\theta - 2\theta$  geometry*). In these geometries the detector and source are located at the intersection points of the goniometer circle (fixed radius) and the focusing circle, whose radius varies with the goniometer angle<sup>88</sup>. The sample is placed tangentially to the focusing circle in the center of the goniometer. The rotation allows to irradiate the sample at different angles and to intercept the refracted X-ray at an emergence angle double compared to the incident one. The goniometer determines the position of the source and the detector during the measurement and therefore the angle of incidence and scattering.

The information obtainable from X-ray diffraction is many. The position of the peaks allows to derive the interplanar distances (Bragg equation), the crystalline system, the crystallographic cell size and to make a qualitative analysis. For example, from a reflection of the planes (111) of a cubic crystal observed with an angle of incidence  $11.2^\circ$  with  $\text{CuK}\alpha$ , we obtain:

$$d_{(111)} = \frac{\lambda}{2 \sin\theta} = 3,96 \text{ \AA}$$

$$d_{(111)} = \frac{a}{(h^2 + k^2 + l^2)^{\frac{1}{2}}} = a/3^{1/2}$$

$$a = 3^{1/2} \cdot d_{(111)} = 6.87 \text{ \AA}$$

From the knowledge of the interplanar distances in relation to the diffraction angles, it is possible to trace the triads of the Miller indices that define the orientation of the different crystallographic planes and then determine the crystalline structure of the sample. The qualitative analysis is carried out by comparing the diffractogram of the unknown sample with those present in the various databases and then tracing the identity of the different crystalline phases. From the intensity of the peaks, it is possible to obtain information about the intensity of a phase (structure factor) or several phases and carry out a structural and quantitative analysis (with/without standard). The intensity of the peak is expressed by:

$$I_{hkl} = |F_{hkl}|^2 P \left( \frac{1 + \cos^2\theta}{\sin^2\theta \cos\theta} \right) e^{-2M} \quad \text{Eq. (2.IX)}$$

where  $|F_{hkl}|^2$  is the structural factor and indicates scattering of X-ray by electron, atom, unit cell; P is the multiplicity factor, for example (100), (010) and (001) contribute to the same reflection; the third term is the Lorenz-Polarization factor which expresses the effect of rotating crystal and the last is the temperature factor which expresses the thermal vibration. The positions of the atoms in the unit cell affect the intensity of the diffracted radiation, but not its direction. The atomic positions can be determined by measuring the diffracted intensities ( $I \sim F^2$ , with F structure factor). Quantitative analysis can be carried out according to three different methods: the external standard method consists in comparing the lines of a substance in the sample with the lines of the same substance in its pure state; the internal standard method consists in comparing the lines of the test substance with those of a standard substance mixed with the sample in known proportions; the direct comparison method uses as reference lines those of a second phase in the mixture that constitutes the sample under examination. The width of the peaks depends on the microstructure and imperfections of the material and provides information about the size of the crystals and their deformation, in **Fig. 2.4**. The size of the crystal can be estimated through the Scherrer equation:

$$D = K\lambda / \{B \cos\theta_B\} \quad \text{Eq. (2.X)}$$

In which D is the crystallite size, K is the Scherrer constant (0.87 ~ 1.0) and  $\lambda$  is the wavelength of the radiation. The effect of the crystalline deformation affects the position and width of the peak itself: the XRD technique is in fact also used for the measurement of residual stresses. The background noise (background) depends on the random interactions of the radiation with the air, the diffractometer *etc.*

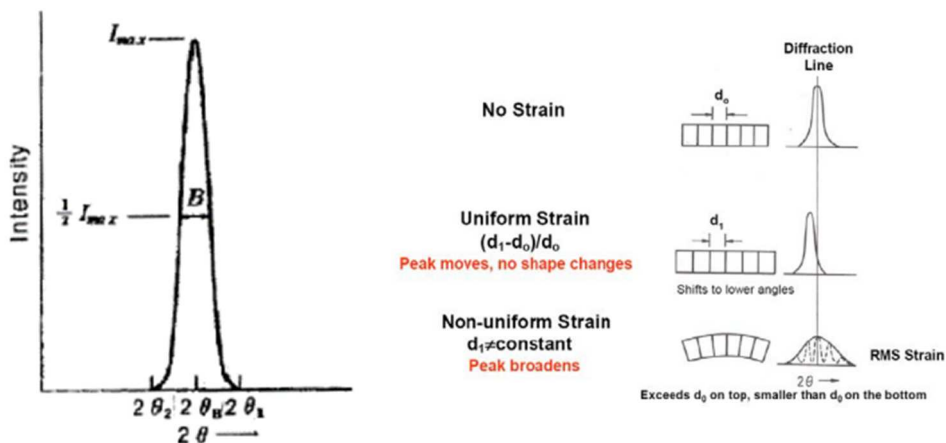


Figure 2.4. Peak width (left); influence of crystalline deformation (right).

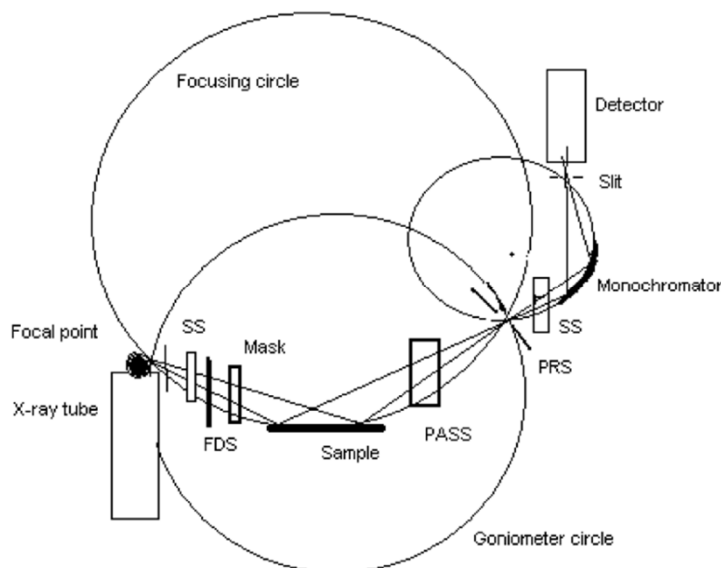


Figure 2.3. Geometry of Bragg-Brentano. The abbreviations used are: SS for Solar slit, FDS for fixed divergence slit, PASS for programmable anti-scattering slit, PRS for programmable receiving slit. Radius of Goniometer (RG), radius of focusing circle (RF) and radius of monochromator (RM) can be related as  $RF = [RG/2 \sin(\theta)]$ .

## 2.3 – FTIR, Fourier-transform infrared spectroscopy

It is a technique that allows the recognition of the functional groups present in a molecule and it is based on the absorption of IR radiation (IR is divided into three main regions, NIR with a wavenumber between  $12800\text{--}4000\text{ cm}^{-1}$ , MIR with  $\tilde{\nu}$  between  $4000$  and  $200\text{ cm}^{-1}$  and FIR with  $10 < \tilde{\nu} < 200$ ), which influences the distance and the bond angles leading to a vibration of the latter. A fundamental requirement for a molecule to be IR active is that, during the vibration, there is a variation in its dipole moment, so if the molecule has a center of symmetry all the symmetrical vibrations with respect to the center itself are IR inactive. The vibrations can be of stretching ( $\nu$ ) as regards the variation of the bond lengths, which can in turn be symmetrical ( $\nu_a$ ) or asymmetrical ( $\nu_{as}$ ), or of bending as regards the modification of the bond angles, which can occur at the interior of the plane ( $\delta$ ) which contains

the links, with the two phenomena of scissoring and rocking, or even outside the plane ( $\pi$ ), with the phenomenon of twisting and wagging. The stretching vibrations can be modeled using the harmonic oscillator model<sup>89</sup> with oscillation frequency  $\nu$  ( $\text{cm}^{-1}$ ):

$$\nu = (1/2\pi c)\sqrt{k(m_1 + m_2)/m_1 m_2} \quad \text{Eq. (2.XI)}$$

$m_1$  and  $m_2$  (g) the masses of the atoms or chemical groups involved in the bond,  $k$  ( $\text{dyne}\cdot\text{cm}^{-1}$ ) the bond strength (the spring tenseness) and  $c$  the speed of light ( $\text{cm}\cdot\text{sec}^{-1}$ ). From the energy point of view, the potential energy of a two-mass system in the harmonic oscillator model is:

$$E = \frac{1}{2}kx^2 \quad \text{Eq. (2.XII)}$$

and the quantum treatment describes vibrational energy as:

$$E = h\nu/2(k/(m_1 + m_2)/m_1 m_2))^{1/2}(\nu + 1/2) \quad \text{Eq. (2.XIII)}$$

with  $\nu$  vibrational quantum number,  $k$  constant of force,  $h$  Planck's constant and  $m_1$  and  $m_2$  masses of atoms. The energy value for  $\nu = 0$  is not zero but  $E = \frac{1}{2} h\nu$ , *Zero-point energy*. The various vibrational energy levels are quantized. Functional groups can be associated with characteristic infrared absorption bands, which correspond to the fundamental vibrations of the functional groups<sup>89</sup>, in fact, each vibration is associated with a single frequency which is the only one that will be absorbed by that precise functional group. For a nonlinear molecule with  $N$  atoms, there are  $3N-6$  vibrational motions of the molecule atoms<sup>89</sup>. In an FTIR spectrum there are two types of signals commonly called peaks: those related to the presence of particular functional groups ( $4000-1500 \text{ cm}^{-1}$ ) in which the vibrations of the main functional groups are observed, and those considered to be fingerprint ( $1500-400 \text{ cm}^{-1}$ ) in which the deformations essentially depend on the molecular architecture, so the peaks of variable intensity and number are specific and uniquely represent each single compound. The design of many interferometers used for infrared spectrometry today is based on that of the two-beam interferometer<sup>90</sup> originally designed by Michelson in 1891<sup>91</sup> even if many other two-beam interferometers have subsequently been designed that may be more useful than the Michelson interferometer for certain specific applications<sup>90</sup>. This device can divide a beam of radiation into two paths and then recombine the two beams after a path difference has been introduced, which produces interference between the two rays; the variation of intensity of beam emerging from the interferometer is measured as a function of the path difference by a detector. An example of the interferometer is shown in **Fig. 2.5**.

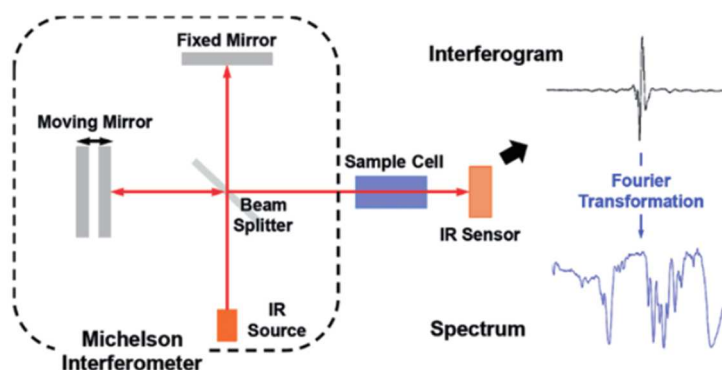


Figure 2.5. Michelson interferometer.

It consists of three mirrors: a semi-transparent central one (*beamsplitter*), a fixed one (*fixed mirror*) and a mobile one (*movable mirror*, that can be at constant speed, continuous scan interferometer, or be held at equally spaced points for fixed short periods and stepped rapidly between these points, a step-scan interferometer<sup>90</sup>). The radiation emitted by the source arrives at the semi-transparent mirror, where it is partially reflected to the fixed mirror and partially transmitted to the movable mirror; when the two radiations return to the beamsplitter, constructive or destructive interference phenomena occur, since they have travelled through different optical paths. Since the optical path of one of the radiations varies over time, the interference between the radiations and the transmittance of the sample will also vary over time. The graph that shows the transmittance of the sample as a function of time is called an interferogram and through the mathematical operator Fourier transform is transformed into a spectrum that shows the transmittance as a function of the wave number. To measure the path difference, a laser beam is sent through the interferometer generating a sinusoidal signal where the separation between successive maxima is equal to the wavelength of the laser (typically a 632.8 nm HeNe laser is used).

The path difference between the beams that travel to the fixed and movable mirrors and back to the beamsplitter is called retardation, and at it is given the symbol  $\delta$ . If the movable mirror is moved at constant velocity, the signal at the detector will be seen to vary sinusoidally. A maximum is registered each time that the retardation is an integral multiple of  $I_0$ . At the intensity of the beam at the detector measured as a function of retardation is given the symbol  $I'(\delta)$ . When  $\delta = \lambda_0 n$  (where  $n$  is an integer) the intensity of the radiation which arrives at the source is equal to the intensity of the source  $I(\tilde{\nu})$ , for other values instead, the intensity of the beam at the detector, or interference record, is given by:

$$I'(\delta) = 0.5I(\tilde{\nu})(1 + \cos 2\pi\tilde{\nu}_0\delta) \quad \text{Eq. (2.XIV)}$$

In reality, the amplitude of the interferogram as observed after detection and amplification, is proportional not only to the intensity of the source but also to the beamsplitter efficiency, detector response, and amplifier characteristics. The equation should be modified considering all these contributions which may be set equal to  $B(\tilde{\nu}_0)$ . The simplest equation representing the interferogram in terms of signal  $S(\delta)$  (in volts), from the amplifier is:

$$S(\delta) = B(\tilde{\nu}_0)\cos 2\pi\tilde{\nu}_0\delta \quad \text{Eq. (2.XV)}$$

Mathematically,  $S(\delta)$  is said to be the cosine Fourier transform of  $B(\tilde{\nu}_0)$ . The spectrum is calculated from the interferogram by computing the cosine Fourier transform of  $S(\delta)$ , which accounts for the name given to this spectrometric technique: Fourier transform spectrometry.

The transmittance of any sample at wavenumber  $\tilde{\nu}$  is given by the ratio of the radiant power emerging from the rear face of the sample at that wavenumber  $I(\tilde{\nu})$  to the power of the radiation at the front face of the sample,  $I_0(\tilde{\nu})$ . The transmittance of a pure sample of thickness  $b$  (cm) at wavenumber  $\tilde{\nu}$  is given by Beer's law as:

$$T(\tilde{\nu}) = \frac{I(\tilde{\nu})}{I_0(\tilde{\nu})} = \exp[-\alpha(\tilde{\nu})b] \quad \text{Eq. (2.XVI)}$$

where  $\alpha(\tilde{\nu})$  is the linear absorption coefficient ( $\text{cm}^{-1}$ ) at  $\tilde{\nu}$ . The absorbance of the sample at  $\tilde{\nu}$ ,  $A(\tilde{\nu})$ , is given by:

$$A(\tilde{\nu}) = \log_{10} \frac{1}{T(\tilde{\nu})} = \frac{1}{\ln 10} \alpha(\tilde{\nu})b \quad \text{Eq. (2.XVII)}$$



where  $(1/\ln 10)\alpha(\tilde{\nu})$  is the absorptivity at  $\tilde{\nu}$ ,  $a(\tilde{\nu})$ . If the sample is a mixture, the absorbance of each component  $i$ , at concentration,  $c_i$ , is given by Beer's law as:

$$\log_{10} \frac{1}{T(\tilde{\nu})} = A_i(\tilde{\nu}) = a_i(\tilde{\nu})bc_i \quad \text{Eq. (2.XVIII)}$$

and the total absorbance is given by:

$$A(\tilde{\nu}) = \sum_{i=1}^N [a_i(\tilde{\nu})bc_i] \quad \text{Eq. (2.XIX)}$$

The absorbance, and not the transmittance, of any component is proportional to its concentration in the sample<sup>90</sup>, however it is rarely measured directly. To measure the absorbance spectrum of a sample, the ratio of the single-beam spectra of the sample and background is first calculated to yield the transmittance spectrum, which is then converted to absorbance with equation.

The other components of the FTIR spectrometer include the source, the detector and the optics part.

The ideal source of continuous mid-infrared radiation is a high-temperature blackbody. The most common mid-infrared source used in FT-IR spectrometers is a resistively heated silicon carbide rod, commercially known as a Globar; several early FT-IR spectrometers were equipped with simple resistively heated wire coils, such as nichrome or Kanthal. The production of NIR requires reaching higher temperatures. The usual source that is used for FIR spectrometry is a high-pressure mercury lamp<sup>90</sup>. A good source must be stable and provide constant power over time, it must provide a frequency range that covers everything of interest and all of them must be supplied with the same sufficiently high power.

Infrared detectors can be divided into two types<sup>90</sup>: thermal detectors and quantum detectors. Thermal detectors operate by sensing the change in temperature of an absorbing material and their output may be in the form of an electromotive force (e.g., thermocouples), a change in the resistance of a conductor (e.g., bolometers) or semiconductor (e.g., thermistor bolometers), or the movement of a diaphragm caused by the expansion of a gas. The main problem is the response time of several milliseconds, which is too long for the high frequencies generated by today's FT-IR spectrometers. The alternative method of detecting infrared radiation depends on the interaction of radiation with the electrons in a solid, causing the electrons to be excited to a higher energy state, as in quantum detectors. The sensitivity of quantum detectors usually increases with wavelength (up to the cut-off), as the number of photons for a given amount of energy increases. Semiconductor detectors are often used in the mid- and near-infrared in particular mercury cadmium telluride detectors are by far the most commonly used in MIR.

As for the optics, in laboratory FT-IR spectrometers the radiation emitted by the source is collected and collimated, passed through the interferometer, brought to a focus in the sample compartment and refocused onto the detector. The beam from the source is usually collimated with an off-axis segment of a paraboloidal mirror before it is passed through the interferometer. It is rare that the central ray of the collimated beam coincides with the axis of the paraboloid; thus, the segments of the paraboloidal mirrors used in FT-IR spectrometers are usually referred to as off-axis paraboloids. The other optics that may be found in FT-IR spectrometers include plane, ellipsoidal, toroidal, and aspherical mirrors. The primary purpose of plane mirrors in FT-IR spectrometers is simply to ensure that the optical bench is as compact as possible. A cone of light emanating from one focus of an ellipsoid is reflected

to the other focus. Thus, it is always possible to replace the two paraboloids taking the beam from the sample compartment to the detector by a single off-axis segment of an ellipsoid (again, this is usually known as an off-axis ellipsoid).

The preparation of the sample is different depending on the physical state in which it is found. As for liquids, a small drop of the compound must be placed on one KBr plates and a second plates is placed on top by rotating it by a quarter to obtain a thin film. If you want to analyse a solid in solution it must be dissolved in a suitable solvent with few covalent bonds since they absorb the IR, anhydrous and transparent to radiation in the region of interest; the water cannot be used otherwise it would dissolve the KBr pads and the broad water band might also mask important bands of your compound. The drop of the solution is then placed between two discs of KBr or NaCl as occurs for liquids. For gas analysis, they must be placed in a suitable cell in which the vacuum has been previously made. To analyse a solid sample, it must be dispersed in a KBr pads: 1 mg of the sample and 100 mg of KBr are introduced into a mortar and pounded until a homogeneous and impalpable mixture is obtained, which is transferred to a tablet machine.

FTIR is a versatile technique that allows us to identify the functional groups present, evaluate the purity of a sample (comparison with a known compound), determine its structure with the help of other analysis, recognize a compound by comparing the spectra in the banks data and determine the strength of the bond.

The preparation of the samples and the use of the instrument used for the analysis of this thesis are described in the third chapter.

## 2.4 – Density measurement, Helium Pycnometer<sup>31,92,93</sup>

The pycnometer (from the Greek πυκνός (puknos), "dense") is an instrument used to determine the density of a material. There are several different types of density<sup>92</sup> (**Table 2.1**), in particular the most used are the bulk, true and skeletal density and they are distinguished by the types of volume used. Bulk volume is the macroscopic volume of a sample that includes solid material volume and all pore spaces, true volume, on the contrary, only consists of the actual volume of the molecules or atoms that make up the material and excludes all pores (accessible and inaccessible); the skeletal volume excludes all spaces that are accessible to the outside but includes the volume of all closed pores that are physically inaccessible. From the definitions of these three volumes follow as many definitions of density: the bulk density is defined as the mass of the solid divided by the volume it occupies that includes the pores (ASTM D5004); true density is the mass of a particle divided by its volume, excluding open pores and closed pores (BSI, *British Standards Institute*); skeletal density is the ratio of the mass of solid material to the sum of the volumes of the solid material and closed (or blind) pores within the material (ASTM D3766). There are numerous methods for manually determining volume and density<sup>92</sup>: pycnometry (Specific Gravity Bottles); hydrostatic weighing (Displacement Method), in which the volume of a solid sample is determined by comparing the weight of the sample in air to the weight of the sample immersed in a liquid of known density or, when determining volume by directly measuring the displaced volume, also fine particles or gases can be used as the displacement medium; hydrometers which is a vertical float that measures the density or specific

gravity of a liquid or liquid/solid suspension (slurry); float-sink or Suspension (Buoyancy) Method which requires a liquid of known and adjustable density in which the sample is placed: the density of the liquid is adjusted until the sample either begins to sink or float, or is suspended at neutral density in the liquid; and so on.

The displacement method is the underlying principle used in all automated volume determining methods among which the gas pycnometer, used in this thesis for the determination of the skeletal density and the true density of the printed scaffolds.

A gas pycnometer typically consists of a sample chamber and a reference chamber of known, calibrated volumes,  $V_{SH}$  and  $V_r$ , respectively. Very careful calibration of these volumes must be performed to ensure accurate measurements. **Fig. 2.6** shows an example of a possible configuration. The sample of unknown volume is weighed and placed into the sample holder, filling the available space approximately three-quarters full, which is then quickly loaded (within a few seconds) into the sample chamber to avoid the uptake of moisture and other atmospheric contaminants. After sealing, the pressure within the sample chamber is measured  $P_{SH}$  and also the pressure in the isolated reference chamber is measured,  $P_r > P_{SH}$ . A valve isolating the two chambers is opened and the pressure  $P_{sys}$  of the system is allowed to equilibrate. The gas law,  $PV = nRT$  is applied to determine the volume of the unknown (supposing  $T$  and  $n$  constant). The larger the volume of the unknown, the higher will be the final system pressure. Mathematically, in the initial conditions we have:

$$P_{SH}(V_{SH} - V_S) + P_r V_r = nRT \quad \text{Eq. (2.XX)}$$

And after the valve has been opened, we have:

$$P_{sys}(V_{SH} + V_r - V_S) = nRT \quad \text{Eq. (2.XXI)}$$

The resolution leads to obtaining the unknown volume  $V_S$ :

$$V_S = \frac{P_{sys}V_{SH} + P_{sys}V_r - P_{SH}V_{SH} - P_r V_r}{P_{sys} - P_{SH}} \quad \text{Eq. (2.XXII)}$$

The gas pycnometer is the most used method for calculating the skeletal density, which can be calculated through the equation:

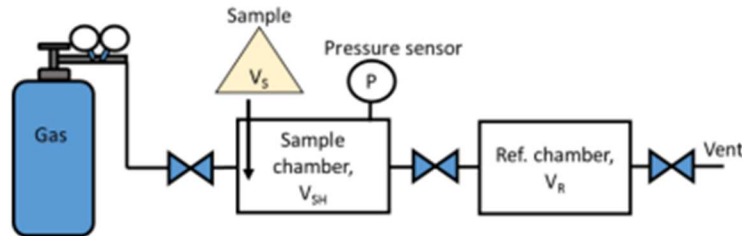
$$\rho_S = \frac{m_S}{V_S} \quad \text{Eq. (2.XXIII)}$$

With the use of a gas probe with a small kinetic diameter, such as helium, at 0.26 nm, nearly all the accessible pore spaces and surface roughness of the sample could be accessed to give the best approximation of the skeletal volume of the sample. The accuracy and precision of the gas pycnometer in the determination of skeletal volume and density can be quite high but relies greatly on the sample material and on the analysis gas being free of moisture. The gas pycnometer is used in a wide variety of applications and found in several configurations: manual and automated, single sample chamber and multi-chambered, and fixed chamber volume and multiple volume designs.

True density can also be measured through this instrument by pulverizing the solid scaffold into a very fine powder to be inserted into the sample chamber. Bulk density of scaffolds can be measured using a digital scale and caliper.

If the bulk density ( $\rho_b$ ) and the skeletal density ( $\rho_s$ ) are calculated, it is possible to calculate the percentage of porosity (%P) of the structures using the following equation:

$$\%P = 1 - \left(\frac{\rho_b}{\rho_s}\right) \quad \text{Eq. (2.XXIV)}$$



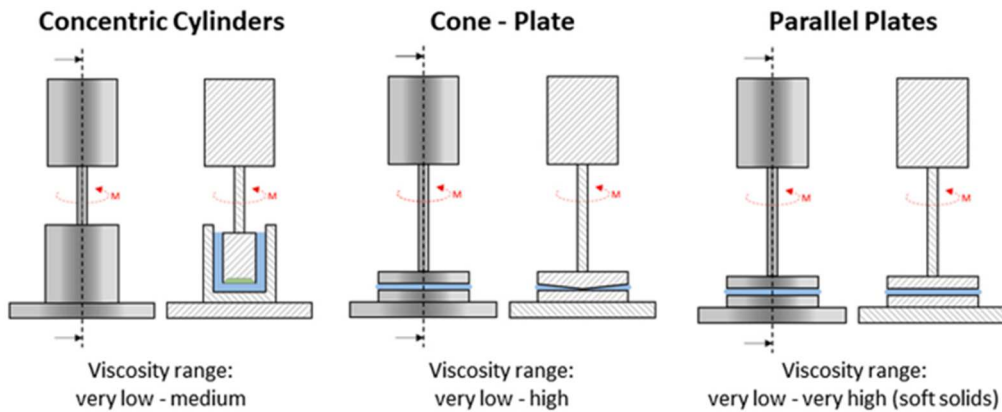
**Figure 2.6.** Example of a helium pycnometer with the sample chamber before the reference chamber. A pressure sensor is located at the sample chamber and gives pressure reading of  $P$ .  $V_{SH}$  is the volume of the sample chamber.  $V_R$  is the volume of the reference chamber and  $V_S$  is the skeletal volume of the sample.

Density Definitions	Volumes Included in Definition				
	Solid Material Volume	Open Pore Volume	Closed Pore Volume	Inter-particle Void Vol.	"External Void" volume
<b>Absolute powder density:</b> The mass of powder per unit of absolute volume (BSI).	X				
<b>Apparent particle density:</b> The mass of a particle divided by its apparent (particle) volume (BSI).	X		X		
<b>Apparent powder density:</b> The mass of a powder divided by its apparent volume (BSI).	X	X	X	X	
<b>Bulk density:</b> (also called Bulk powder density): The apparent powder density under defined conditions (BSI).					
The mass of the particles divided by the volume they occupy that includes the space between the particles (ASTM D5004).	X	X	X	X	
The ratio of the mass of a collection of discrete pieces of solid material to the sum of the volumes of: the solids in each piece, the voids within the pieces, and the voids among the pieces of the particular collection (ASTM D3766).	X	X	X	X	
<b>Effective particle density:</b> The mass of a particle divided by its volume including open pores and closed pores (BSI).	X	X	X		
<b>Envelope density:</b> The ratio of the mass of a particle to the sum of the volumes of: the solid in each piece and the voids within each piece, that is, within close-fitting imaginary envelopes completely surrounding each piece (ASTM D3766).	X	X	X	X	X
The ratio of the mass of a particle to the envelope volume of the particle (implied by BSI).	X	X	X		X
<b>Skeletal density:</b> The ratio of the mass of discrete pieces of solid material to the sum of the volumes of: the solid material in the pieces and closed (or blind) pores within the pieces (ASTM D3766).	X		X		
<b>Tap density</b> (also called Tap powder density): The apparent powder density obtained under stated conditions of tapping (BSI).	X	X	X	X	
<b>Theoretical density:</b> The ratio of the mass of a collection of discrete pieces of solid material to the sum of the volumes of said pieces, the solid material having an ideal regular arrangement at the atomic level (ASTM).	X				
<b>True density</b> (also called True particle density): The mass of a particle divided by its volume, excluding open pores and closed pores (BSI).	X				

**Table 2.1.** Definitions of various types of densities that follow from the volume definitions. BSI = British Standards Institute, ASTM = American Society for Testing and Materials. Voids that connect to the surface are referred to as open pores; interior voids inaccessible from the surface are called closed or blind pores. 'External void volume' will refer to the void volume between solid surface and that of a closely fitting envelope surrounding the object. It does not include pores that penetrate the interior of the particle. The interparticle spaces is relative to solid material in granular or powdered form.

## 2.5 – Rheometer

A rheometer is a device used to measure the way in which a fluid flows in response to applied forces. There are two distinctively different types of rheometers: rheometers that control the applied shear stress or shear strain are called rotational or shear rheometers, whereas rheometers that apply extensional stress or strain are extensional rheometers. Rotational or shear rheometers are precise instruments able to apply a wide range of shear stresses, shear strains and shear rates to a sample, using specific geometrical configurations and controlling the environmental conditions. The most common configurations are concentric cylinders, cone-plate and parallel plates, where the upper part moves and the lower part is static (**Fig. 2.7**). Specimens can be tested in rotational or oscillatory mode, the latter also known as dynamic testing. In the first one, the upper part rotates in the same direction all the time, whereas in the second one it oscillates sinusoidally with a specific amplitude and frequency. The parallel plate geometry is the most adequate for highly viscous materials, such as the ceramic pastes used for DIW. The gap between plates is variable, although it is recommended to be at least 10 times the size of the biggest particles within the sample<sup>23</sup>.



**Figure 2.7.** Rotational rheometer. Schemes of the commercial geometrical configurations.

The parallel plate configuration is used very often for polymer melts, blends and composites and the shear rate felt by each element of fluid varies in the radial position.

$$\dot{\gamma} = \frac{r\omega}{\delta} \quad \text{Eq. (2.XXV)}$$

$$\tau_R = \frac{3M}{2\pi R^3} \left(1 + \frac{1}{3} \frac{d \ln M}{d \ln \dot{\gamma}}\right) \quad \text{Eq. (2.XXVI)}$$

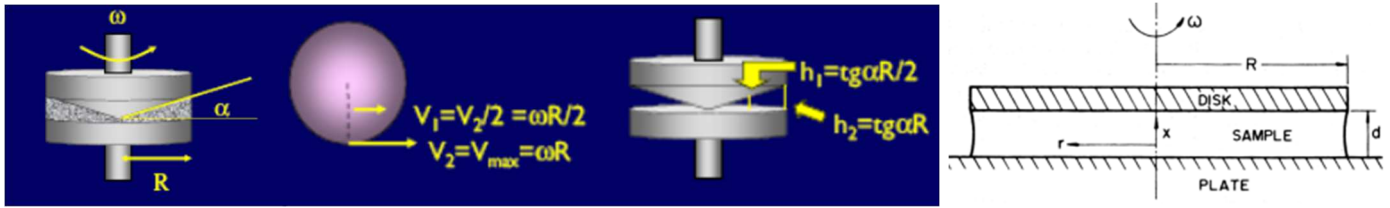
For the cone and plate configuration, the liquid is placed on horizontal plate and a shallow cone placed into it; the angle between the surface of the cone and the plate is around 1-2 degrees but can vary depending on the types of tests being run. This geometry allows to generate a constant shear rate.

$$\dot{\gamma} = \frac{V_1}{h_1} = \frac{V_2}{h_2} = \frac{\omega}{tg\alpha} \sim \frac{\omega}{\alpha} \quad \text{Eq. (2.XXVII)}$$

$$\tau_R = \frac{3M}{2\pi R^3} \quad \text{Eq. (2.XXVIII)}$$

$$\eta = \frac{3M\alpha}{2\pi\omega R^3} \quad \text{Eq. (2.XXIX)}$$

The parameters of the equations are shown in **Fig. 2.8**. As regards the discussion on the rheological behaviour of fluids, see Chapter 4.



**Figure 2.8.** The first two images from the left represent a cone-plate configuration while the rightmost image represents a parallel plate geometry.

## 2.6 – Microscopy (from the lectures of the "Characterization of materials" course)

The optical microscope (OM) is the simplest. By means of lenses it magnifies the image of the sample illuminated with light in the spectral range of the visible. The surface to be observed is placed on a table orientable, in the center of which there is a hole for the passage of light. The light coming from a source, suitably collimated by diaphragms and condensers, is directed through a mirror to the surface of the specimen after passing through the objective. The reflected light is concentrated again in the lens; the light signal is deflected from the prism towards the ocular lens which allows an enlarged view of the sample. Finally, the signal can be deflected by a mirror and sent to a photographic screen or a camera. The total magnification is given by the product of the magnification of the objective for that of the intermediate optics for that of the ocular.

Electron microscopy, on the other hand, allows the observation of samples with magnification and resolution 1000 times higher than ordinary optical microscopy and is based on the interaction between matter and electron beam.

The Scanning Electron Microscope (SEM) exploits the generation of a high-energy electron beam in vacuum. The beam is focused by a lens system and deflected to scan an area of the sample. The beam-sample interaction generates various signals that are acquired by appropriate detectors and then processed to form a 3D grey-level image. An electron beam with kinetic energies between 1 and 30 keV and said primary electrons, is generated by an electron gun (cathode) located on the top of the column. The beam is attracted to the anode, condensed by collimating lenses and focused through objective lenses on the sample massive, that is of sufficient thickness not to be completely crossed by the incident electrons. The electron beam hits the sample, producing X-rays, Auger electrons, absorbed electrons, secondary electrons, backscattered. The set of possible electron paths in the medium defines the interaction volume which, with the same energy, is inversely proportional to Z and defines the spatial resolution. These electrons are collected by a detector for secondary electrons and one for backscattered electrons, converted into electrical signals and amplified. These are converted into pixels and processed by a computer system. X-rays are collected by a Si(Li) detector. It reveals information on the morphology of the sample through the analysis of secondary and backscattered electrons and its composition through the analysis of the X-rays emitted. Its structure is represented in **Fig. 2.9**. The illumination source is an electron gun between 5 and 30 kV in very

high vacuum, so that the average free path of the electrons is greater than the source-sample distance and there is no bombardment by molecular ions; the sources can be thermionic (Tungsten filament cathode, Lanthanum hexaboride cathode (LaB<sub>6</sub>)) following Richardson's law (Eq. (2.VI)), or field emission (tungsten monoblock).

The parameters that characterize the sources are the diameter of the cross-over  $d_0$ , the energy distribution of the extracted electrons  $\Delta E$  and the brightness  $\beta$  equal to the current density emitted per solid angle ( $A\ cm^2\ sr^{-1}$ ):

$$\beta = 4i_b/(\pi d_0 \alpha_0)^2 \quad \text{Eq. (2.XXX)}$$

Generally, the sources are classified, with the same beam size and operating conditions, according to the brightness as it has been shown that it cannot exceed a maximum value taken as an index. Electromagnetic lenses consist of a cylindrical core of soft iron containing a winding of iron coils. When current is passed, a magnetic field is generated, concentrated in a small point from the air gap, and acts on the electron by deflecting its motion and making it helical thanks to the Lorentz force. Each lens is characterized by the parameter  $\alpha$  angular aperture equal to  $r/f$  where  $f$  is the distance between the center of the lens and the focus called focal distance and  $r$  is the effective radius of the lens determined by the diaphragm associated with the lens. The optical system of an SEM can be schematized as consisting of three lenses: two condensers and one objective, between them there is a diaphragm that controls the final aperture. All three lenses result in a reduction in the size of the beam relative to the source. Electronic lenses generate various types of aberrations including spherical, chromatic and astigmatism. To compensate for these irregularities, the instrument is equipped with a compensation coil system that allows to minimize the aberrations and the asymmetry of the field produced by the lens coils. They allow you to scan the beam along an area of the sample. A pair of coils deflects the beam along the x axis, a second pair along the y axis. Another important component are the signal detectors. The secondary electron detector is on the side of the sample, eccentric with respect to the electro-optical axis to give three-dimensionality; the backscattered electron detector is perforated and coaxial to the electro-optical axis and placed above the observation region (here the number of backscattered is maximum); the X-ray detector is placed to the side and is inclined to have a large collection angle.

The importance of determining the final size of the electron beam lies in the fact that this parameter has a decisive influence on the resolution that the instrument can reach, since the smaller the final size of the beam, the smaller the volume from which the various signals come. The final diameter,  $d_0$ , for an ideal lens system (free of aberrations) is given by:

$$d_0 = M_t d_c \quad \text{Eq. (2.XXXI)}$$

where  $M_t$  is the product of the de-multiplications  $M$  of each lens (the two condenser lenses and the objective lens) and  $d_c$  is the size of the electronic emission source. In reality, the aberrations present in real lenses cause the final dimension to be greater than that indicated in Eq. (2.XXXI). Resolution is the minimum distance between two objects for which the two objects appear distinct. In scanning microscopy, the resolution depends on multiple factors related to the signal generation area including the intensity and width of the primary beam, the aberrations of the electronic lenses and the type of signal generated. If the spot size is small, there is greater resolution, but it also generates a reduced number of electrons so the intensity of the signal decreases as the signal-to-noise ratio decreases,

resulting in noisier images. Depth of field is defined as the spatial interval along the optical axis within which each object is in focus. The wide depth of field obtainable with SEM compared to conventional optical microscopy is due to the fact that in SEM the angular apertures of the objective are typically smaller than the angular apertures of the objective lenses in optical microscopy.

The transmission electron microscope (TEM) is similar to SEM in that they both employ an electron beam directed at the sample. This means that many components such as the electron gun, condenser lens and vacuum system are similar in both instruments. However, the methods by which these images are produced and enlarged are completely different; while the SEM is mainly used for the study of surfaces, the TEM provides information about the internal structure of the analysed sample.

	MO	SEM
Magnification range	1-1000	10-10000
Resolution		
<i>Ordinary</i>	5 $\mu\text{m}$	0.1 $\mu\text{m}$
<i>For accurate observations</i>	0.2 $\mu\text{m}$	20 nm
<i>Limit</i>	0.1 $\mu\text{m}$	1 nm
Depth of field	0.1 mm a 10x	10 mm a 10x
	1 $\mu\text{m}$ a 100x	1mm a 100x
Ambient	versatile	requires vacuum

Table 2.2. A comparison between OM and SEM microscopies is reported.

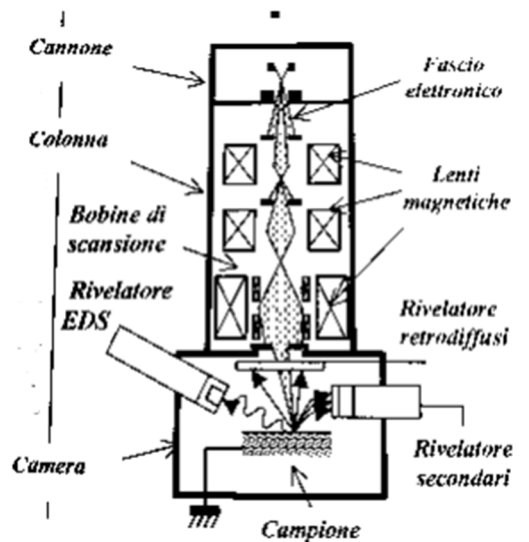


Figure 2.9. SEM structure.



## 2.7 – Mechanical characterization: compression test (*tec-science.com*)

A compression test is a mechanical test in which a material responds to forces that compress, squash, crush and flatten the specimen. It is a fundamental mechanical test, similar in nature to tensile and bend tests. This test is typically conducted by applying compressive pressure to a test specimen using platens or specialized fixtures with a testing machine that produces compressive loads. During a compression test, properties of the material including sample stress and strain are measured and data are plotted as a stress-strain diagram. Data is used to determine the compressive strength, elastic limit, yield point, yield strength and modulus of elasticity. Compression testing is often done to a break (rupture) or to a limit. When the test is performed to a break, break detection can be defined depending on the type of material being tested. This test is less significant for testing metallic materials compared to tensile test; but it is used when the material is brittle in tension, or when a material's behaviour under large and permanent strains is desired. For ductile materials such as mild steel or most Al-alloys, it is not necessary to perform the compression test because in those materials, the yield limits under tension and compression are generally the same, On the other hand, in some materials such as brittle and fibrous ones, the tensile strength is considerably different from compressive strength, so it is necessary to test them in compression. Brittle materials in tension can thus prove themselves to be quite strong in compression, due to the fact that the compression test tends to increase the cross-sectional areas of specimens, preventing necking to occur, and cracks tend to remain closed in compression; in compression, a single large flaw is not fatal (as it is in tension).

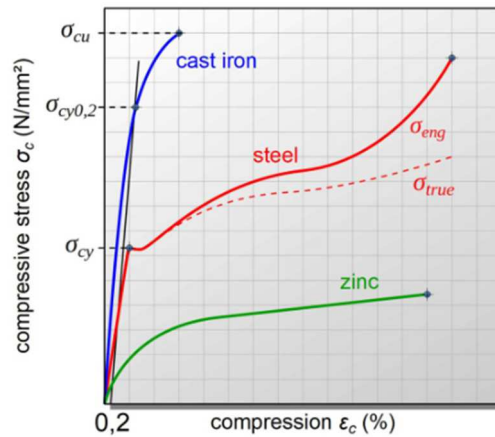
The test is conducted in a similar way to that of tension except that force is compressive and the specimen contracts along the direction of the stress. Brittle materials in compression typically have an initial linear region followed by a region in which the shortening increases at a higher rate than does the load. Thus, the compression stress-strain diagram has a shape that is similar to the shape of the tensile diagram. These materials behave elastically up to certain load, and then fail suddenly by splitting or by cracking in the way. The compression test specimen is comparatively simple in shape, and the length of the test piece should not be too great, because it is necessary to avoid buckling. The compression test specimen either a cylinder with a ratio of length to diameter  $L/D < 2$  to avoid non-axial motion, or the specimen may be in the form of a cube. The curve recorded during the test (geometry-dependent) is then converted into a geometry-independent compressive stress diagram. To determine the engineering compressive stress  $\sigma_c$ , the compressive force  $F_c$  is always referred to the initial cross-sectional area  $S_0$  analogous to the tensile stress and irrespective of the actual cross-sectional area:

$$\sigma_c = \frac{F_c}{S_0} \quad \text{Eq. (2.XXXII)}$$

The compressive stress is always determined on the basis of the initial cross-sectional area and not the actual cross-section. The specimen compression  $\varepsilon_c$  is obtained in the analogous way to the tensile strain by referring the shortening of the specimen  $\Delta h$  to the initial height  $h_0$  (usually given as a percentage):

$$\varepsilon_c = \frac{\Delta h}{h_0} \cdot 100 \quad \text{Eq. (2.XXXIII)}$$

**Fig. 2.10** shows the compression behaviour of a brittle specimen (cast iron) and a ductile specimen (steel) as well as the stress curve of a ductile specimen with low strength (zinc).



**Figure 2.10.** Stress-compression curve.

Due to bulging effects during the test, the cross-sectional area increases and the true compressive stress inside is lower than the engineering compressive stress. The true compressive stress curve therefore runs below the engineering stress curve. According to the compressive stress-strain curve, the material behaviour under pressure can be divided into different regions. If a compression test is subjected to relatively little pressure, the deformation will completely decrease after the stress has been removed. This elastic region can be seen in the diagram on the basis of the almost straight line. At high stress, however, the elastic limit is exceeded and permanent deformation is maintained even after the force is removed (plastic region). For some materials, this limit can be seen very clearly in the diagram by the discontinuous transition from a straight line to a curve. The stress limit at which a specimen is just about squeezed without plastic deformation in a compression test is also referred to as the compressive yield strength  $\sigma_{cy}$  (compressive flow limit). The compressive yield point is to be regarded as an analogy to the yield point for tensile loading. To determine the yield if the plastic transition is not clearly noted the compressive offset yield strength at 0.2% deformation is used. This 0.2% compressive offset yield strength  $\sigma_{cy0.2}$  is to be interpreted as the stress at which a compression of 0.2% remains permanently after the sample has been relieved. Due to the high frictional forces between the upper side of the specimen and the pressure plate or between the underside of the specimen and the base, the compression is not uniform over the specimen height. Rather, the specimen sticks to the contact point and does not allow any deformation there, while the middle part of the specimen can flow away to the side. Depending on the ductility of the sample, a more or less pronounced bulging occurs during the compression test. The onset of a crack in ductile materials or the sudden break in brittle specimens is characterized by the so-called (ultimate) compressive strength  $\sigma_{cu}$ . This strength parameter is to be considered in analogy to the ultimate tensile strength for tensile loading. In addition, the compression test can be used to determine the permanent compression after fracture, the so-called fracture compression or also called compression at break  $A_c$ . In summary, in **Table 2.3** is given a comparison of the characteristic values of the tensile test and the compression test.

<b>Parameter</b>	<b>Tensile test</b>	<b>Compression test</b>
Nominal stress	Tensile stress $\sigma$	Compressive stress $\sigma_c$
Relative change in length	Strain $\epsilon$	Compression $\epsilon_c$
Flow limit	Yield strength $\sigma_y$	Compressive yield strength $\sigma_{cy}$
Alternative limits	0,2% offset yield strength $\sigma_{y0,2}$	0,2% compressive offset yield strength $\sigma_{cy0,2}$
Failure parameter	Tensile strength $\sigma_u$	Compressive strength $\sigma_{cu}$
Relative permanent change in Length	Fracture strain A (elongation at break)	Fracture compression $A_c$ (compression at break)
Relative permanent cross-Sectional change	Reduction in area Z	Increase in area $\Psi$

**Table 2.3.** Comparison of the characteristic values of the tensile test and the compression test.

## Chapter 3

### Materials and methods

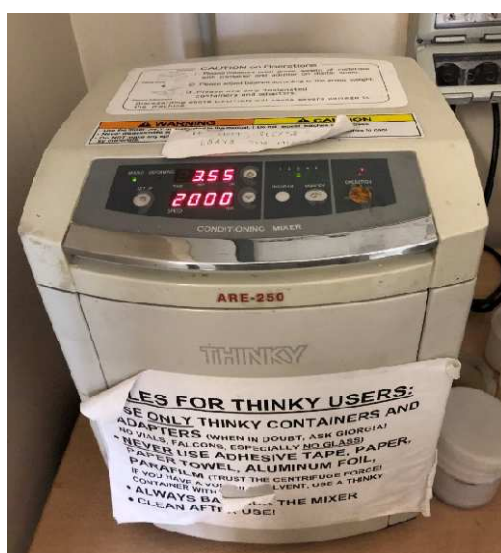
#### *3.1 – Preparation of the ink*

The first objective of this study was to find a formulation of an ink based on preceramic polymers that possessed the suitable properties, in particular at the rheological and curing level point of view, to be used in the UV Assisted DIW technique for printing suspended and self-supporting structures, capable of withstanding the pyrolysis heat treatment necessary for ceramization without destruction and excessive deformation of the structures themselves. The approach<sup>11</sup> used was that of blending two preceramic polymers: the primary polymer is a photo-sensitive polymer which contains the acrylic groups necessary to form a polymerized network upon UV light illumination, while the secondary preceramic polymer, non-photosensitive, possesses a high ceramic yield to avoid a high shrinkage during pyrolysis and excessive deformation of the samples and, since it does not require specific functional groups, it leaves a high freedom of choice.

Various solutions and compositions have been tested both as regards the choice of the polymer with a high ceramic content and as regards the choice of the photo-sensitive one. In **Tables 3.2** the various compositions tested are reported and in **Table 3.1** a list of the various chemicals used. At the end of the optimization process, the three inks underlined in the tables were selected. In §4.1.1 the selection process of these three inks will be analysed and the reasons that led to discard the other solutions tested.

The production of all the inks was carried out with the same procedure, changing only from time to time the composition and quantity of the components. The mixing of the components took place inside a plastic cup whose tare weight was measured and marked in order to subsequently evaluate the complete evaporation of the solvent. A precision analytical balance to the fifth decimal place was used for the weighing of the various materials. First, the preceramic polymer with a high ceramic content was introduced inside the cup. Being in the form of powder, it is advisable to mix it briefly with a spatula, to remove any lumps or packings that are difficult to remove with the mixing process. To it is added the solvent, in this work isopropanol, necessary for the formation of a homogenous, stable blend without macroscopic phase separation, even over time. The solvent is necessary only during the preparation phase and before transferring the finished ink to the syringe for printing, it is necessary to check that it is completely evaporated, checking that the mass of the cup containing the ink is equal to the tare weight plus the sum of the masses of the components except isopropanol. If the measurement should result in isopropanol residues, it is good to do some mixing steps in order to make it evaporate completely or leave the container still under the extractor hood. The mixture was first briefly mixed manually to mix the powder and solvent well and then stirred in a conditioning mixer (*ARE-250, THINKY*, in **Fig. 3.1**) for 5 minutes at 2000 rpm. Before starting the mixing program, the counterweight is adjusted using a crank handle, it must be similar to that of the cups and the container is positioned inside a holder of the most suitable shape. If after this step there were still

present lumps and the powder wasn't uniformly dissolved, the mixture was stirred for another 2-3 minutes under the same conditions to have a mixture free from agglomerates. During this first mixing step, the cup was covered with parafilm on which a small hole was made, to avoid excessive evaporation of the solvent which would compromise the addition of the other constituents. Then the photopolymer was added and also the photoinitiator necessary to supply the radical starting groups in order to activate a polymerization process. This work is based on the use of the photoinitiator Irgacure®819 and no catalysts were added for promoting the crosslinking of the preceramic polymers in any ink composition. After the introduction of the last component, the mixture undergone another step of stirring (3 minutes at 2000 rpm) always covered with the parafilm. The last operation consists in another mixing (6 minutes at 2000 rpm) but this time without covering with parafilm for the evaporation of the solvent and in a subsequent degassing step (2 minutes at 2000 rpm) to remove the bubbles present inside the mixture which cause problems during printing and subsequent heating treatment. If the mixer overheats excessively, it is advisable to wait for it to cool before proceeding to a new mixing phase to avoid damage to the machinery and facilitate cooling by inserting the cooling piece to keep in the fridge. It is better not to completely evaporate the solvent inside the mixer, but to finish the evaporation by placing the cups under the extractor hood; it is therefore advisable to prepare the inks the day before printing and leave them overnight under the hood. To prevent light illumination from the surrounding environment the inks inside the cups have to be wrap in aluminium foils, otherwise the curing process may begin, rendering the mixture unusable. For printing, the inks were transferred into a special syringe capable of blocking UV rays and protecting the ink inside from premature polymerization and, after inserting the piston and the closure cap, a defoaming step at 2000 rpm for 2 min was performed to release the air entrapped during the loading procedure. It is a good idea to wait a few minutes before printing, as the degassing step may have slightly heated the syringe and the material inside it, leading to a falsification of the rheological properties of the ink; in particular, the ink may be more liquid and with a lower viscosity due to the increase in temperature compared to ambient temperature conditions.



*Figure 3.1. Conditioning mixer (ARE-250, THINKY).*

### 3.1.1 – Chemicals

#### 3.1.1.1 – Photoinitiator

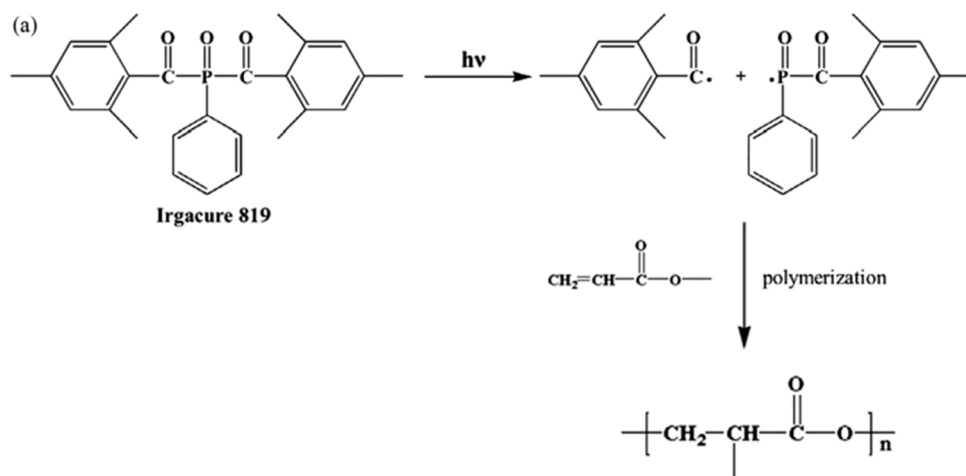
In this study, Irgacure®819 was used as a photoinitiator. Irgacure 819 (phenylbis(2,4,6-trimethylbenzoyl)phosphine oxide<sup>94</sup>) is a versatile photoinitiator for radical polymerization of unsaturated resins upon UV light exposure, which comes in the form of an impalpable yellow powder. In **Fig. 3.2** the photodissociation process and the resulting free radicals from Irgacure 819 are illustrated. The performance of a photoinitiator is closely related to its absorption ability at the wavelengths emitted by the light source and in particular in the case of free radical photopolymerization it is the dominant factor affecting the performance, compared to the quantum efficiency of the photoinitiator cleavage into initiating radicals, which turns out to be less significant<sup>94</sup>. A study of the performance of selected photoinitiators<sup>94</sup> compared different radical photoinitiators by studying the UV spectra through an EPP2000C spectrometer and calculating the extinction coefficients ( $\epsilon$ ) at the wavelengths di 320 nm e 365 nm. Large values of  $\epsilon$  indicate a high probability of absorption at a given wavelength, improving the polymerization kinetics and overall conversion and they were calculated from the absorbance values, using the Beer-Lambert law<sup>95</sup>:

$$Abs_{\lambda} = \epsilon_{L/(mol\ cm)} [c_{mol/(L)}] L_{cm} \quad \text{Eq. (3.I)}$$

where Abs is the absorbance at each wavelength,  $\epsilon$  is the molar extinction coefficient, [c] is the concentration of the photoinitiator in the solution and L is the optical path length.

The comparison values are reported in **Table 3.3**. From the values of the extinction coefficient, it can be seen that Irgacure 819 has one of the highest extinction coefficients at 320 nm and the highest at 365 nm, thus resulting in the best photoinitiator at 365 nm, i.e., at longer wavelengths. Another study calculated the extinction coefficients of a series of PIs, including Irgacure 819 in the range 360-550 nm. The spectrum of Irgacure 819 shows a  $\lambda_{max}$  at 370 nm which is associated with an  $\epsilon_{max}$  of  $300 \pm 10$  (L/mol cm) and although its  $\epsilon_{max}$  is in the UV-A region, its absorption profiles extend into the visible range.

Since the UV system used during printing produces radiation with a wavelength around 400 nm, the choice of the PI Irgacure 819 appears appropriate in view of its good performance in this range of wavelengths. The amount of PI introduced into each ink was equal to 2% by weight of the photopolymer and to study the effect of the variation of its concentration in the polymerization process, during the optimization of the inks it was tried to vary the content from 2% to 4%. No photoabsorber was used.



**Figure 3.2.** Photoinduced cleavage of Irgacure 819.

Photoinitiator	$\lambda_{max}$ [nm]	$\epsilon_{320nm}$ [ $dm^3 mol^{-1} cm^{-1}$ ]	$\epsilon_{365nm}$ [ $dm^3 mol^{-1} cm^{-1}$ ]
<i>Free-radical photoinitiators:</i>			
Irgacure 907	305	9770	131
Irgacure 819	250	4640	767
TPO	296	1510	424
Irgacure 127	260	271	35
Irgacure 651	244	172	126
Irgacure 184	244	90	22

**Table 3.3.** Absorption characteristics of photoinitiators.

### 3.1.1.2 – Preceramic polymer with high ceramic yield

The two preceramic polymers with high ceramic yield used belong to the category of polyorganosiloxanes, which are inorganic/organic hybrid compounds comprised of Si–O–Si units as the polymeric backbone [for more details §1.5]. The general formula is  $[R_2SiO]_n$  for linear or cyclic polysiloxanes and  $[RSiO_{1.5}]_n$  for crosslinked polysilsesquioxanes. The ceramic composition and yield depend to a great extent on the functional group present in the polymer. For example, polysiloxanes containing phenyl groups show lower ceramic yields and higher free carbon contents relative to polysiloxanes where R is methyl, exclusively<sup>96</sup>. They are entrapped by the polymerized network during printing, decreasing the weight loss of the blends, due to their high ceramic yield.

The MK polymer is a solid solvent free poly(methylsilsesquioxane) polymer with  $[CH_3SiO_{1.5}]_n$  basic structure and falls under the silicone resin group. The powder has a softening range between 45 and 60°C, a good solubility in organic solvents and is insensitive to air or moisture<sup>54</sup>. The polymer possesses approximately 2 mol.% hydroxy and ethoxy groups, as functional units. A representation of its structure is in **Fig. 3.3.a,b**. With evolution of water and ethanol by polycondensation reaction, the formation of a three dimensional network with Si–O–Si alternating units as the backbone takes place<sup>54,97</sup>. The thermogravimetric analysis of this polymer shows three regions of mass losses: 200-

450°C (~ 12%) due to polycondensation resulting in the release of water, ethanol and methanol, 450-600°C (~ 3%) and 600–800°C (~8%) which correspond to the loss of hydrogen and methane, exclusively<sup>96</sup>. At 1000°C the mass loss is approximately 15%.

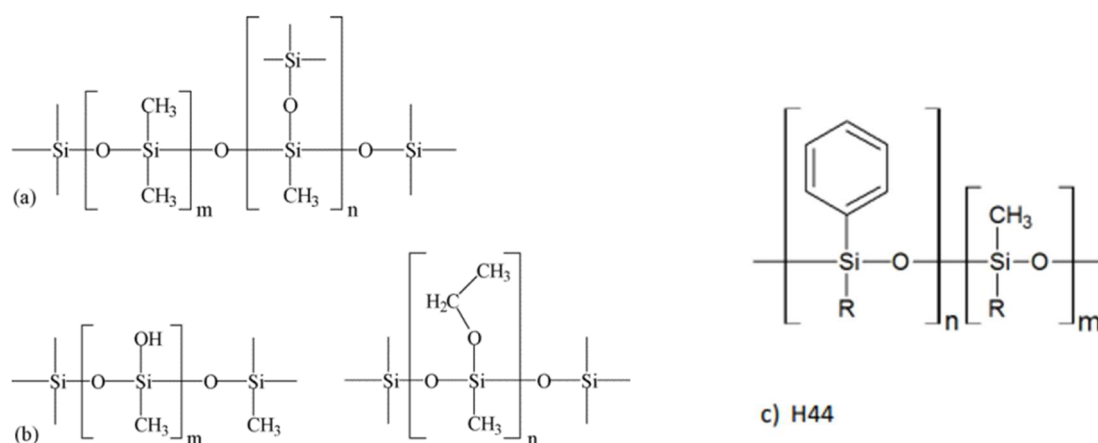
Silres®H44 is a silicone resin containing phenyl-methyl side groups (**Fig. 3.3.c**). Containing phenyl groups, it presents a loss in mass greater than MK, around 27%, from the results of the TGA and quite in agreement with the data present in the supplier's data sheet. It too has a softening point in the 45-60°C temperature range. **Table 3.4** shows some characteristics of the two polymers considered deriving from a study conducted by Takahashi *et al*<sup>98</sup>.

Type of resin	Name	M <sub>w</sub> (g/mol)	M <sub>w</sub> /M <sub>n</sub>	T <sub>g</sub> (°C)	Weight loss (air, 100°C, 2h)	Weight% relative groups (by-products are water and ethanol during crosslinking)
Methyl	MK	9400	3.6	41.9	0.7	A few
Methylphenyl	H44	2100	1.8	43.0	0.1	3

**Table 3.4.** Molecular and thermal properties of silicone resins.

The final choice was to use the preceramic polymer H44 since it is able to form a homogeneous blend with the photopolymer and the solvent, the samples after pyrolysis preserve the shape and in particular the ink with it presents an optimal viscosity for the printing unlike inks containing MK which were too viscous.

As solvent, the isopropanol [(i)-propyl alcohol CH<sub>3</sub>CHOH; formula weight 60.10; specific gravity 0.78; melting point -85.8 °C; boiling point 82.5°C [*Perry Chemical Engineer's Handbook*], vapor pressures of 42.6 hPa] was chosen since the preceramic polymers show a good solubility in it and it evaporates easily, allowing to have an ink in which it has completely disappeared. This avoids the release of gas phases during pyrolysis which can cause defects and breakages.



**Figure 3.3.** (a) Section of the molecular structure of the commercial poly(methyl-silsesquioxane) MK linear and crosslinked polymer network units; (b) structural units containing OH- and OEt- functional groups; (c) structure of H44.



### 3.1.1.3 – Photopolymer

In this study we analysed several photopolymers including TEGO RC 711, Evonik Industries, Germany. TEGO®RC Silicones are functional silicone polymers. The functional groups are firmly linked to the silicone backbone. The products are 100% polymeric materials and contain no solvents. UV curing requires the addition of a photoinitiator (PI). There are two UV curable silicone release systems on the market: the first is based on silicone acrylate and cures via a free radical mechanism, whilst the other uses epoxy silicones and cures in the presence of a cationic photo-catalyst. The free radical polymerization of the acrylate groups is much faster compared to the cationic polymerization; therefore, full cure is reached more quickly. TEGO RC 711 is acrylate-modified methylsiloxane curable via radical mechanism; its chemical nature is represented in **Fig. 3.4**. During the printing, the highly acrylated, photosensitive RC 711 provided the reactive end groups capable of forming a continuous polymer network acting as a frame which traps Silres H44<sup>11</sup>. It has a viscosity of 0.59 Pa·s and a Newtonian behavior<sup>99</sup>. The thermal behaviour of TEGO RC 711 was analysed with the TGA. It demonstrates a significant loss of mass, up to 90% at 1000°C. Between 150 and 250°C there is the silanol and methoxide loss and subsequently between 350-500°C there is the methyl and acrylic loss which represents the greatest loss<sup>99</sup>.

The mass yield of TEGO RC 711 is related with the degree of polymerization and Scherzer and Decker<sup>100</sup> showed that for acrylated polymers the bond conversion depends on the illuminator intensity and exposure time. In particular, they studied the effect of various parameters on the polymerization kinetics. An increase of the photoinitiator concentration strongly enhances both the polymerization rate and the final conversion of the acrylate groups whereas the induction period is far less influenced. The polymerization rate is proportional to the square root of the intensity of the incident UV light. With increasing functionality, the initial polymerization rate strongly increases and the obtainable final conversion decreases. This behaviour is due to the higher initial concentration of acrylate groups and the higher viscosity of the resin as the functionality increases. Both factors accelerate the reaction in the initial stage of cure, whereas the rapidly rising cross-link density and the gel effect limit the extent of final conversion. The exposure time also affects the degree of conversion. The total degree of cure decreases with increasing duration of the exposure which is equivalent to an increasing conversion. The polymerization continues for a short time after the UV light has been turned off and then the polymerization rate rapidly slows down. For a polymer with long functional branches as TEGO RC 711, an ultrafast polymerization is expected at the expense of reduced crosslinking of the polymer backbone leading to high mass loss. The final ceramic yield for this preceramic polymer is related to its degree of functionalization, the final crosslinked network and the pyrolysis temperature<sup>99</sup>.

TEGDA (tetra (ethylene glycol) diacrylate) and PETTA (pentaerythritol tetraacrylate) are photopolymer whose structure is represented in **Fig. 3.4**. The first has been tested mainly in the inks to which we have added R106 fumed silica since it has refractive index close to that of fumed silica<sup>40</sup>, allowing to reduce the scattering phenomenon which reduces the penetration depth of the radiation. The second turned out to have good properties in fact it constitutes the photopolymer of two of the optimal inks.

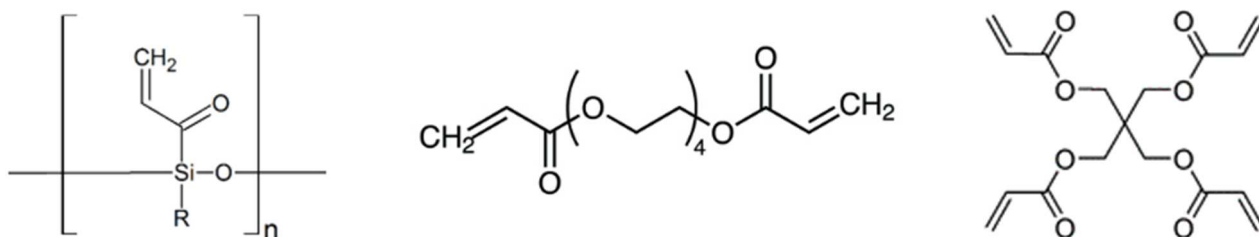


Figure 3.4. Chemical structure of TEGO RC 711 (left); TEGDA (center); PETTA (right).

<b>Photoinitiators</b>	Irgacure®819
<b>Preceramic polymers</b>	MK Silres® H44
<b>Photosensitive preceramic polymers</b>	TEGO®RC 711 TEGDA PETTA Fun to Do
<b>Ceramic powder</b>	R106
<b>Solvents</b>	Isopropanol

Table 3.1. Chemicals.

Components	A		B		C		D		E	
	m (g)	m (%)	m (g)	m (%)	m (g)	m (%)	m (g)	m (%)	m (g)	m (%)
SILRES®H44	3	66.5	3	59.8	3	54.2	6	42.5	6	42.1
TEGO®RC 711	0.5	11.1	1	19.9	1.5	27.2	6	42.5	6	42.1
Irgacure®819	0.01	0.2	0.02	0.4	0.03	0.5	0.12	0.8	0.24	1.7
Isopropanol	1	22.2	1	19.9	1	18.1	2	14.2	2	14.1
Tot.	4.51	100	5.02	100	5.53	100	14.12	100	14.24	100

Components	F		G		H		I		L	
	m (g)	m (%)	m (g)	m (%)	m (g)	m (%)	m (g)	m (%)	m (g)	m (%)
SILRES®H44	6	54.3	6	59.8	6	62.3	6	58.8	6	61.3
TEGDA	3	27.1	2	19.9	1.6	16.6	2	19.6	1,6	16.4
Irgacure®819	0.06	0.5	0.04	0.4	0.032	0.3	0.04	0.4	0.032	0.3
R106	-	-	-	-	-	-	0.16	1.6	0.15	1.5
Isopropanol	2	18.1	2	19.9	2	20.8	2	19.6	2	20.5
Tot.	11.06	100	10.04	100	9.632	100	10.2	100	9.782	100

<b>M</b>		<b>N</b>	
6	61.2	6	58.3
1.6	16.3	2	19.5
0.048	0.5	0.04	0.4
0.15	1.5	0.24	2.3
2	20.5	2	19.5
9.798	100	10.28	100

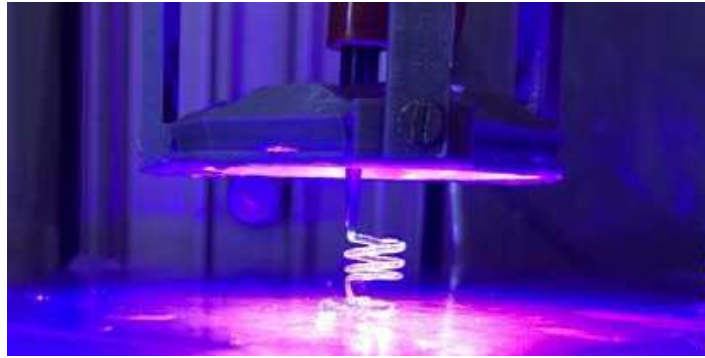
<b>Components</b>	<b>O</b>		<b>Components</b>	<b>P</b>		<b>Q</b>	
	m (g)	m (%)		m (g)	m (%)	m (g)	m (%)
MK	6	62.3	H44	6	60	6	57.1
TEGDA	1.6	16.6	Fun to Do	2	20	2.5	23.8
Irgacure®819	0.032	0.3	Isopropanol	2	20	2	19.1
Isopropanol	2	20.8	Tot.	10	100	10.5	100
Tot.	9.632	100					

<b>Components</b>	<b>R</b>		<b>S</b>		<b>T</b>		<b>U</b>	
	m (g)	m (%)	m (g)	m (%)	m (g)	m (%)	m (g)	m (%)
SILRES®H44	6	59.8	6	54.3	6	59.6	6	53.9
PETTA	2	19.9	3	27.1	2	19.8	3	27
Irgacure®819	0.04	0.4	0.06	0.5	0.08	0.8	0.12	1.1
Isopropanol	2	19.9	2	18.1	2	19.8	2	18
Tot.	10.04	100	11.06	100	10.08	100	11.12	100

**Tables 3.2.** Inks compositions.

### 3.2 – Printing process

The printing apparatus consists in a hybrid system made up of a UV set up of UV-LED chips mounted on a delta printer (*Delta 2040 Turbo 2, WASP, Italy*). The chips are positioned in a circular manner on a suitably shaped support that arranges them around the dispensing system, consisting of a syringe and a nozzle capable of protecting the ink contained from environmental radiation and from that of the UV set up itself. The dispensing system is connected to an air pressure digital dispenser (*DC 307, Vieweg GmbH, Germany*) which controls the extrusion pressure and is operated by means of the small buttons that regulate the dispensing modes (manual, time, cycle). The LEDs are oriented, their radiation is focused just below the nozzle tip, enabling fast photopolymerization in air right after the ink extrusion and, being arranged in a circular way, they allow the radiation to reach the printed piece uniformly (**Fig. 3.5**).



*Figure 3.5. LEDs orientation.*

The printer consists in an aluminium, plexiglass and polycarbonate chamber in which nylon wheels that slide on anodized steel profiles, allow the movement of a three-dimensional moving platform, in which the x and y dimensions belong to the horizontal plane while the z direction belongs to the vertical plane. The syringe fixing system is screwed onto the plate and the syringe, equipped with a nozzle connected to the pressure dispenser, is inserted into it and also the support for the UV setup is placed. The syringe was fitted with UV-blocking tapered nozzle with an internal diameter of 0.58 mm. Tapered nozzles typically have larger diameters at the entrance, and a smaller diameter at the tip, a feature which provides a more favourable pressure gradient than cylindrical ones, dictated by the cone-half angle and tip diameter<sup>101</sup>. During the various printing tests, 0.41 and 0.84 mm nozzles were also used; the smaller the nozzle, the more pronounced are the problems related to clogging. A plastic film was placed on the printing surface as a substrate and was made to adhere perfectly with acetone. In this way the pieces once printed can be easily removed by lifting the film and folding it, without the risk of breakage or damage due to the fragility of the samples or with the risk of crushing and deforming self-supporting structures. It is important that the film is completely adhered to the printing surface and that there are no bubbles between the two, otherwise during printing it is possible that it is lifted and drawn by the ink, compromising the shape fidelity of the pieces. As a first print operation you need to set the distance between the nozzle tip of the extruder and the substrate, which greatly influences the cross-sectional geometry of the extrudate. Using the "modify Z MAX" command, the syringe returns to the initial position  $(x; y; z) = (0; 0; 0)$  and you can set the height between the nozzle tip and the printing plane; the same can be adjusted manually even during printing by simply raising or lowering the syringe in its housing. The adjustment of the distance presupposes the knowledge of the Gcode file, since it can already be contained within it, so in this case the nozzle must be practically in contact with the substrate, without however bumping or crawling on the plane, because this leads to the deformation of the tip and therefore of the dimensions of the outgoing filament. Usually, the distance is about the same size as the nozzle diameter. Once the height has been set, whatever the variation of the axes, the print will start from the pre-set position. The Gcode file to be printed is then selected from the machine's SD card. §3.2.2 will give a brief description of the files used by the machine. During printing, two important parameters to adjust are the printing speed and the pressure of the pump which is used as a driving force to extrude the ink. The pressure is adjusted through a knob in the digital dispenser. When setting the pressure, it is a good idea to start from zero every time and set the pressure at the beginning of printing without making more changes, since it is difficult to evaluate the actual value. Therefore, once a pressure has been set, what is going to vary is the printing speed. The speed of the machine is expressed in relative terms as a percentage of that set

in the Gcode file. In a Gcode file, the speed can be kept constant throughout the printing, or it can be changed in each printed filament. §3.2.1.2 describes the effect of these two printing parameters and that of other variables. To ensure print fidelity, it is necessary that the printing speed and pressure are matched to obtain a constant and uniform filament with the dimensions as close as possible to that of the nozzle. In fact, part of this thesis focused on finding the correlation printing speed-pressure for the three inks selected as the best. For the study of this correlation, we printed suspended spiral structures with a radius of 4 mm and a pitch of 2.5 mm. For the evaluation of other properties, different structures were printed, such as scaffolds, which will be reported during the description of the results.

One of the main problems encountered during printing is the presence of air bubbles. The presence of air bubbles inside the ink in the syringe leads to the formation of discontinuities within the thread. If the bubbles are small and inside the filament, they do not cause big deformation but porosity in the pyrolyzed samples; if instead the small bubbles reach the surface they cause a reduction in the diameter of the thread and a distortion, i.e., the filament is not deposited in the correct point. If the bubbles are larger, the filament may break, leading to partial structures or clogging of the nozzle. In particular, for the suspended spiral structures, the presence of bubbles was extremely harmful as it effectively interrupted the printing process. The presence of bubbles increased as the ink ran out, in fact a sign that the ink was running out was the presence of many bubbles. To reduce their number as much as possible, the degassing phase is important. Another problem was the tendency of the inks to curl at the exit of the nozzle instead of appearing as a uniform filament. This phenomenon appeared the more the more the nozzle was used: probably occlusions due to cured material inside modified the exit section of the nozzle and the ink filament was unable to exit in a linear manner but had to modify the trajectory to overcome the obstacles. To avoid this phenomenon, it is important to clean the nozzle after each print, extracting any cones of cured material and properly clean the edges with acetone in order to make them less sticky and prevent the filament from sticking to them. In extreme cases in which it is not possible to stem the problem, it is good to change nozzle and recover those used, by cleaning and blowing with compressed air to eliminate all impurities. During the printing process it is advisable to turn on the UV light only after the filament has stabilized in order to avoid breakage of the same or clogging of the nozzle. Another problem encountered related to all extrusion processes is die swelling. This phenomenon, also known as the Barus effect, is a common effect in the processing of polymers. During the entry into the nozzle the material is compressed and after the exit of the die there is a partial recovery or "swell" back to the former shape. Die swell is a phenomenon directly related to entropy and the relaxation of the polymer within the flow stream and their viscoelastic nature. Before entering the die the polymer has a constant flow and has a roughly spherical conformation, maximizing entropy. Extrusion through the die causes an increase in flow rate and the polymers lose the spherical shape, assuming an elongated conformation with the macromolecules aligned with the flow direction. Physical entanglements may relax, if the time scale of the polymer within the die is long enough. At the exit of the die, the remaining physical entanglements cause the polymers to regain a portion of its former shape and spherical volume, to return to the roughly spherical conformation that maximizes entropy. The disentanglement of polymer chains is a kinetic process, and so, the longer the die is, the more time is given for the physical entanglements within the polymer to disentangle. With a longer die and a slower polymer flow stream, less pronounced die swell will be observed. The die swell ratio percentage can be calculated using Eq. (3.II):

$$\text{Percent die swell} = \frac{D_{\text{extrudate}} - D_{\text{die}}}{D_{\text{die}}} \cdot 100 \quad \text{Eq. (3.II)}$$

This phenomenon causes an increase in the diameter of the extruded filament which can compromise the shape fidelity of the printed pieces. With the optimization of printing parameters such as speed and pressure, it is possible to bring the effective diameter of the filament as close as possible to that of the die so that the die swelling does not compromise the shape. It is a complex and difficult phenomenon to quantify, since it depends on the rheological characteristics of the ink and on the operating parameters and overlaps with other phenomena present during printing, such as for example the tension imposed on the wire for the movement of the printer which tends to cause elongation in the print direction and a narrowing of the section which would act in the opposite way to swelling.

### 3.2.1 – Printing parameters

#### 3.2.1.1 – Effect of standoff distance

The distance between the nozzle tip (also called standoff distance) of the extruder and the substrate greatly influences the cross-sectional geometry of the extrudate. A smaller height led to a wider filament because the newly extruded filament spread out laterally, due to the extrusion between the needle and the substrate<sup>102</sup> and decreasing the standoff distance to less than ~50% of the nozzle diameter leads to increased flow resistance<sup>101</sup>. On the contrary, when the standoff distance increased ( $h > 3D$ )<sup>103</sup>, the weight of the filament was distributed along a larger area, resulting in an increase in the diameter of the filament and its instability, it is no longer continuous but is break up into discrete droplets due to the Plateau-Rayleigh instability and has poor adhesion to the substrate<sup>101</sup>. Moreover, a high standoff distance increases the travel time of the filament through air relative to drying time or the time of exposure to UV radiation if the ink is photocurable, causing the ink to solidify before touching the substrate, leading to clogging of the nozzle itself or to have poor adhesion to the substrate and poor layer to layer bonds. Wang and Shaw<sup>104</sup> identified a critical height  $h_c$  for a given set of the extrusion rate, nozzle diameter and nozzle moving speed, expressed in Eq. (3.III)

$$h_c = \frac{V_d}{v_n D_n} \quad \text{Eq.(3.III)}$$

$V_d$  is the volume of the slurry extruded per unit time ( $\text{cm}^3/\text{s}$ ),  $v_n$  the nozzle moving speed with respect to the substrate ( $\text{mm}/\text{s}$ ), and  $D_n$  the nozzle diameter ( $\text{mm}$ ). When  $h < h_c$  there will be a squeezing effect and an alteration of the contact angle between the ink filament and substrate. Conversely, if  $h > h_c$  there will be enough space for the ink to occupy, in this case the contact angle is only controlled by ink rheology and surface energy of the substrate<sup>101,104</sup>. In general, a standoff distance of about the same size as the nozzle diameter is recommended in order to achieve continuous ink filament, improve layer to layer bonds, as well as adhesion to the substrate and avoid deposition time delay.<sup>101,103</sup>

#### 3.2.1.2 – Effect of printing speed and pressure

In general, similar to Eq.(3.III), the observed pattern is that, at a constant flow rate ( $Q$ ) and standoff distance ( $h$ ), there is critical printing speed at which the filament diameter equals the nozzle diameter ( $D$ )<sup>101,104</sup>.

$$u_c = \frac{Q}{hD} \quad \text{Eq. (3.IV)}$$

If the speed is less than this value, the filament is compressed and the flow is forced; if the speed is higher, the filament tends to be stretched and if it is further increased there is unstable and discontinuous prints in the form of drops. At excessive speeds, therefore, the filament is put in tension and there is a longitudinal elongation and shrinkage of the diameter. Furthermore, if the speed is too high, the material does not have enough time to cure, giving rise to bent filaments or collapse of the structures, since the previous layers are not solidified when the following ones arrive, leading to the merging of the two layers. An advantage of having a high printing speed is the time savings. On the other hand, if the speed is too low, there is a risk of having a deformed filament and clogging phenomena occur inside the nozzle, which interrupt printing.

For the pressure, the applied pressure allows the ink to flow smoothly through the syringe and the needle. The value of the pressure to be applied depends on the rheological properties of the ink: larger applied pressure is required to extrude the ink with larger viscosity and yield stress. About the influence of pressure in the print, too high pressure causes an incorrect deposition of the thread which is no longer linear and uniform but appears irregular and meandering. It causes irregularities in the printed structures and the shape obtained differs from that contained in the Gcode file. In particular, there is an increase of the diameter of the extruded filament. To balance the excessive pressure, it would be necessary to print at really high speed that does not always allow the ink to cure completely, given the shorter time for printing and therefore the shorter time of exposure to UV light. A pressure that is too low, on the other hand, causes the nozzle to clog more easily, the ink cures inside, the filament breaks and it leads the formation of incomplete structures. These two parameters influence each other and must be coordinated to obtain better printing conditions.

Mathematical models can be applied to predict the optimal printing conditions using as input data measures from rheological characteristics of the ink<sup>23</sup>. One of the most used models to describe shear-thinning is behaviour the Ostwald-de Waele model or the power law (Eq. (3.V)), which is defined as:

$$\eta = k\dot{\gamma}^{n-1} \quad \text{Eq. (3.V)}$$

where  $\eta$  is viscosity,  $k$  is a constant called consistency index (defined as the viscosity when the shear-rate is  $1 \text{ s}^{-1}$ ),  $\dot{\gamma}$  is the shear rate, and  $n$  is the shear-thinning index, also referred to as flow index or power-law index. The extrusion velocity during printing can be calculated from the shear stress<sup>105</sup>:

$$\tau = \left(\frac{\delta v}{\delta r}\right)^n \quad \text{Eq. (3.VI)}$$

where  $n$  is the shear-thinning parameter derived from the power law,  $v$  is the extrusion velocity of the fluid, and  $r$  is the radius of the needle. Considering that the shear stress is proportional to the applied pressure and the radius of the nozzle, the velocity of extrusion can be determined using the following Eq. (3.VII)<sup>105</sup>:

$$v = \frac{n}{n+1} \left(\frac{\Delta p}{2LK}\right)^{1/n} (R^{n+1/n} - r^{n+1/n}) \quad \text{Eq. (3.VII)}$$

For example, this model has been applied as initial screening to determine the printability of bioinks based on alginate, gelatin-alginate blends<sup>106</sup> and poloxamer 407<sup>105</sup>. Another model used to describe shear-thinning behaviour and which is valid in low shear rate regions is the Herschel-Bulkley model,

Eq. (3.VIII), which relates the shear stress ( $\tau$ ) to the yield stress ( $\tau_0$ ), shear rate, and the shear-thinning parameters of the power law (k and n):

$$\tau = \tau_0 + k\dot{\gamma}^n \quad \text{Eq. (3.VIII)}$$

The Herschel-Bulkley model is quite useful, because it includes both the yield stress and shear response and even considers wall slipping within the needle.

As far as pressure is concerned, in a recent study<sup>102</sup> it was shown that the optimal pressure found for printing and the minimum extrusion pressure Eq. (3.IX), calculated by modeling the ink flow inside the nozzle with the Hagen-Poiseuille model and directly proportional to the yield stress of the ink are very close. This further demonstrates how rheological characteristics can be used to predict optimal printing parameters.

$$P_{min} = \frac{4lt_s}{d} \quad \text{Eq. (3.IX)}$$

The Hagen-Poiseuille law<sup>23</sup>, as a laminar flow of a Newtonian fluid through a cylindrical pipe, can be used to model the ink flow inside the nozzle to an initial approximation:

$$Q = \frac{\pi D^4 \Delta P}{128 \mu L} \quad \text{Eq. (3.X)}$$

Where  $\Delta P$  is the pressure difference across the nozzle length (L),  $\mu$  is dynamic ink viscosity, D is the nozzle diameter. Khalil & Sun<sup>107</sup> developed a modified form of Eq. (3.X) to account for Non-Newtonian flow behaviours, Eq. (3.XI), while Eq. (3.XII) describes the ink flow without using a cylindrical nozzle but assuming it tapered<sup>108</sup>.

$$Q = \left( \frac{n}{3n+1} \right) \pi \gamma_0^{\frac{n-1}{n}} \left( \frac{\partial P}{\partial z} \right)^{\frac{1}{n}} R^{\frac{3n+1}{n}} \quad \text{Eq. (3.XI)}$$

$$Q = \frac{\pi D_i^3 D_t^3}{32} \left[ \frac{3n \Delta P \tan \theta_c}{2\mu (D_i^{3n} - D_t^{3n})} \right] \quad \text{Eq. (3.XII)}$$

Where  $D_i$  e  $D_t$  are the diameters of the nozzle entrance and exit respectively. In summary, the ink flow rate is inversely proportional to the viscosity ( $\mu$ ), directly proportional to the applied pressure (P), inversely proportional to the pipe length (L), and directly proportional to the nozzle diameter.

### 3.2.1.3 – Substrate<sup>101</sup>

The interaction between the ink and the ambient air around it and the surface properties of the substrate play a critical role in determining the final print quality. Print resolution, geometry and adhesion to the substrate can be directly inferred from the rheological ink properties, surface properties of the substrate, as well as the prevailing ambient condition<sup>101</sup>. The contact angle is the primary quantitative parameter used to predict or quantify the effect of this interaction substrate-ink. The degree at which ink wets the substrate is governed by the ink-substrate interaction and is usually measured by the equilibrium (static) contact angle ( $\theta_e$ ). According to Young's equation, the wetting characteristics relating the surface energy to the equilibrium contact angle, where the three phases are in mechanical equilibrium with each other, is given by Eq. (3.XIII):

$$\sigma_{sa} = \sigma_{sl} + \sigma_{la} \cos \theta_e \quad \text{Eq. (3.XIII)}$$



where  $\sigma_{sa}$ ,  $\sigma_{sl}$ , and  $\sigma_{la}$  represents the interfacial energy between substrate and air, the substrate and liquid, and liquid and air respectively. If the ink is too fluidic, there will be extensive spreading, which is aggravated if the surface energy of the substrate is far greater than that of ink. Conversely, if the ink is on the upper end of the viscosity spectrum, it beads up, which may cause a discontinuity in the ink filaments and poor adhesion to the substrate. On real surfaces however, there are metastable states giving rise to dynamic contact angle. The contact angle formed because the expansion of ink filament is known as the advancing contact angle ( $\theta_a$ ). In contrast, the contact angle resulting from contraction of ink filament is referred to as receding contact angle ( $\theta_r$ ). The angle hysteresis is the difference between the advancing and receding contact angle:

$$H = \theta_a - \theta_r \quad \text{Eq. (3.XIV)}$$

A small contact angle (i.e.,  $\theta \rightarrow 0^\circ$ ) is indicative of a strong ink-substrate interaction, with maximum possible spreading until an equilibrium configuration, which minimizes the surface energy, is attained, typical of Newtonian inks which have low viscosity, low surface energy relative to the substrate. The final shape is determined by the difference in surface energy between ink and substrate. For non-Newtonian inks (shear-thinning inks) ink spreading is more inhibited. With appropriate ink rheology, the filament may contract after deposition to yield a nearly rectangular cross-sectional area with a flattened top. The literature is widespread with examples indicating the crucial influence of substrate on print resolution<sup>109,110</sup>. From these works it can be concluded that there are three primary methods of controlling the shape and resolution of the prints: (1) treating the substrate with hydrophobic materials to create a low energy surface will limit excessive spreading of low-viscous inks, (2) using highly viscous inks in place of surface modification of the substrate will generally yield better output than substrate treatment, (3) surface properties of the substrate (e.g., porosity, irregularity of the surface) is the main driver for hysteresis effect and would determine final print geometry.

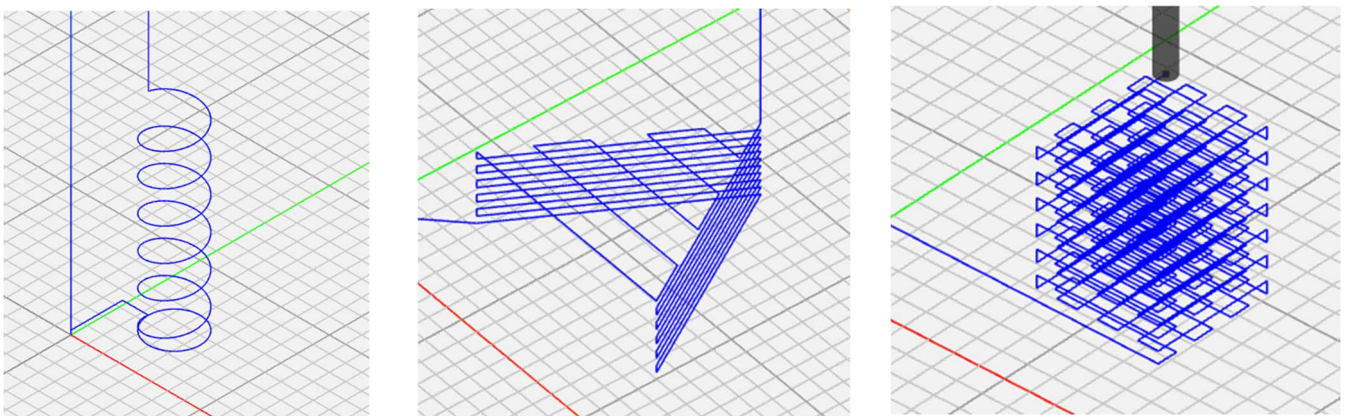
### 3.2.2 – Computer-Aided Design Technology<sup>5</sup> and Gcode

The development of AM is intimately related to the development of computers and 3D CAD modeling. AM takes full advantage of many of the important features of computer technology, including the processing power, graphics capability, machine control, networking and integration. Additive Manufacturing technology makes use of the output from 3D solid modeling CAD software. CAD (*Computer-Aided Design*) is the use of a computer to aid in the creation, design, modification, analysis, and optimization of a component. Early CAD systems were extremely limited by the display technology but have undergone considerable development thanks to the request from CAM (*Computer-Aided Manufacturing*) which represents the means to transform virtual CAD models into real products. CAM produces the code for control machine tools (numerically controlled machinery) to fabricate a component. The AM technique was one of the first to require the need for 3D solid modeling CAD as opposed to an use only for surfaces. CAD technology has evolved rapidly according to these guidelines: realism, user interface, engineering content, speed, accuracy, complexity, usability. It is possible to calculate the volumes and masses of models, to investigate fits and clearances according to tolerance variations, and to export files with mesh data for finite element analysis. All AM techniques therefore start from a software model that fully describes the external

geometry and is built through any type of professional CAD software. The CAD file can be saved as .stl which is the format that AM machines accept and which has become the de facto standard. The .stl format is a file format, binary or ASCII, used in AM through CAD software. It represents a solid whose surface has been discretized by triangles, for each of which the three spatial coordinates, x, y, z, of the vertices and a vector to describe the orientation of the normal to the surface, are defined. The .stl format is an intermediate step between the perfectly and mathematically described geometry of the CAD and the machine language of the printer. The .stl file can be built within a conventional 3D CAD system, or through other techniques including Reverse Engineering Technology, which obtains geometric data from an object, Haptic-Based CAD, in which the models are constructed from basic geometric shapes that are then combined in different ways to make more complex forms, CAM, CAE (*Computer-Aided Engineering*), that is the use of a computer to simulate the effects of various physics applied to a component or system and others. Few AM machines, however, interpret the .stl format directly, which must be sliced into layers as G-code, that is a programming language for computer numerical control, that offers sequential lines of instructions, each telling the machine to perform a specific movement or task.

### *G-code*

As described above, it is possible to switch from a three-dimensional drawing to a Gcode file through the use of programs such as "Slic3r", or you can write the code directly on a sheet of the "notepad". For this thesis I used Gcode files already present in the SD card and I wrote the files relating to the scaffolds directly on the notepad. Some examples are shown in **Fig. 3.6**.



**Figure 3.6.** Examples of Gcode files: spiral (left); "A" test (center); scaffold (right).

### *3.2.3 – UV setup*

The UV setup consists of a series of UV-LED chips arranged in a circular pattern by way of an attachment ring above the filament. The height of the ring, and thus the UV zone, must be adjusted such that the filament is exposed to the UV radiation slightly after extrusion. This allows the increase

in rigidity upon curing, to occur away from the extrusion point, however, the UV radiation must remain as close as possible to the extrusion point in order to reproduce the specific path of the moving extrusion device<sup>11</sup>.

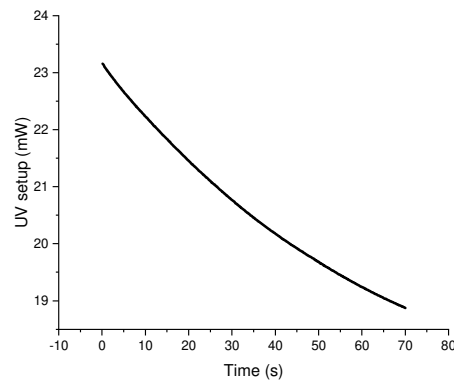
Initially the intensity of the UV light was unknown, but it was still possible to make a comparison between the various inks, for example by evaluating the degree of stiffness after printing and the ability of the structure to maintain its shape, since all were subject to the same irradiation. With the arrival of the power meter (*Thorlabs, PM400 Optical Power Meter*) it was possible to measure the intensity of the setup. The sensor was positioned below and in the center of the UV setup in order to reproduce as closely as possible the conditions experienced by the filament and measure an intensity as real as possible. The reported value was around 70 mW but was not stable and dropped rapidly over time to as low as 30-20 mW, probably due to overheating of the LEDs. For prints of a certain duration or if several pieces were printed in succession without leaving some time for the LEDs to cool down, it happened that during the test the light began to flicker or went out completely due to damage to the welded contacts. A cooling system and a system that adjusts the intensity to a maximum of about 23 mW was therefore added. Also in this case the intensity decreases over time but with a lower gradient and the phenomena of overheating and the risk of damage and breakdown of the setup are reduced. **Fig. 3.6** shows the graph showing the intensity data as a function of time measured by the power meter with an initial intensity of 23 mW. In this work, therefore, the first printing tests were carried out at an intensity of 70 mW, while subsequently the intensity was 23 mW. In this way it is possible to evaluate how the intensity of the light affects the degree of curing, the printing parameters and the rigidity of the printed structures.

The intensity of the lamp [*Omniculture, series 2000*] was also measured with the power meter to have the absolute values and correlate them to the percentage values shown on the device. Since it was used in conjunction with the rheometer, its intensity values were measured by positioning the sensor in the center of the glass plate of the same, after having fitted the mobile light at a predetermined distance from it; they are shown in **Table 3.5**. The measured intensity is constant over time, at the limit you can see minimal variations of the order of 0.1 mW with a decreasing trend at intensities greater than 10%. The rheological tests related to the gelation point were carried out starting from an intensity of 4% (about 74.3 mW) while the calculation of the curing depth was carried out at 1% intensity, equal to about 23.9 mW, to evaluate the time of curing at minimum power.

Light [*Omniculture, series 2000*] was also used at the beginning of this thesis work, for the first ink compositions tested, during printing instead of the UV setup. The device was positioned next to the printer and during printing the head containing the light was directed towards the structure during production. A configuration of this type, however, could compromise the uniformity of the curing since not all points of the printed structure receive the same lighting even if the light source is moved around the point of extrusion. Furthermore, the light is not focused exactly on the exit point of the filament, so the real intensity perceived by the latter may be lower than that read in the device due to dispersion phenomena. It was therefore decided to use the UV setup.

% Intensity	mW	% Intensity	mW
1	23.9	11	134.0
2	40.8	12	140.4
3	57.3	13	146.5
4	74.3	14	152.3
5	85.1	15	157.8
6	95.6	16	164.1
7	104.4	17	169.7
8	112.4	18	174.2
9	120.6	19	179.0
10	127.0	20	183.5

**Table 3.5.** Absolute values of the intensity of the lamp [Omniculture, series 2000].



**Figure 3.7.** Decrease over time in the intensity of the UV setup, measured on the power meter (Thorlabs, PM400 Optical Power Meter).

### 3.3 – Polymer to ceramic conversion: Pyrolysis

After shaping and cross-linking, the preceramic part has to be converted into a ceramic. This conversion leads to the decomposition or elimination of organic moieties (such as methyl, phenyl, vinyl groups) and Si–H, Si–OH, or Si–NH<sub>x</sub> groups. You can use heat treatments or not, but the most used ceramization process is undoubtedly the oven pyrolysis. The term pyrolysis indicates a chemical decomposition process of a compound obtained by applying thermal energy in the absence of an oxidizing agent. During heating in the presence of oxygen, combustion takes place, which generates heat and produces oxidized gaseous compounds; instead, by carrying out the same heating in anoxic conditions, the material undergoes the splitting of the original chemical bonds with the formation of different products. **Table 3.6** shows other examples of different ceramization treatments with respect to that of oven pyrolysis<sup>58</sup>. In the chemical vapor deposition<sup>112</sup> and plasma spraying techniques, used for the production of ceramic coatings, the ceramization takes place thanks to the high temperatures of the plasma or the heated substrate that decompose the precursor; laser pyrolysis<sup>113</sup> has the advantage of the selectivity of the area to be treated, but at the same time problems related to damage

and absorption by the polymer of that radiation may arise; microwave pyrolysis is not a widely used technique, since preceramic polymers do not absorb at that wavelength for which hybrid processes are used<sup>114</sup>; ion irradiation<sup>115</sup> is a nonthermal process in which the ceramization occurs via cleavage of C–H bonds and elimination of hydrogen and the residual carbon is converted to diamond-like carbon clusters; hot pressing<sup>116</sup> and spark plasma sintering<sup>117</sup> have been applied for consolidation of already pyrolyzed powders rather than as ceramization methods.

Ceramization/consolidation methods	References <sup>58</sup>
Oven pyrolysis	Blum <i>et al.</i> <sup>74</sup>
Hot isostatic pressing	Liew <i>et al.</i>
Hot uniaxial pressing	Breval and colleagues <sup>116</sup>
Spark plasma sintering	Wan and colleagues <sup>117</sup>
Chemical vapour deposition	Bouyer <i>et al.</i> <sup>112</sup>
Plasma spraying	Krüger and Raymond
Radiation pyrolysis (rapid thermal annealing)	Chandra and Martin
Laser pyrolysis	Colombo and colleagues <sup>113</sup>
Laser pyrolysis + high pressure	Dzivenko <i>et al.</i>
Microwave pyrolysis	Danko <i>et al.</i> <sup>114</sup>
Ion irradiation	Pivin and colleagues <sup>115</sup>

**Table 3.6.** Ceramization/Consolidation Techniques Applied to Preceramic Polymers.

In this study, an oven pyrolysis in an inert atmosphere of nitrogen in flow was opted: the inert atmosphere of nitrogen serves to eliminate competitive combustion reactions and the purge rate of the gas must be kept at a value that is sufficient to prevent the decomposition and redeposition of vapours released during polymer decomposition. The samples were placed on a refractory crucible and inserted inside the cylindrical chamber of the furnace with a clamp long enough to allow their positioning approximately in the center of the chamber itself. The oven closing operations were carried out by tightening the cover, equipped with gaskets with screws, and bolts and a pressure gauge was connected to it through the opening which is supplied, in turn connected to a vacuum pump. The vacuum is produced and the correct sealing of the vacuum is checked and therefore the validity of the closing operations. The system is then brought back to ambient pressure by repressurizing the chamber with nitrogen. The valve is then activated to activate the continuous flow of nitrogen by adjusting its input through the observation of a bottle partially filled with liquid (water) connected to the nitrogen output: the presence and speed of formation of gas bubbles is evaluated inside the liquid by adjusting the nitrogen pressure at the inlet accordingly. The temperature profile to be performed is then set by choosing the heating speed, the temperature at which to carry out the maintenance and the time of the same; it is possible to perform multistep heating.

The profile performed for all the samples is in fact multistep and is as follows: 2°C/min up to 350°C then stay for 30 minutes, another 2°C/min up to 425°C and stay 30 minutes, then 2°C/min up to 600°C and stay 1 hour and then always 2°C per minute and reach 1000°C and stay for 1 hour. The low heating rate and the stops at intermediate temperatures are used to avoid excessive thermal shocks

and to reduce the thermal stress imposed on the samples, which would lead to the formation of cracks or breaks on the pyrolyzed samples.

### 3.4 – Characterization of the inks

A rotational rheometer (*Kinexus Lab+*, *Netzsch, Germany*) was used for the rheological characterization of the inks. Each test involves the insertion of the most appropriate geometry, the test parameters and the loading of the sample. It takes place after setting the zero gap, placing a quantity of ink capable of completely covering the geometry inserted on the plate and removing the excess once the set gap has been reached. A UV-plate system accessory (*KNX5007, Netzsch, Germany*) equipped with UV lamp [*Omniculture, series 2000*] was employed for photorheological characterization using an 8 mm parallel plate geometry and a 0.29 mm gap. An amplitude strain control single frequency test was performed by varying the intensity of the UV light to compare the achievement of the gel point between the three inks and evaluate how it affects the gelation time. The UV lamp was inserted in the appropriate space by fixing it with the pin at a distance sufficiently far from the glass plate; in such a way the relative intensity of the same was the same among all the tests; to achieve this, the intensity was measured in the center of the plate by means of UV power meter (*Thorlabs, PM400 Optical Power Meter*) before the start of each test series. The UV lamp was switched on 30 s from the start of the test which lasted a total of 70 s. It was used at 1°/40 mm cone-plate geometry for the analysis of the other rheological properties of the inks. The shear rate dependence of viscosity was determined by performing a flow sweep test, a rotational test that applies an increasing shear rate and measures the evolution of viscosity. The range of shear rate used was 0.1-100 s<sup>-1</sup> with a gap of 0.03 mm. An amplitude sweep test was performed, which applies an increasing deformation at a constant frequency, which implies an increasing shear rate, and measures the evolution of the storage and loss modules. The frequency was 1 Hz, the gap 0.03 mm and the shear strain range 0.1-100%. A three intervals thixotropy test (3ITT), gap 0.29 mm, was performed to follow the evolution of the shear viscosity: (i) 0.1 s<sup>-1</sup> strain for 30 s at 1 Hz; (ii) 100 s<sup>-1</sup> of shear rate for 30 s; (iii) 0.1 s<sup>-1</sup> strain for 2 min at 1 Hz; during the last step, the UV light was switched on for different time intervals (0 s, 1 s, 5 s). The rheometer was also used for the evaluation of the curing depth as a function of exposure time.

To evaluate the self-supporting capabilities, a test “A” was carried out (**Fig. 3.6 (center)**): an A-shaped structure was designed and printed, whose sides, made up of different layers of material 5 mm high in the file, represented the supporting ends for a series of suspended filaments of decreasing length. This test evaluates filament collapsing and sagging as the distance of the supports varies. The height reached by the filament was measured at various distances from the extremes for all five filaments and a graph showed the trend as well as the influence of the speed printing parameter. Initially the idea to measure the ability of the filament to resist collapse under its own weight was to use a support consisting of two sliding halves able to bridging a gap at increasing distance and subsequently evaluate the deflection or the area under the filament as in the work of Ribeiro *et al.*<sup>118</sup>, who used a row of pillars at increasing distances (16, 8, 4, 2, 1 mm) on the model of Therriault *et al.*<sup>119</sup>. They have calculated the angle of deflection  $\theta$ , which is a measure of the deformation suffered by the filaments due to the discrepancy between the gravitational force, given by the filament’s own

weight, and inertia, measured by yield stress and storage modulus of the ink, and at the same time they created a theoretical model for filament collapse that correlates the yield stress of the link with  $\theta$ . The Eq. (3.XV) can be derived from the equilibrium of the force of gravity with the force resulting from the material resistance to yield in an infinitesimal volume:

$$\theta = \sin^{-1} \left( \frac{\rho g L}{\sigma_s} \right) \quad \text{Eq. (3.XV)}$$

where  $\rho$  is the density of the material,  $g$  is the gravitational acceleration and  $\sigma_s$  is the yield stress of the material. The experimental and theoretical values show the same trend. Our problem, however, was that the filament was not able to adhere to the support, so it broke into drops even before starting the suspended part. The second method used to evaluate the self-supporting capabilities of the ink was the printing of cantilever beam structures. The structures consisted of a vertical section 1 cm high and a horizontal section 2 and 4 cm long respectively, printed at constant pressure and variable speed. The deflection was calculated by placing the structures on graph paper, through the tangent of the ratio  $\Delta y/\Delta x$ , in which  $\Delta y$  represents the difference between the theoretical height (1 cm) of the end of the filament with the real one and  $\Delta x$  represents the length of the same (2 or 4 cm). During printing, at the end of the horizontal stroke, it was necessary to immediately stop the delivery of the ink in order to avoid the formation of accumulations of material that behave as weights at the free end of the filament, distorting the results of the filament's ability to withstand its weight; furthermore, the repositioning of the syringe in the initial position may involve the lifting of the horizontal tip due to the contact of the last drop of ink coming out of the nozzle and therefore stretching and deformation, which also in this case can alter the deflection data. The analysis was conducted only for the ink 6H44-3PETTA-4%PI due to the difficulty of obtaining the same structures with the other two inks and is reported for completeness in Chapter 4 even if it does not prove to be very reliable and representative. Hence the A test is adopted to evaluate self-supporting skills.

### *3.5 – Characterization of printed and pyrolyzed samples*

The morphological analysis of the printed samples was done through the optical microscope equipped with an AxioCam ERc55 camera. Objective 1.6x and the camera adapter 0.5x were fixed while the optovar magnification could be varied by turning the appropriate wheel. The magnifications used were 0.65x and 1.25x. The microscope was used to analyse the cross sections and the pitch of the printed spirals to compare them with the expected shape and evaluate how the variation of the pressure and printing speed parameters influenced the shape fidelity and which correlation existed between them. The diameter and pitch of the spirals were measured through the image processing program ImageJ. The microscope analysis was also used for the evaluation of the multi-layered structures printed (scaffolds) in order to assess the constancy of the filament diameter, merging with focus on the intersection-overlay of two filaments, the pore geometry, the shape retention of circular filaments and layer stacking. From the acquired photos, the shrinkage of the single filament of the scaffolds during pyrolysis was also evaluated by measuring the cross section again through the ImageJ program. During the acquisition of photos, it is important to orient the plane of interest parallel to the lens in order to capture an image that represents the actual size of the sample and is not distorted.

Pyrolyzed scaffolds were observed by scanning electron microscopy at 10 kV and at various magnifications from 50x to 1500x to evaluate the presence of cracks or defects and the ability of the filament to maintain a circular section and self-sustain between two supports.

The shrinkage of the scaffolds during the ceramization was calculated by measuring with a digital caliper the x, y, z dimensions of the structures before and after pyrolysis, using the formula:

$$S = [(d_0 - d)/d_0] \cdot 100 \quad \text{Eq. (3.XVI)}$$

Where  $d_0$  represents the length in a generic direction before pyrolysis and  $d$  represents the length in the same direction after pyrolysis. Since the scaffolds were not perfectly regular in all directions, more measurements were made, and the average value was considered.

The density of the pyrolyzed samples was measured with a helium pycnometer (*Ultrapyc 3000, Anton Paar*). For the calculation of the skeletal density, pieces of scaffold were inserted inside the sample holder, after weighing them and calibrating the instrument. The same tool was used for the calculation of the true density of the material on very finely ground powders of scaffolds. The target pressure was 18.0000 psi, the flow direction mode implied having the first entry into the sample chamber and the flow mode was monolith. 5 runs were repeated for each sample and the average value was evaluated.

Thermogravimetry analysis was performed on the samples obtained after printing for the three inks and also on the individual components of the inks: H44, PETTA and TEGO. As the last two are liquid, a mixture was prepared between the photopolymer and the photoinitiator in the same concentration as that used in the ink (4%) and a drop of each of the two mixtures was curing with the UV-LEDs system. The analysis was conducted from room temperatures up to 1000°C, with a heating rate of 5°C min<sup>-1</sup>.

Fourier transform infrared spectroscopy (Jasco) in the range of 550-4500 cm<sup>-1</sup> was performed to investigate the photopolymerization process, the bonds-conversion and the curing degree. The curing degree of the three inks was analysed by evaluating how the peaks related to some bonds varied with the variation of the exposure time to UV light and the pyrolyzed material was also analysed. KBr tablets were prepared as a reference with the use of a manual tablet machine for powders (*Specac, GS15011, 15 tons*). The KBr ionic salt is used as a reference since, being devoid of covalent bonds, it is transparent to infrared. 100 mg of finely ground KBr in an agate mortar were introduced into the tablet compactor and kept under pressure at 10 tons for 3 minutes before being extracted. It is necessary that the material is distributed evenly, so the tablet is transparent and no white lumps form. KBr is extremely sensitive to humidity as it is hygroscopic and its container must be kept in an oven at 75°C. For the analysis of the ink subjected to different curing times, a drop of ink dissolved in isopropanol was deposited on several KBr tablets then irradiated with UV light with an intensity of about 23 mW, similar to printing conditions, for different times. The pyrolyzed material was analysed by dispersing 5 mg of finely ground pyrolyzed samples in 100 mg of KBr and grinding both powders together to then create a tablet. In this way, however, the tablets were black and not transparent, so others were prepared in which only 1 mg was dispersed, and they were found to be more transparent and suitable for analysis. For the use of the spectrometer the suitable sample holder cell was inserted and the background line relative to the KBr reference was first recorded with the same acquisition parameters used then for the recording of the samples, number of scan 64, resolution 4.0 cm<sup>-1</sup>, range



4500-550 cm<sup>-1</sup>. Then we moved on to the analysis of the various samples and the processing of the results through the correction of the noise elimination and the creation of the base line and normalization.

The X-ray diffraction (*Bruker AXS D8 Advance, Bruker Corp., Italy*) was performed on pyrolyzed body and UV-cured samples after powdering them in an agate mortar. For the reduction to powder, samples of pyrolyzed and non-pyrolyzed scaffolds were chosen, which were placed inside an agate mortar after careful cleaning of the instruments using acetone and compressed air to avoid the presence of impurities resulting from previous analysis. The mortar was covered with parafilm on which a hole was made to pass the pestle, in order to retain all the fragments produced during the grinding. Once the powder was obtained, the samples to be inserted into the machine were prepared: a disk of powder was made by filling and levelling a special shaped mold which was then fixed at the analysis point. The voltage and current settings of the diffractometer were 40 KV and 40 mA, respectively. The scan angle ranges from 15° to 70° with a scan speed of 1 scan s<sup>-1</sup> and a step size of 0.05°. All three pyrolyzed materials and only the two PETTA-based inks in the form of green body were analysed since the ink containing TEGO after printing and before pyrolysis proves to be too soft to be reduced to powder. The Match! software package (*Crystal Impact GbR, Bonn, Germany*) was used for phase identification in particular of any impurities present, supported by data from PDF-2 database (*ICDD-International Center for Diffraction Data, Newtown Square, PA, USA*).

Mechanical compression tests were carried out on pyrolyzed scaffolds at room temperature using an “Instron 1121 UTM” machine. The machine is equipped with two steel plates, the lower one fixed and the upper one movable. Once the piece has been positioned in the center of the lower plate and after having placed some paper all around in order to prevent any pieces from spreading everywhere, the upper plate is lowered with a manual controller, so that it is as close as possible to the upper face of the sample. The closer you can get the better because the time required by the entire test will be shorter (the upper piston in fact reaches the contact of the sample at an extremely low speed), but you have to be careful not to lower the plate too much, as you risk crushing the cube of material weakening it and then falsifying the test result. Once the plate has been positioned sufficiently close, the test is started from the program.

The preload set was 0.5 N and the deformation rate was set at 0.5 mm/min. Before loading a subsequent sample, it is advisable to clean the two dishes from the residues of the previous one. The data that appear on the display show the strength as a function of elongation. To obtain a stress-strain curve, the data must be converted into stresses and strains:

$$\sigma = \frac{F}{A} \quad \text{Eq. (3.XVII)}$$

$$\varepsilon = \frac{\Delta h}{h_0} \cdot 100 \quad \text{Eq. (3.XVIII)}$$

where  $\sigma$  is the applied force, F the force applied by the machine, A the area of the resistant section,  $\varepsilon$  the deformation of the sample,  $h_0$  the initial height of the sample and  $\Delta h$  the decrease in height during the test (elongation in output). The samples were prepared by levelling the two parallel surfaces then in contact with the plates, so that they were as straight and uniform as possible, free from peaks or undulations, so that the contact area was flat and not concentrated in the higher irregularity. The levelling was obtained by polishing the cubes with a polishing machine: the treatment was carried out

on a 500-grit paper with running water throughout the processing. The samples were then placed in the oven at 75° for the drying and the height corresponding to  $h_0$  was subsequently measured.

## Chapter 4

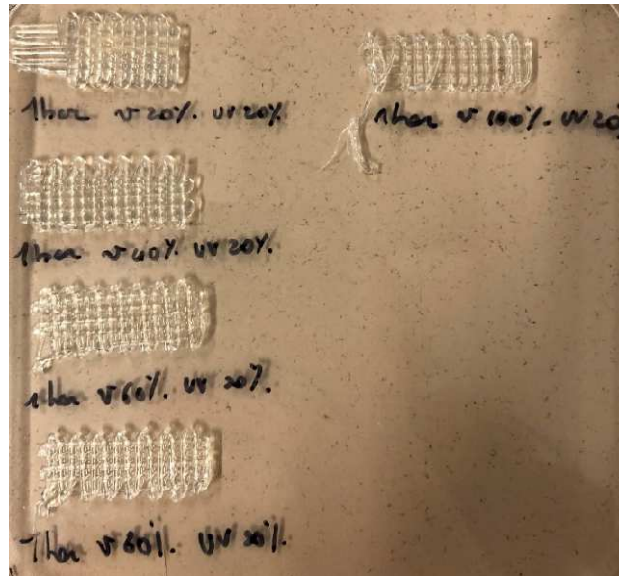
### Characterization

#### 4.1 – Inks

##### 4.1.1 – Optimization

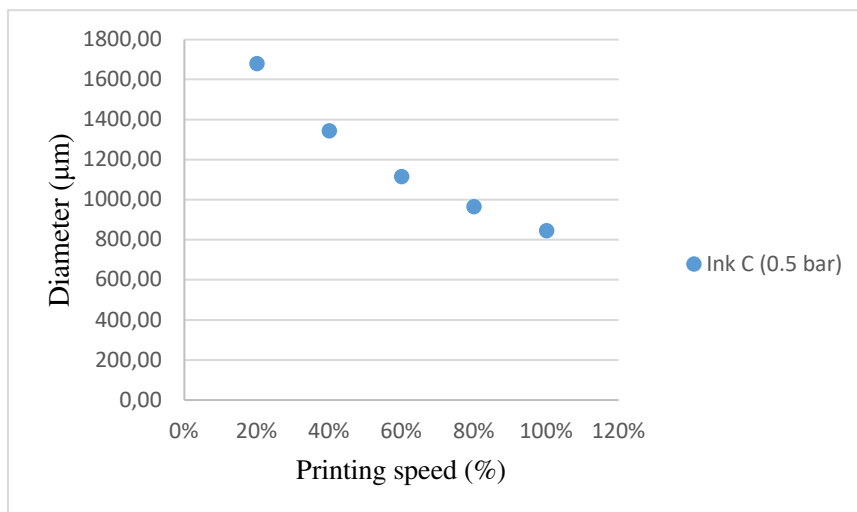
Various ink compositions were tested, in order to obtain one with optimal properties for printing. The three compositions A, B and C in Table 3.II were initially prepared, with H44 as preceramic polymer and TEGO as photopolymer. All inks were prepared using the method described in §3.1. We printed a "weft and warp" structure consisting of two layers of parallel filaments oriented to each other at 90°, forming an intertwined structure with small square holes. The light source used for curing was the lamp Omnicure, series 2000, and the intensity used was 20%. The speed inside the Gcode file was 450 mm/min and we printed at speeds of 20%, 40%, 60%, 80% and 100% at a pressure of 1 bar to evaluate how the speed parameter influenced the shape fidelity of the filament. The influence of the intensity of UV light on the printability of the samples was also evaluated, by varying the intensity of the radiation during printing. The structures thus obtained were then sectioned with a cutter and observed under the microscope to analyse the section of the filament, to assess whether it maintained a circular shape with an aspect ratio close to one, if the diameter was close to that of the nozzle and if the two layers remained distinct, or if at the points of contact the two layers merged due to little curing. A two-layer structure was chosen (**Fig. 4.1**) because, if the filament had been printed directly on the substrate and the section evaluated, the roundness would have disappeared since the part in contact with the substrate tends to be flattened, due to the phenomena of surface tension, the weight of the material above and the dragging motion of the nozzle. The second layer is not affected by this crushing problem since it is raised by the first, so the sections are more representative of the ink's ability to cure quickly enough to maintain a circular shape of the filament. The structures printed with composition inks A and B were extremely sticky, were very flexible and the filament had not maintained the size of the nozzle but had expanded until it merged on each parallel stroke. When cut with the cutter, they were very soft and the section of the filaments was deformed by the cut itself, which made it more oval. These compositions had too low photopolymer content in relation to the total weight of the mixture to allow rapid and complete curing. The C ink seemed able to produce fairly rigid structures and able to respect the design contained in the Gcode file. From a visual examination of the structures printed with this last ink at constant pressure, it could be seen that the diameter of the filaments decreased as the printing speed increased: at 20% the filaments were completely deformed and melted in all points; as the speed increased, the diameter decreased and the parallel filaments were detached and no longer fused, the holes began to be seen even if they had an irregular shape and not the original square shape of the file; at high speeds (100%) the structure was more similar to the drawn one, with the thinner and clearly distinguishable filament, separate layers

and square holes. For this ink composition, the structures were printed at three different pressures, 0.5, 1 and 1.5 bar, and the effect of the speed parameter was evaluated for each.



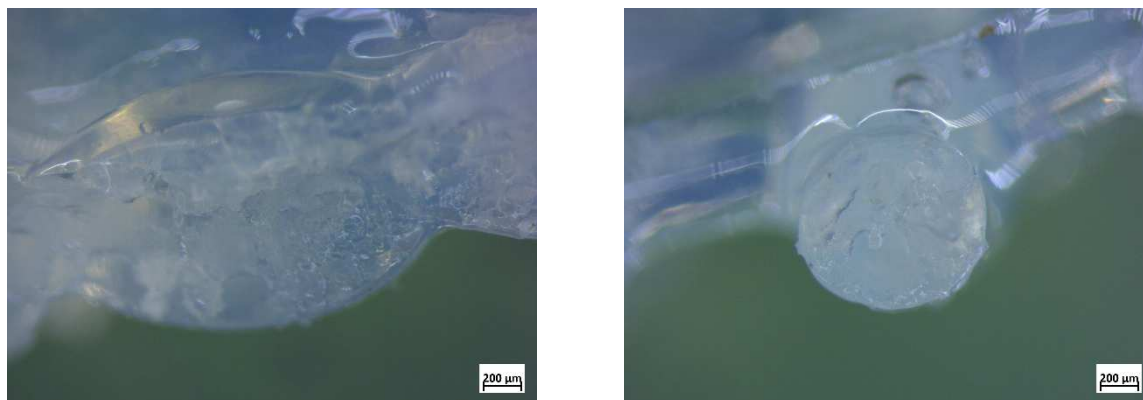
*Figure 4.1. Two-layer structure used in the first prints.*

The analysis of the sections under the microscope and the calculation of their diameter through the ImageJ program, confirmed the trend of decreasing diameter with increasing speed, represented in **Fig. 4.2**, a trend valid for all pressures. At the same pressure, the sections of the filaments are more oval at lower speeds while at higher speeds they are more rounded. In **Fig. 4.3** a comparison between two sections printed at a speed of 20% and 100% at 0.5 bar. As the pressure increases, it is necessary to use a higher printing speed to obtain distinct and circular filaments; in fact, at the same speed, the filaments at a pressure of 0.5 bar are more circular than those printed at a double pressure of 1 bar. For higher pressures, however, the diameter of the filament is still greater than that at the pressure of 0.5 bar despite the increase in speed and for 1.5 bar the structures are very deformed and the filaments fused together. An excessive increase in speed in fact leads to a shorter curing time and therefore the ink does not have sufficient time for the polymerization process which makes it rigid.



**Figure 4.2.** Diameter-speed correlation for ink C at a pressure of 0.5 bar.

The nozzle used for the printing are 840 µm. Even in the "best" printing conditions, i.e., at a low pressure of 0.5 bar and 100% speed, the diameter of the filament obtained is greater than that of the nozzle: in fact, a diameter of approximately 850 µm is reached. This is certainly due to the phenomenon of die swelling, which is characteristic of the extrusion processes of plastic materials, but may also be due to the ink's poor ability to cure quickly, due to a still too low amount of photopolymer. To evaluate this, the same ink was used to print spiral suspended structures with arms having a radius of 4 mm and a pitch of 2.5 mm. The structures were unable to support themselves, the spiral arms collapsed on top of each other and did not keep their shape. This composition was therefore also discarded because it had too low photopolymer quantity.



**Figure 4.3.** Comparison between two sections of filaments printed with C ink at 0.5 bar. Left speed 20%, right speed 100%. Photo under the optical microscope.

The amount of photopolymer was therefore increased in a 1:1 ratio with respect to the preceramic polymer, again 2 wt.% of PI (composition D). Spiral structures were always printed and in this case they solidified quickly and were able to self-sustain. A problem with this composition could be the pyrolysis heat treatment since such a large quantity of photopolymer could lead to exaggerated shrinkage that would have created cracks or breaks in the piece. Some spiral samples have been

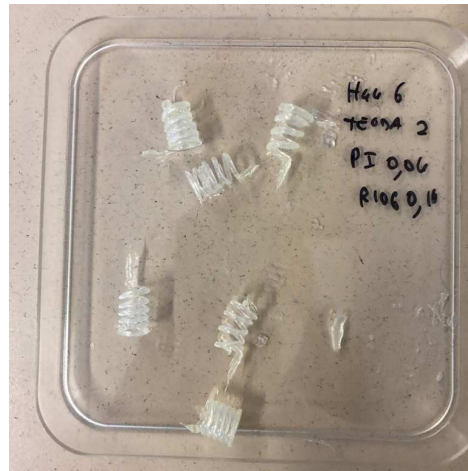
pyrolyzed and have been shown to withstand heat treatment without considerable deformation or breakage.

It was decided to try to change photopolymer and to use TEGDA. The cups in which the ink has been prepared must be covered with aluminium paper otherwise the polymerization occurs partially even in visible light and you find yourself with a cured ink disk after the isopropanol evaporation phase under the hood. Three compositions were tested, F, G, H, with a different TEGDA content. The first composition had an H44:TEGDA ratio of 2:1 and was extremely liquid. When the material was extruded even at the minimum pressure necessary to make it flow out of the nozzle, there was the formation of droplets and not of a continuous filament capable of producing a coherent and uninterrupted trace. Even when the pressure was brought to zero, there was the formation of a drop on the tip which, once reached a critical size, detached and fell on the substrate; it was as if the force of gravity were enough to make the ink come out of the nozzle in the form of drops. The printing of the spirals was impossible due to the continuous breaking of the filament. Composition G also showed the same problems despite a lower quantity of TEGDA. Composition H had better rheological behaviour, was slightly less liquid and it was possible to print spiral structures. Despite having a better behaviour than the two previous compositions, during the extrusion there is not the formation of a continuous filament, but it displayed partial fiber formation, with the presence of drops also in this case. The spiral structures are deformed and difficult to make due to the interruptions of the filament, despite trying to optimize the printing speed and pressure parameters.

To try to adjust the rheological properties of the ink, it was decided to introduce a new component, fumed silica R106. Fumed silica (FS) is a finely divided amorphous silicon dioxide produced by high temperature hydrolysis of silicon tetrachloride in an oxygen-hydrogen flame<sup>120</sup>. Silica particles can be seen at three scales: primary particles of around 5-30 Å in size formed at high flame temperature; these particles are not stable and fused together to form stable aggregates of around 100-250 nm, then leaving the flame the silica aggregates stick together by physico-chemical surface interactions, building up large micron-sized agglomerates and finally fluffy flocks<sup>120</sup>. Because of the enormous surface area (50-400 m<sup>2</sup>/g) of these particles, the surface silanol functional groups, which impart a hydrophilic character to the material, and the surface siloxane bond, play a major role in the behaviour of fumed silica. FS is known to be a thickening<sup>121</sup> and thixotropic agent<sup>27</sup>. Silica (especially fumed silica) is in fact known for its ability to enhance the viscosity of organic media and this can be understood as the opposite of stabilization<sup>121</sup>. It derives from the formation of interparticle linkages. When such linkages are formed extensively and span the sample volume, the result is a colloidal gel. During the process of gelation, the initial viscous liquid is converted into a self-supporting material which exhibits elastic character. As for the thixotropic behaviour, it means that the viscosity of the dispersion will decrease under shear, but will return to its initial value after a rest time<sup>120</sup>.

The composition with 2 wt.% compared to the total fumed silica, has a higher viscosity, however the spirals are not able to hold the shape. The ink is still excessively liquid, it comes out of the nozzle at the minimum pressure too quickly and the various arms are compressed on each other, as shown in **Fig. 4.4**. The structures are less transparent than those printed with R106-free ink compositions. We tried to reduce the amount of photopolymer, composition L, to make the ink less liquid. The ink does not cure immediately exiting the nozzle due to the low photopolymer content and due to the fumed

silica particles that affect the light beam by scattering, which depends on the ceramic volume fraction, particle size and the refractive index difference between the ceramic and the liquid.



**Figure 4.4.** Composition spirals in the figure with 2% of the total FS. The shape is not maintained.

Another way followed was to change the non-photosensitive preceramic polymer. We have replaced the H44 with MK. The tested composition (O) was found to be extremely viscous, extrusion from the nozzle was almost impossible even at pressures of 4-5 bar and, being not very transparent, it was not even able to solidify with exposure to UV light. I wanted to try to use a mixture of preceramic polymers with a high ceramic content to evaluate if a composition such as 2 g H44 1g MK 0.8 g TEGDA and 0.016 g PI could be the solution to the problems of viscosity and curability. Unfortunately, the components were not miscible and during the preparation of the ink there was a separation of phases and formation of agglomerates. So, the solution was to go back to using H44 with two approaches: increase the percentage of PI while maintaining a smaller quantity of photopolymer, composition M, or increase the photopolymer and consequently the quantity of fumed silica to counterbalance the rheological properties with the shear thickening effect, composition N.

The first of the two compositions did not prove to be effective. The spirals remained soft and foldable like springs, while we are interested in rigid pieces; the structures were also unable to self-sustain perfectly. All the tests conducted so far have been performed with variable nozzles of 0.84, 0.58 and 0.41 mm, on spiral structures with a fixed radius of 4 mm and variable pitch (2, 2.5, 3, 4 mm), manually adjusting the pressure and speed to every nozzle and composition. With the second composition with 3% silica by weight with respect to the total, there is a slow and incomplete curing probably due to the high scattering by the FS particles, for which the structures are not able to self-sustain and maintain the form, or due to the still insufficient quantity of photopolymer. By visually comparing the printed pieces of the compositions containing silica with those of the compositions without silica, it was decided not to use it as a component anymore as it worsens the printability of the inks.

It was decided to try two other very reactive photopolymers which therefore should cure completely and more quickly, to allow to print structures faithful to those contained in the Gcode. The first photopolymer, Fun to Do, already contains the PI inside, so it is not necessary to add Irgacure 819. This resin is designed to be ultra-fast during curing, has a very broad range of activity, from very short wavelengths of 225 nm to the near/visible of 415 nm. It also has an ultra-low shrinkage

(funtodo.net). As regards the composition P, there are no phase separations between H44 and the photopolymer and the viscosity is suitable for the extrusion of a continuous filament. However curing is not fast enough to create self-supporting structures. The printed spirals were actually sufficiently rigid, but the shape did not reflect the drawn one, the trace was wavy due to the instability of the various revolutions which, not being sufficiently rigid, swayed during printing giving rise to deformed and wavy spirals. Trying to increase the quantity of the photopolymer, composition Q, the situation worsened in terms of rheology, the filament deformed and reached diameters much greater than those of the nozzle, probably due to the die swelling and gave way to stubby spirals with non-existent pitch. The other photopolymer tested was PETTA. The first composition tested contained an H44:PETTA ratio equal to 3:1 with a PI content equal to 2% by weight of the photopolymer, composition R. This ink can produce a continuous filament, in **Fig. 4.5**, and it is possible to print spirals that are capable of self-sustaining and that keep their shape well.



*Figure 4.5. Formation of the continuous filament of the ink composition 6H44-2PETTA-2%PI.*

Regarding the two best compositions found, R: 6 g H44 2 g PETA 0.04 g PI (2%) and D: 3 g H44 3 g TEGO 0.06 g PI (2%), vertical and inclined structures of 30° and 60° were printed for comparison. Both compositions can produce vertical structures and inclined filaments of various angles. The ink structures containing the PETTA photopolymer appear more rigid than those containing TEGO, since in the latter case the amount of photopolymer is equal to 50% of the total weight. In **Fig. 4.6** some printed structures are represented. As for the inclined filaments, as the length of the filament increases, the phenomena of deflection and deformation of the same increase so that it is not possible to print too long. For vertical filaments, the phenomenon of the increase in diameter as a function of the height from the substrate is observed. To obtain fine filaments the speed must be greatly increased with the risk of not leaving sufficient time for the material to cure and therefore have soft structures that flex.





**Figure 4.6.** Vertical and inclined structures. Filaments inclined by 60°, on the left TEGO on the right PETTA (left). In the image on the right vertical filament of PETTA.

To evaluate whether the increase of the Irgacure 819 photoinitiator could be a solution to increase the curing speed of the material and therefore the ability to print at higher speeds, two new ink formulations were prepared that contain 4% by weight of the photoinitiator with respect to the polymer photosensitive, E: 3 g H44 3 g TEGO 0.06 g PI (819) 4% and T: 6 g H44 2 g PETA 0.04 g PI (819) 4%.

In addition, to evaluate whether an increase in the quantity of photopolymer could increase the shape fidelity of the structures and have a positive effect on the printability, the last two ink compositions S and U were prepared, respectively with 2% and 4% photoinitiator always for evaluate if its increase would favour a faster curing.

Among the many compositions the best ones were:

D: 6 g H44 6 g TEGO 2% PI

E: 6 g H44 6 g TEGO 4% PI

R: 6 g H44 2 g PETTA 2% PI

S: 6 g H44 3 g PETTA 2% PI

T: 6 g H44 2 g PETTA 4% PI

U: 6 g H44 3 g PETTA 4% PI

A comparison was made between these compositions to evaluate how two parameters, the quantity of the photoinitiator and the quantity of the photopolymer, can influence the printability and shape fidelity of the printing samples. Spirals with a radius of 4 mm and pitch 2.5 mm were printed at different pressures and speeds in order to evaluate for each ink how these two parameters also affect the printing. For all the spirals, photos were taken and the pitch between the arms and the diameter of the filament were measured. The results are reported in §4.1.2.

All subsequent experiments and analysis were conducted only on compositions E, T, U.

For an ink based on preceramic polymer it is extremely important to have the proper rheological and curing properties for a reproducible and faithful print to the design, but it is also important that the printed structures withstand the pyrolysis heat treatment. A green body for each composition was then subjected to pyrolysis treatment to understand if the structures held up or if there were excessive deformations. The structures containing TEGDA during pyrolysis melt before reaching decomposition, so that the structures are destroyed, while those containing Fun to Do resist but the inks do not have a good printability, so they have not been considered anymore. Structures containing TEGO or PETTA resist heat treatment without breaking or excessive deformation.

#### *4.1.2 – Printability and Shape fidelity*

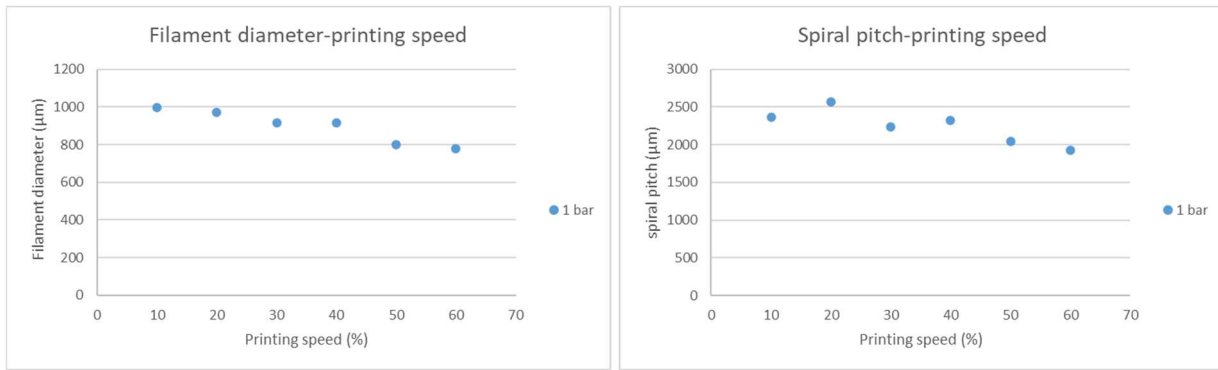
There is a distinction to be made between 'deposable' and 'printable'<sup>122</sup> ink. An ink can be depositable when the used Additive Manufacturing machine is able to extrude it, on the other hand they are defined printable when they are homogeneous, have an appropriate viscosity and rheological properties such as to be easily extrudable, maintain the shape after printing, reach sufficient density of the material after sintering, while maintaining adequate dimensional control. The evaluation of the term printability must take into account so many parameters of the printing process that it is impossible to give a unique definition and often this hinders the comparison of different inks.

There are various approaches to the evaluation of an ink and they can be distinguished on the basis of how they are related to the different stages of the printing process (pre- and post-printing for example). Rheological properties are the physicochemical parameters with the largest influence on inks printability<sup>123</sup> and act as predictors of the potential shape fidelity. It is important to evaluate the shear-thinning behaviour, the yield stress which can counter deformation from gravity or surface tension, a potential predictor of how well an ink holds its shape after extrusion, the elastic recovery, the time dependent response of the material after shear induced deformation and the damping factor ( $\delta$ ). A detailed description of the rheology is found in §4.1.3. Moreover, since the filament is the primary constituent of all the samples produced through the extrusion technique, it is important to evaluate its formation as well as the maintenance of the shape of the single and multilayer structures. The extrusion of the filament occurs when the extrusion pressure exceeds the yield stress of the ink; homogenous inks will result in constant extrusion forces<sup>123</sup>. It is possible to easily evaluate the tendency of the ink to form continuous drops or filaments through an initial screening method and thus identify the optimal printing settings. The ability to form filament and display uniform extrusion is directly associated with the material's shear-thinning and rapid shear recovery behaviour<sup>105</sup>. If it is possible to obtain a continuous filament, its uniformity can be evaluated through the measurement of diameter (the diameter of the filament normalized on the diameter of the nozzle gives us the spreading ratio), height and aspect ratio as a predictor of shape fidelity and to optimize printing settings; the tendency to collapse of the filament by measuring the stability of a single filament to bridge a distance without sagging due to gravity and its own weight, calculating the angle of deflection  $\theta$  or the area below the filament; filament fusion that defines the pore closure of two filaments which remarks the time dependent ink flow in delayed or post extrusion cross-linking<sup>123</sup> and that can be evaluated with a straightforward test which consists in printing a filament with a stepwise narrowing of the filament

spacing<sup>118</sup>: the fused part will be greater as the separation decreases and for inks with lower yield stresses. In addition to the single filament, it is important to evaluate the uniformity and homogeneity of planar structures, consisting of 1-2 layers and subsequently multilayer structures. It is important to evaluate the diameter at the intersection of two filaments, as an index of how much the filament relaxes and spreads onto the underlying layer and semi-quantitative methods have been introduced to evaluate the circularity of printed filaments and shape fidelity of the pores<sup>123,124</sup>. From the last test, a printability index Pr can be obtained based on the observation of the pore area in a 0-90° laydown pattern in which ideally it should be square in the x-y plane. If the printability index is equal to one (square shape transversal pore geometry) we have high geometric accuracy, while if  $Pr < 1$  and  $Pr > 1$  we have a more round or irregular shaped transversal geometry and so lower accuracy. Low viscosity and nonoptimal gelation conditions are some of the underlying causes for these deviations, e.g., the merging of filaments and the resulting low shape fidelity<sup>124</sup>. In multilayer structures the layer stacking indicating the shape retention of circular filaments is analysed by comparing the height of the computer designed sample to the height of the printed one<sup>123</sup>.

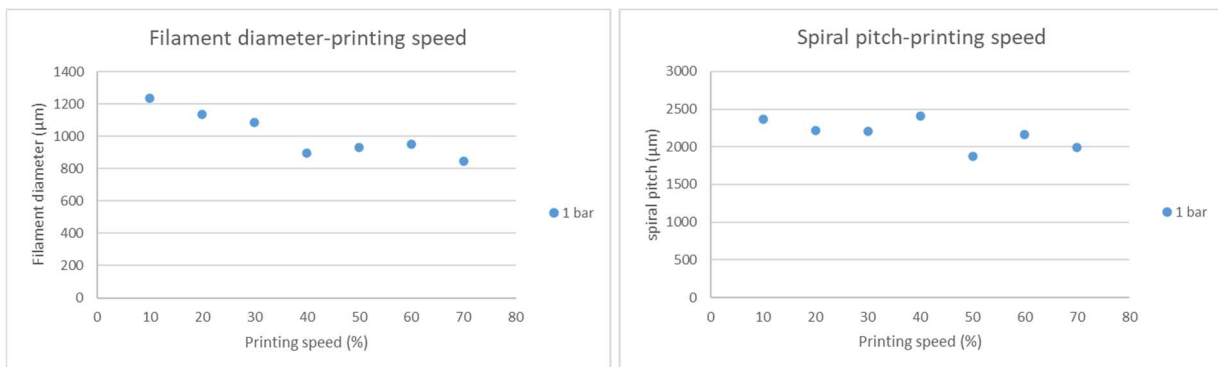
#### 4.1.2.1 – Spirals

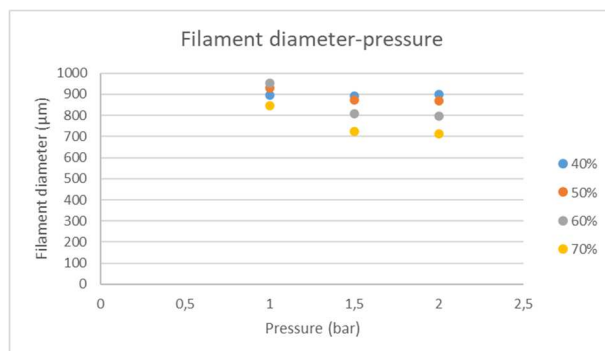
To analyse the printability and shape fidelity of the inks and to evaluate how the pressure and printing speed parameters influence the process, we printed spiral pieces with a radius of 4 mm and a pitch of 2.5 mm at various speeds and pressures for the inks chosen as the best, also evaluating the influence of the amount of photoinitiator and photopolymer. The first ink to be evaluated was 6H44-2PETTA-2%PI. From the graph in **Fig. 4.7**, it can be seen that as the printing speed increases, there is a decrease in the diameter of the filament and the average pitch of the spiral. However, the diameter of the cross section reached is far from that of the nozzle due to the swelling phenomenon and perhaps due to a too low quantity of photoinitiator which does not allow rapid curing and makes the filament widen at the exit. To evaluate the pressure-speed correlation, it is important that the ink is presented with the same rheological characteristics at each print. The instability in the conditions of the ink, the fact that it can be more or less liquid, is largely attributable to the amount of isopropanol inside it; if it is not completely evaporated, ink remains more liquid and therefore it is possible to print at lower pressures. It is therefore important to completely eliminate the solvent during the mixing phase to obtain constant properties and to avoid that its presence causes cracking phenomena during the ceramization. The instability of the inks found during the first prints could also be attributed to other parameters such as the environmental temperature, however, by controlling the quantity of isopropanol parameter, the rheological properties proved to be constant over the months of work. The temperature is an influential parameter if the syringe is not allowed time to cool after degassing. The pressures at which this ink has been printed are 1, 1.5 and 2 bar. At lower pressures either it was not possible to extrude the filament, the material cured too quickly with respect to the flow so the nozzle was obstructed; at higher pressures the output flow was too strong and instability was created in the filament which was therefore wavy and then, it would have been necessary to print at such high speeds as not to allow curing. The relationship between speed and decrease in diameter as the printing speed increases is valid for all three pressures used.



**Figure 4.7.** Increase in diameter and pitch as print speed increases for 6H44-2PETTA-2%PI ink. The graphs refer to a pressure of 1 bar. The same trend is recorded for the other pressures of 1.5 and 2 bar respectively.

The 6H44-2PETTA-4%PI ink was compared to evaluate if a higher PI content could actually contribute to increasing shape fidelity. Also in this case, the spirals do not have a perfect shape, in the sense that the pitch is not perfectly constant but increases from the first arm up. The filaments maintain the cylindrical shape, but the spirals become at a variable pitch more than constant one. This may be due to the fact that the various layers of filament are subjected to different forces as regards the nozzle, which tends to drag it up, and the weight of the underlying material, which is now rigid, can no longer be deformed and increases from coil to coil. However, more likely, it is caused by the fact that the first layers are the most uncertain, since the UV light is not always turned on as soon as the ink flow rises from the substrate, because you have to wait for the filament to be uniform and not folded. The first layers are therefore settling and the trace solidifies in a different point than where it would have had if the UV light and solidification had started when it detaches from the substrate. Furthermore, the section of the filament is not constant: it maintains the cylindrical shape but increases as you go up towards the last layers; the first layer has a shape and a diameter quite faithful to the nozzle at the correct speed, while as you go up it “deforms”, and the section increases. This may be caused by the fact that the intensity of the UV light isn’t constant during printing but decreases, allowing for less and slower curing that causes the filament to overflow after exiting the nozzle. The graphs relating to the 6H44-2PETTA-4%PI ink are shown in **Fig. 4.8**. As the printing speed increases, both the section and the pitch decrease, even if the latter is irregular. The third graph shows the filament diameter vs. pressure of extrusion for the ink 6H44-2PETTA-4%PI. The one relating to the mixture containing 2% of PI is also not reported since with 2% of PI there were not three or more speeds at which it was possible to obtain a sample for all three pressures.

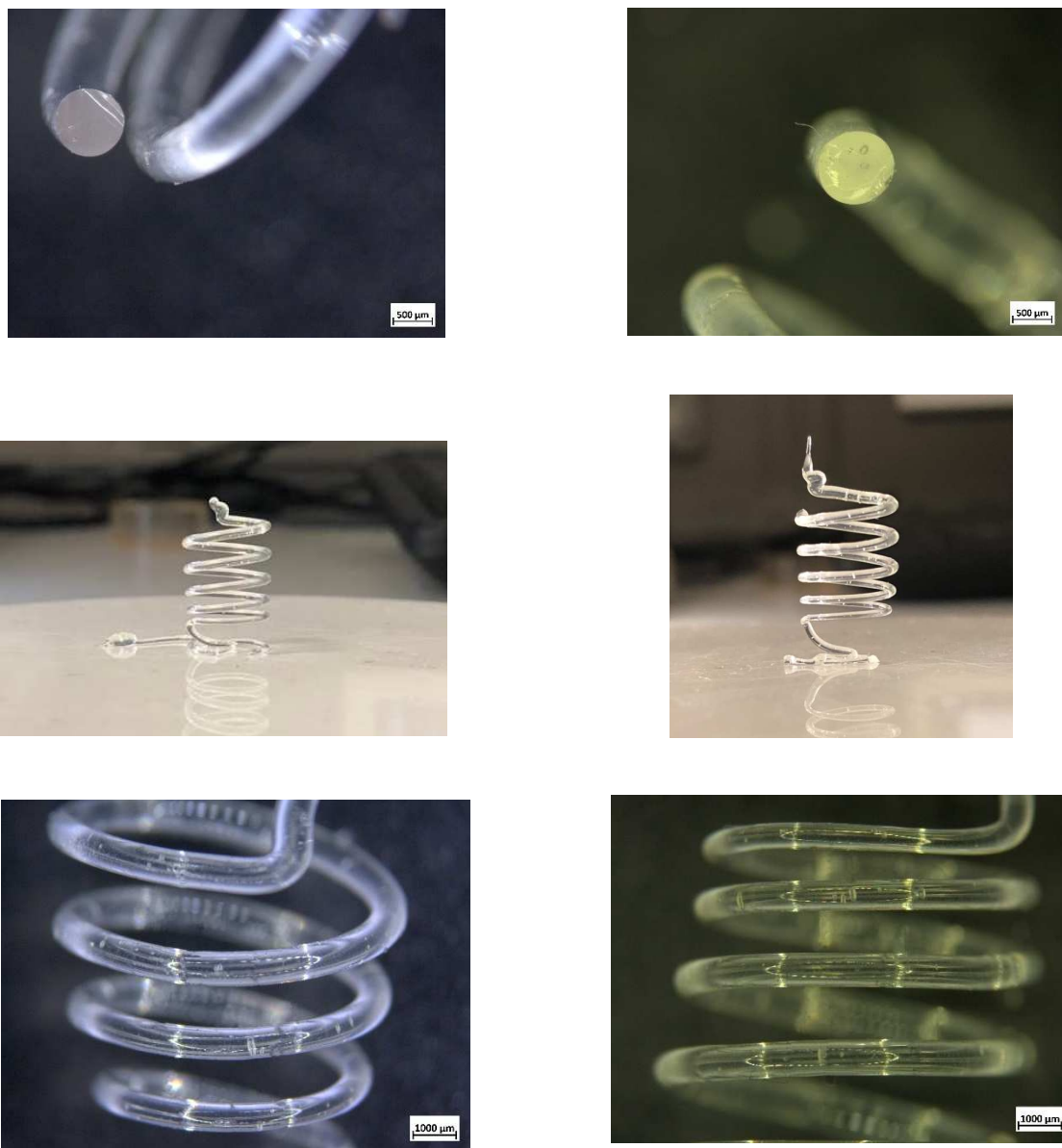




**Figure 4.8.** The two graphs at the top represent the increase in the diameter and pitch of the spirals as the printing speed for the 6H44-2PETTA-2%PI ink increases. The graph below represents filament diameter vs. extrusion pressure according to different printing speeds for the ink 6H44-2PETTA-4%PI.

The variation of the lateral diameter was also evaluated, i.e., the lateral view of the filament as the speed and pressure parameters varies, not shown here. It shows the same trends reported for the cross-section. **Fig. 4.9** shows the images under the optical microscope of the spirals made with the inks 6H44-2PETTA-2%PI and 6H44-2PETTA-4%PI for a direct comparison. From the photos and graphs it can be seen that, in both cases, the cross-section is shown to be circular throughout the spiral thanks to the symmetrical arrangement of the UV source. It was obtained by cutting the spiral at different heights and photographing under the microscope the sections then analysed with ImageJ, (round of 0.922 and 0.921 at 1 bar 10%). However, the diameter of the filament differs from that of the nozzle in both cases, it is still far from that of the 580 µm nozzle and settles at a value higher than 600 µm for the maximum speeds reached during the press. At 4% PI, they are able to reach printing speeds higher than 2% before the structures are deformed and not standing. The fact that the actual size of the nozzle is not reached but only larger is obtained, is due to swelling after exiting the nozzle. This phenomenon practically consists in the fact that during the transit in the nozzle, the polymer chains are aligned along the direction of the shear stress, but as soon as they come out, they are no longer all aligned in the same direction but swell and are distributed randomly. So the size of the filament will always be greater than that of the nozzle. The trend that can be seen is that of a decrease in the cross section as the speed increases, for both inks, so this is in accordance with the theory. The pitch of the spirals is not constant within the same sample and increases from the first lap. This is due to the instability of the ink in the first layers as previously described and may also be due to the nozzle which, when it rises from the last layer to the final position, pulls behind the spiral and then makes it fall again like a spring, modifying the pitch of a structure that is not perfectly rigid. The average pitch, on the other hand, decreases with increasing speed, probably due to the shorter curing time which makes the structures softer and more prone to crushing of the coils. For both compositions, speeds close to 100% are reached at pressures of 1-1.5 bar, therefore, it is possible to print suspended structures at 450 mm/min. The two inks will not have different rheological properties (since PI does not change the rheology at all), and they do not seem to have different shape fidelity; ink containing 4% PI would allow printing at slightly higher speeds but does not significantly increase shape fidelity.

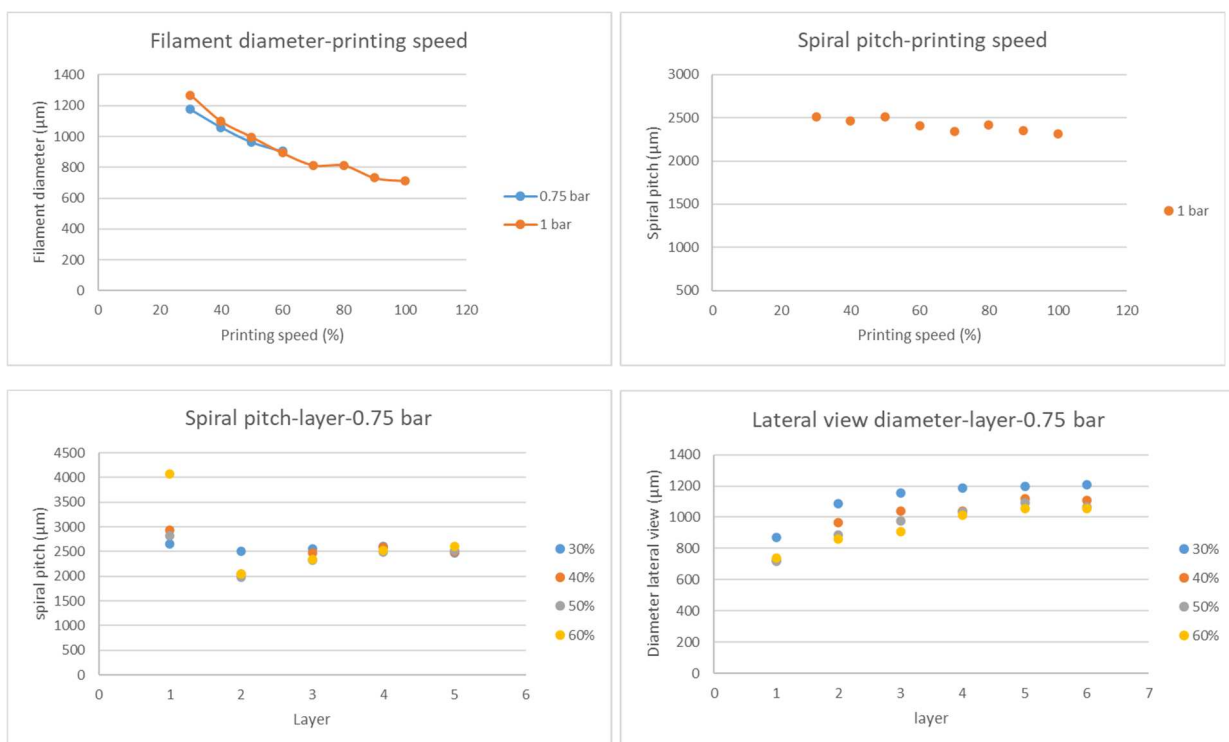
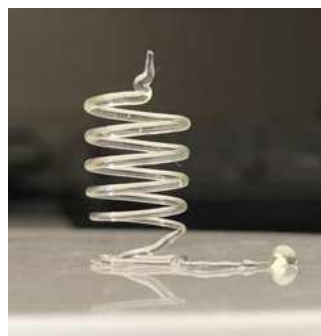
In theory, pressure should be an influential parameter to control swelling and therefore improve the fidelity of the shape. In particular, the trend should be that increasing the pressure at a fixed speed, the swelling should be worse because more material is pushed out and therefore the filaments will have more bulge and a larger diameter. For the ink 6H44-2PETTA-4%PI the comparison between the various pressures shows instead that there are no definite trends or notable differences.



**Figure 4.9.** Comparison of spirals printed with 6H44-2PETTA-2%PI (left) and 6H44-2PETTA-4%PI (right) inks. The cross sections refer to spirals both printed at 1 bar at 40% speed.

Since these two compositions still show some shortcomings in terms of shape fidelity, we tried to optimize the composition by varying the quantity of photopolymer, adopting the composition H44 6 g PETTA 3 g PI 4%, with 4% of PI since they were not registered significant variations between 2 and 4%, but could allow printing at higher speeds. Initially I thought that increasing the amount of photopolymer could lead the ink to be too liquid. In reality, it manages to form a continuous thread and is easily extrudable. The pressures at which we printed are lower due to the lower viscosity of the ink: 0.75 bar, 1 bar and 1.5 bar. The last pressure is excessive, and the outgoing flow is too high, the filament arches and does not cure; 0.5 bar is a pressure at which it is not possible to print at too low speeds because the material cures too quickly and very close to the nozzle, so much so that it clogs it or there is a fragmentation of the track. **Fig. 4.10** shows the graphs relating to the printing parameters. From a visual analysis, the pitch of the spirals is more constant and during printing it

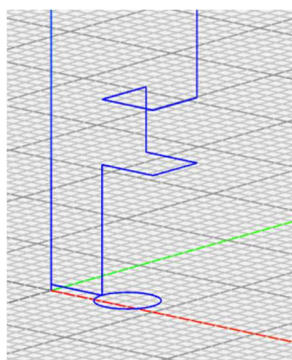
seems that the material cures more quickly. At a pressure of 1 bar, it is possible to print at higher speeds than ink with 2 g of PETTA. From the graphs you can see how the cross-section trend with speed is always the same: it decreases as speed increases. As for the pitch on each layer, it seems more constant, in the sense that after some initial instability it approximates well to 2.5 mm. The instability of the first layers certainly depends on the fact that the curing does not always start at the same point, but we wait for the filament to come out continuously and linearly to turn on the UV source. However, it appears more precise and constant than that at 2 g PETTA. As for the lateral diameter, it grows as the layer increases as it also happens for the cross-section and then it seems to have an approximately asymptotic behaviour at a constant value. It could be due to the fact that the UV light drops in intensity and then settles down to a certain value. As for the pressure, I tried to see how cross section varies and there is a slight hint of the right trend that it must have: when the pressure increases, the cross section also increases because it overflows more.



**Figure 4.10.** Graphics relating to 6H44-3PETTA-4%PI ink and image of the spiral.

Any other graphs are shown in **Fig. 4.1.A** in appendix.

Other suspended geometries were also tried with this ink. A free-form structure with suspended right angles was printed, which consists of vertical and horizontal sections, shown in **Fig. 4.11**.



**Figure 4.11.** Free form structure.

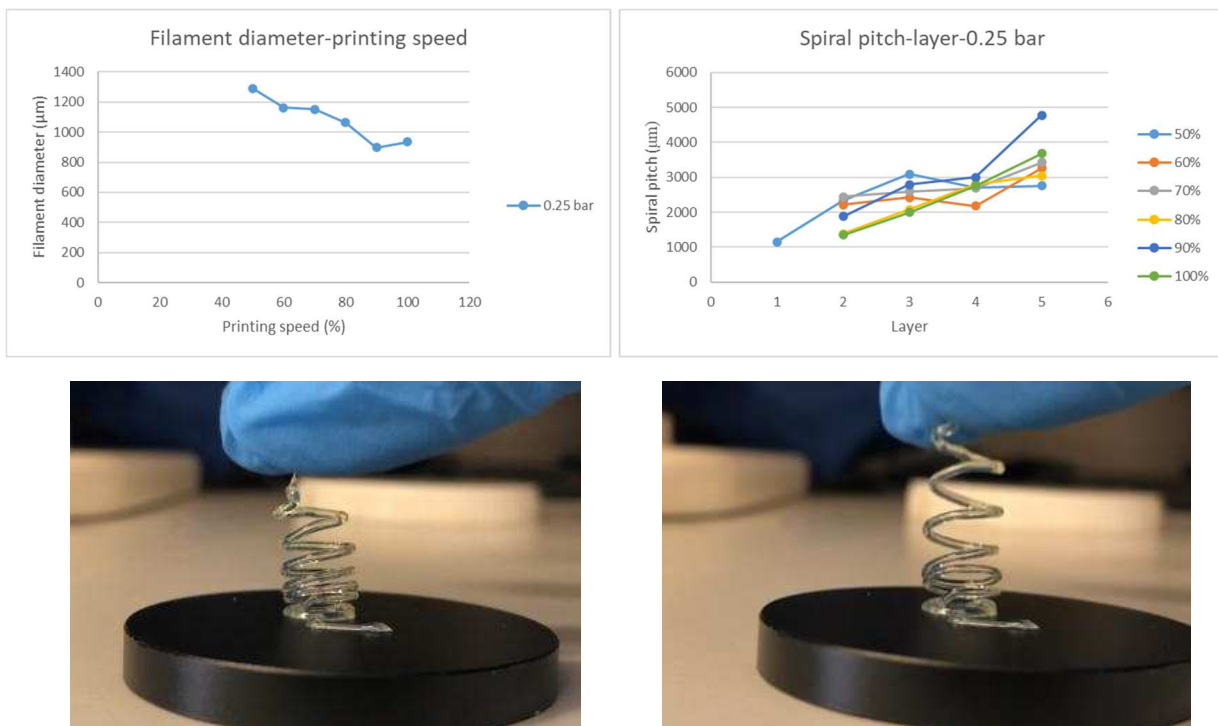
It keeps its shape well even if it is complex to adjust the printing speed so that the diameter of the filament is constant. In fact, there is an increase in the diameter of the filament between the various sections as you go up in the structure, if the printing speed is kept constant. This may be due to die swelling but also from the fact that the intensity of the UV light decreases over time, so the intensity of the radiation is lower and the material cures less and more slowly, making the wire assume a larger diameter than that of the nozzle. In addition, in the vertical sections, if the speed is too low, the filament tends to be unstable and give rise to micro spirals. To overcome the problem of non-constant diameter, it is possible to increase the speed progressively during printing. In particular, in the vertical sections the speed must be particularly high to avoid an excessive enlargement of the diameter of the wire as soon as it comes out of the nozzle, since the material that comes out is affected by the resistance of the one below just cured and therefore has a more tendency to be crushed and pushed on the edges with respect to a horizontal segment, where the output material does not meet the same resistance and is not forced to re-enter. By increasing the speed, a decrease in the diameter and its proximity to the size of the nozzle can be seen; however, an excessively high speed does not allow the ink to cure as soon as it comes out of the tip, so there are distortions, the right angles become blunt and the structure loses definition. The presence of bubbles inside the ink becomes extremely harmful because it interrupts the continuity of the filament. In the vertical sections a higher speed is required than in the horizontal ones and this can be achieved by modifying the Gcode, assigning different speeds to each segment. For these free form structures, the speed inside the Gcode is 100 mm/min and the percentage speed used in the printer ranged from a minimum of 100% up to 330% to obtain thin vertical structures. **Table 4.1.A** shows the values of the diameters of the various segments that make up the green samples of four free form structures measured with a digital caliper. Structures A, B and C were printed at constant speed but increasing it from A to C and in fact we can see how the diameter progressively increases within the same structure but decreases slightly from A to C; the structure D was printed by gradually increasing the speed manually and it can be seen instead how the diameter decreases.

These printing tests were performed with UV light of initial intensity of 70 mW.

The same analysis regarding the pressure and speed parameters was conducted on the 6H44-6TEGO-4%PI ink; however, the intensity of the light used was 23 mW because the power limiter had already been added to the UV setup. The ink is much more liquid; without applying pressure the quantity contained in the tip comes out in the form of drops and a perfect drop forms at rest. The spirals were printed at the very low pressure of 0.25 bar. The spirals began to form without the ink curing inside the nozzle at about 50% speed and by increasing the speed obviously the diameter of the filament



approached that of the nozzle, however, they are very soft. This is probably due to the low intensity of the UV light. The structures are however able to sustain themselves and have an acceptable shape fidelity. Up to 90% of speed they support each other, that is, it means that the material cures and stiffens sufficiently. At higher speeds the various arms collapse on each other, cancelling the step since they do not have sufficient strength to resist the weight of the others and are soft due to the fact that they do not have enough time to cure completely. Moreover the too high speed causes distortions of the underlying layers already soft in themselves which are dragged in a circular motion by the ink still attached to the nozzle. Raising the pressure was not possible. The results are shown in **Fig. 4.12**. At 70 mW surely the structures would be more rigid as the vertical and inclined ones printed for comparison.



**Figure 4.12.** Results relating to 6H44-6TEGO-4%PI ink.

#### 4.1.2.2 – Deflection

As regards the evaluation of the deflection of the inks and therefore the ability to print filament suspended between two structures, different methods have been adopted. Initially, the idea was to use a support capable of sliding, which would allow to print filaments of various lengths and then evaluate their self-supporting ability and shrinkage after pyrolysis. However, problems were encountered in the interaction between the filament and the support that did not allow us to continue on this path. Another idea was to print trapezoid structures in order to simulate the two supports and the filament supported by them: in the downward stretch, however, the UV setup collided with the horizontal filament, breaking it. The third approach was to print cantilever beam structures. They were printed with 6H44-3PETTA-4%PI ink and 6H44-2PETTA-4%PI ink was also tested. The structures show a length of 2 and 4 cm. Only the data relating to the ink 6H44-3PETTA-4%PI are reported. The deflection was measured on graph paper and the variation in diameter along the filament was then

measured by sectioning it in points more or less distant from the free end, structures in **Fig. 4.13**. From the measurement of the sections, you can see how the diameter increases as you get closer to the free end. This fact can be attributed to swelling and to the fact that the original intensity of 70 mW decreases over time. This trend appears to be greater for lower speeds. I tried to calculate the linear variation of the diameter and evaluate if the slope of these lines varied with increasing speed. You can in see in **Table 4.1** a general trend of decrease in the slope but there is a lot of instability.

6H44-3PETTA-4%PI	Printing speed (%)	Equation of the line
0.75 bar		
20 mm		
	30	$y = -33,776x + 769,93$
	40	$y = -35,638x + 787,81$
	50	$y = -7,3142x + 652,55$
	60	$y = -15,205x + 575,81$
	70	$y = -15,638x + 571,28$
	80	$y = -7,6052x + 497,09$
40 mm		
	30	$y = -27,548x + 855,23$
	40	$y = -34,695x + 824,96$
	50	$y = -22,913x + 751,71$
	60	$y = -11,338x + 588,05$
	70	$y = -6,0887x + 554,11$
	80	$y = -11,124x + 522,86$

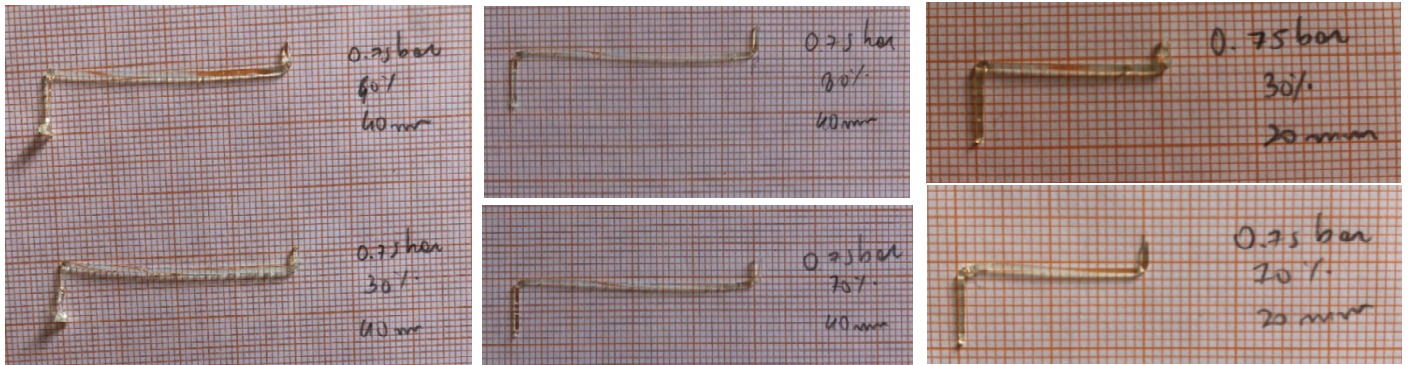
**Table 4.1.** Linear variation of the diameter along the cantilever beams.

For the measurement of the deflection, I measured the height difference of the tip of the filament with respect to the horizontal on graph paper and then I calculated the angle of deflection, reported in **Table 4.2**.

6H44-3PETTA-4%PI	Printing speed (%)	Deflection angle
0.75 bar		$\theta = \arctg(\Delta y/L)$
20 mm	30	5,71°
	40	5,71°
	50	4,29°
	60	1,43°
	70	5,71° but there was instability in the corner
	80	Broken and instability in the corner
40 mm		
	30	5,71°
	40	5°
	50	4,29°
	60	4,29°
	70	2,86°
	80	2,86°

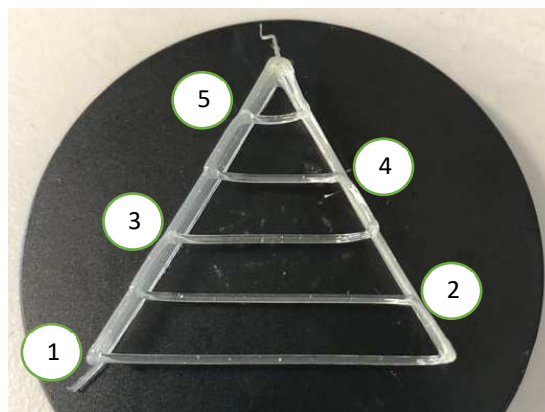
**Table 4.2.** Deflection angle.

There is a tendency for deflection to decrease as print speed increases.



**Figure 4.13.** Cantilever beam structures.

In the end, to really evaluate the deflection we used the test "A" described in §3.4 and represented in **Fig. 4.14**. It was carried out for the three inks 6H44-3PETTA-4% PI; 6H44-2PETTA-4% PI and 6H44-6TEGO-4% PI. The intensity of the UV light used was limited to 23 mW after the introduction of the cooling system. For the cross section an average value was evaluated on each filament while for the heights different values were taken along the same filament.



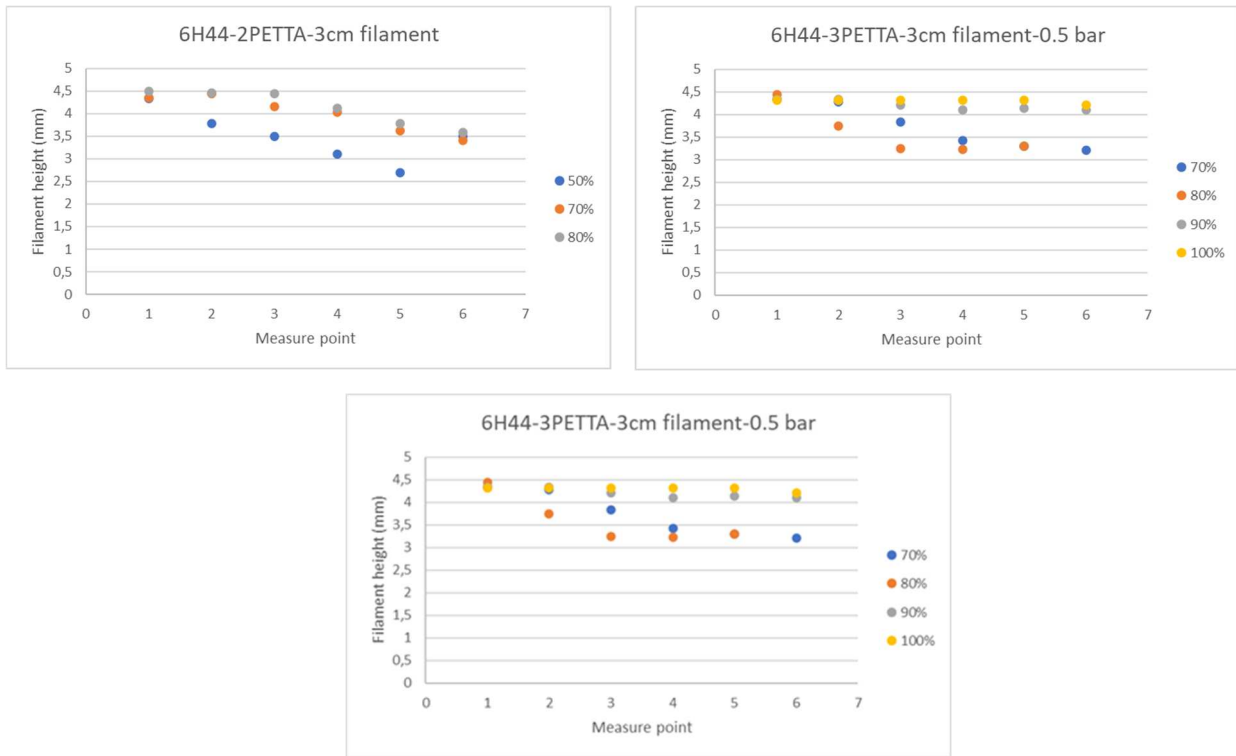
**Figure 4.14.** "A" test.

The 6H44-6TEGO-4% PI ink proved extremely difficult to print and was unable to produce suspended filaments between the two supports due to its low viscosity and softness. The filaments 3 cm long were completely lying on the substrate, the shorter filaments (2.3, 1.7, 1.1, 0.6 mm, from 2 to 5) also did not show self-supporting abilities. For the 6H44-2PETTA-4% ink, several samples were printed at a pressure of 1 bar with increasing printing speed, 50%, 70% and 80% to evaluate how it affected the ability to form suspended filaments. The pressure was kept constant, the speed was progressively increased and kept constant during the printing of the suspended filaments. From **Table 4.3** it can be seen how the average diameter decreases with increasing speed, as it was possible to expect from the analysis conducted on the spirals; the same happens for the other ink composition. For the 2PETTA ink at 1 bar and 80% speed and for the 3PETTA ink at 0.5 bar and 100% speed the diameter is close to that of the 0.58 mm nozzle. In **Fig. 4.15** you can evaluate the variation in height

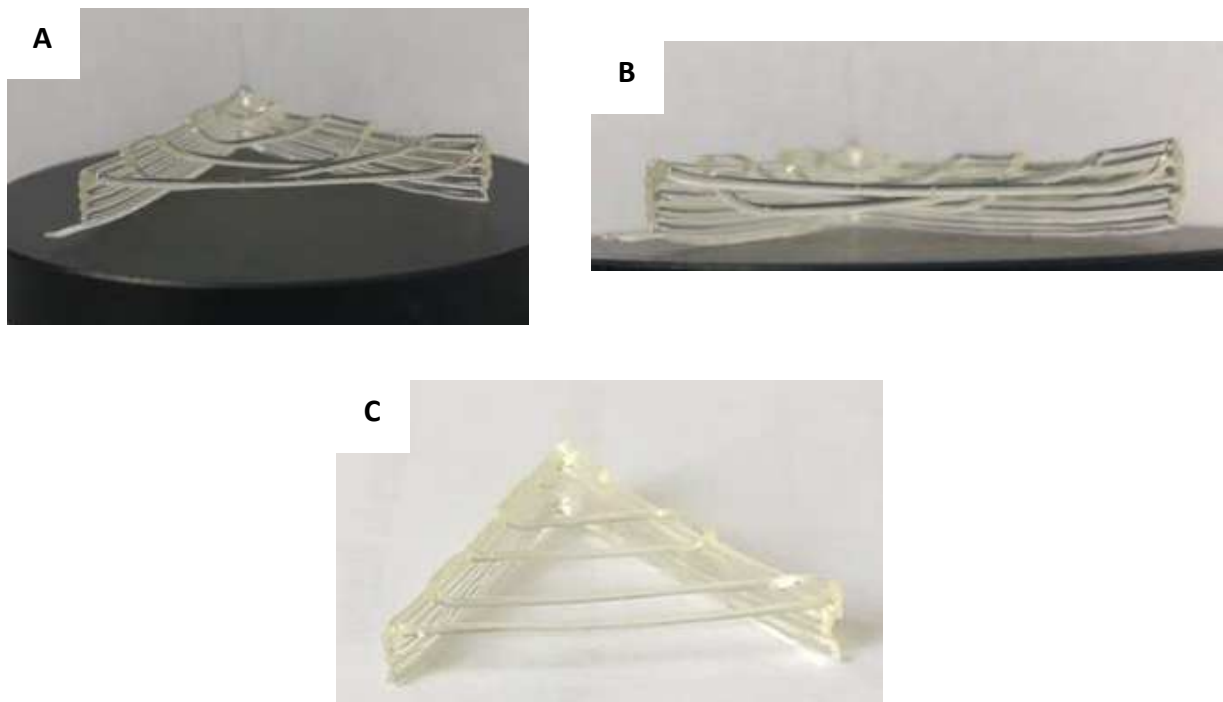
of the filament of 3 cm as you proceed from one extreme to the other. The measuring points are 6 to 3 cm, so they are 0.5 mm apart from each other. The initial heights are less than 5 mm of the Gcode file due to the printing of the two lateral supports that differs from that of the file. Point 1 corresponds to the initial extreme and point 6 just before the final extreme. The print direction is from left to right so you can see that there is a deflection of the filament. The deflection however decreases with the increase of the printing speed: for samples printed at 80% the filament remains constant for about 1.5 cm compared to those printed at 50% that begin to deflect immediately. The same trend occurs for the 6H44-3PETTA-4% ink. In particular, it can be observed that at the pressure of 0.5 bar the filaments are more linear than at higher pressures with the same printing speed. At a speed of 100%, (450 mm/min in Gcode) the height of the filament is almost the same along its entire length, an indication of good self-support skills. For the other speeds, the deflection trend is not linear but there is the formation of a belly, whose minimum is not central but is shifted towards the second extreme depending on the direction of printing; only in filament 5 the minimum is central. **Table 4.4** shows the minimum values reached and the variation with the initial height. The measurement points are relative to the length of the various filaments. The variation in height decreases as you move towards shorter filaments, although there is instability with respect to this trend, due to problems encountered during printing. However, it is logical to expect shorter filaments to be more linear and the inks show to be able to support themselves for distances around 0.5-1cm. **Fig. 4.2.A** shows a comparison between the filaments of different lengths. Filaments 2 and 4 have a print direction opposite to that of odd filaments. The measurement data were then turned in order to evaluate the deflection trend. As was expected, the shorter filaments turn out to be more linear and with less deflection. Of the two inks, the best in terms of self-support capacity is the 6H44-3PETTA-4% ink; has more photopolymer, cures faster and is able to print longer suspended filaments.

Ink	Pressure (bar)	Printing speed (%)	Average diameter ( $\mu\text{m}$ )	Standard deviation
6H44-2PETTA-4%	1	50	0.644	0.019596
		70	0.638	0.017205
		80	0.578	0.036
6H44-3PETTA-4%	0.75	80	0.68	0.016733
		90	0.674	0.020591
		100	0.634	0.018547
		110	0.618	0.023152
		70	0.68	0.025298
	0.5	80	0.652	0.023152
		90	0.624	0.016248
		100	0.592	0.014697

**Table 4.3.** Average filament cross-section.



**Figure 4.15.** Height variation at various measurement points for the longer filament for the ink 6H44-2PETTA.4% (top left) and 6H44-3PETTA-4% (top and right and bottom) at different printing speeds.



**Figure 4.16.** Images of the “A” test samples. Figures A and B represent the 6H44-2PETTA ink at 80% printing speed. The deflection of the filament can be seen. Figure C represents the 6H44-3PETTA ink at 0.5 bar 100%. It can be seen that the filaments, even the longest, appear straight.

Ink	Pressure (bar)	Printing speed	Filaments	$h_0$	$h_{min}$	$\Delta\%$	
6H44-2PETTA-4%	1	50%	1	4.34	2.69	38%	
			2	4.66	3.95	15%	
			3	4.55	3.82	16%	
			4	5.02	4.89	2.6%	
			5	5.3	4.29	19%	
		70%	1	4.36	3.40	22%	
			2	4.88	3.36	31%	
			3	5.2	3.86	26%	
			4	5.24	4.79	8.6%	
			5	5.31	5.15	3%	
		80%	1	4.49	3.58	20%	
			2	4.8	4.28	11%	
			3	4.74	4.22	10%	
			4	4.8	4.56	5%	
			5	4.98	4.72	5%	
	6H44-3PETTA-4%	0.75	80%	1	4.3	2.3	46%
				2	3.93	1.9	51%
				3	3.77	2.9	23%
				4	3.2	2.81	12%
				5	4.3	4.02	6,5%
		90%	1	4.27	2.3	46%	
			2	4.35	2.15	51%	
			3	4.2	2.5	40%	
			4	4.36	3.18	27%	
			5	5.16	3.96	23%	
		100%	1	4.02	2.81	30%	
			2	4.18	3.41	18%	
			3	4.4	3.22	27%	
			4	4.57	3.6	21%	
			5	5.08	4.1	19%	
		110%	1	4.63	4.12	11%	
			2	4.6	4.12	10%	
			3	5.26	4.42	16%	
			4	5.08	4.48	12%	
			5	5.47	5.38	1.6%	
0.5	70%	1	4.33	3.3	24%		
		2	4.27	2.45	43%		
		3	4.64	2.4	48%		
		4	4.42	3.71	16%		
		5	4.60	4.13	10%		
		80%	1	4.43	3.23	27%	
			2	4.38	3.7	16%	
			3	4.6	3.41	26%	
			4	4.55	3.98	13%	
			5	4.66	3.83	18%	
		90%	1	4.34	4.1	5.5%	
			2	4.43	3.89	12%	
			3	4.63	4.03	13%	
			4	4.5	3.96	12%	
			5	4.3	3.7	14%	
	100%	1	4.31	4.2	2.5%		

			2	4.3	4.2	2.3%
			3	4.31	4.17	3.2%
			4	4.3	4.22	1.9%
			5	4.36	4.36	0%

**Table 4.4.** Minimum height reached by the filament and percentage variation compared to the initial extreme.

#### 4.1.3 – Rheology<sup>23</sup>

A fluid subjected to an external load is affected by shear stresses and deforms irreversibly, while an elastic solid deforms reversibly (like a spring), thanks to the strength of the atomic bonds. The fluid opposes a resistance to sliding, a sort of internal friction between the adjacent layers of the same that requires the application of a force to maintain the flow, which is called viscosity. The Ostwald-de Waele power law describes the behaviour of a viscous material (general, even for non-Newtonian fluids):

$$\tau = K(\dot{\gamma})^n \quad \text{Eq. (4.I)}$$

where  $(\dot{\gamma})$  is the shear rate, K is the flow consistency index (Pa·s<sup>n</sup>) and n is the flow behaviour index. The apparent viscosity, described by the shear rate ratio, is defined:

$$\eta = K(\dot{\gamma})^{n-1} \quad \text{Eq. (4.II)}$$

so, by combining the two equations it results:

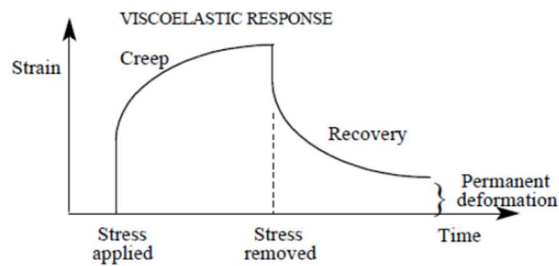
$$\tau = \eta(\dot{\gamma}) \quad \text{Eq. (4.III)}$$

Depending on the value of the n index, different behaviours can be distinguished, and viscous materials can be classified into Newtonian if n = 1, pseudoplastic if 0 < n < 1 and dilating if n > 1. In Newtonian fluids the viscosity remains constant as the shear rate varies, while in pseudoplastic materials the viscosity decreases as the shear rate increases, due to the alignment of the molecules or particles along the direction of motion with respect to the chaotic state at rest. The dilating fluids, on the other hand, exhibit a behaviour contrary to shear-thinning since their viscosity increases as the shear rate increases. For some fluids, it is necessary to apply a certain yield stress so that they begin to flow: if they exhibit a linear behaviour they are called Bingham plastics, while if the behaviour is non-linear plastic they are called Herschel-Buckley and the mathematical model which describes their behaviour is:

$$\tau = \tau_0 + K\dot{\gamma}^n \quad \text{Eq. (4.IV)}$$

In addition to depending on the shear rate, for some types of fluid the viscosity is a function of time and further classification can take place in Newtonian, thixotropic and rheopectic. For Newtonian fluids it is as independent of time as it was of shear rate. Thixotropic fluids show a decrease in viscosity over time when a constant shear stress is applied due to the destruction of interactions, instead rheopectic fluids show an increase in viscosity over time associated to shear-induced microstructural consolidation of the material. Many non-Newtonian fluids exhibit viscoelastic

behaviour, i.e., a combination of elastic (solid like) and viscous (fluid like) behaviour, like in **Fig. 4.17**.



**Figure 4.17.** Viscoelastic behaviour.

When constant stress is applied, they undergo instantaneous deformation as a result of the stretching of the inter- and intra-atomic bonds, but a delayed viscous component can also be noted which represents the sliding of the molecules; when the stress is removed they undergo an instant recovery of the elastic part and a progressive recovery over time of the viscous part up to a state of equilibrium, which can be a total recovery of the deformation or the maintenance of a certain amount of permanent deformation. Viscoelasticity is studied by applying a sinusoidal deformation or stress. In a perfectly elastic solid, the stress and strain are in phase, while for a viscous material they are ninety degrees out of phase. The viscoelastic behaviour arises in the middle, with a phase shift between stress and deformation  $\delta$  between 0 and 90°. The overall modulus  $G^*$  calculated through an oscillating test as the relationship between stress and strain, represents the resistance of the material to deform. It consists of two contributions, the storage modulus  $G'$  and the loss modulus  $G''$ . The storage modulus  $G'$  (Pa) represents the elastic portion of the viscoelastic behaviour, which describes the solid-state behaviour of the sample. The loss modulus  $G''$  (Pa) characterizes the viscous portion of the viscoelastic behaviour, which can be seen as the liquid-state behaviour of the sample. Viscous behaviour arises from the internal friction between the components in a flowing fluid. This friction is related to the development of heat in the sample and, consequently, to the transformation of the deformation energy into thermal energy, which is absorbed by the sample and is dissipated, becoming no longer available for further deformation of the material. So  $G''$  represents the loss of energy. On the contrary, the elastic behaviour is related to the stored energy in a deformed material: when the load is released, the stored energy becomes the force that brings the material back to its original condition. So  $G'$  represent the amount of energy garnered in the material. When  $G'$  is larger than  $G''$  the material has a solid-like behaviour, whereas when  $G''$  is larger than  $G'$  the material has a liquid-like behaviour, which means that it flows. The  $G''/G'$  ratio is the loss tangent or  $\tan(\delta)$  and gives information on the balance between the viscous and elastic components.

#### *Flow curve*

The shear rate dependence of viscosity can be determined by performing a flow sweep, a rotational test that applies an increasing shear rate and measures the evolution of viscosity. For optimal measurement it is good to start from low shear rates and then increase until you reach the shear rate experienced by the ceramic paste while being extruded through the nozzle of the 3D printer. By fitting the curve obtained with the Oswald-de Waele Power Law Model it is possible to calculate the value of  $n$  and  $K$ . The results reveal the shear-thinning behaviour or not of the material. For ceramic inks used with the DIW technique a shear-thinning behaviour is desirable. Once the  $n$  index is known, the Rabinowitch expression allows to estimate the shear rate for a non-Newtonian fluid starting from the Newtonian one.



### *Amplitude sweep test*

Viscoelasticity is usually characterized by means of oscillatory tests, in particular the amplitude sweep test. This test applies an increasing strain at constant frequency, which implies an increasing shear rate, and measures the evolution of the storage and loss modules. In a typical graph, three regions can be distinguished. In the first region on the left, known as the linear viscoelastic region (LVR), the modulus  $G'$  remains constant and is greater than the modulus  $G''$  and its value coincides to the elastic modulus of a solid material, known as  $G'_{eq}$ . The value of the shear stress at the limit of the LVR is the yield stress ( $\tau_y$ ) and the point is defined as the yield point, from which the module  $G'$  begins to decrease due to the irreversible deformation of the internal structure. In the second region,  $G'$  is even greater than  $G''$  but the yield stress has been overcome, which points to a solid-like behaviour with irreversible deformation. When  $G''$  equals  $G'$ , the flow point is reached which represents the transition from solid-like to liquid-like behaviour, which is reached at the flow stress  $\tau_f$ . In the third region after this point we have  $G' < G''$ , which implies the flow of the material due to a progressive breakage and ordering of the internal structure. For inks in which ceramic particles are present, their introduction considerably increases the  $G'_{eq}$  modulus, the yield stress and the flow stress, in relation to their amount, and shift of the yield point to smaller shear strains. The flow strain is less affected by the ceramic fraction, tending to decrease with increasing ceramic content, whereas is more sensitive to the polymer concentration, increasing with the amount of polymer. The amplitude sweep test can be conducted in both strain and stress control<sup>23</sup>. It provides crucial information to assess the printability of ceramic pastes: the elastic modulus at rest ( $G'_{eq}$ ), the yield stress, when the material starts to deform plastically ( $\tau_y$ ) and the flow stress, when the material starts to flow ( $\tau_f$ ). For the DIW technique it is advisable to find the right balance between an ink that has a high elastic modulus and yield stress so that the printed structure maintains its shape and does not collapse, but at the same time it is necessary to have a low flow stress to reduce the force of extrusion required.

### *Three interval thixotropy test*

During the extrusion process, the ink undergoes different types of flow: initially it flows slowly inside the syringe, then it undergoes a rapid acceleration inside the nozzle where high shear rates are reached and finally it goes out to the nozzle and the effort drops suddenly to zero<sup>123</sup>. To obtain a good shape fidelity in self-supporting 3D-structures it is important that the ink has a rapid transition kinetics from fluid-like flow to solid-like behaviour and that it restores its elastic behaviour immediately after being extruded as a filament. The rheological test that provides this information is the three interval thixotropy test (3ITT), which can be performed either in rotational or oscillatory modes. This test involves the application of three consecutive steps with different shear rates: a very small shear rate, within the LVR of the amplitude sweep, that simulates the rest state of the ink while advancing slowly through the 3D printing cartridge; (2) a very high shear rate, above the flow point and as close as possible to  $\dot{\gamma}_{max}$ , that mimics the extrusion process through the small nozzle; and (3) a very small shear rate again that simulates the rest state of the ink after being deposited. The goal is to assess whether the ink recover the solid-like behaviour quickly enough to maintain the extruded shape and whether the restored module is high enough to ensure a good printing fidelity and the self-supporting capacity of the printed structure and in the second section it is assessed whether the ink has time-dependent characteristics which ensure that the printing parameters must be continuously adjusted.

### *Rheological properties as printability predictors*

Some rheological properties can be considered as key predictors of printability aspects: the first group is linked to the extrudability of an ink and is composed by the flow stress ( $\tau_f$ ), the minimum shear stress to make the ink flow, related to the necessary pressure to extrude the material, and the flow behaviour index ( $n$ ), correlated to the Newtonian properties or not of the fluid. Desirable is shear-thinning behaviour that requires less pressure. The second group is related to shape fidelity and includes the storage modulus at rest ( $G'_{eq}$ ), the damping factor ( $G''/G'$ ), which allows to evaluate the behaviour of the ink at rest (either elastic ( $G''/G' < 1$ ) or viscous ( $G''/G' > 1$ )) and the yield stress ( $\tau_y$ ). The characterization of the thixotropy of the inks is also a relevant aspect that gives information on shape fidelity<sup>125</sup>.

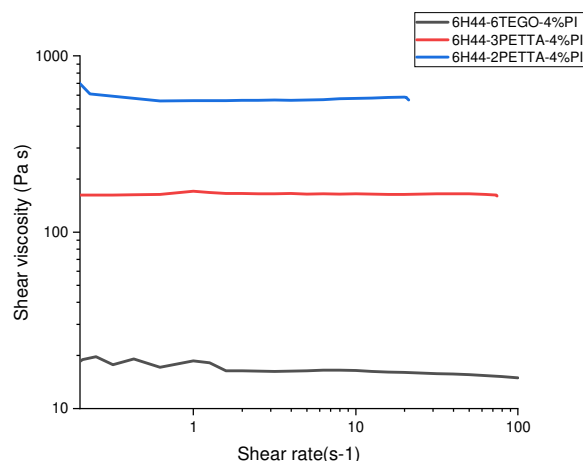
### *Photo-rheology*

To investigate the effects of UV light intensity on the changing of viscosity during curing process, several light intensities were selected to identify the differences in curing<sup>126</sup>. The inks were cured under different light intensities to understand the effect on the curing process. Because the different amounts of free radicals released in the resin<sup>126</sup> under the different light intensities, this last affect the curing rate. Although the final viscosity range is in the same magnitude, the time to reach this viscosity varies with intensities. Furthermore, the initiation time, which defines as the time from the beginning of UV light initiation to the start of viscosity increasing, also shows difference. With the increase of the light intensity, the initiation time decreases correspondly with the light intensity.

## **Results**

### *4.1.3.1 – Flow curve*

Viscosity was evaluated through a rotational test that applies an increasing shear rate and measures the evolution of viscosity. The range of shear used was 0.1-100  $s^{-1}$ . The curves show great instability in the first part, at low shear rates. The curves relating to the three inks are shown in **Fig. 4.18**. It can be noted that the 6H44-2PETTA-4%PI ink has the highest viscosity, about 570 Pa·s, while the one containing TEGO has a viscosity of an order of magnitude lower, around 17 Pa·s at low shear rate. This is due to the different quantity of polymer present in the mixture which, being a liquid component, tends to lower its viscosity: the first ink has a quantity of photopolymer equal to about 25% by weight with respect to the total while the other ink has a quantity of 50%; the 6H44-3PETTA-4%PI ink has an intermediate behaviour (viscosity of 160 Pa·s) between the two, presenting a photopolymer content of about 30% by weight. The greater the quantity of photopolymer in the mixture, the lower the viscosity and therefore the pressure required during extrusion. This is confirmed by the printing tests that require a very low extrusion pressure for the ink containing TEGO, about 0.25 bar, while they require pressures higher than 1 bar for the ink with 2 g of PETTA.



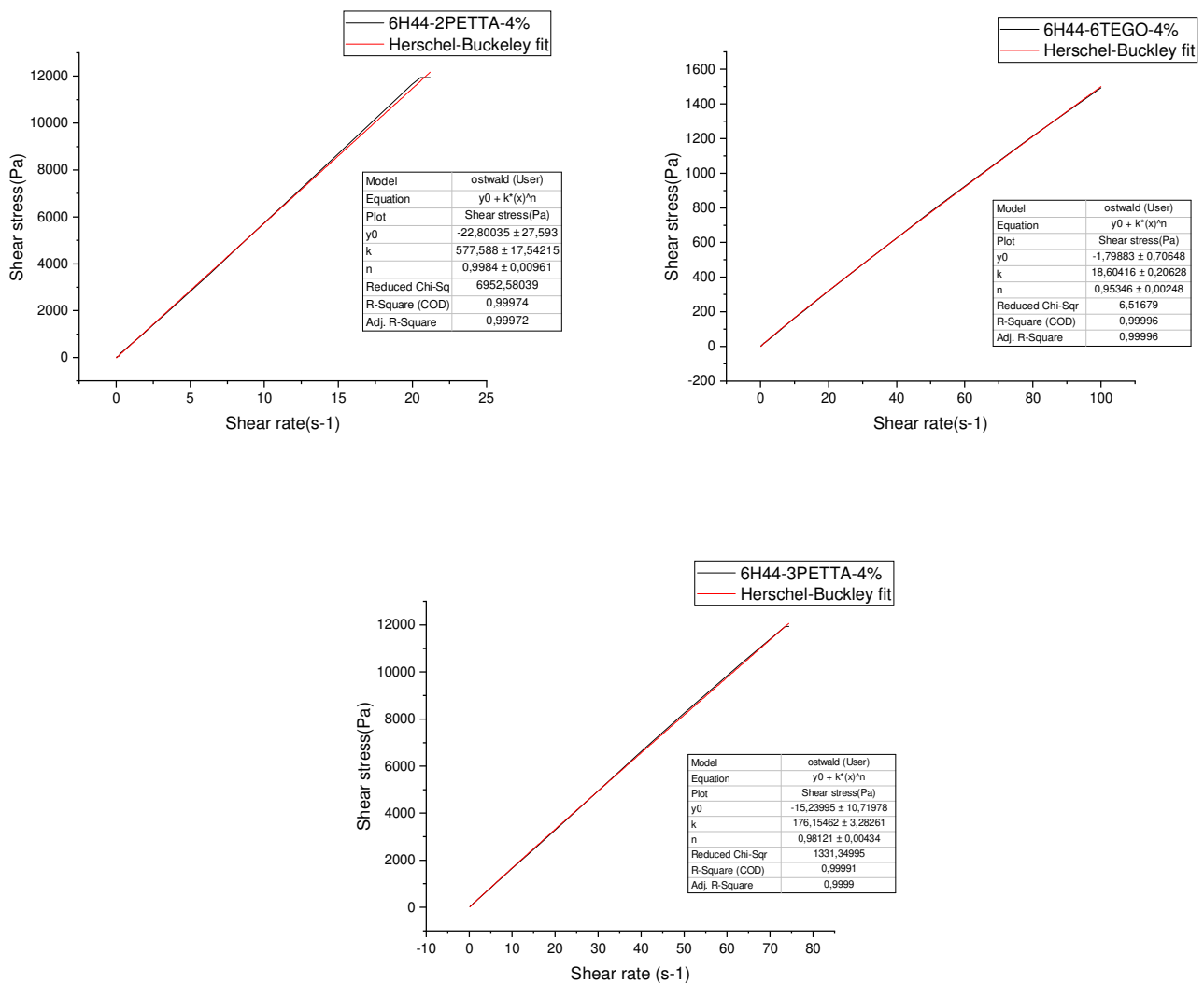
**Figure 4.18.** Viscosity profiles.

To evaluate if the inks had Newtonian behaviour the viscosity curves were fitted using the power law model, which is given by Eq. (4.II). The term  $n$  is the power law index, defines the viscosity behaviour: (i) shear-thickening if  $n > 1$ , (ii) Newtonian if  $n = 1$  or (iii) shear-thinning if  $n < 1$ . The curve of  $\ln\eta - \ln\dot{\gamma}$  was plotted based on the ink viscosity curves. By fitting the slope and intercept, the consistency index  $K$  and the power law index  $n$  of the inks were obtained, respectively. The values obtained are shown in **Table 4.5**.

	$n$	$K$ (Pa·s <sup><math>n</math></sup> )
6H44-6TEGO-4%PI	0.97	17.25
6H44-3PETTA-4%PI	0.99	165.0
6H44-2PETTA-4%PI	1.01	532.4

**Table 4.5.** Values of  $n$  and  $K$  obtained from the viscosity curves.

The inks have values of  $n$  close to 1: they therefore have a practically Newtonian behaviour, as can be seen from **Fig. 4.18**, in which no variations in viscosity are observed as a function of shear rate. The larger the deviation of  $n$  from 1, the more non-Newtonian is the behaviour of the fluid; in our case they do not show particular shear-thinning properties usually desired for the inks used in the DIW technique. The one that has minor  $n$  and therefore a more shear thinning behaviour is the ink containing TEGO: in it, in fact, the polymer content is higher and being it a viscoelastic material, it is correct to think that its large quantity in the mixture can play a preponderant role in determining the rheological properties. The **Fig. 4.19** shows the stress rate vs shear rate graphs. They were fitted with the Herschel-Buckley equation to evaluate the two parameters  $K$  and  $n$  using a different method and to understand if the inks developed in this work can be fit with a yield pseudo-plastic model. The data relating to  $n$  and  $K$  agree with those calculated through the viscosity curves. Furthermore, the inks do not seem to have a yield stress to overcome to make the macromolecules flow. This feature was also investigated through the Amplitude sweep test.



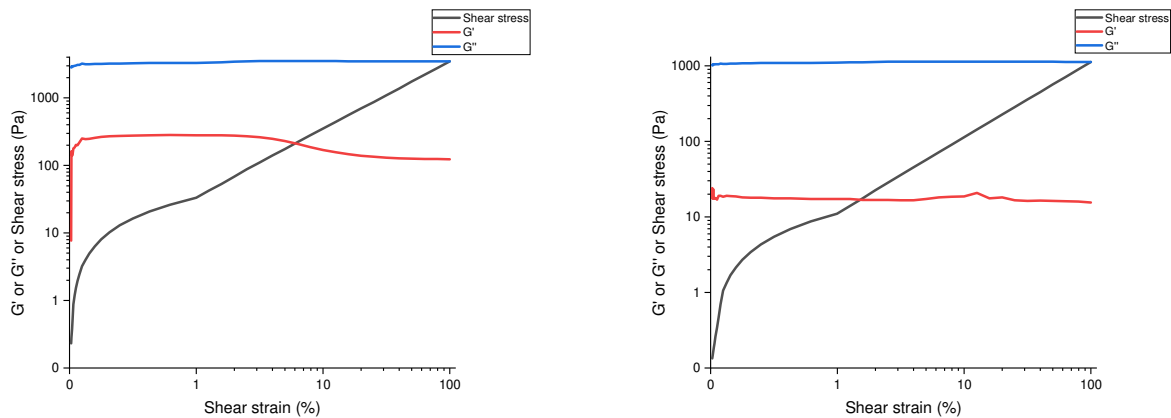
**Figure 4.19.** Shear stress versus shear rate where the red lines are the Herschel-Buckley fits.

#### 4.1.3.2 – Amplitude sweep test

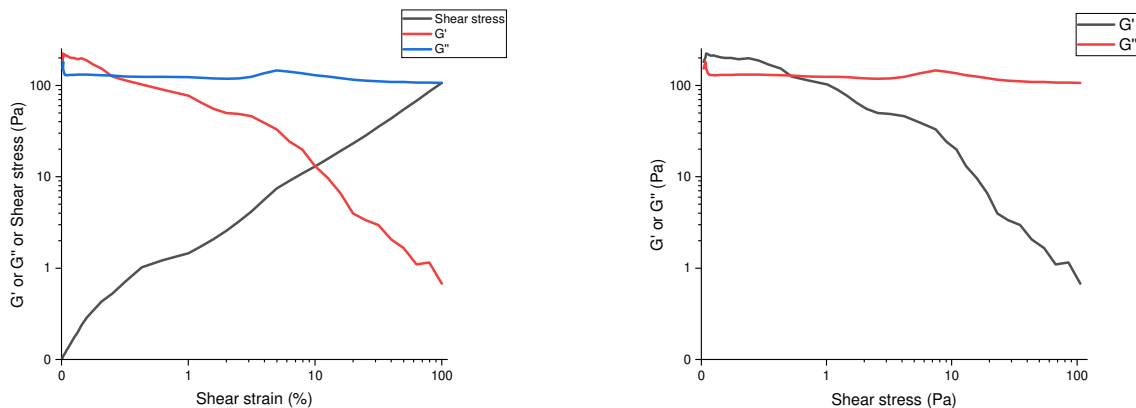
It was carried out to study the viscoelasticity of the three inks. Viscoelasticity is the property of some materials to undergo elastic deformations associated with viscous deformations and is typical of polymeric materials, in fact they consist of long chains randomly distributed in the absence of applied stress, which are then able to align themselves in the presence of stress. For amplitude sweeps, the deformation of the measuring system is increased stepwise from one measuring point to the next while keeping the frequency at a constant value. The measuring results of amplitude sweeps are usually presented as a diagram with strain (or shear stress) plotted on the x-axis and storage modulus  $G'$  and loss modulus  $G''$  plotted on the y-axis. The limit of the linear viscoelastic region is first determined. The curve relative to  $G'$  is used, which in this region is constant: storage modulus is considered not strain-dependent for variation up  $\pm 5\%$  (according to the standards ISO 6721-10 and EN/DIN EN 14770) or  $\pm 10\%$  (according to ASTM D7175 and DIN 51810-2). In this region if  $G' > G''$ , then the sample shows a gel-like or solid structure and can be termed a viscoelastic solid material.

However, if  $G'' > G'$ , the sample displays a fluid structure and can be termed a fluid. Subsequently, having exceeded the yield point, term of the LVR,  $G'$  starts decreasing, which is associated to the beginning of the break-down of the internal structure, leading to irreversible deformation. The elastic behaviour still dominates over the viscous ( $G' > G''$ ) until the flow point is reached and represents the transition from solid-like to liquid-like behaviour.

For the three inks developed in this thesis the results are shown in **Fig. 4.20.a,b**. The two inks containing PETTA do not show viscoelastic behaviour: the  $G''$  module is always greater than  $G'$  so they are associated with fluid behaviour. The ink containing TEGO, on the other hand, shows a low shear rate region in which  $G'$  is higher. In this region the shear stress increases linearly with the shear rate, which is associated to a solid-like behaviour with mainly elastic deformation. If we use the ASTM D7175 and DIN 51810-2 standard for the evaluation of the end of the LVR region, it occurs at approximately 0.079% shear strain and at a stress of 0.189 Pa. This value would represent the value of the yield stress necessary to make the ink flow. It is so low that the ink should be considered free of yield behaviour, in accordance with what was previously reported. The flow point, at which  $G' = G''$ , represents the transition from solid-like to liquid-like behaviour and from the graph in **Fig. 4.20.b**, a value of 0.72 Pa can be obtained. The value is low so in reality even the 6H44-6TEGO-4%PI ink does not have a strong viscoelastic behaviour but is fluid.



**Figure 4.20.a.** Amplitude sweep test at a frequency of 1 Hz of 6H44-2PETTA-4% (left) and 6H44-3PETTA-4% (right).

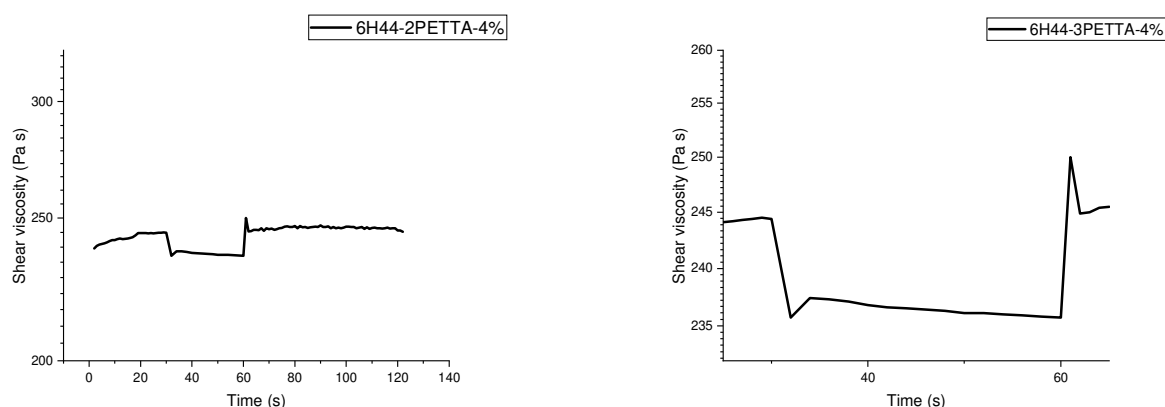


**Figure 4.20.b.** Amplitude sweep test at a frequency of 1 Hz of 6H44-6TEGO-4%.

In conclusion, therefore, the three inks appear as Newtonian fluids, do not have an evident shear thinning behaviour, do not exhibit yield stress and do not have a marked viscoelastic nature. The sample shows  $G'' > G'$  in the LVE region, and therefore the character of a fluid, cannot have a flow point because it is always liquid. The three inks do not have by themselves a sufficient module for the creation of structures that maintain their shape, but thanks to the use of UV light it increases in magnitude thanks to the formation of a polymeric network that allows the creation of free-form structures.

#### 4.1.3.3 – Three interval thixotropy test

The idea was to perform the test in two conditions: those of a printing process without UV light present after extrusion and those instead in the presence of UV light, with the UV light turned on in the third phase for different time intervals, respectively 1 and 5 s. The tests were difficult to perform, the data extremely scattered and inconsistent. As was logical to expect given the previous evaluations on the rheological properties, there is no significant variation in viscosity in the three shear rate intervals and therefore we cannot speak of a more or less immediate recovery of the initial viscosity after the second stretch. In the second section, at high shear rates, it is possible to evaluate if the ink shows a time-dependent behaviour (thixotropic and rheopectic effects), which would complicate the extrusion process, since the printing parameters, such as printing speed, would need to be continuously adjusted to preserve a constant flow of the material. In **Fig. 4.21** it can be seen how the 6H44-3PETTA-4%PI ink hints at a tendency to be thixotropic.



**Figure 4.21.** 3ITT chart for the two PETTA-containing inks. In the left image you can see how the viscosity does not significantly decrease with the sudden change of the shear rate and how in the third section it recovers the initial value. The graph on the right represents the second section of the test conducted for the 6H44-3PETTA-4% ink in which a decrease in viscosity is recorded with the passage of time.

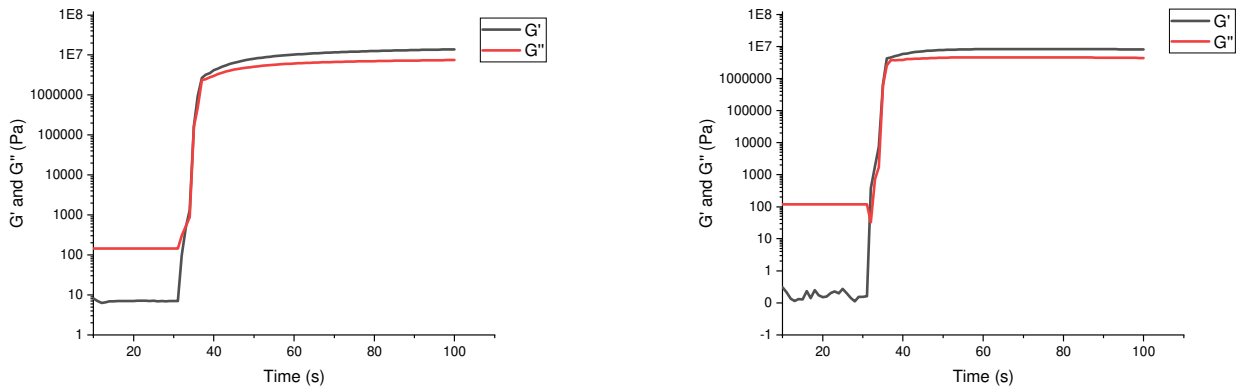
The tests conducted with the power on of UV light show an increase in viscosity obviously due to the formation of the solid polymeric network, which allows the formation of a rigid cured part with very rapid shape retention, thus validating the freeform ability of the hybrid technique. Although the light remains on for 1 s there is an increase in viscosity up to  $10^3$  Pa·s and with increasing irradiation time (5s), the viscosity further increases reaching  $10^5$ - $10^6$  Pa s. During the printing process, the deposited filament remains subject to UV irradiation as the print progresses, therefore additional curing can be assumed. The properties of photorheology will be covered in the following section.

#### 4.1.4 – Photorheology and UV response

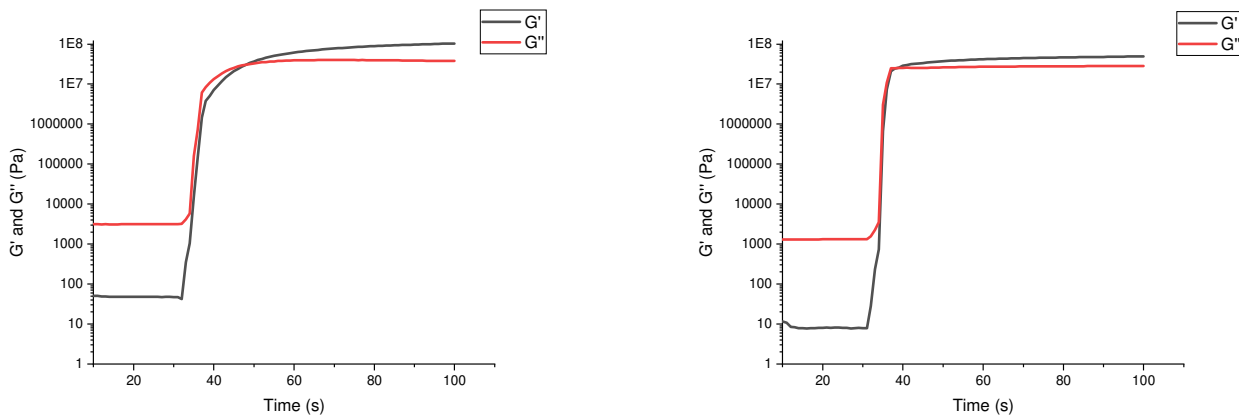
##### 4.1.4.1 – Photorheology

The effect of cure on rheology was studied under oscillatory shear as the material was exposed to UV-light. Initially it can be seen as  $G'' > G'$  for all inks. 30 s from the start of the test, the UV light is turned on. After a certain time from switching on, a time that decreases as the intensity of the UV light increases, there is a rapid and significant increase in the values of both modules and the transition to  $G' > G''$  indicating a liquid-like to solid-like transition<sup>127</sup>. After the intersection point, it is proved that the ink has the ability to maintain its shape in this state<sup>54</sup>. Fast gelation was crucial to solidify the printed lines in place after ink deposition. In addition, a high gel state modulus guaranteed shape retention of the deposited lines and allowed for printing of self-supporting structures. After activating the UV light, there is a rapid simultaneous increase in the magnitude of the shear modules for all three inks. The increase rate of the storage energy modulus is greater than that of the loss modulus, and the intersection point of samples varies according to the intensity of the UV light. The lowest UV light intensity used was 4-5% as it was similar to the initial printing conditions we printed the spirals, around 73 mW. Then the intensity was progressively increased up to a maximum of 20% to evaluate its influence on the gelation point. The **Fig. 4.22.a,b,c** shows the results for the three inks registered at the minimum and maximum intensity tested. The peaks in the initial section of some curves are due to instability during the measurement and to calculate the values reached by the modules, an average was made between all the curves, not just those represented. It is observed how the shear modules rapidly rose in magnitude from  $10^1$ - $10^2$  Pa to  $10^7$ - $10^8$  Pa, starting a few seconds after the UV lamp is turned on. In fact, none of the three inks show an instantaneous change, no gelation time is less than 1-2 s, despite this, the increase in the storage modulus in the first seconds is sufficient to guarantee the maintenance of the shape of the pieces and their self-support abilities and in the case of scaffolds, to ensure that one layer is able to support those above. The fastest to cure is the composition ink 6H44-6TEGO-4%PI, which shows a gelation point of 5 s after switching on the UV lamp even at an intensity of 5%. It is the fastest of the three inks to reach the gelation point and the intensity of the UV light does not seem to affect the achievement of the intersection point or the value of the modules at the end of the test. Inks that reach this point more rapidly would be advantageous in that faster deposition rates could be used. The  $G'$  module reaches a value of about  $1.4 \cdot 10^7$  Pa. The other two inks containing the PETTA photopolymer instead, show a longer time to reach the gelation point, about 15 s due to the lower intensity of UV radiation, which is reduced to about 8 seconds as the intensity increases. For these two inks the  $G'$  modulus reaches the value of about  $6 \cdot 10^7$  Pa for the ink containing 2 g of PETTA and  $1.3 \cdot 10^8$  Pa for that with the H44:PETTA ratio equal to 2:1. This may justify the fact that the samples printed with 6H44-6TEGO-4%PI ink remain softer than the others: the material is able to cure quickly but reaches lower elastic modulus values so that the structures are more deformable. The **Fig. 4.23** shows the variation of the gel point as a function of the intensity of the UV light, and the values are shown in **Table 4.6**. The 6H44-6TEGO-4%PI ink does not show a variation, the line is practically constant, a factor that implies rapid curing even at low UV intensities. The 6H44-3PETTA-4%PI ink shows a rapid decrease in gelation time going from 4% to 6% intensity while then the trend slows down and approaches 8 seconds; a further increase in UV intensity therefore would not favour a faster curing. The 6H44-2PETTA-4%PI ink is the slowest of the three to reach the gelation point, at each intensity its point in the graph is above that of the other two inks; it shows a constant, almost linear, decrease in time. The difference in the gelation time of

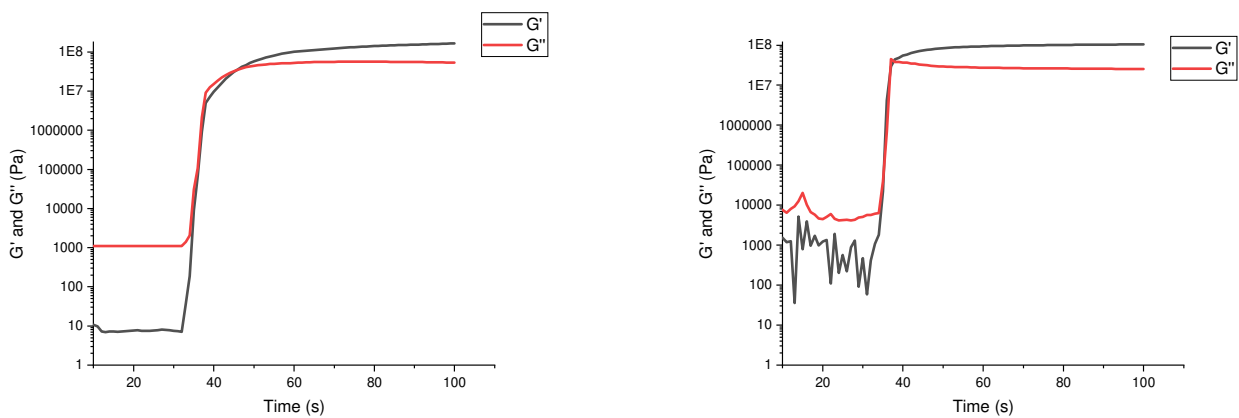
the three inks derives from the different content of photopolymer present and the relative quantity of photoinitiator: the higher the content, the faster the gelation time. However, an excessive photopolymer content could compromise the stiffness of the piece leading to lower shear modules values. The intensity of the light, on the other hand, does not seem to affect the value reached by the modules.



**Figure 4.22.a.** Reaching the gelation point for the 6H44-6TEGO-4%PI ink at 5% UV intensity (left) and 20% (right).

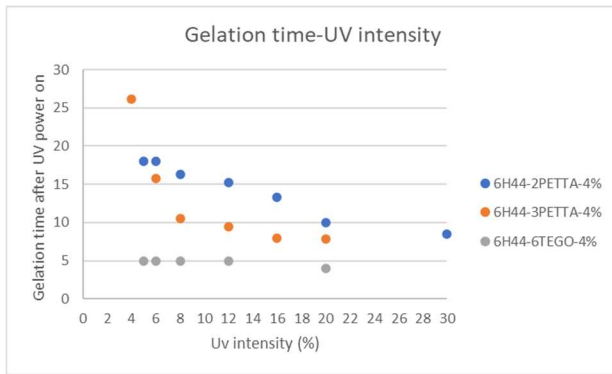


**Figure 4.22.b.** Reaching the gelation point for the 6H44-2PETTA-4%PI ink at 5% UV intensity (left) and 30% (right).



**Figure 4.22.c.** Reaching the gelation point for the 6H44-3PETTA-4%PI ink at 4% UV intensity (left) and 20% (right).

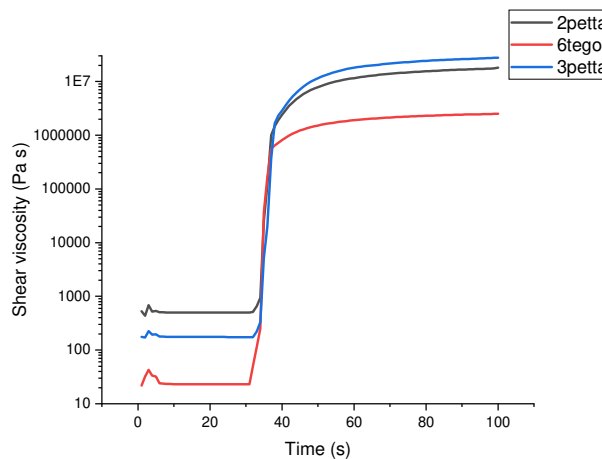




UV intensity (%)	Time to reach gelation point (s)		
	6H44-2PETTA-4%	6H44-3PETTA-4%	6H44-6TEGO-4%
4		26,2	
5	18		5
6	18	15,8	5
8	16,3	10,5	5
12	15,2	9,5	5
16	13,3	8	
20	10	7,8	4
30	8,5		

**Figure 4.23.** Variation of the gel point according to the intensity of the UV light. **Table 4.6.** Numerical values.

**Fig. 4.24** shows how viscosity varies as a function of time for a UV intensity equal to 73 mW. When the UV light is turned on 30 s from the start of the test, there is a sharp increase in its value, about 5 orders of magnitude. This means that even if the reaching of the gelation point takes more than a few seconds, the viscosity instead increases immediately as well as the modules and therefore the material is able to maintain the shape during the printing process. Before switching on, the 6H44-2PETTA-4% ink shows the higher viscosity (524 Pa·s) and the 6H44-6TEGO-4% ink the lower viscosity (22 Pa·s) as confirmed by the need for respectively higher printing pressures for the first mixture. After switching on the UV light, the viscosity reached by inks containing PETTA is higher ( $\approx 2 \cdot 10^7$  Pa·s versus  $2 \cdot 10^6$  Pa·s for TEGO), which, together with the higher modulus value, explains the greater stiffness compared to TEGO samples.

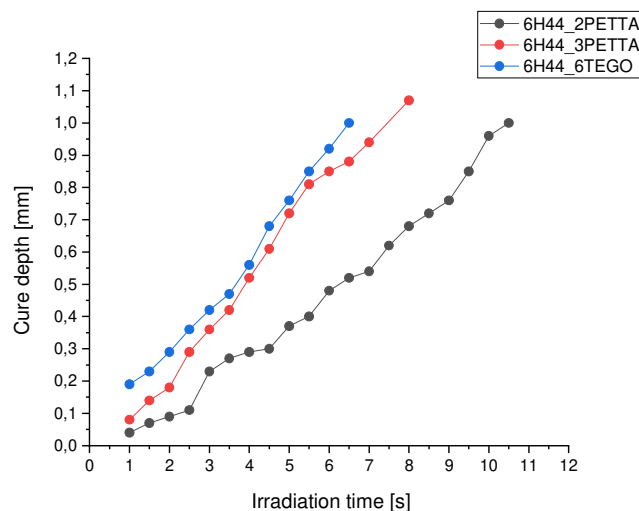


**Figure 4.24.** Variation of viscosity as a function of time.

#### 4.1.4.2 – Determination of cure depth

UV-curing during extrusion resulted in a core-shell structure in the printed filament cross-section where the shell is located at the surface exposed to UV light and the core is the internal material which would have little UV-exposure<sup>127</sup>. The cure depth is the penetration depth of the UV-light for a certain exposure time at a constant irradiance. To measure the cure depth, a series of ink drops were deposited individually on a plastic film and then exposed to UV light of constant intensity equal to that used during printing, for different exposure times. Cure depth was determined by removing uncured ink

after exposure with isopropyl alcohol and measuring the thickness of the solid material remaining. The exposure time required to reach one millimeter of cured material thickness was evaluated. The Omnicure UV lamp series 2000, was used, inserted in the rheometer for which the plate glass was used to deposit the drop of ink. The drops were not directly deposited on the glass plate as it would have been difficult to remove the thin layer of cured material to measure its thickness, but on a plastic film made to adhere perfectly to the glass plate thanks to ethanol: in this way to measure the thickness of the cured material it was enough to remove the polymeric film and with a digital caliper measure the thickness of the portion of the cured drop. If the thickness was not sufficiently consistent to be detached from the film and measured by itself, the measurement was made directly on the plastic film by subtracting the thickness of the latter, 0.05 mm, from the obtained value. The UV lamp was suitably placed at such a distance from the glass plate so that the intensity of light absorbed by the drop was the same for all three ink formulations, near 23 mW (1%). To be sure of this, the intensity of the UV light in the center of the glass plate was measured with the sensor (*Thorlabs, PM400 Optical Power Meter*) both in the presence and absence of the plastic film. The two values differ slightly: in the presence of the plastic film adhered thanks to ethanol, the intensity value is slightly lower for the same distance from the lamp, probably due to absorption or scatter effects due to ethanol and the film. The values used are therefore those in the presence of the film since they are the real perceived by the drop. The measurements were conducted at 1% lamp intensity which corresponds to about 23.90 mW, a condition similar to that of printing. **Table 4.2.A** shows the values of cure depth as a function of exposure time to UV light.



**Figure 4.25.** Curing depth of the three inks as a function of exposure time.

From the graph in **Fig. 4.25** it can be seen how the 6H44-6TEGO-4% ink has a higher curing rate probably thanks to the high content of photopolymer and photoinitiator and how after a second of exposure it has reached a thickness of cured material more than twice that achieved by the other two inks. The slowest ink to cure is 6H44-2PETTA-4% due to the fact that it contains the least amount of photopolymer and photoinitiator: to reach 1 mm of drop curing thickness it needs an exposure time of 11.5 s, greater than that required by the 6H44-3PETTA-4% ink to reach the same thickness (about 8 s) and almost double that required by the 6H44-6TEGO-4% ink (7s).

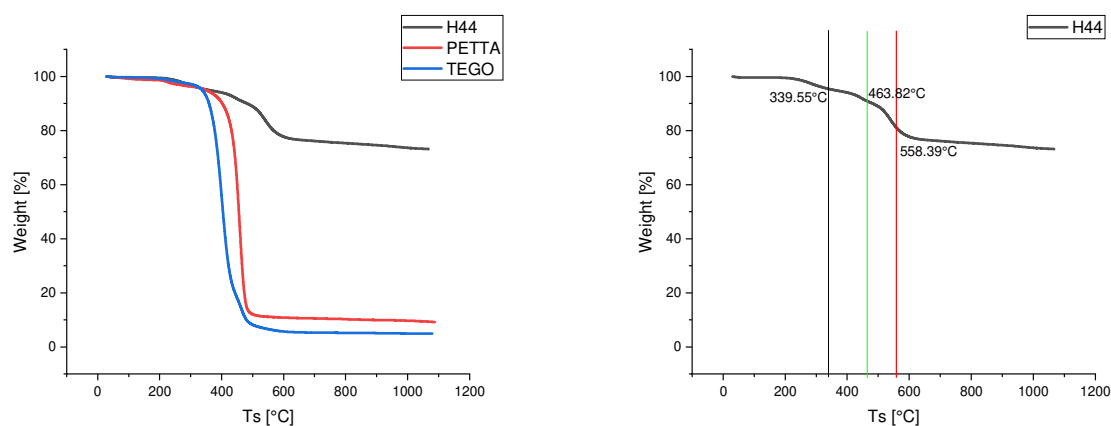
## 4.2 – Printed and pyrolyzed samples

### 4.2.1 – TGA

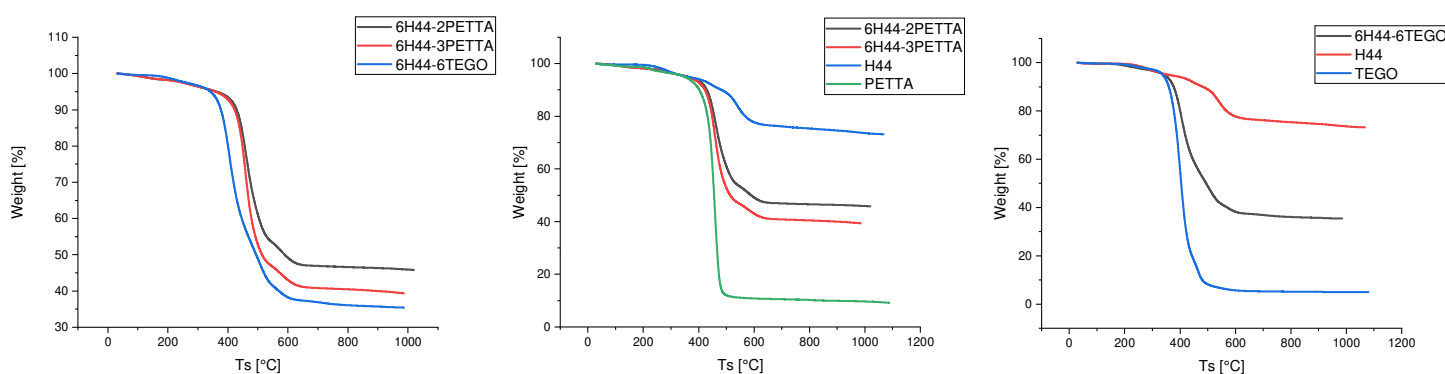
Thermogravimetry analysis was performed on the samples obtained after printing for the three inks and also on the individual components of the inks: H44, PETTA and TEGO. As the last two are liquid, a mixture was prepared between the photopolymer and the photoinitiator in the same concentration as that used in the ink (4%) and a drop of each of the two mixtures was curing with the UV-LEDs system. The analysis was conducted from room temperatures up to 1000°C.

### **Results**

TGA of cured 3D printed specimens shows the ceramic conversion of cured components. Thermogravimetric analysis shows how the behaviour of the inks derives from a combination of the behaviour of the constituents of the mixture. In **Fig. 4.26** the curves of the pure constituents H44, TEGO and PETTA are shown, while in **Fig. 4.27** the curves relating to the three inks and a comparison between them and the pure components are shown. The pure photocurable polymer RC 711 had a very limited ceramic yield, less than 10%, due to the linear nature of the main polymeric chains<sup>74</sup>. In comparison, the relatively branched, cross-linked, or ring-type (necklace) polymers, exhibited higher ceramic yields. The presence of a crosslinked structure or the capability of a polymer to cross-link further at low temperatures retards the thermolytic retroversion reaction that causes the splitting out of volatile cyclomers and linear oligomers from the polymer skeleton. Conversely, the retroversion reaction is promoted by polymer flexibility in the temperature range 200 to 450°C; any factors that constrain the flexibility (e.g., crosslinking, branching, rings, cages and bulk organic groups) or increase the latent reactivity of the polymer will result in higher ceramic yields<sup>74</sup>. Furthermore, the ceramic yields are clearly affected by the pyrolysis behaviour of the hydrocarbon substituents. Ceramic yields increase as a direct consequence of carbon incorporation<sup>74</sup>. For the pure silicone resins H44, the limited low temperature weight loss associated with thermal crosslinking, followed by the typical decomposition occurring with gas release in the polymer to ceramic transition region (~ 400 to 800°C), all well described in the literature<sup>58</sup>, were visible. The same features were retained in all the blends, indicating that the simple mixture of the polymers did not modify their pyrolysis behaviour. The pure component H44 shows a mass loss of about 20%, TEGO greater than 90% and PETTA around 90%. By making the first derivative of the TGA curve it is possible to determine the maximum peak temperature of each mass loss. For pure TEGO and PETTA there is a single notable mass loss at 400 and 458°C respectively. As regards H44, the notable points are shown in the graph: it shows the greatest loss of mass at 558°C, between 500 and 600°C the actual ceramization takes place with the release of the reaction gases.



**Figure 4.26.** TGA pure components of the inks.



**Figure 4.27.** Comparison of TGA inks with each other and with respect to pure components.

The three inks 6H44-6TEGO-4%, 6H44-3PETTA-4% and 6H44-2PETTA-4% show a behaviour similar to that of the components of the blends, intermediate. The maximum mass loss occurs in the temperature range of 400-500°C, 407.9°C for 6H44-6TEGO, 459.3°C for 6H44-3PETTA and 459.6°C (calculated with the DTA) for 6H44-2PETTA and the ceramic yields are respectively approximately 35%, 40% and 45%. The significant losses in mass occur at practically the same temperature as those of the photopolymer used. A higher content of H44 in proportion in the mixture results in a higher ceramic content. A higher ceramic content leads to lower shrinkage and better mechanical properties. Despite significant mass losses (up to 65%), the printed and subsequently pyrolyzed samples are able to maintain their shape, exhibit isotropic shrinkage and are able to withstand compression stresses in the order of units-tens of MPa.

#### 4.2.2 – Scaffolds

The three developed inks were used to fabricate scaffolds starting from suitable Gcode models. Three Gcode models of scaffolds were prepared: all three consist of layers of parallel filaments alternating planes of 90° and have the dimensions of the base of 12 x 12 mm while the height is variable. The lowest has a height of 5 mm, the intermediate of 8 mm and the highest of 12.6 mm. The height was changed simply by increasing the number of layers in the Gcode file. The first layer is deposited at a nozzle-substrate distance of 0.46 mm equal to 80% of the size of the nozzle while the subsequent height increases have been set at 0.58 mm, since maintaining the 0.46 mm it is found that the new layer fails to settle on the one previously cured. There is a clogging of the nozzle which begins to plow and destroy the underlying layers; this could be due to the fact that the filaments already cured do not have exactly the size of the nozzle due to the swelling and the non-immediate curing so that the height available for the new filament is actually less, so the ink is compressed and pushed towards the nozzle, so clogging phenomena occur. It was therefore decided to slightly increase the variation in z of each layer to 0.58 mm, equal to the diameter of the nozzle. A larger increase caused ripples and irregularities in the filament. Within each layer the various segments are spaced by an increase in y or x, respectively by orientation, of 2 mm which is therefore the distance that an ink filament must be able to cover itself self-sustaining and without giving rise to sagging phenomena; two parallel filaments of an underlying layer act as ends for the suspended filament of the next layer. The analysis with an optical microscope and SEM of the green samples and then of the pyrolyzed ones made it possible to establish whether the filament was able to cover this distance without deflection effects. The intensity of the UV light used for printing the scaffolds was 23 mW. In fact, since the printing lasted a few minutes (~ 4 mm), an excessive intensity, such as the 70 mW used for printing the spirals, which required just one minute as the time of the operations, caused damage to the connections between the LED chips which overheated, began to flicker, or jumped completely. A cooling system has therefore been added and a limitation on the power of the UV light set to a maximum of 23 mW. However, the intensity was not stable and decreased over time as shown in Fig. 3.7. During printing, the most difficult parameter to control was speed. The pressure was kept constant while the speed was gradually increased throughout the printing: keeping it constant, in fact, there were phenomena of interruption of the filament and clogging of the nozzle. It was as if the ink became more liquid as printing proceeded, so at the same speed and pressure the outgoing flow increased, which consequently clogged the nozzle after curing. This could derive from the fact that the UV set-up heated up quite a bit during printing and could therefore transmit heat to the material inside the syringe and the nozzle, decreasing its viscosity. Touching the syringe as soon as the printing of a scaffold was finished actually it is slightly warm; the phenomenon could instead be due to a thixotropic nature of the inks which would show a viscosity which decreases over time with the same applied shear strain. In any case, the speed was gradually increased during printing: the first layer was the one printed at a lower speed to allow good adhesion to the substrate and avoid the formation of drops instead of a continuous filament, then it was increased without exaggerating otherwise the ink did not have the time to cure and therefore maintain the circular shape of the filament. At too high speed the filament also could not reproduce the shape in the file, the corners were smoothed, the overlying filaments did not find the support of the lower ones and yielded corners were created as shown in **Fig. 4.3.A**. The most critical points of the print are in fact the curves, the parts close to them

and the vertices where one plane ends and the next begins, where the direction of the machine becomes orthogonal to the previous one. For each ink composition, several scaffolds were printed to pyrolyze them and subsequently evaluate the mechanical properties of compression. The 6H44-6TEGO-4%PI ink proved to be the most difficult to print due to its low viscosity and high curing speed, but in the end acceptable scaffolds were obtained which prove to be rigid, unlike the spirals that with this ink are very soft. The scaffolds are stiff probably due to the fact that the material is subjected to UV light for much longer time. They are also more yellowish due to the high content of Irgacure 819. Another parameter that affects the success and shape fidelity of the scaffolds is the fact of using a nozzle for the first time or in subsequent prints. A new nozzle allows to obtain quite precise filaments, while with use, the filament quality decreases and there are more distortions and contact between segments. **Fig. 4.28** shows the images obtained under the optical microscope for the best green scaffolds; the scale bar is 1000 $\mu$ m. The average dimensions of the printed scaffolds measured with the caliper are:

- 6H44-2PETTA-4%PI: 12.85 x 12.70 mm of base x-y and height 4.40, 8.10 and 12.8 mm for the three different heights;
- 6H44-3PETTA-4%PI: 12.98 x 12.9 mm and heights 4.36, 6.96 and 12.13 mm;
- 6H44-6TEGO-4%PI: 12.88 x 12.82 mm and the only intermediate height 7.35 mm.

Compared to the geometry present in the Gcode the values differ widely, some heights are probably lower due to the failure of some layers in particular on the corners, given the absence of support, while the base is slightly greater, probably due to the thickness of the filament that in the Gcode file has no size. Overall however, they quite faithfully respect the desired dimensions. In **Fig. 4.3.A**, on the other hand, some images relating to scaffolds are shown. In these images the printing parameters have not been suitably combined so the scaffolds result in a form that does not reflect the Gcode: the side view highlights how the various layers have collapsed one on the other, the reduction of the space along the z axes resulted in a higher mutual interfusion between adjacent layers of rods with an increase in the contact area at the joints; the filaments are not able to self-sustain but deflect, there is a lack of support on the corners due to the design not respected, which involves a collapse of some vertices; furthermore, from the top view, you can see how the filament is thick, imprecise and does not maintain the same shape and section, but widens at the contact points, so that the holes in the lattice tend to take on a rounded rather than square shape.

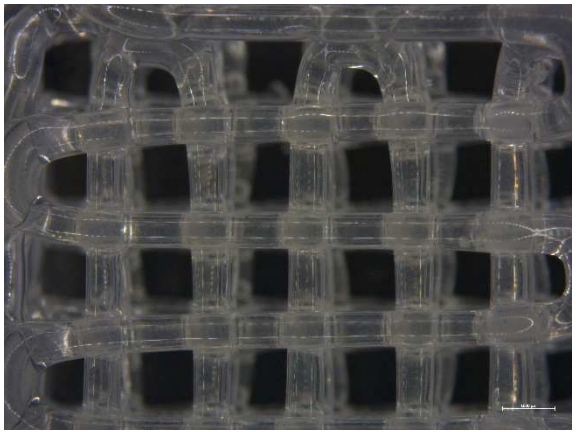

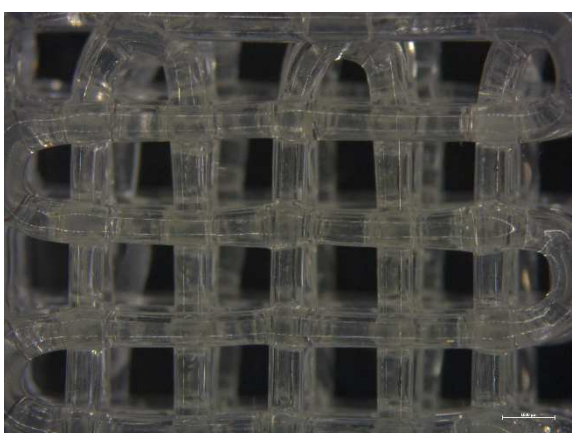

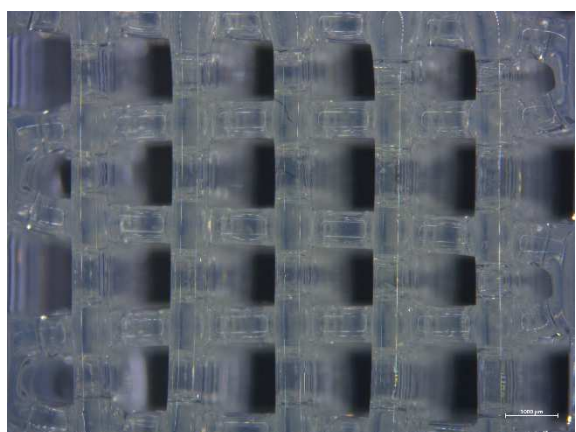
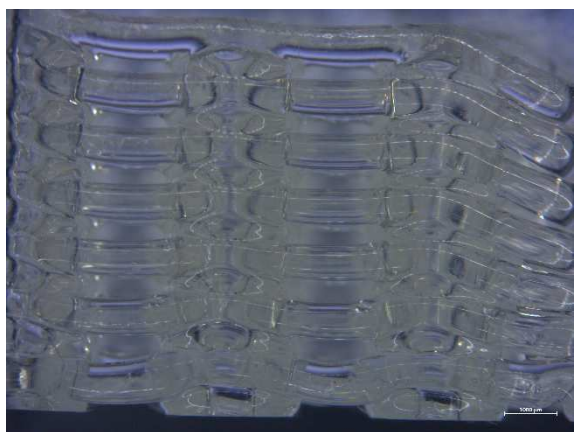
From **Fig. 4.28** it can instead be seen how the optimization of the printing leads to obtaining scaffolds that have a sufficiently regular lattice. The filament has a constant section, in the points of contact with the underlying layer there is no merging and widening due to the fusion, the pores show a relatively square area on the x-y plane so that the printability index approaches 1 leading to good geometrical accuracy. The filament diameter was measured through the ImageJ program and the average value for the three inks is: 696  $\mu$ m for 6H44-3PETTA-4%PI, 704  $\mu$ m for 6H44-2PETTA-4%PI and 748  $\mu$ m for 6H44-6TEGO-4%PI; it is greater than that of the nozzle due to the radial expansion of the extrudate occurring when the material leaves the nozzle, however it is relatively constant; thickening may occur in the curved areas of change of direction. The spacing between adjacent rods on the x-y plane is of approximately 1.218 mm, 1.230 mm and 1.232 mm for the three inks in the order previously reported. The spaces between adjacent rods are 540, 550 and 380  $\mu$ m

respectively along the z axis for the three compositions. The reduction of the space along the z axes in the third ink containing TEGO resulted from the fact that the filament diameter is greater so that the portion of free space between successive layers is reduced. The open porosity is geometrically ordered and interconnected in all three dimensions. From the lateral view it can be seen how the filaments are able to remain straight in the areas between the contact points and the various layers can be distinguished well even if in the vertices there is a slight collapse of the structure due to the instability created by the change of direction. Among the three inks, the one that has the least shape fidelity is TEGO since most of the scaffolds have a filament that widens slightly at the contact points and greater instability. You may notice air bubbles inside some filaments but otherwise no defects are noticed. The **Fig. 4.29** shows an internal section obtained after cutting a sample of 6H44-2PETTA-4%PI ink: the sections are circular and well aligned and the rods remain straight even inside the scaffold, the value of the cross section differs from that of the nozzle resulting greater (about 750  $\mu\text{m}$ ) and you notice a slight decrease in the same as you proceed towards the higher layers.





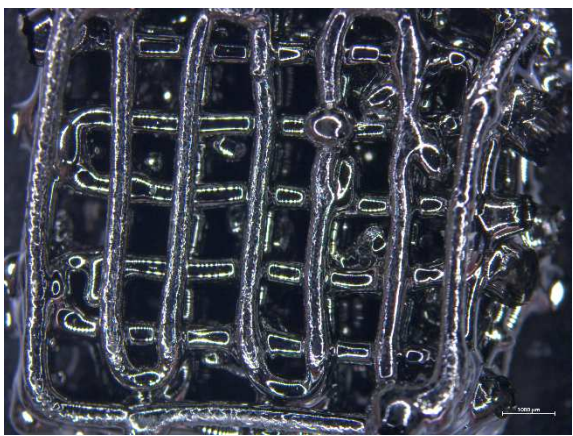
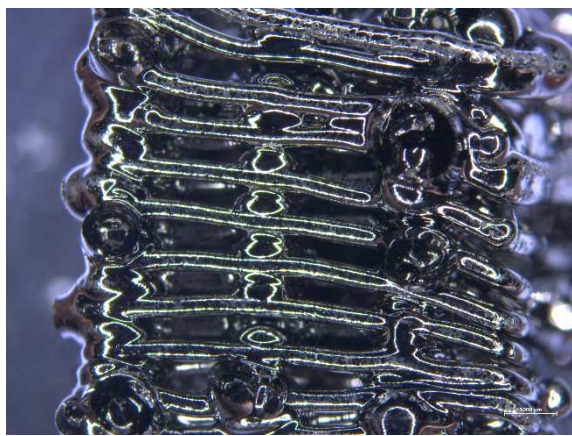
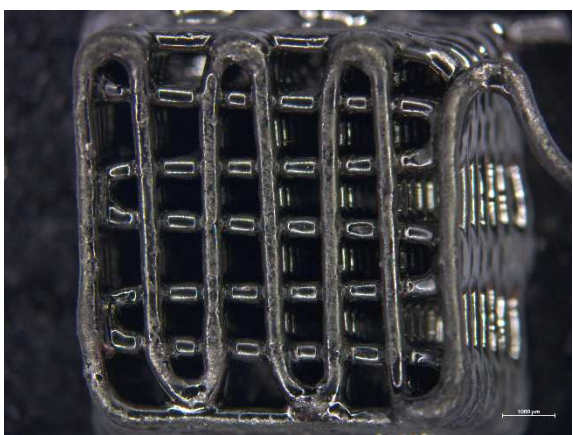
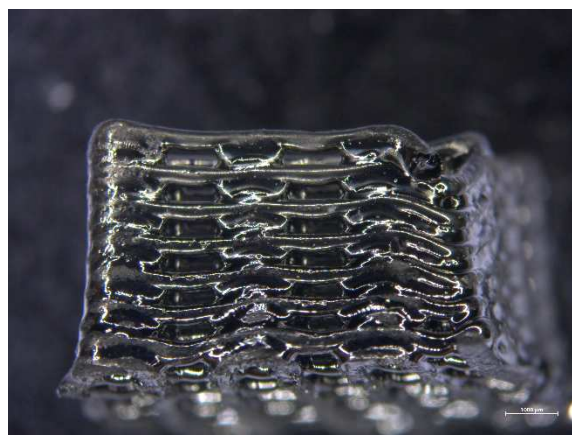
*Figure 4.29. Internal section of 6H44-2PETTA scaffold.*

The scaffolds were subjected to pyrolysis treatment and the optical microscope images of the pyrolyzed samples were reported in **Fig. 4.30**. The samples retain their shape, however there is a slight deformation of the structure and a loss of geometric definition. The average dimensions on the x-y plane and on the z spacing are respectively for the composition T, U and E of 879, 873 and 690  $\mu\text{m}$  (x-y) and 306, 430 and 262  $\mu\text{m}$  for the spacing in z. Nevertheless, the filaments remain continuous, clearly distinguishable from each other and the pores still take on an almost square shape. The rods also appear free of cracks. From the lateral view you can see the maintenance of the spacing in z and the filaments that remain straight. From the images it is also possible to notice a slight interpenetration fusion of the layers on the vertices of the structures and the presence of small spherical areas that interrupt the continuity of the filament in some sections or cause distortions. These areas are bubbles and can appear closed or exploded. They probably derive from those enclosed in the green bodies which, during the heat treatment, coalesce and reach the surface of the rods. The presence of gas bubbles inside the ink is therefore an extremely important problem and it is necessary to perform an accurate degassing step and pay attention to how the ink is deposited inside the syringe to try to avoid it. For example, you could suck the ink rather than introduce it before the piston.

Ink	Top view	Lateral view
6H44-2PETTA-4%PI		
6H44-3PETTA-4%PI		
6H44-6TEGO-4%PI		

**Figure 4.28.** The scaffolds were printed 0.75 bar for 3 PETTA, 1 bar for 2 PETTA and 0.25 bar for TEGO with a speed up to 150-200% of the 450 mm/min of the Gcode.

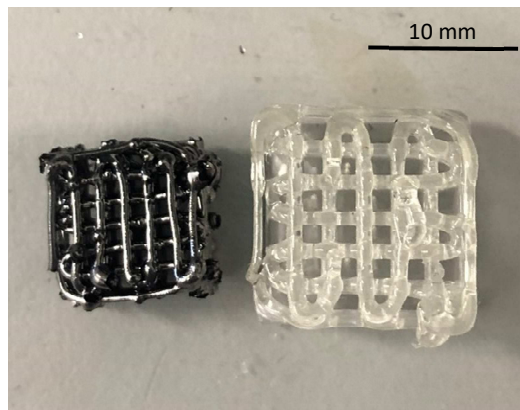


Ink	Top view	Lateral view
6H44-2PETTA-4%PI		
6H44-3PETTA-4%PI		
6H44-6TEGO-4%PI		

*Figure 4.30. Pyrolyzed scaffolds.*

### 4.2.3 – Shrinkage

The dimension of the scaffolds was measured by means of a digital caliper, before and after the heat treatment, thus allowing the calculation of the shrinkage occurring during ceramization due to the release of the organic phase, **Fig. 4.31**. The shrinkage along all three dimensions of the scaffolds and then also of the single filament both from the outside and from the internal section was calculated after the breaking of the specimens through compression tests. For each scaffold different measurements were taken along the x, y and z directions and an average value was calculated since the sides of the solid were not always parallel, especially the top face. In fact, some filaments could slightly protrude from the underlying ones in the x and y directions while in z the height varied according to whether the measurement was made in the center or on the vertices: it has in fact been described how the change of direction near the vertices caused instability to the filament (a phenomenon worsened by an excessive printing speed) which therefore did not always respect the Gcode design; the vertices were sometimes lower due to the collapse and lack of support, while the central part respected the file more faithfully



**Figure 4.31.** Comparison between scaffolds before and after pyrolysis.

The shrinkage was calculated with Eq. (3.XVI). For each ink, several scaffolds were measured, and an average value was calculated, reported in **Table 4.7**. The other values are shown in **Table 4.3.A**.

Inks	x(%)	y(%)	z(%)	Single filament (view from side) %	Single filament (view from above) %
6H44-2PETTA-4%PI	21.83	21.24	19.76	32.69	36.64
6H44-3PETTA-4%PI	20.63	20.70	20.17	36.96	37.74
6H44-6TEGO-4%PI	35.48	35.90	33.77	43.36	44.60

**Table 4.7.** Shrinkage.

For each ink in the three directions the shrinkage assumes more or less the same value, which indicates that we can speak of isotropic shrinkage and this factor contributes to the possibility of producing undistorted parts. In the x and y direction it is necessary to take into account that there are effects of

interaction with the crucible during pyrolysis, while the z direction is not affected by constraints. Sometimes it also happens that the measured shrinkage in z (thickness) direction is greater than those on the x-y plane due to a gravitational effect causing an anisotropic flow during heating. In this case, however, the value of the shrinkage in z is not greater and is very close to that of the x-y plane, making the piece isotropic in its behaviour to heat treatment. For the two compositions containing PETTA the shrinkage settles at around 20%, a value which is found in some papers relating to SiOC ceramic deriving from preceramic polymers<sup>96,8</sup>. For the ink containing TEGO it is greater, around 35%, certainly due to the fact that the quantity of photosensitive polymer is greater, so that there is a greater loss of material (confirmed by the results of the TGA) and therefore of volume. The single filament, it has a higher shrinkage rate than the structure as a whole. The cross-section reduction for inks 6H44-3PETTA-4%PI and 6H44-2PETTA-4%PI is respectively 22.39% and 28.32%, measured after breaking in the compression test.

#### 4.2.4 – SEM

The scaffolds were observed by SEM and the images are shown in **Fig 4.32**. From the SEM images it can be seen that the printed lattice grid structure still maintains its structural integrity after sintering, not perfectly as deformations are present, but the various filaments of the different layers are still distinguishable. The filaments are horizontal between two successive support points without showing deflection phenomena: the optimized ink compositions are therefore able to create ceramic structures consisting of suspended filaments even if for short distances, about 1-2 mm. The structures of the ink 6H44-2PETTA-4%PI show a better shape fidelity. In those deriving from the ink 6H44-3PETTA-4%PI it is possible to notice porosity probably caused by air bubbles already present in the ink inside the syringe during the printing process, which have been incorporated by the filaments more or less superficially, and by the release of gaseous phases during the ceramization process. They are visible in particular in **Fig, 4.32.b**, figure A, where we see filaments interrupted by exploded bubbles. However, both these compositions show circular sections in the internal regions, two adjacent and successive filaments do not merge, except in a few cases (probably this distortion is always due to the presence of air bubbles), an indication that each layer has solidified before printing the next, allowing the new one to find a rigid substrate. The pores in the z-x and z-y planes are almost rectangular in shape in the first ink, which results in a printability index  $Pr$  close to 1, which indicates little merging of the filaments and an acceptable geometric accuracy. In the second ink, on the other hand, the pores tend to take a more rounded shape, indicating a lower geometric accuracy. In the ink containing TEGO, almost circular and very small pores are observed, indicating a marked fusion at the intersection of two filaments, caused by the fact that the reticules of each layer remain soft even after curing, so there is a fusion of the structure. In fact, unlike the two previous inks, the sections cut along the z direction are not circular at all, they are merged with each other at the intersection points: collapse of the filament circularity is caused by poor or slow stabilization of the ink after dispensing and more generally low viscosity and nonoptimal gelation conditions are some of the underlying causes for these deviations, e.g., the merging of filaments and the resulting low shape fidelity. The 6H44-6TEGO-4%PI ink, in fact, has a lower viscosity than the other two compositions and despite

the fact that the material is cured fast, it remains soft and less rigid, resulting in a worse shape fidelity of both printed and pyrolyzed pieces.

It can be seen from the images that there are gaps after sintering between some layers, but they are caused by the printing process and not by the poor adhesion of the ink to the underlying layers. The densification degree of the structure is high. On the surface of the rods and on the sections there are no cracks or defects, not even in the most critical contact areas, and there are no particles that usually appear instead with increasing sintering temperature and grow gradually, mainly because of the growth of amorphous  $\text{SiO}_2$  and  $\beta\text{-SiC}^{54}$ . The traces of the fracture planes of the various rods can be seen on the cross sections.

It can therefore be concluded that all three inks do not exhibit excessive deformation due to sagging in the spanning portion of the filaments, which is larger than their diameter, demonstrating the good suitability of the rheological properties of the preceramic ink for the DIW process, and the homogeneous shrinkage occurring during pyrolysis. Nearly circular cross-sections in the samples furthermore indicate that the two inks 6H44-2PETTA-4%PI and 6H44-3PETTA-4%PI have an acceptable degree of shape retention and ability to support the upper layers during printing, due to the fast recovery of the viscosity of the ink upon exiting from the nozzle, unlike 6H44-6TEGO-4%PI ink. The same can be said for the bonding between perpendicular filaments belonging to adjacent layers, good for the first two inks and fused for the third. High magnification shows that inside a filament no macro-pores or macro-cracks are visible, indicating that no significant defects are present after pyrolysis. Magnifications range from 30x to 1500x. Each photo below shows the acquisition data and the scale bar.

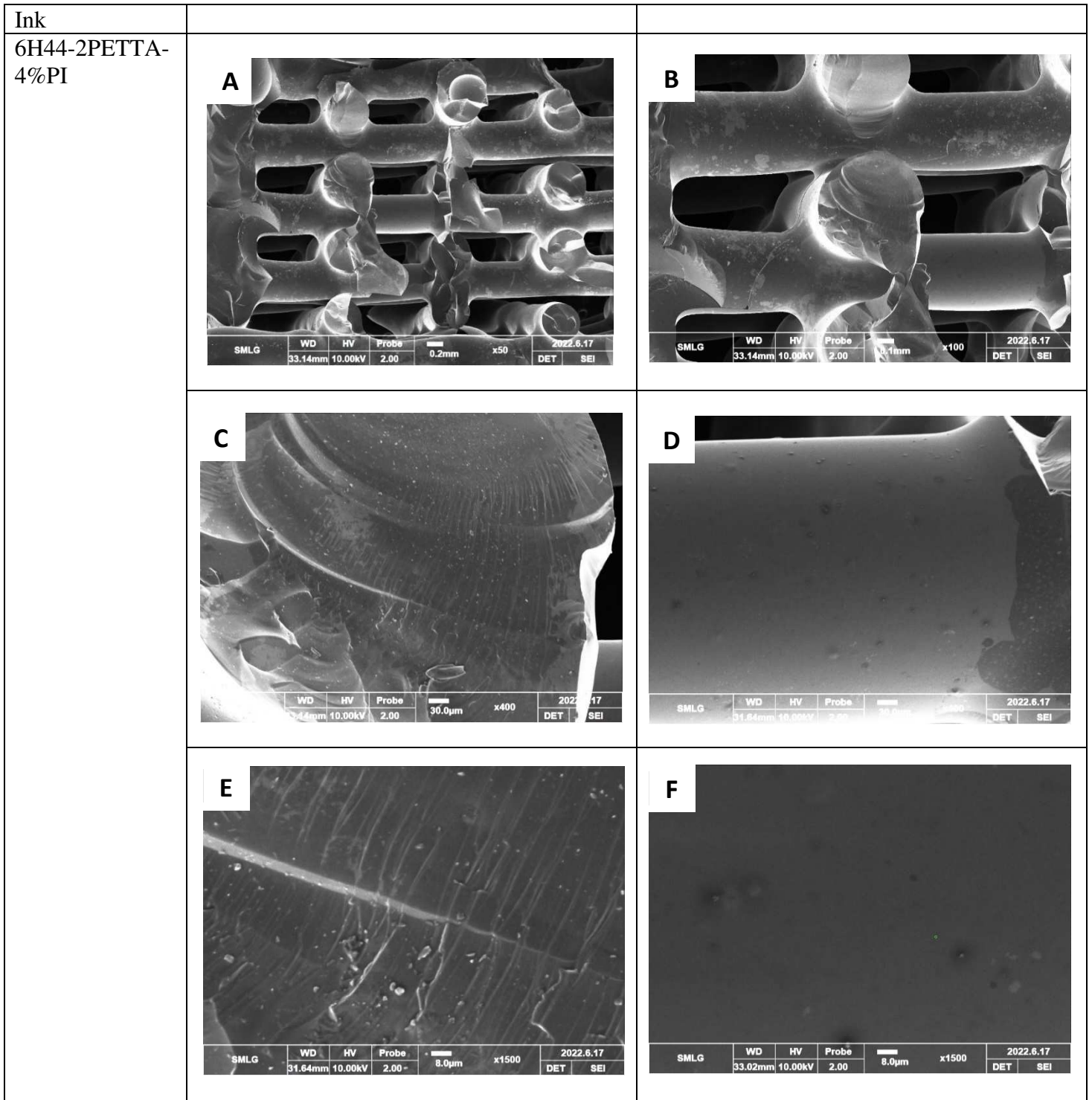


Figure 4.32.a. SEM images for 6H44-2PETTA-4%PI ink.

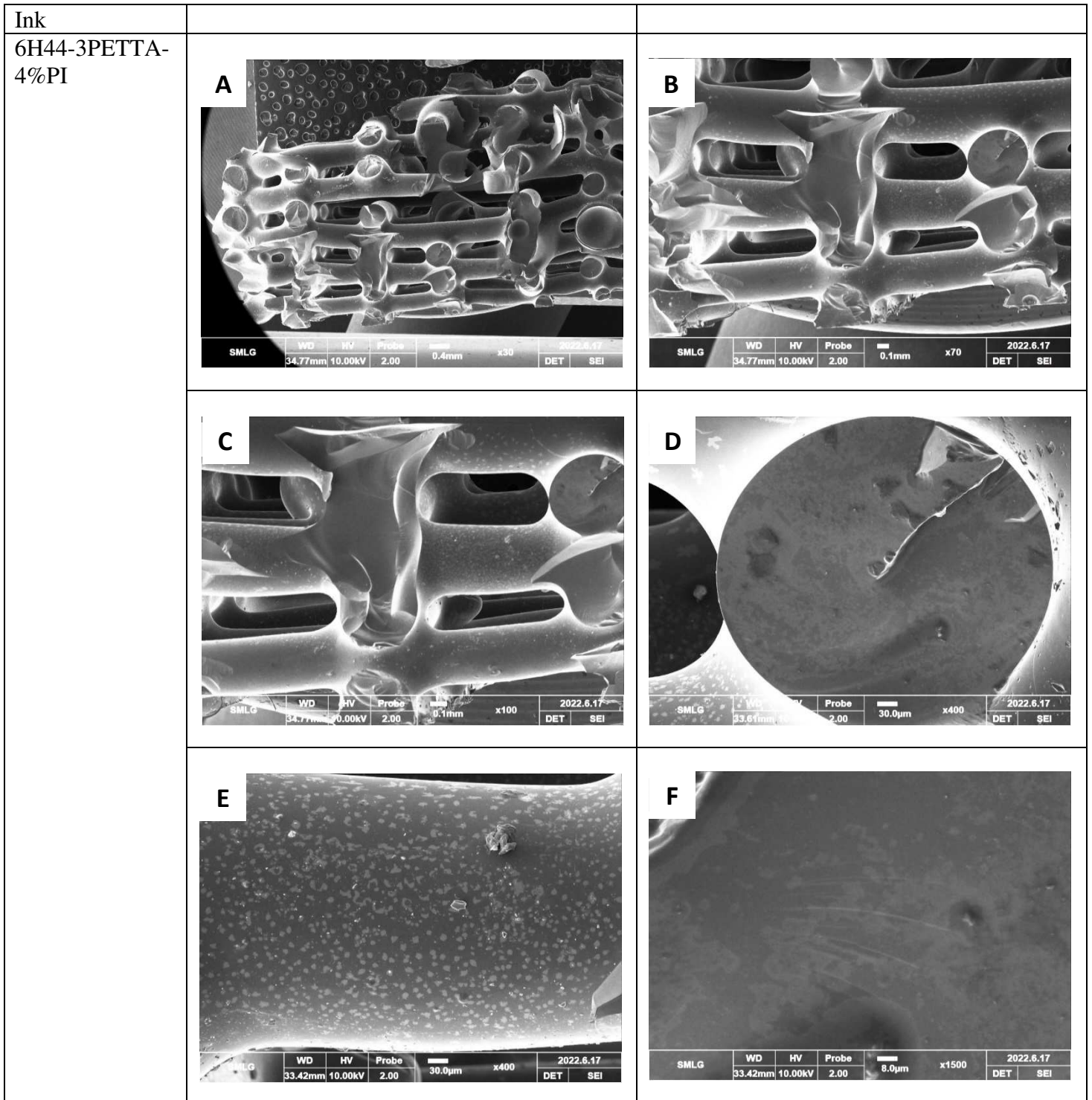


Figure 4.32.b. SEM images for 6H44-3PETTA-4%PI ink.

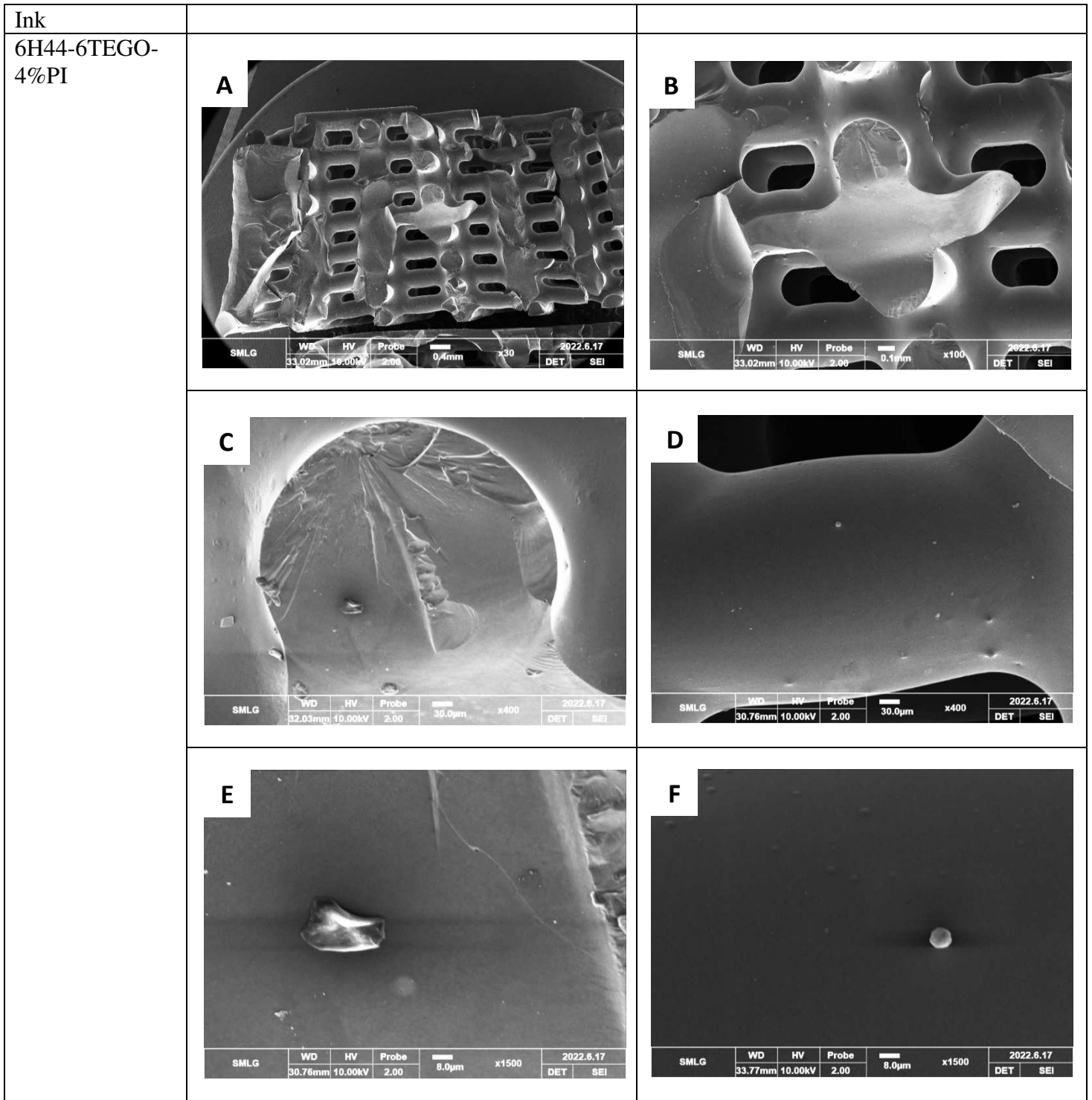


Figure 4.32.c. SEM images for 6H44-6TEGO-4%PI ink.

#### 4.2.5 – Density

Skeletal density was measured using the helium pycnometer (*Ultrapyc 3000, Anton Paar*), in **Fig. 4.33**. For the calculation of the skeletal density, pieces of scaffold were inserted inside the sample holder after weighing them and calibrating the instrument. The same tool was used for the calculation of the true density of the material on very finely ground powders of scaffolds. 5 runs were repeated for each sample and the average value was evaluated. **Table 4.8** shows the results; the results of each measurement are reported in **Table 4.4.A**.

	$\rho_s$ (g/cm <sup>3</sup> )	Vol (cm <sup>3</sup> )	% Variance	$\rho_t$ (g/cm <sup>3</sup> )	Vol (cm <sup>3</sup> )	% Variance
6H44-3PETTA-4%PI	1.6566	0.0495	0.6783%	2.1239	0.0546	1.9084
6H44-2PETTA-4%PI	1.6607	0.0464	1.1438%	2.1122	0.0601	0.4792
6H44-6TEGO-4%PI	1.7429	0.0734	0.7728%	2.0030	0.0634	1.6659

**Table 4.8.** Skeletal and true density for the three inks.

If the two values of skeleton and true density are close this is an indicator of limited closed porosity. In this case, however, the value of the real density is greater than that of the skeleton density, which indicates the presence of closed porosity. This closed porosity can derive from the gas bubbles contained in the filament during printing which then coalesces during pyrolysis without bursting. The percentage difference of  $\rho_t$  with respect to  $\rho_s$  is equal to 28.21%, 27.19% and 14.92% respectively for the three inks in the order in the table (calculated through:  $[(\rho_t - \rho_s) / \rho_s] \cdot 100$ ). The ink containing TEGO therefore shows a minor difference between the two density values: closed porosities are present but to a lesser extent than the other two compositions. This data is in line with the optical microscope images of the pyrolyzed samples which show a presence reduced surface area of bubbles in the TEGO-containing scaffolds compared to the two compositions containing PETTA.

In §2.4 we saw how the different definitions of density derive from as many distinctions on the volume that can be considered. Depending upon the measurement method then various types of volumes can be determined. The determination of two or more volume values by different methods, allows extraction of porosity information by the application of simultaneous equations<sup>92</sup>, although by these analytical methods, porosity information is a by-product of volume determinations and not the primary emphasis. There are several definitions of porosity<sup>92</sup>, for example an open pore is a cavity or channel with access to an external surface, a closed pore is a cavity with no access to an external surface, interstitial void is an opening in a rock or soil that is not occupied by solid matter or void space between particles and then the distinction between macro-, meso- and micro- pores (respectively diameter > 50 nm, diameter from about 2 nm to 50 nm and diameter less than about 2 nm). The skeletal volume is given by the sum of the volume of the solid material plus that of the closed porosities, the true volume is equal to the volume of the solid material, while the bulk volume is equal to the total volume which includes both solid material and voids. It can be measured with a caliper by measuring the three dimensions x, y, z of the scaffold. From measurements of bulk volume ( $V_B$ ) and skeletal volume ( $V_{Sk}$ ), total porosity  $V_{Pt}$  can be determined from the Eq. (4.V):

$$V_{Pt} = V_B - V_{Sk} \quad \text{Eq. (4.V)}$$



The bulk volume can be calculated by measuring the sides of the scaffolds with the caliper. The skeletal volume is provided by the pycnometer. The  $V_{Pt}$  value allows percent porosity to be calculated by the simple relationship:

$$\% \text{ Porosity} = \phi = (V_{Pt}/V_B) \cdot 100 \quad \text{Eq. (4.VI)}$$



**Figure 4.33.** Helium pycnometer (Ultracyc 3000, Anton Paar).

#### 4.2.6 – Mechanical properties

A compression test was carried out due to the brittleness of the material in tension. For the calculation of the mechanical properties, the force and elongation data obtained by the machinery were converted into stresses and strains. To calculate the effective contact area, only the filaments of the weft were considered, the area of the empty spaces was subtracted from the measurement of the total area, calculated by multiplying the measure of the lengths of the sides in x and y direction measured with the caliper. The calculation of the area of the empty spaces was carried out through the ImageJ analyser, calculating the average diameter of the filaments. The initial height  $h_0$  necessary for the calculation of the deformations was measured with the digital caliper in the z direction after leveling the faces of the scaffolds then parallel to the plates of the machinery. For each composition, several tests were carried out and the maximum stress that the samples could tolerate was calculated; the average value between the various tests was considered. The average values are reported in **Table 4.9**, while in **Table 4.5.A** the values obtained from all the specimens are reported. In **Fig. 4.34** the stress-strain graphs are represented, one for each material. The results vary significantly from sample to sample, there is a greater dispersion of the results as regards the breaking stress compared to other properties; the calculated standard deviation values are high, obtained by the formula:

$$\sigma = \sqrt{\frac{\sum(x_i - \mu)^2}{N}} \quad \text{Eq. (4.VII)}$$

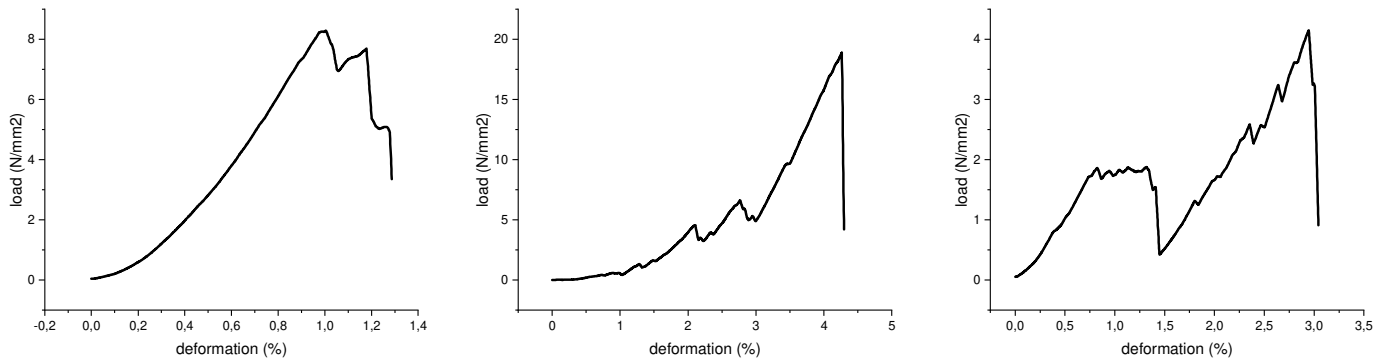
where  $x_i$  is the stress value obtained from each test,  $\mu$  is the average value and  $N$  is the number of tested specimens.

Ink	Stress (MPa)	$\sigma$	Strain (%)	$\sigma$
6H44-2PETTA-4%PI	6.233	1.560	1.506	0.589
6H44-3PETTA-4%PI	4.847	0.483	1.842	0.624
6H44-6TEGO-4%PI	15.947	3.201	4.472	1.363

*Table 4.9. Mean stress and strain values and standard deviations.*

The samples produced, being ceramic in nature, should show a brittle behaviour: brittle materials are characterized by low or zero plastic deformation and the breaking processes take place in two stages, formation and propagation of cracks. The typical stress-strain curve should therefore have a first linear stretch of elastic deformation, a yield not highlighted by a sudden variation in the slope of the diagram and subsequently the failure without further deformation. The fracture section of brittle materials usually appears flat and orthogonal to the direction of application of the stress since the fracture occurs by propagation of the same in a plane orthogonal to the maximum normal stress acting. The graphs in **Fig. 4.34** show how the trend of the stress-strain curve is not exactly monotonous up to failure, but how there are phases of decrease and increase in stress that alternate with increasing deformation. This is caused by the partial failure of the wires that make up the lattice: it, as in composite materials in which the failure of some fibers does not lead to the failure of the material, does not cause the immediate breakage of the piece. The test and deformation can continue as the remaining filaments are still able to carry the load. Since the layers are rotated 90° to each other, the regularity of the structure makes the scaffold possess continuous solid columns in the vertical direction, forming pillars better resisting the applied compression pressure. With the increase of the applied effort, partial breaks accumulate until the resistance of the sample decreases so much as to give complete structural failure. Differently from cellular structures such as foams, these log-pile scaffolds did not display any load bearing capability after reaching the maximum stress and were subjected to catastrophic failure. The behaviour varies greatly from sample to sample, there are in fact samples that show an almost linear trend up to failure while other samples that show many variations in stress before failure. This can be caused by the different defectiveness of the samples. The more defects there are, such as air bubbles incorporated in the filaments, the greater the settlements and the lower the total compressive strength of the piece. Samples produced with 6H44-6TEGO-4% PI ink have the maximum strength and maximum deformation at break; in fact, from the analysis with an optical microscope and SEM they show fewer defects related to the presence of bubbles and a more linear and homogeneous structure. They therefore prove to be the most resistant despite the green bodies being softer than those of the other two inks. The greater resistance of this material may be due to the fact that the filaments in the scaffolds are not only resting on the underlying ones as in the case of inks containing PETTA, which show a minor merging and fusion of the various layers. They are fused so they have a greater resistant section, as if the piece were massive rather than alveolar. The fracture sections (in Fig. 4.32) do not show signs of plastic deformation and in some

you can see the fracture lines starting from a point on the surface, a defect from which the crack has propagated.



**Figure 4.34.** Strain-strain graphs for scaffolds produced with inks: 6H44-2PETTA-4%PI (left), 6H44-6TEGO-4%PI (center), 6H44-3PETTA-4%PI (right).

**Fig. 4.35** shows a strength-density compression graph made with GRANTA EduPack 2021 to compare the properties of our materials obtained through the compression tests with those of the other material classes. The density values used are those of the skeletal density. They are placed close to the classes of non-technical ceramics (they are generally divided into two types: those based on cement and those that are fired, during which a molten glassy phase forms that bonds the other non-molten components into a solid mass) and of polymers. If the geometric density had been used, which is lower than the skeletal one, because the volume considered is greater since the open pores are also taken into consideration, the materials would have been closer to the class of foams. Foams are a hybrid of solid material with gas; the important design variables in the structure of a foam are the relative density (how much of the volume is taken up by the solid), the pore size and whether the cells are open or closed. They are ideal for manufacturing cores for lightweight sandwich structures. The dashed line represents the selection line with index  $I = \sigma_c/\rho$  which allows to maximize or minimize it for a comparison between the materials.

For a comparison with the data available in the literature, numerous papers can be found<sup>56,128,129</sup> which report the production and mechanical characterization of SiOC samples obtained using various approaches, ceramic/metal foams and carbon/graphene aerogels reported or AM of ceramic polymer. In particular, a recent study<sup>130</sup> reports the creation of SiOC scaffolds through the DIW technique from a preceramic polymer that reach compressive strength up to about 33 MPa. The resistance of the structures depends not only on the composition of the ink but also on the spacing between filaments, the angle of deflection between adjacent layers and not on the size of the filament<sup>130</sup>. Reducing the spacing between filaments the resistance increases as it decreases the porosity. From these observations, it is therefore possible to print scaffolds with an architecture which maximizes the desired properties for a specific application.

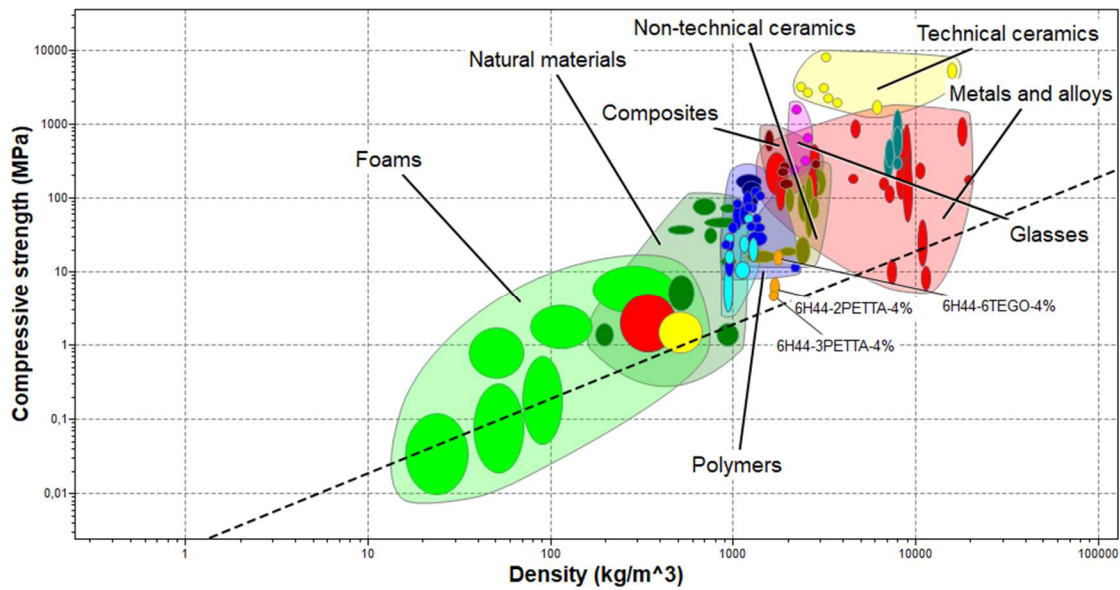


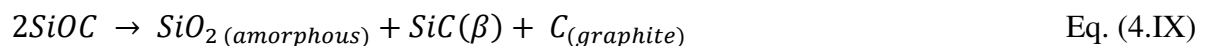
Figure 4.35. Image of the compressive strength as a function of density generated with the "CES edupack" program.

#### 4.2.7 – XRD

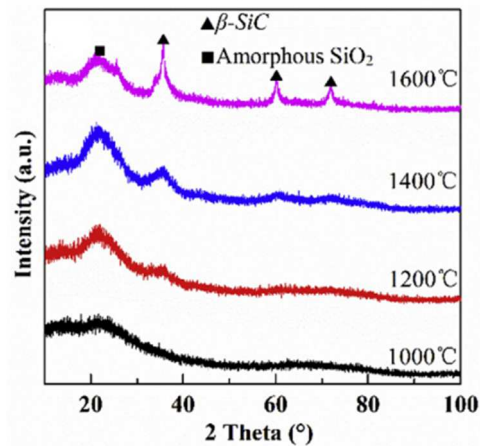
The XRD spectrum of a glass of SiOC composition varies with the variation of the temperature and the pyrolysis atmosphere of the sample, since it reflects the evolution of the microstructure. At pyrolysis temperatures of 1000-1200°C the XRD patterns have an amorphous SiO<sub>2</sub> halo at ~ 22°<sup>131</sup>, attributed to a short-range order in the packing of silica tetrahedra, and a broad peak at ~ 43°; the latter can be assigned to disordered carbon of a turbostratic structure<sup>131,132</sup>. Turbostratic carbon (t-carbon) is generally regarded as a variant of hexagonal-graphite (h-carbon). Both the h-graphite and t-carbon are stacked up by graphene layers with a regular spacing but with different stacking ordering degree. h-graphite is an ordered AB stacking structure, but the graphene layers of t-carbon may randomly translate to each other and rotate about the normal of graphene layers<sup>132</sup>. The peak at ~ 43° is attributed to the (101) planes in h-graphite and its intensity decreases as φ<sub>m</sub> increases, a factor that allows to evaluate the quantities of deviation (rotation, translation, curvature and positive fluctuation of interlayer spacing) of graphene layers may appear in t-carbon<sup>132</sup>. Wei *et al.*<sup>54</sup> analyzed X-ray diffraction patterns of samples pyrolyzed in argon at higher temperatures, up to 1600°C. As the temperature increases, the diffraction peak of amorphous SiO<sub>2</sub> gradually increases in the range 1000-1400°C, slightly decreases at 1600°C due to the carbon thermal reduction reaction<sup>54</sup>, Eq. (4.VIII):



At temperatures greater than 1200°C the diffraction peaks of 35.76°, 60.16°, and 71.95° corresponding to the (111), (220), and (311) crystallographic planes of β-SiC<sup>133</sup> appear, further strengthened at 1600°C (Fig. 4.36). The variation of the peaks shows a continuous increase in the degree of crystallinity<sup>54</sup>. SiC formation can be understood as follows<sup>134</sup>: during the pyrolysis of the preceramic at 1100°C-1400°C, the following reactions take place:

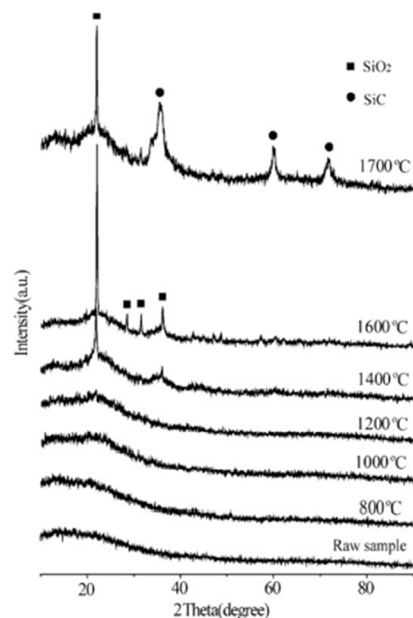


and the carbon thermal reduction reaction Eq. (4.VIII). Eq. (4.IX) represents the separation of the Si–O–C glassy matrix, with free carbon homogenously dispersed and embedded inside the matrix, in a more stable SiO<sub>2</sub> glassy matrix, amorphous SiC, and highly disordered graphite-like carbon<sup>135</sup>. The phase separation leads to no mass loss, but the carbothermal reaction causes more mass loss because of the fugitive CO gas<sup>134</sup>.



**Figure 4.36.** X-ray diffraction pattern of SiOC ceramic obtained at increasing pyrolysis temperature<sup>54</sup>.

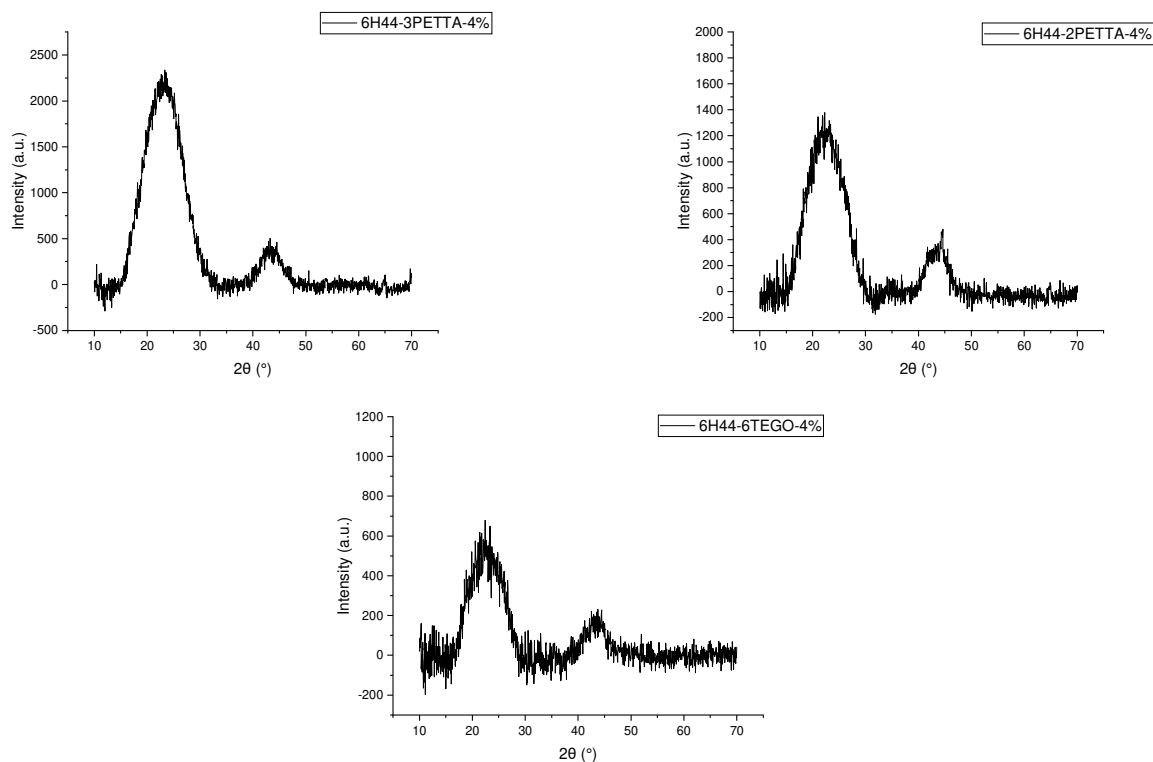
A study on the high-temperature behaviour of silicon oxycarbide glasses in air environment<sup>136</sup> shows that at temperatures above 1400°C, cristobalite is present which is related to the oxidation of SiOC network<sup>136</sup> and at temperatures above 1600°C peaks of β-SiC phase are found due to carbothermal reductions occurring between SiO<sub>2</sub> and free carbon, **Fig. 4.37**.



**Figure 4.37.** XRD patterns of SiOC samples annealed in air environment at various temperatures<sup>136</sup>. The green bodies were pyrolyzed in flowing high purity argon (purity > 99.999%) with a heat rate of 20 °C/min up to 1000°C held for 1 h. Then these glasses were in the furnace starting from room temperature and heating up to 800, 1000, 1200, 1400, 1600, and 1700°C in laboratory air environment.

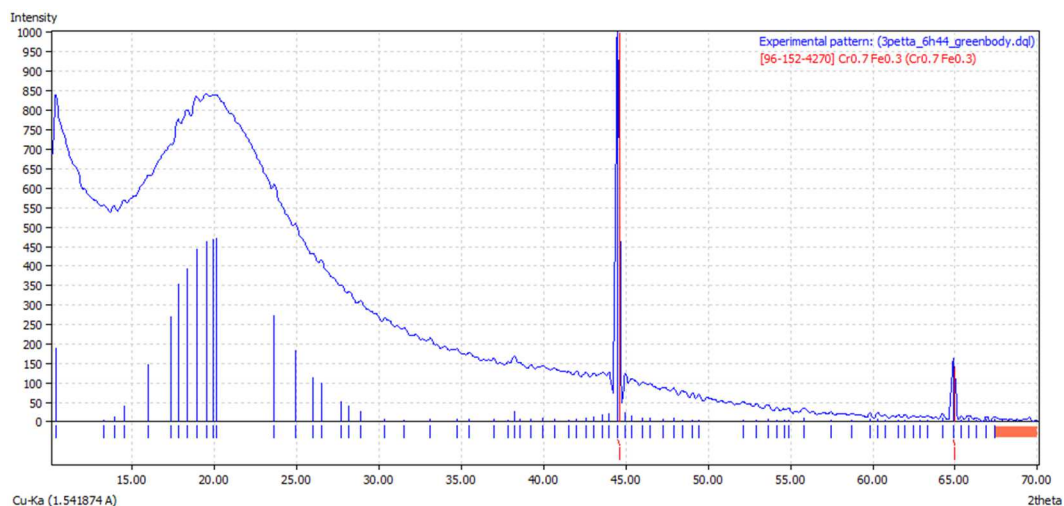
## Results

**Fig. 4.38** shows the graphs relating to the pyrolyzed samples of each ink. The X-ray patterns of the pyrolyzed samples of each ink show a halo peak around  $22^\circ$  characteristic of amorphous  $\text{SiO}_2$  and a lower broad peak at  $\sim 43^\circ$  characteristic of free carbon, in accordance with the data found in the literature<sup>54,134,136</sup> as regards a samples of preceramic resins subjected to pyrolysis treatment at low temperatures up to  $1200^\circ\text{C}$ . There are no single sharp peaks, which testifies to the absence of crystalline phases and confirms the totally amorphous nature of the samples. There are no obvious differences between the three inks.



**Figure 4.38.** X-ray patterns of the pyrolyzed samples of each ink.

For comparison, the green bodies relating to the two inks 6H44-2PETTA-4%PI and 6H44-3PETTA-4%PI were also analysed before undergoing the pyrolysis treatment, the last represented in **Fig. 4.39**. The 6H44-6TEGO-4%PI ink was not analysed due to the impossibility of reducing the green bodies to powder due to their flexibility and softness. In figure you can see the soft peak at  $22^\circ$  but two sharp peaks appear at the angles  $44.69^\circ$  and  $64.89^\circ$ . By analysing these patterns with the Match! Software, it was possible to associate the peaks with metallic impurities of iron and chromium, probably present during the preparation of the powder as residues of previous analysis.



**Figure 4.39.** Green body of 6H44-3PETTA-4% ink in Match! software and revelation of impurities.

#### 4.2.8 – FTIR

The infrared absorption spectra of the ink during the light-curing process are shown in **Fig. 4.40**. The results indicate that the absorption peak at  $2972\text{ cm}^{-1}$  is the  $\text{-C-H}$  asymmetric stretching vibration peak,  $1727\text{ cm}^{-1}$  is the  $\text{-C=O}$  stretching vibration peak,  $1638\text{ cm}^{-1}$  is the  $\text{C=C}$  stretching vibration peak,  $1271\text{ cm}^{-1}$  is the  $\text{-Si-CH}_3$  symmetric bending peak<sup>54</sup>. With increasing UV irradiation time, the stretching vibration absorption peak of  $\text{C=C}$  at  $1638\text{ cm}^{-1}$  decreased and also the peak around  $1407\text{ cm}^{-1}$ , characteristic of  $\text{C=C}$  twisting. The peak at  $1727\text{ cm}^{-1}$  tends to shift to a large wave number, as shown in **Fig. 4.41** and particularly visible in the spectrum of the 6H44-6TEGO-4%PI ink. The decrease in the peak intensities at  $1298\text{ cm}^{-1}$  attributed to  $\text{-C-C=O-}$  skeletal vibrations also demonstrate the progress of polymerization. All these results indicate that the acrylate groups undergo radical polymerization under excitation with UV light, forming a three-dimensional network structure.

Fourier-transform infrared spectrometry was used to investigate the conversion rate of vinyl groups of inks under different UV exposure time and further curing degree. Relative to Band Ratio Method was adopted to quantify the curing degree by relative intensity of FTIR peak attributed to  $\text{C=C}$  at  $1600\text{-}1645\text{ cm}^{-1}$ , between UV-exposed and non-UV-exposed inks, with FTIR peaks attributed to  $\text{C=O}$  stretching absorption at  $1671\text{-}1805\text{ cm}^{-1}$  as inner standard peak since it is unchanged during the reaction<sup>137</sup>. The conversion rate  $\alpha$  determined by exposure time  $t$  was calculated using:

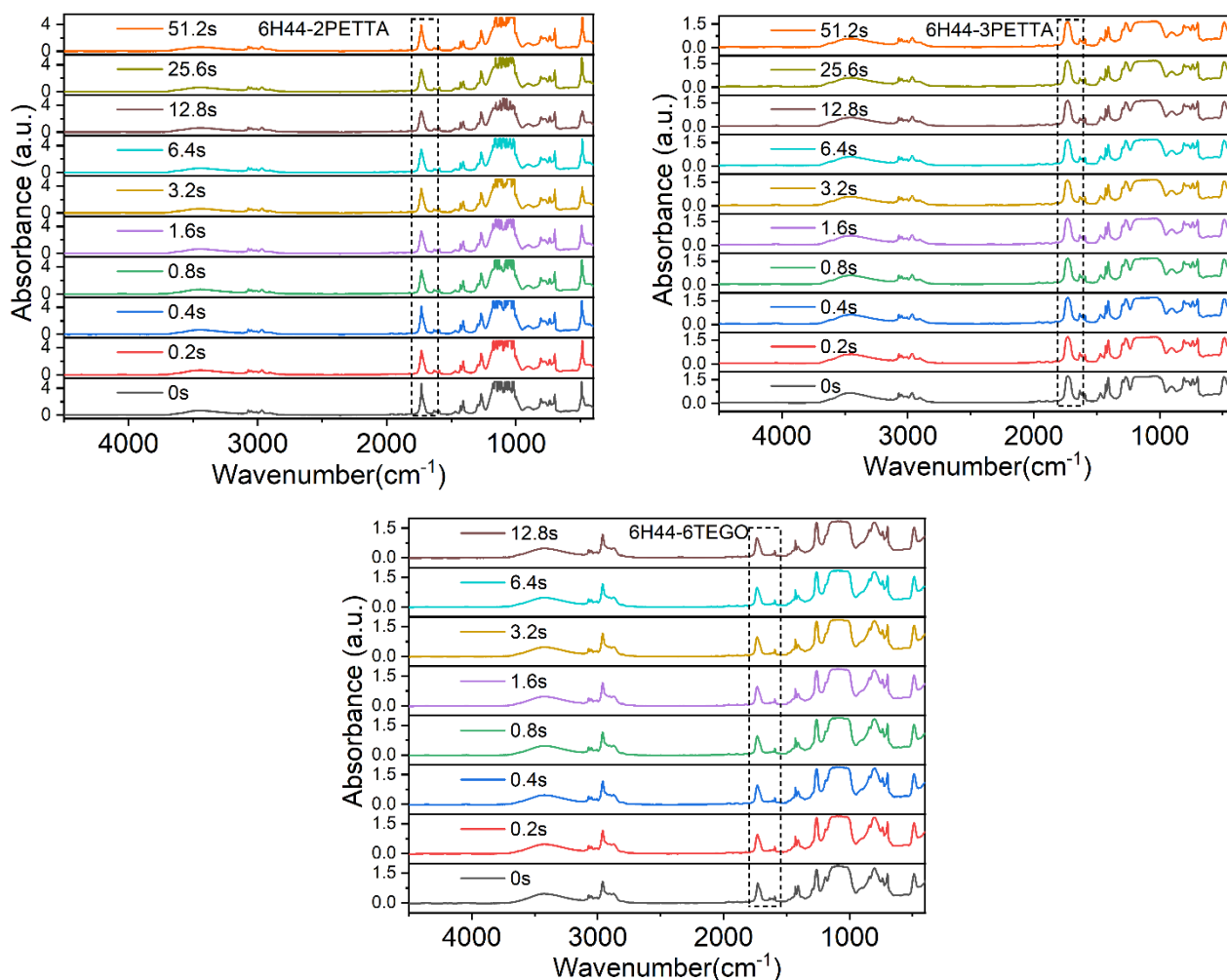
$$\alpha(t) = \left( 1 - \frac{\frac{A_{\text{C=C}}^0}{A_{\text{C=O}}^0}}{\frac{A_{\text{C=C}}^t}{A_{\text{C=O}}^t}} \right) \cdot 100\% \quad \text{Eq. (4.X)}$$

Where  $A_{\text{C=C}}^0/A_{\text{C=O}}^0$  is the integral area of  $\text{C=C/C=O}$  peak before exposure to UV,  $A_{\text{C=C}}^t/A_{\text{C=O}}^t$  at exposure time  $t$ .

**Fig. 4.42** show the changes in the conversion rate of  $\text{C=C}$  as function of ultraviolet irradiation times. The results also show that the conversion rate of all inks grows rapidly within the first 8 seconds and

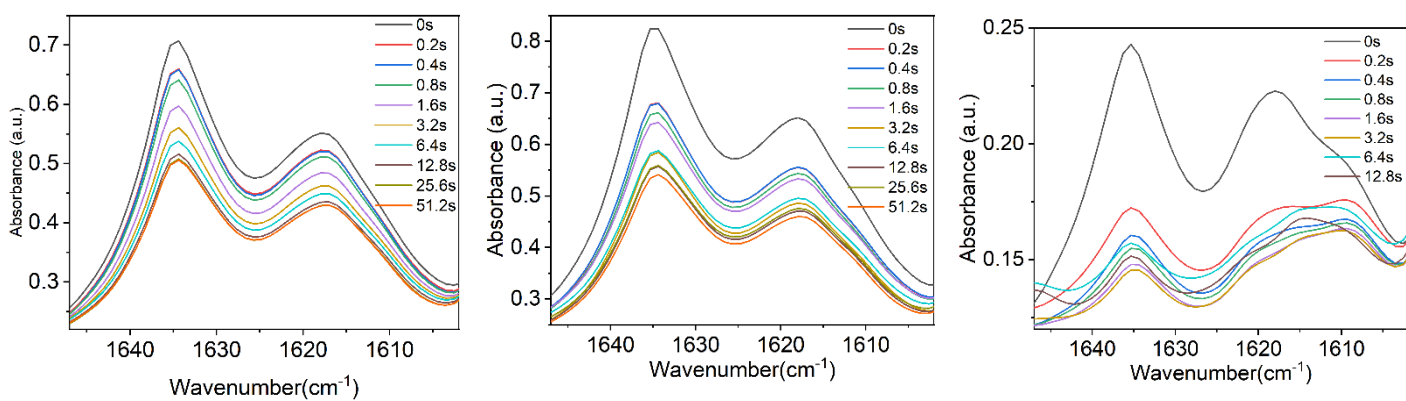
then decreases the growth rate. The conversion rate of 6H44-6TEGO-4% is better than that of the other two inks, it reaches 100% after 30 s of irradiation, while the other two PETTA-containing inks only reach 45%. This may be due to the high amount of photopolymer present in the mixture and therefore also of the photoinitiator, which allows a better conversion of the functional groups. Or it could be due to the fact that the photoinitiator Irgacure 819 has a greater activity with the TEGO component than PETTA, which perhaps requires the use of co-initiators, such as borate salt<sup>138</sup>.

After pyrolysis at 1000°C, the dehydrogenation of the sample was completed, leaving only the wide absorption peaks of Si–O–Si and Si–C bonds, in the range 1000-1200 cm<sup>-1</sup>. A large number of organic carbon chains in the cross-linked network were decomposed and the densification degree is greatly enhanced. The results indicate that the transformation of organic to inorganic has been completed.

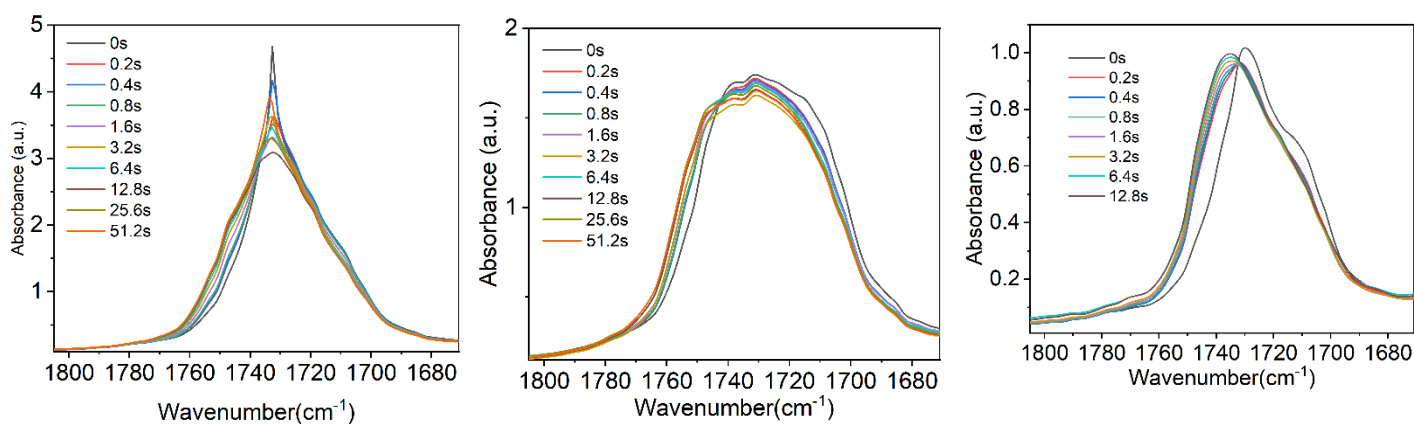


**Figure 4.40.** Infrared absorption spectra of the ink during the light-curing process.

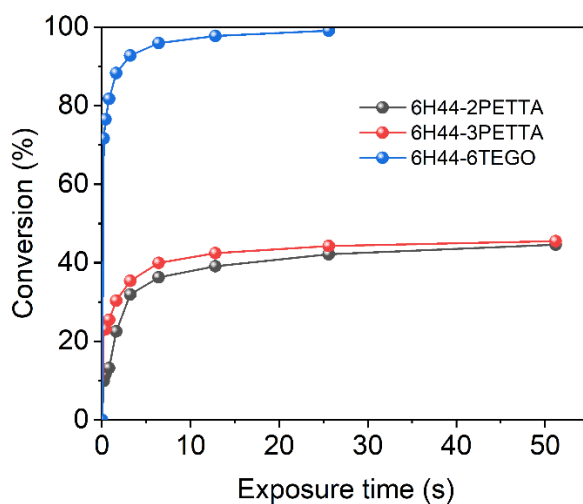




**Figure 4.41.a.** FTIR spectrum in the region 1602-1647 cm<sup>-1</sup>. Inks 6H44-2PETTA-4% (left), 6H44-3PETTA-4% (center) and 6H44-6TEGO-4% (right).



**Figure 4.41.b.** FTIR spectrum in the region 1761-1805 cm<sup>-1</sup>. Inks 6H44-2PETTA-4% (left), 6H44-3PETTA-4% (center) and 6H44-6TEGO-4% (right).



**Figure 4.42.** Conversion rate of C=C as function of ultraviolet irradiation times.

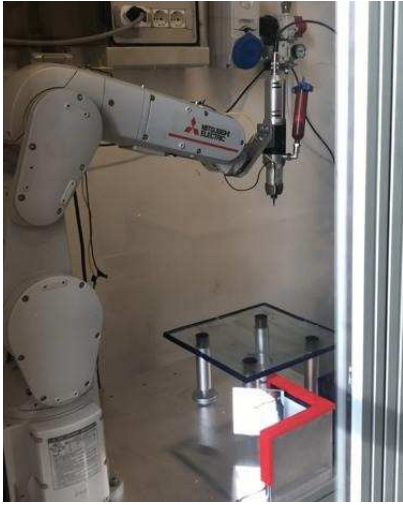
### 4.3 – Robotic arm and complex structures

This section briefly reports two uses of the optimized inks different from those seen previously: the first consists in the use of a different printing method, a robotic arm, while the second concerns the possibility of obtaining a different shape for the green body printed before heat treatment. These tests were carried out at the end of the thesis work period in the laboratory so they do not present any claims of completeness; however, they show alternative approaches on which further work can be done.

#### 4.3.1 – Robotic arm

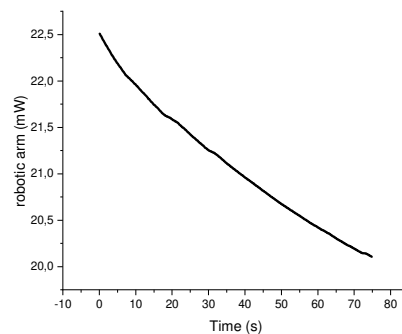
In the last part of this work we tried to print the inks with the use of a robotic arm, shown in **Fig. 4.43**. The advantage of using a robotic arm is the fact that it is possible to print extremely complex geometries that do not present any constraints regarding the movement of the nozzle. In fact, when using the printer, the range of printable geometries was reduced due to the fact that no downward movements of the nozzle were allowed, since its descent would have damaged the structure just printed, due to the encumbrance of the UV setup or of the nozzle itself; it is therefore possible to print only structures that develop on a plane or that rise gradually. The robotic arm, on the other hand, allows complete freedom of movement in space by being able to rotate on multiple axes and in multiple directions. It was equipped with a system of LEDs arranged in a circular manner around the nozzle in order to enable curing exactly at the exit point. Unlike what happened during the use of the printer, in which the pressure was set and the printing speed was varied, in this system the extrusion speed and the movement speed of the arm are correlated and optimized.

The arm consists of a series of joints capable of providing different degrees of freedom, an extrusion head to which the syringe containing the ink is connected, a transparent substrate and a nozzle cleaning system consisting of sponges soaked in solvent. Before starting printing, it is important to adjust the height of the arm with respect to the substrate, its configuration in the center of the plate and adjust the speed in each section of the path. The LED system is turned on only during the construction of the filament and not in the movement paths from one point to another of the structure or when cleaning the nozzle; it is in fact a good idea to clean the nozzle after each single printed filament and before printing greasing the tip with oil to avoid sticking. The intensity of the UV light used was about 23 mW, similar to that of the UV setup after the addition of the cooling system: a higher intensity caused the LEDs to flicker and break due to overheating. All three compositions were rehearsed. A horizontal filament was printed against the substrate to evaluate how the three inks reacted. The composition 6H44-6TEGO-4%PI was not suitable. Its viscosity is too low, it fails to form a continuous filament, drops form and in printing vertical filaments it is unable to produce a constant filament that sustains itself. The composition 6H44-2PETTA-4%PI was then tested: it is not optimal; the printed filaments are excessively soft and the vertical filaments do not retain their shape; this can be caused by a low photopolymer content. The composition 6H44-3PETTA-4%PI was the best: continuous horizontal and also vertical filaments with a height greater than 5 cm were printed, able to maintain the shape, in **Fig. 4.44**. It was therefore chosen for subsequent tests.

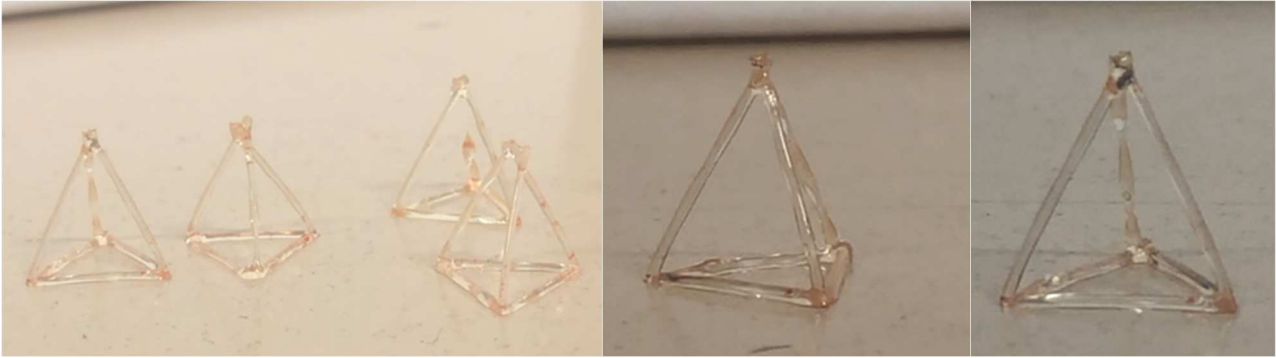


**Figure 4.43.** Robotic Arm (left). **Figure 4.44.** Vertical filament (10 cm, 0.4 mm/min), (right).

Therefore, vertical filaments were initially printed, to evaluate what was the appropriate printing speed. The initial speed tested was 2.5 mm/s. The 4 cm high filaments were able to maintain verticality, but were extremely soft. At 1.25 mm/s the diameter of the printed filament measured with the digital caliper was 0.58 mm equal to that of the nozzle used. By further decreasing the speed to 1 or 0.8 mm/s the structure retained its shape and became more rigid, particularly if an additional 10 s curing time was added after printing. The part of the filament that is more attached to the base is more rigid than the final one: this could be due to the fact that the UV light drops in intensity during the printing process. As in the spirals there was a progressive increase in the diameter of the track due also to the lower intensity of UV radiation which caused a slower curing and therefore a lower shape fidelity; a lower intensity can cause a lower degree of curing and therefore greater flexibility. In **Fig. 4.45** the graph shows how the intensity of UV radiation decreases as a function of time. At a speed lower than 0.4 mm/s the nozzle is too slow and there are obstruction problems. After the optimization phase of the printing parameters, it was decided to print simple 3D structures. The printed structures are tetrahedral and are represented in **Fig. 4.46**.



**Figure 4.45.** The intensity of the UV radiation decreases as a function of the time measured with the power meter (Thorlabs, PM400 Optical Power Meter), (right).



**Figure 4.46.** Tetrahedra printed with the robotic arm.

The triangular base was printed at 4 mm/s to avoid clogging of the nozzle and the inclined filaments at a speed of 0.8 mm/s. From the image you can see that the shape is maintained, in the vertices the material is cohesive and homogeneous even though it comes from three or more distinct traces; the filaments are straight and uniform with the exception of the last which is slightly deformed. This was caused by instability of the ink, as if it became more liquid as printing proceeded and therefore it was necessary to go to higher speeds (1.2 mm/s). The samples were then placed in a UV oven for 15 minutes for complete curing.

These tests were carried out to evaluate the behaviour of the inks in a different printing system that allows the creation of extremely complex geometries. The 6H44-3PETTA-4%PI ink has proven to be suitable for the creation of articulated structures. Continuing on this path, the next step will be to evaluate the resistance to heat treatment of the samples and their mechanical properties to then arrive at the realization of more complex structures.

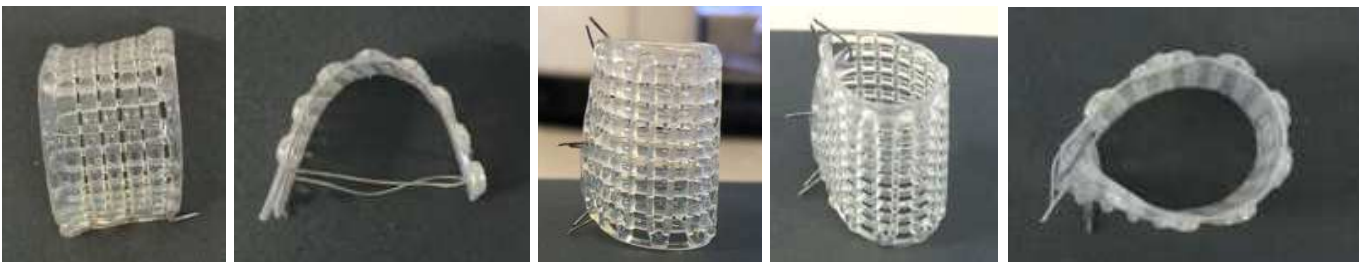
#### 4.3.2 – Complex structures

The samples printed with ink containing TEGO had the disadvantage of being not very rigid and therefore more subject to deformation than those deriving from the other two optimized inks. This flexibility feature was instead exploited for the creation of complex structures capable of being formed after printing and before the pyrolysis treatment. Generally, the inherent brittleness and high hardness of ceramics after pyrolysis, resulting from their ionic or covalent bond, limit their further reconfiguration toward more intricate shapes<sup>139</sup>. A potential alternative is performing the reconfiguration towards the selected architecture using a flexible green body before pyrolysis<sup>139</sup>. To this end, Liu *et al.*<sup>140</sup> printed flexible preceramic parts enhanced by nano particles, and obtained high-resolution complex and mechanically robust ceramics with the use of origami technique. The Origami technique has also been used in the work of Huang *et al.*<sup>139</sup> for the production of SiOC ceramics with intricate 3D morphologies, by additive manufacturing and precisely origami technique, taking advantage of the high printability and flexibility of a commercially available silicone elastomer. Secondary shaping using origami of different 2D layers with varied design, allowed the manufacturing of spiral, flower-like and polyhedron architectures, which are difficult to fabricate without adding supports or by any conventional ceramic fabrication processes. Produced samples showed no cracks or pores and fully retained the given shape after pyrolysis.

The idea was therefore to re-propose this approach using the 6H44-6TEGO-4%PI ink. Flexible green bodies were printed, which underwent a reconfiguration before undergoing the pyrolysis treatment. Threads of 10 cm length were printed which were folded and tied in a simple knot or a double knot, as shown in **Fig. 4.47**. They can maintain the knotted shape even if they have a tendency to return to their original straight configuration and therefore it is not possible to form a small slot; a too small radius of curvature leads to the breaking of the filament. We waited a few days before putting them in the oven and only two samples showed events of breaking or complete opening of the knot, the rest kept the shape well. Small rectangular sheets were also printed consisting of two orthogonal layers which were subsequently folded using wire to make them maintain the “arch” and cylinder structure, as shown in **Fig. 4.48**.



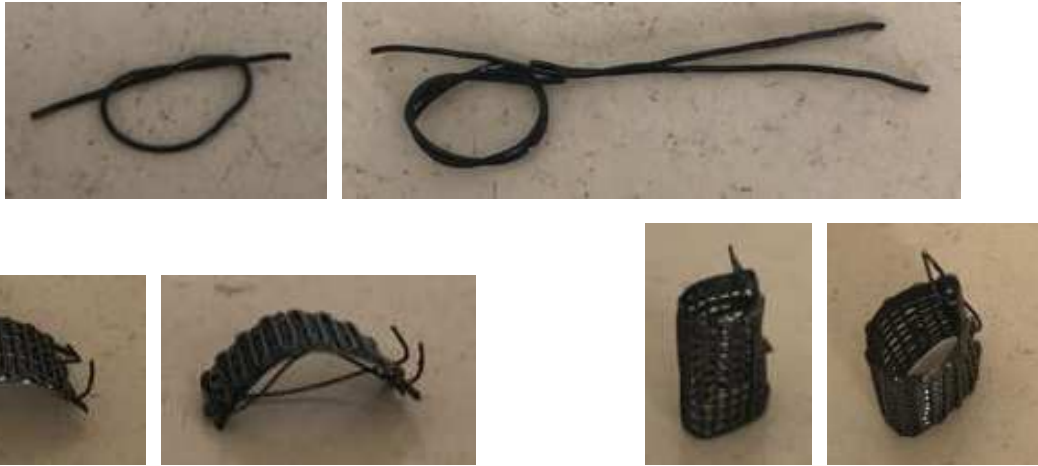
**Figure 4.47.** Non-pyrolyzed knots.



**Figure 4.48.** Arched and cylindrical structures.

The samples were then subjected to the pyrolysis heat treatment at 1000°C. In **Fig. 4.49** the pyrolyzed samples are shown. It can be seen that there have been no drastic ruptures of the structures which are able to maintain sufficiently their shape. The danger was in fact that during the pyrolysis, the onset of cracks could occur especially in the points of greatest curvature, where there could be residual tensile stresses that could cause differential shrinkage and breakage. The structures, on the other hand, are intact and the shrinkage is isotropic. The filaments of the nodes exhibit greater deformations than the structures made up of the layers that instead keep their shape well, perhaps due to the presence of more material.

Continuing on this path, the next work steps are the SEM analysis of the structures to evaluate the integrity of the filament and the possible occurrence of microcracks that would drastically affect the mechanical properties, especially in the contact areas between the two layers and in the tensioned parts. In conclusion, therefore, this approach can be useful for the creation of very complex structures, which can be modeled on request for a specific purpose.



*Figure 4.49. Pyrolyzed samples.*

## Chapter 5

### Conclusions

This thesis work focused on the development and optimization of a preceramic polymer-based ink to be used in the UV Assisted Direct Ink Writing technique. In order to be reactive to UV light and thus give rise to the polymerization and solidification process of the material upon exposure to UV, the mixture must contain a photosensitive polymer. It must also contain a preceramic polymer with a high ceramic content to ensure adequate ceramic yield of the pyrolyzed pieces and avoid excessive deformation and shrinkage. The process of selecting and optimizing the components of the mixture has led to the obtaining of three inks capable of giving rise to free form printed structures self-sustaining. The three optimal compositions are as follows: 6H44-4PETTA-4%PI, 6H44-3PETTA-4%PI and 6H44-6TEGO-4%PI, in which the preceramic polymer with high ceramic content is H44, a silicone resin containing phenyl- methyl side groups, the photopolymers are TEGO and PETTA and the photoinitiator necessary to start the polymerization is in all three cases Irgacure 819, inserted at 4 wt.% with respect to the photopolymer. During the optimization process it was evaluated how the photopolymer and photoinitiator content influenced the printability and shape fidelity of the printed structures. The next step was the optimization of the printing parameters, in particular the printing speed and pressure of extrusion. These two parameters are intimately linked and to obtain structures with good geometric accuracy and shape fidelity to Gcode files, it is important to find the right combination. For all three inks suspended spirals were printed at different speeds and pressures to understand how the size of the filament was changed: at higher pressures, higher speeds are required to obtain valid structures and at the same pressure an increase in speed leads to a decrease of the filament diameter. During printing, problems such as the presence of bubbles inside the ink and the phenomenon of die swelling had to be faced. The samples were subsequently pyrolyzed at 1000°C to evaluate their resistance to heat treatment. All three compositions resist pyrolysis giving rise to ceramic components of SiOC composition. The inks have been characterized from a rheological and photorheological point of view: they show practically Newtonian and non-viscoelastic behaviour. Although therefore they are not shear-thinning as required by most DIW inks, they are suitable for this technique. From the point of view of photorehology, the gelation point was evaluated in relation to the intensity of the UV light and the cure depth. The ink 6H44-6TEGO-4%PI is the fastest to cure of the three and the FTIR analysis for the evaluation of the conversion rate of vinyl groups under different UV exposure time, shows how it reaches a degree of conversion of 100% compared to 45% of PETTA-containing inks. Scaffold structures were printed to evaluate shrinkage after heat treatment, density and mechanical properties of materials. They show good shape retention after pyrolysis and isotropic shrinkage along x, y, and z about 20% for the two compositions containing PETTA and about 35% for the composition containing TEGO, probably due to the high photopolymer content in the mixture in the last composition. Individual filaments undergo greater shrinkage. The mechanical properties have been evaluated with a compression test and the specimens have been shown to withstand maximum stresses up to 15 MPa. SEM analysis show that there are no onset of micro-cracks or defects, except porosity due to air bubbles, during the heat treatment, even in the

most critical points of the scaffolds. They also highlight the ability of the inks to create structures with suspended filaments that do not show sagging effects, even if for distances of 1-2 mm. The deflection of the filaments was also studied in green bodies with the A test. 6H44-3PETTA-4%PI ink is the most suitable for making suspended filaments. The TGA thermal analysis highlighted that the behaviour of the inks derives from a combination of the behaviour of the constituents of the mixture, and that the ceramic content of the pyrolyzed pieces decreases by 45% for the 6H44-3PETTA-4 ink %PI at 35% for 6H44-6TEGO-4%PI ink. Although the loss in mass is considerable, the pieces demonstrate good shape and mechanical properties. XRD analysis has shown that the samples obtained after pyrolysis are completely amorphous ceramic components. In the last part of the thesis work, two different approaches were experimented: the use of a robotic arm as a printing technique that allows greater freedom in the choice of geometries, and the use of the ink 6H44-6TEGO-4%PI, which green bodies are flexible, to incorporate a further modeling step before pyrolysis after printing for the realization of complex structures. In general, developments and a continuation for this work can address the further optimization of the inks, for example with the addition of stabilizers or co-initiators, in solving the problems encountered, such as the presence of bubbles in the ink and their instability, further analysis for a more complete understanding of the phenomena and openness to new approaches.



Appendix

# Appendix

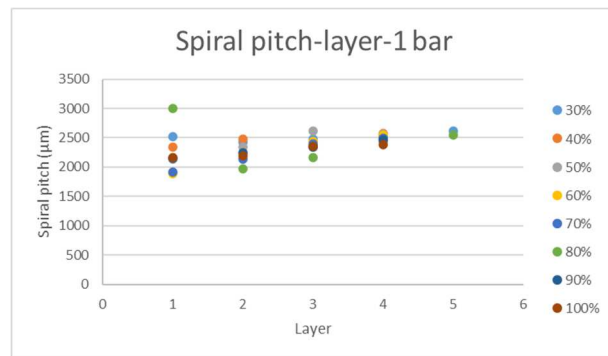
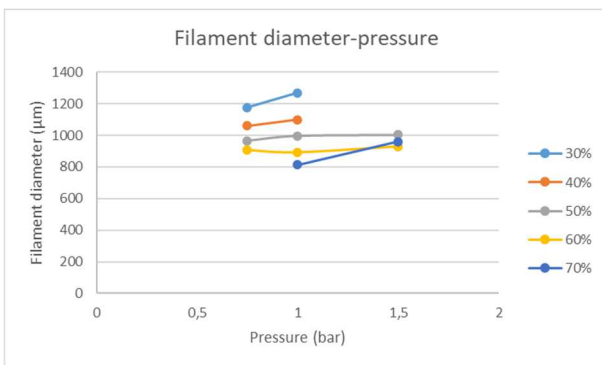
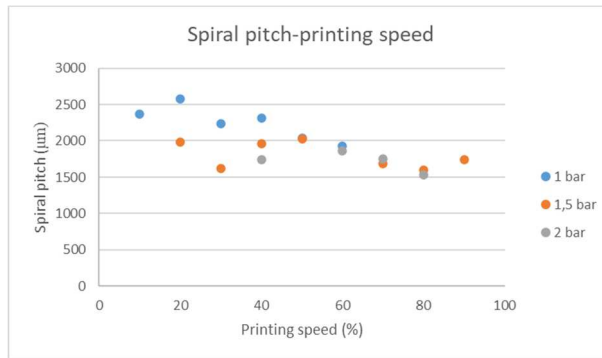
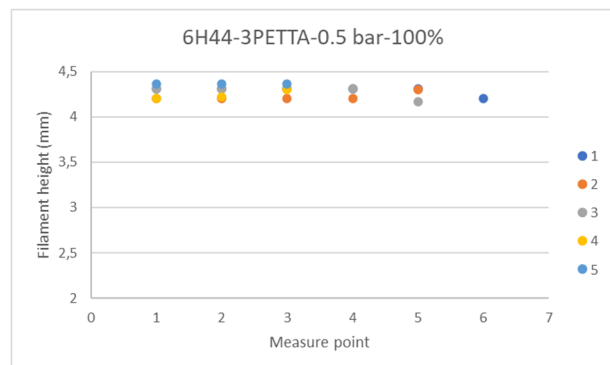
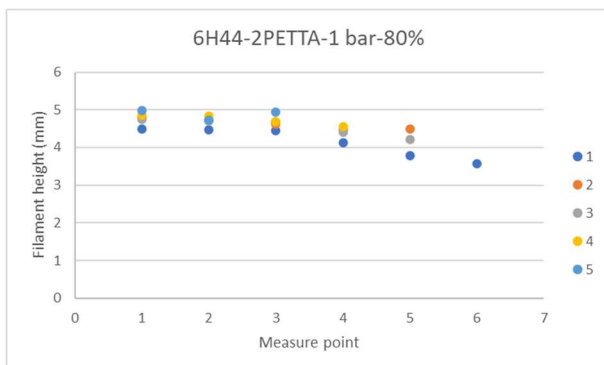


Figure 4.1.A. Above graph relating to the ink 6H44-2PETTA-2%PI. Below graphs relating to 6H44-3PETTA-4%PI ink.

	Diameters of the various filaments (mm)									
	1	2	3	4	5	6	7	8	9	10
A	0.71	0.71	0.65	0.70	0.82	O	0.97	0.95	0.99	O
B	0.69	0.69	0.62	0.70	0.79	O	0.85	0.86	0.92	O
C	0.50	0.59	0.56	0.63	0.67	0.76	0.77	0.86	0.92	O
D	1.07	0.88	0.85	0.81	0.76	O	0.72	0.69	0.67	0.65

Table 4.1.A. Values of the diameters in the various sections of the free-form structure printed with 6H44-3PETTA-4%PI ink. The values are the average ones from a series of measurements. O means the filament was wavy. 1 is the vertical filament at the bottom, 10 is the vertical filament at the top, the numbers follow the printing direction.



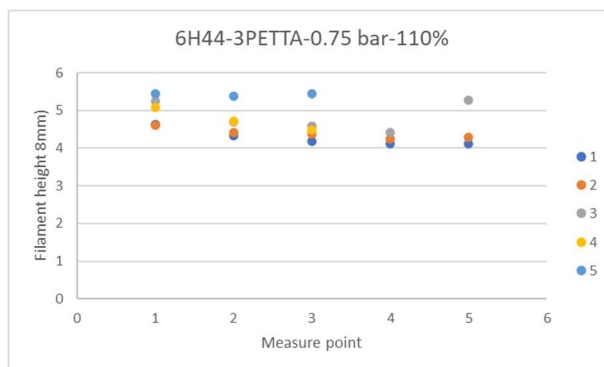


Figure 4.2.A. Comparison between the filaments of different lengths in the “A” test.

Exposure time [s]	Cure depth [mm]		
	6H44_2PETTA	6H44_3PETTA	6H44_6TEGO
1	0.04	0.08	0.19
1.5	0.07	0.14	0.23
2	0.09	0.18	0.29
2.5	0.11	0.29	0.36
3	0.23	0.36	0.42
3.5	0.27	0.42	0.47
4	0.29	0.52	0.56
4.5	0.30	0.61	0.68
5	0.37	0.72	0.76
5.5	0.40	0.81	0.85
6	0.48	0.85	0.92
6.5	0.52	0.88	1
7	0.54	0.94	1.2
7.5	0.62	-	
8	0.68	1.07	
8.5	0.72	-	
9	0.76	1.48	
9.5	0.85	-	
10	0.96	1.8	
10.5	1.0		
11	1.2		
11.5	1.49		

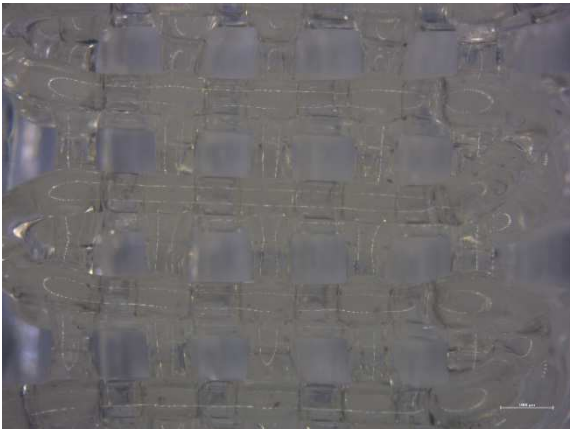
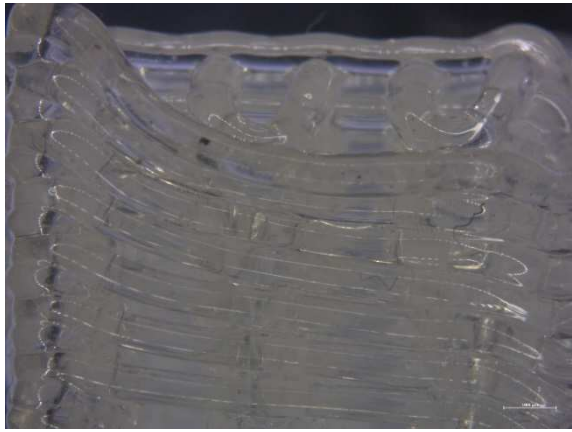
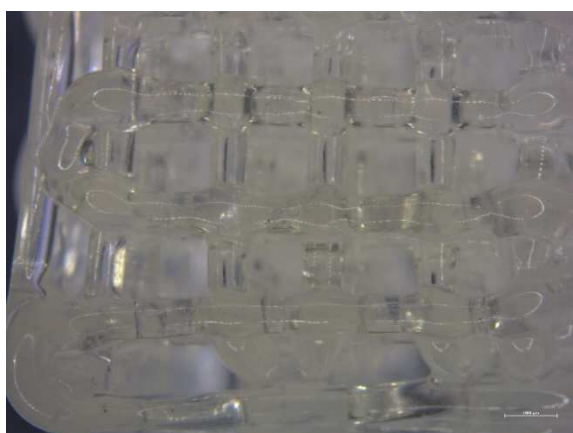

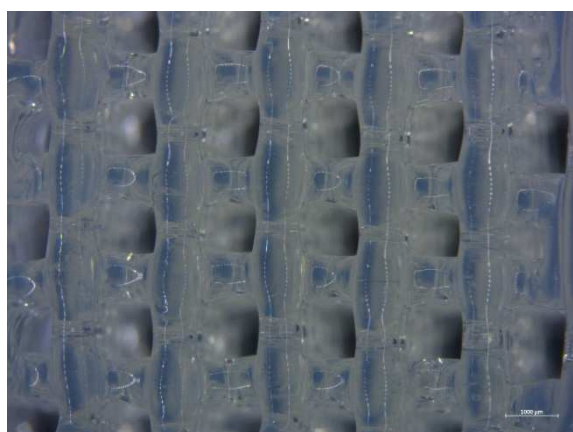
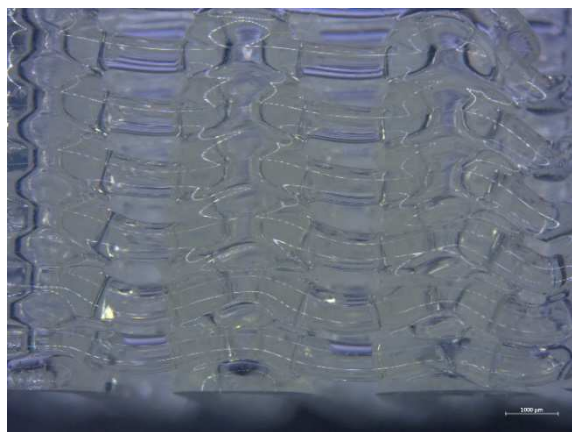
Table 4.2.A. Cure depth as a function of exposure time at UV light.

6H44-2PETTA-4%PI	X	Y	Z	Single filament (view from side)	Single filament (view from above)
A2	13.08 %	17.05 %	14.97 %	36.96 %	32.73 %
B2	18.94 %	19.38 %	5.04 %	34.52 %	35.80 %
C2	19.53 %	20.93 %	16.48 %	27.73 %	37.68 %
D2	23.44 %	20.05 %	24.90 %	40.24 %	31.29 %
E2	22.07 %	20.27 %	21.49 %	32.42 %	39.55 %
F2	25.39 %	22.83 %	22.65 %	27.72 %	36.81 %
G2	25.91 %	23.81 %	26.22 %	28.44 %	37.16 %
H2	26.25 %	25.59 %	26.35 %	33.50 %	42.09 %
Mean	21.83 %	21.24 %	19.76 %	32.69 %	36.64 %

6H44-3PETTA-4%PI	X	Y	Z	Single filament (view from above)	Single filament (view from side)
A3	26.15 %	24.03 %	16.47 %	37.06 %	27.90 %
B3	18.182 %	15.38 %	9.66 %	40.08 %	34.71 %
C3	22.31 %	21.54 %	24.86 %	37.86 %	35.03 %
D3	25.86 %	24.80 %	25.34 %	37.51 %	41.40 %
E3	17.77 %	15.58 %	18.99 %	36.99 %	42.09 %
F3	15.74 %	16.28 %	18.98 %	31.78 %	35.95 %
G3	24.54 %	25.07 %	27.76 %	38.53 %	31.18 %
H3	14.50 %	22.92 %	19.33 %	35.91 %	53.62 %
Mean	20.63 %	20.70 %	20.17 %	36.96 %	37.74 %

6H44-6TEGO-4%PI	X	Y	Z	Single filament (view from above)	Single filament (view from side)
A	37.01 %	37.43 %	36.73 %	42.93 %	47.48 %
B	36.51 %	37.30 %	31.56 %	43.21 %	47.72 %
C	34.01 %	33.33 %	35.12 %	45.66 %	44.57 %
D	36.20 %	36.55 %	32.41 %	52.16 %	42.65 %
E	33.67 %	34.87 %	33.01 %	33.35 %	40.55 %
Mean	35.48 %	35.90 %	33.77 %	43.46 %	44.60 %

**Table 4.3.A.** Shrinkage data.

Ink	Top view	Lateral view
6H44-2PETTA-4%PI		
6H44-3PETTA-4%PI		
6H44-6TEGO-4%PI		

**Figure 4.3.A.** Scaffolds realized with non-optimized printing parameters.

6H44-3PETTA-4%PI	Vol (cm <sup>3</sup> )	$\rho_s$ (g/cm <sup>3</sup> )	T (°C)	Vol (cm <sup>3</sup> )	$\rho_t$ (g/cm <sup>3</sup> )	T (°C)
1	0.0495	1.6652	29.041	0.0525	2.2115	29.107
2	0.0488	1.6800	29.042	0.0542	2.1413	29.106
3	0.0500	1.6392	29.044	0.0553	2.0972	29.105
4	0.0493	1.6617	29.047	0.0550	2.1082	29.106
5	0.0498	1.6474	29.049	0.0561	2.0670	29.105

6H44-2PETTA-4%PI	Vol (cm <sup>3</sup> )	$\rho_s$ (g/cm <sup>3</sup> )	T (°C)	Vol (cm <sup>3</sup> )	$\rho_t$ (g/cm <sup>3</sup> )	T (°C)
1	0.0457	1.6840	28.992	0.0607	2.0924	29.099
2	0.0470	1.6392	28.992	0.0600	2.1184	29.099
3	0.0457	1.6854	28.992	0.0601	2.1118	29.099
4	0.0469	1.6431	28.995	0.0596	2.1316	29.100
5	0.0466	1.6527	28.996	0.0603	2.1073	29.099

6H44-6TEGO-4%PI	Vol (cm <sup>3</sup> )	$\rho_s$ (g/cm <sup>3</sup> )	T (°C)	Vol (cm <sup>3</sup> )	$\rho_t$ (g/cm <sup>3</sup> )	T (°C)
1	0.0743	1.7235	29.084	0.0626	2.0283	29.115
2	0.0725	1.7657	29.083	0.0616	2.0632	29.115
3	0.0730	1.7542	29.084	0.0639	1.9863	29.115
4	0.0739	1.7317	29.084	0.0645	1.9703	29.114
5	0.0736	1.7402	29.084	0.0645	1.9701	29.115

**Table 4.4.A.** Density measurements.

Specimen	Stress (MPa)	Strain (%)
6H44-2PETTA-4%PI-A	5.190	2.420
6H44-2PETTA-4%PI-B	8.295	1.000
6H44-2PETTA-4%PI-C	7.972	1.087
6H44-2PETTA-4%PI-D	4.866	1.027
6H44-2PETTA-4%PI-E	4.840	1.995
6H44-3PETTA-4%PI-A	5.511	1.264
6H44-3PETTA-4%PI-B	4.802	1.735
6H44-3PETTA-4%PI-C	4.150	2.944
6H44-3PETTA-4%PI-D	4.925	1.426
6H44-6TEGO-4%PI-A	18.892	4.263
6H44-6TEGO-4%PI-B	19.394	6.022
6H44-6TEGO-4%PI-C	12.743	5.230
6H44-6TEGO-4%PI-D	12.758	2.371

**Table 4.5.A.** Values of mechanical properties.

## Bibliography

1. Stuecker J. N., Miller J. E., Ferrizz R. E., Mudd J. E., Cesarano J. Advanced Support Structures for Enhanced Catalytic Activity. *Ind. Eng. Chem. Res.* 2004; 43, 51-55.
2. Rau D. A., Herzberger J., Long T. E., Williams C. B. Ultraviolet-Assisted Direct Ink Write to Additively Manufacture All-Aromatic Polyimides. *ACS Appl. Mater. Interfaces.* 2018; 10, 34828-34833.
3. Pierin G., Grotta C., Colombo P., Mattevi C. Direct Ink Writing of micrometric SiOC ceramic structures using a preceramic polymer. *J. Eur. Ceram. Soc.* 2016; 36, 1589-1594.
4. Jiménez M., Romero L., Domínguez I. A., Espinosa M. D. M., Domínguez M. Additive Manufacturing Technologies: An Overview about 3D Printing Methods and Future Prospects. *Hindawi, Complexity*, 2019.
5. Gibson I., Rosen D., Stucker B., Khorasani M. Additive Manufacturing Technologies, Third edition, *Springer*.
6. Travitzky N., Bonet A., Dermeik B., *et al.* Additive manufacturing of ceramic-based materials. *Adv. Eng. Mater.* 2014; 16 (6), 729-754.
7. Zocca A., Colombo P., Gomes C. M., Günster J. Additive Manufacturing of Ceramics: Issues, Potentialities, and Opportunities. *J. Am. Ceram. Soc.* 2015; 98 (7), 1983-2001.
8. Zocca A., Gomes C. M., Staude A., Bernardo E., Günster J., Colombo P. SiOC ceramics with ordered porosity by 3D-printing of a preceramic polymer. *J. Mater. Res.* 2013, 28 (17), 2243-2252.
9. Friedel T., Travitzky N., Niebling F., Scheffler M., Greil P. Fabrication of polymer derived ceramic parts by selective laser curing. *J. Eur. Ceram. Soc.* 2005; 25, 193-197.
10. Pham T. A., Kim D. P., Lim T. W., Park S. H., Yang D. Y., Lee K. S. Three-dimensional SiCN ceramic microstructures via nano-stereolithography of inorganic polymer photoresists. *Adv. Funct. Mater.* 2006; 16(9), 1235-1241.
11. Schmidt J., Colombo P. Digital light processing of ceramic components from polysiloxanes. *J. Eur. Ceram. Soc.* 2018; 38 (1), 57-66.
12. Dermeik B., Travitzky N. Laminated Object Manufacturing of Ceramic-Based Materials. *Adv. Eng. Mater.* 2020; 22 (9).
13. Hahn H. T. Thermomechanical analysis of the laminated object manufacturing (LOM) process. *Rapid. Prototyp. J.* 1999; 4 (1), 26-36.
14. Gomes C. M., Oliveira A. P. N., Hotza D., Travitzky N., Greil P. LZSA glass-ceramic laminates: Fabrication and mechanical properties. *J. Mater. Process. Technol.* 2008 206, 194-201.
15. Schindler K., Roosen A. Manufacture of 3D structures by cold low pressure lamination of ceramic green tapes. *J. Eur. Ceram. Soc.* 2009; 29 (5), 899-904.
16. Klosterman D., Chartoff R., Graves G., Osborne N., Priore B. Interfacial characteristics of composites fabricated by laminated object manufacturing. *Compos. Part A: Appl. Sci. Manuf.* 1998; 29 (9-10), 1165-1174.
17. Lakhdar Y., Tuck C., Binner J., Terry A., Goodridge R. Additive manufacturing of advanced ceramic materials. *Prog. Mater. Sci.* 2021; 116, 100736.

18. Mott M., Evans J. R. G. Solid freeforming of silicon carbide by inkjet printing using a polymeric precursor. *J. Am. Ceram. Soc.* 2001; 84, 307-313.
19. Cesarano robocasting.pdf.
20. Kalita S. J., Bose S., Hosick H. L., Bandyopadhyay A. Development of controlled porosity polymer-ceramic composite scaffolds via fused deposition modeling. *Mater. Sci. Eng. C.* 2003; 23, 611-620.
21. Bandyopadhyay A., Panda R. K., Janas V. F., Agarwala M. K., Danforth S. C., Safari A. Processing of piezocomposites by fused deposition technique. *J. Am. Ceram. Soc.* 1997; 80 (6), 1366-1372.
22. Chabera P., Boczkowska A., Witek A., Oziębło A. Fabrication and characterization of composite materials based on porous ceramic preform infiltrated by elastomer. *Bull. Polish Acad. Sci. Tech. Sci.* 2015; 63 (1), 193-199.
23. Del-Mazo-Barbara L., Ginebra M. P. Rheological characterisation of ceramic inks for 3D direct ink writing: A review. *J. Eur. Ceram. Soc.* 2021; 41 (16), 18-33.
24. Golafshan N., Vorndran E., Zaharievski S., *et al.* Tough magnesium phosphate-based 3D-printed implants induce bone regeneration in an equine defect model. *Biomaterials.* 2020; 261.
25. Minas C., Carnelli D., Tervoort E., Studart A. R. 3D Printing of Emulsions and Foams into Hierarchical Porous Ceramics. *Adv. Mater.* 2016; 28, 9993-9999.
26. Peng E., Zhang D., Ding J. Ceramic Robocasting: Recent Achievements, Potential, and Future Developments. *Adv. Mater.* 2018; 30, 1802404.
27. Zocca A., Franchin G., Elsayed H., *et al.* Direct Ink Writing of a Pre-ceramic Polymer and Fillers to Produce Hardystonite (Ca<sub>2</sub>ZnSi<sub>2</sub>O<sub>7</sub>) Bioceramic Scaffolds. *J. Am. Ceram. Soc.* 2016; 99, 1960-1967.
28. Kousaalya A. B., Kumar R., Sridhar B. T. N. Thermal conductivity of precursor derived Si-B-C-N ceramic foams using Metroxylon sagu as sacrificial template. *Ceram. Int.* 2015; 41, 1163-1170.
29. Li Y. H., Ahn K. D., Kim D.P. Synthesis and properties of UV curable polyvinylsilazane as a precursor for micro-structuring. *Polym. Adv. Technol.* 2015; 26, 245-249.
30. Chen H., Wang X., Xue F., Huang Y., Zhou K., Zhang D. 3D printing of SiC ceramic: Direct ink writing with a solution of pre-ceramic polymers. *J. Eur. Ceram. Soc.* 2018; 38 (16), 5294-5300.
31. Fiocco L., Elsayed H., Badocco D., *et al.* Direct ink writing of silica-bonded calcite scaffolds from pre-ceramic polymers and fillers. *Biofabrication.* 2017; 9 (2).
32. Zhou S., Mei H., Chang P., Lu M., Cheng L. Molecule editable 3D printed polymer-derived ceramics. *Coord. Chem. Rev.* 2020; 422, 213486.
33. Liao J., Chen H., Luo H., Wang X., Zhou K., Zhang D. Direct ink writing of zirconia three-dimensional structures. *J. Mater. Chem. C.* 2017; 5, 5867-5871.
34. Compton B. G., Lewis J. A. 3D-printing of lightweight cellular composites. *Adv. Mater.* 2014; 26, 5930-5935.
35. Guo S. Z., Gosselin F., Guerin N., Lanouette A.M., Heuzey M.C., Therriault D. Solvent-cast three-dimensional printing of multifunctional microsystems. *Small.* 2013; 9, 4118-4122.
36. Ellis J., Mavromatos N. E., Nanopoulos D. V., Sakharov A. S. Cosmology: Synchrotron radiation and quantum gravity. *Nature.* 2004; 428.
37. Maeng W. Y., Jeon J. W., Lee J. Bin, Lee H., Koh Y. H., Kim H. E. Photocurable ceramic/monomer feedstocks containing terpene crystals as sublimable porogen for UV curing-assisted 3D plotting. *J. Eur. Ceram. Soc.* 2020; 40 (9), 3469-3477.
38. Chen K., Kuang X., Li V., Kang G., Qi H. J. Fabrication of tough epoxy with shape memory effects by UV-assisted direct-ink write printing. *Soft Matter.* 2018; 14, 1879-1886.

39. Ligon S. C., Liska R., Stampfl J., Gurr M., Mülhaupt R. Polymers for 3D Printing and Customized Additive Manufacturing. *Chem. Rev.* 2017; 117, 10212-10290.
40. De Marzi A., Giometti G., Erler J., Colombo P., Franchin G. Hybrid additive manufacturing for the fabrication of freeform transparent silica glass components. *Addit. Manuf.* 2022; 54, 102727.
41. Jiang F., Drummer D. Curing kinetic analysis of acrylate photopolymer for additive manufacturing by photo-DSC. *Polymers.* 2020; 12, 1-11.
42. Chen K., Zhang L., Kuang X., *et al.* Dynamic Photomask-Assisted Direct Ink Writing Multimaterial for Multilevel Triboelectric Nanogenerator. *Adv. Funct. Mater.* 2019; 29, 1903568.
43. Moraes R. R, Garcia J. W., Barros M. D., *et al.* Control of polymerization shrinkage and stress in nanogel-modified monomer and composite materials. *Dent. Mater.* 2011; 27, 509-519.
44. Lin J. T., Liu H. W., Chen K. T., Cheng D. C. Modeling the Kinetics, Curing Depth, and Efficacy of Radical-Mediated Photopolymerization: The Role of Oxygen Inhibition, Viscosity, and Dynamic Light Intensity. *Front. Chem.* 2019; 7 (760).
45. Hoyle C. E., Bowman C. N. Thiol-ene click chemistry. *Angew. Chemie. Int. Ed.* 2010; 49, 1540-1573.
46. Ligon-Auer S. C., Schwentenwein M., Gorsche C., Stampfl J., Liska R. Toughening of photo-curable polymer networks: A review. *Polym. Chem.* 2016; 7, 257-286.
47. Gorsche C., Koch T., Moszner N., Liska R. Exploring the benefits of  $\beta$ -allyl sulfones for more homogeneous dimethacrylate photopolymer networks. *Polym. Chem.* 2015; 6, 2038-2047.
48. Steinmann B., Schulthess A. Radiation-Curable Liquid Composition for Stereolithography. *US*. Published online 1999, Patent Number: 5,972,563.
49. Xu C., Webb W. W. Measurement of two-photon excitation cross sections of molecular fluorophores with data from 690 to 1050 nm. *J. Opt. Soc. Am. B.* 1996; 13 (3).
50. Halloran J. W. Ceramic Stereolithography: Additive Manufacturing for Ceramics by Photopolymerization. *Annu. Rev. Mater. Res.* 2016; 46, 19-40.
51. Halloran J. W., Tomeckova V., Gentry S., *et al.* Photopolymerization of powder suspensions for shaping ceramics. *J. Eur. Ceram. Soc.* 2011; 31, 2613-2619.
52. Guo Y., Xu J., Yan C., *et al.* Direct Ink Writing of High Performance Architected Polyimides with Low Dimensional Shrinkage. *Adv. Eng. Mater.* 2019; 21, 1-8.
53. Wu T., Jiang P., Zhang X., *et al.* Additively manufacturing high-performance bismaleimide architectures with ultraviolet-assisted direct ink writing. *Mater. Des.* 2019; 180, 107947.
54. Wei L., Li J., Zhang S., *et al.* Fabrication of SiOC ceramic with cellular structure via UV-Assisted direct ink writing. *Ceram. Int.* 2020; 46, 3637-3643.
55. De Hazan Y., Penner D. SiC and SiOC ceramic articles produced by stereolithography of acrylate modified polycarbosilane systems. *J. Eur. Ceram. Soc.* 2017; 37, 5205-5212.
56. Zanchetta E., Cattaldo M., Franchin G., *et al.* Stereolithography of SiOC Ceramic Microcomponents. *Adv. Mater.* 2016; 28, 370-376.
57. Zak C. Eckel, Chaoyin Zhou, John H. Martin, Alan J. Jacobsen, William B. Carter, Tobias A. Schaedler. Additive manufacturing of polymer-derived ceramics. *Science.* 2016; 351(6268).
58. Colombo P., Mera G., Riedel R., Sorarù G. D. Polymer-derived ceramics: 40 Years of research and innovation in advanced ceramics. *J. Am. Ceram. Soc.* 2010; 93, 1805-1837.
59. Wen Q., Yu Z., Riedel R. The fate and role of in situ formed carbon in polymer-derived ceramics. *Prog. Mater. Sci.* 2020; 109, 100623.



60. Mixtures H., Silicon O. F. United States Patent, 1974; 3,853,567.
61. King D., Apostolov Z., Key T., Carney C., Cinibulk M. Novel processing approach to polymer-derived ceramic matrix composites. *Int. J. Appl. Ceram. Technol.* 2018; 15, 399-408.
62. Riedel R., Mera G., Hauser R., Kloneczynski A. Silicon-based polymer-derived ceramics: Synthesis properties and applications-A review. *J. Ceram. Soc. Japan.* 2006; 114 (6), 425-444.
63. Schulz M. Polymer derived ceramics in MEMS/NEMS - A review on production processes and application. *Adv. Appl. Ceram.* 2009; 108 (8).
64. Ionescu E., Sen S., Mera G., Navrotsky A. Structure, energetics and bioactivity of silicon oxycarbide-based amorphous ceramics with highly connected networks. *J. Eur. Ceram. Soc.* 2018; 38, 1311-1319.
65. Gao Y., Mera G., Nguyen H., Morita K., Kleebe H. J., Riedel R. Processing route dramatically influencing the nanostructure of carbon-rich SiCN and SiBCN polymer-derived ceramics. Part I: Low temperature thermal transformation. *J. Eur. Ceram. Soc.* 2012; 32, 1857-1866.
66. Mera G., Riedel R., Poli F., Müller K. Carbon-rich SiCN ceramics derived from phenyl-containing poly(silylcarbodiimides). *J. Eur. Ceram. Soc.* 2009; 29, 2873-2883.
67. Takeda M., Saeki A., Sakamoto J. I., Imai Y., Ichikawa H. Effect of hydrogen atmosphere on pyrolysis of cured polycarbosilane fibers. *J. Am. Ceram. Soc.* 2000; 83, 1063-1069.
68. Galusek D., Reschke S., Riedel R., *et al.* In-Situ Carbon Content Adjustment in Polysilazane Derived Amorphous SiCN Bulk Ceramics. *J. Eur. Ceram. Soc.* 1999; 19, 1911-1921.
69. Kleebe H. J., Blum Y. D. SiOC ceramic with high excess free carbon. *J. Eur. Ceram. Soc.* 2008; 28, 1037-1042.
70. Li X., Wang Y. Complex impedance study on polymer-derived amorphous silicon carbonitride. *Ceram. Int.* 2017; 43, 13560-13564.
71. Duan W., Yin X., Li Q., Schlier L., Greil P., Travitzky N. A review of absorption properties in silicon-based polymer derived ceramics. *J. Eur. Ceram. Soc.* 2016; 36, 3681-3689.
72. Ionescu E., Balan C., Kleebe H. J., *et al.* High-temperature creep behavior of SiOC glass-ceramics: Influence of network carbon versus segregated carbon. *J. Am. Ceram. Soc.* 2014; 97, 3935-3942.
73. Saha A., Raj R., Williamson D. L. A model for the nanodomains in polymer-derived SiCO. *J. Am. Ceram. Soc.* 2006; 89, 2188-2195.
74. Blum Y. D., Schwartz K. B., Laine R. M. Pre-ceramic polymer pyrolysis - Part 1 Pyrolytic properties of polysilazanes. *J. Mater. Sci.* 1989; 24, 1707-1718.
75. Hurwitz F. I., Farmer S. C., Terepka F. M., Leonhardt T. A. Silsesquioxane-derived ceramic fibres. *J. Mater. Sci.* 1991; 26, 1247-1252.
76. Zeschky J., Höfner T., Arnold C., *et al.* Polysilsesquioxane derived ceramic foams with gradient porosity. *Acta. Mater.* 2005; 53, 927-937.
77. Pantano C. G., Singh A. K., Zhang H. Silicon oxycarbide glasses. *J. Sol-Gel Sci. Technol.* 1999; 14, 7-25.
78. Babonneau F., Thorne K., Mackenzie J. D. Dimethyldiethoxysilane/Tetraethoxysilane Copolymers: Precursors for the Si-C-O System. *Chem. Mater.* 1989; 1, 554-558.
79. Ellis R. B. Method of making electrically conducting glass and articles made therefrom. *United States Pat Off.* 1951; 2,556,616.

80. Kleebe H. J., Gregori G., Babonneau F., Blum Y. D., MacQueen D. B., Masse S. Evolution of C-rich SiOC ceramics. *Int. J. Mater. Res.* 2006; 97, 699-709.
81. Blum Y. D., MacQueen D. B., Kleebe H. J. Synthesis and characterization of carbon-enriched silicon oxycarbides. *J. Eur. Ceram. Soc.* 2005; 25, 143-149.
82. Sasaki Y., Nishina Y., Sato M., Okamura K. Raman study of SiC fibres made from polycarbosilane. *J. Mater. Sci.* 1987; 22, 443-448.
83. Dasgupta K., Sathiyamoorthy D. Disordered carbon - Its preparation, structure, and characterisation. *Mater. Sci. Technol.* 2003; 19, 995-1002.
84. Trassl S., Motz G., Rössler E., Ziegler G. Characterisation of the free-carbon phase in precursor-derived SiCN ceramics. *J. Non Cryst. Solids.* 293-295 (2001) 261-267.
85. Wang K., Ma B., Li X., Wang Y., An L. Structural evolutions in polymer-derived carbon-rich amorphous silicon carbide. *J. Phys. Chem. A.* 2015; 119, 552-558.
86. Cordelair J., Greil P. Electrical conductivity measurements as a microprobe for structure transitions in polysiloxane derived Si-O-C ceramics. *J. Eur. Ceram. Soc.* 2000; 20, 1947-1957.
87. Monthieux M., Delverdier O. Thermal Behavior of (Organosilicon) Polymer-Derived Ceramics. V: Main Facts and Trends. *J. Eur. Ceram. Soc.* 1996; 16, 721-737.
88. Kriegner D., Matěj Z., Kužel R., Holý V. Powder diffraction in bragg-brentano geometry with straight linear detectors. *J. Appl. Crystallogr.* (2015); 48, 613-618.
89. Berthomieu C., Hienerwadel R. Fourier transform infrared (FTIR) spectroscopy. *Photosynth. Res.* 2009; 101, 157-170.
90. Griffiths P. R. Fourier Transform Infrared Spectrometry. *Science.* 1983.
91. Michelson A. A. XXVIII. Visibility of interference-fringes in the focus of a telescope. *London, Edinburgh, Dublin Philo.s Mag. J Sci.* 1891; 31.
92. Webb P. A.. Volume and Density Determinations for Particle Technologists. Micromeritics Instrument Corp. 2/16/01.
93. Nguyen H. G. T., Horn J. C., Bleakney M., Siderius D. W., Espinal L. Understanding material characteristics through signature traits from helium pycnometry. *Langmuir.* 2019; 35.
94. Nowak D., Ortyl J., Kamińska-Borek I., Kukuła K., Topa M., Popielarz R. Photopolymerization of hybrid monomers: Part I: Comparison of the performance of selected photoinitiators in cationic and free-radical polymerization of hybrid monomers. *Polym. Test.* 2017; 64, 313-320.
95. Neumann M. G., Miranda W. G., Schmitt C. C., Rueggeberg F. A., Correa I. C. Molar extinction coefficients and the photon absorption efficiency of dental photoinitiators and light curing units. *J. Dent.* 2005; 33, 525-532.
96. Harshe R., Balan C., Riedel R. Amorphous Si(Al)OC ceramic from polysiloxanes: Bulk ceramic processing, crystallization behavior and applications. *J. Eur. Ceram. Soc.* 2004; 24, 3471-3482.
97. Moysan C., Riedel R., Harshe R., Rouxel T., Augereau F. Mechanical characterization of a polysiloxane-derived SiOC glass. *J. Eur. Ceram. Soc.* 2007; 27, 397-403.
98. Takahashi T., Kachta J., Mümstedt H. Melt rheology and structure of silicone resins. *Rheol. Acta.* 2001; 40, 490-498.
99. Alcaraz A. M., Maria Schmidt J. E., Colombo P., Martinez C. Fabrication of ceramic particles from preceramic polymers using stop flow lithography. *J. Eur. Ceram. Soc.* 2021; 41, 3314-3320.
100. Scherzer T., Decker U. Real-time FTIR-ATR spectroscopy to study the kinetics of ultrafast photopolymerization reactions induced by monochromatic UV light. *Vib. Spectrosc.* 1999; 19, 385-

398.

101. Udofia E. N., Zhou W. Microextrusion based 3D printing - A review. *Solid Free Fabr. 2018 Proc. 29th Annu. Int. Solid Free Fabr. Symp. - An Addit. Manuf. Conf. SFF 2018*. Published online 2020, 2033-2060.
102. Yang J., Wang H., Zhou B., Shen J., Zhang Z., Du A.. Versatile Direct Writing of Aerogel-Based Sol-Gel Inks. *Langmuir*. 2021; 37, 2129-2139.
103. Cao Y., Zhou L., Wang X., Li X., Zeng X. MicroPen direct-write deposition of polyimide. *Microelectron Eng.* 2009; 86, 1989-1993.
104. Wang J., Shaw L. L. Rheological and extrusion behavior of dental porcelain slurries for rapid prototyping applications. *Mater. Sci. Eng. A*. 2005; 397, 314-321.
105. Paxton N., Smolan W., Böck T., Melchels F., Groll J., Jungst T. Proposal to assess printability of bioinks for extrusion-based bioprinting and evaluation of rheological properties governing bioprintability. *Biofabrication*. 2017; 9 (4).
106. Ouyang L., Yao R., Zhao Y., Sun W. Effect of bioink properties on printability and cell viability for 3D bioplotting of embryonic stem cells. *Biofabrication*. 2016; 8(3).
107. Khalil S., Sun W. Biopolymer deposition for freeform fabrication of hydrogel tissue constructs. *Mater. Sci. Eng. C*. 2007; 27, 469-478.
108. Li M., Tian X., Schreyer D. J., Chen X. Effect of needle geometry on flow rate and cell damage in the dispensing-based biofabrication process. *Biotechnol Prog.* 2011; 27, 1777-1784.
109. Boley J. W., White E. L., Chiu G. T. C., Kramer R. K. Direct writing of gallium-indium alloy for stretchable electronics. *Adv. Funct. Mater.* 2014; 24, 3501-3507.
110. Blake Perez K., Williams C. B. Characterization of in-situ conductive paste extrusion on polyjet substrates. *25th Annu. Int. Solid Free Fabr. Symp; An Addit. Manuf. Conf SFF 2014*.
111. Lebel L. L., Aissa B., El Khakani M. A., Therriault D. Ultraviolet-assisted direct-write fabrication of carbon nanotube/polymer nanocomposite microcoils. *Adv. Mater.* 2010; 22, 592-596.
112. Bouyer E., Schiller G., Müller M., Henne R. H. Thermal plasma chemical vapor deposition of si-based ceramic coatings from liquid precursors. *Plasma Chem. Plasma Process.* 2001; 21, 523-546.
113. Colombo P., Martucci A., Fogato O., Villoresi P. Silicon Carbide Films by Laser Pyrolysis of Polycarbosilane. *J. Am. Ceram. Soc.* 2001; 84, 224-226.
114. Danko G. A., Silbergliitt R., Colombo P., Pippel E., Woltersdorf J. Comparison of microwave hybrid and conventional heating of preceramic polymers to form silicon carbide and silicon oxycarbide ceramics. *J. Am. Ceram. Soc.* 2000; 83, 1617-1625.
115. Pivin J. C., Colombo P. Ceramic coatings by ion irradiation of polycarbosilanes and polysiloxanes: Part I Conversion mechanism. *J. Mater. Sci.* 1997; 32, 6163-6173.
116. Ishihara S., Gu H., Bill J., Aldinger F., Wakai F. Densification of precursor-derived Si-C-N ceramics by high-pressure hot isostatic pressing. *J. Am. Ceram. Soc.* 2002; 85, 1706-1712.
117. Wan J., Gasch M. J., Mukherjee A. K. Silicon Nitride – Silicon Carbide Nanocomposites Fabricated by. *J. Am. Ceram. Soc.* 2002; 86, 526-528.
118. Ribeiro A., Blokzijl M. M., Levato R., et al. Assessing bioink shape fidelity to aid material development in 3D bioprinting. *Biofabrication*. 2018;10 (1).
119. Therriault D., White S. R., Lewis J. A. Rheological behavior of fugitive organic inks for direct-write assembly. *Appl. Rheol.* 2007; 17, 1-8.
120. Paquien J. N., Galy J., Gérard J. F., Pouchelon A. Rheological studies of fumed silica-

- polydimethylsiloxane suspensions. *Colloids Surfaces A Physicochem. Eng. Asp.* 2005; 260, 165-172.
121. Raghavan S. R., Walls H. J., Khan S. A. Rheology of silica dispersions in organic liquids: New evidence for solvation forces dictated by hydrogen bonding. *Langmuir.* 2000; 16, 7920-7930.
  122. Faes M., Vleugels J., Vogeler F., Ferraris E. Extrusion-based additive manufacturing of ZrO<sub>2</sub> using photoinitiated polymerization. *CIRP J. Manuf. Sci. Technol.* 2016; 14, 28-34.
  123. Schwab A., Levato R., D'Este M., Piluso S., Eglin D., Malda J. Printability and Shape Fidelity of Bioinks in 3D Bioprinting. *Chem. Rev.* 2020; 120, 1028-11055.
  124. Ouyang L., Yao R., Zhao Y., Sun W. Effect of bioink properties on printability and cell viability for 3D bioplotting of embryonic stem cells. *Biofabrication.* 2016; 8 (3).
  125. Nan B., Galindo-Rosales F. J., Ferreira J. M. F. 3D printing vertically: Direct ink writing free-standing pillar arrays. *Mater. Today.* 2020; 35, 16-24.
  126. Jiang F., Wörz A., Romeis M., Drummer D. Analysis of UV-Assisted direct ink writing rheological properties and curing degree. *Polym. Test.* 2022; 105, 107428.
  127. Clarkson C. M., Wyckoff C., Parvulescu M. J. S., Rueschhoff LM, Dickerson MB. UV-assisted direct ink writing of Si<sub>3</sub>N<sub>4</sub>/SiC preceramic polymer suspensions. *J. Eur. Ceram. Soc.* 2022; 42, 3374-3382.
  128. Li Z., Chen Z., Liu J., *et al.* Additive manufacturing of lightweight and high-strength polymer-derived SiOC ceramics. *Virtual Phys. Prototyp.* 2020; 15, 163-177.
  129. Kumar R., Jain H., Sriram S., *et al.* Lightweight open cell aluminum foam for superior mechanical and electromagnetic interference shielding properties. *Mater. Chem. Phys.* 2020; 240, 122274.
  130. Huang K., Elsayed H., Franchin G., Colombo P. Additive manufacturing of SiOC scaffolds with tunable structure-performance relationship. *J. Eur. Ceram. Soc.* 2021; 41, 7552-7559.
  131. Peña-Alonso R., Sorarù G. D., Raj R. Preparation of ultrathin-walled carbon-based nanoporous structures by etching pseudo-amorphous silicon oxycarbide ceramics. *J. Am. Ceram. Soc.* 2006; 89, 2473-2480.
  132. Li Z. Q., Lu C. J., Xia Z. P., Zhou Y., Luo Z. X-ray diffraction patterns of graphite and turbostratic carbon. *Carbon.* 2007; 45, 1686-1695.
  133. Ma R., Erb D., Lu K. Flash pyrolysis of polymer-derived SiOC ceramics. *J. Eur. Ceram. Soc.* 2018; 38, 4906-4914.
  134. Ma R., Lu K., Erb D. Effect of solvent in preparation of SiOC bulk ceramics. *Mater. Chem. Phys.* 2018; 140-146.
  135. Saha A., Raj R. Crystallization maps for SiCO amorphous ceramics. *J. Am. Ceram. Soc.* 2007; 90, 578-583.
  136. Xu T., Ma Q., Chen Z. High-temperature behavior of silicon oxycarbide glasses in air environment. *Ceram. Int.* 2011; 37, 2555-2559.
  137. Wu K. C., Halloran J. W. Photopolymerization monitoring of ceramic stereolithography resins by FTIR methods. *J. Mater. Sci.* 2005; 40, 71-76.
  138. Kabac J., Kostrzewska K., Jurek K. Squaric acid derivative effects on the kinetics of photopolymerization of different monomers. *RSC Adv.* 2016; 6, :74715-74725.
  139. Huang K., Elsayed H., Franchin G., Colombo P. Complex SiOC ceramics from 2D structures by 3D printing and origami. *Addit. Manuf.* 2020; 33, 101144.
  140. Liu G., Zhao Y., Wu G., Lu J. Origami and 4D printing of elastomer-derived ceramic structures. *Sci. Adv.* 2018; 4, 1-11.

